Max-Planck Institut für Kolloid- und Grenzflächenforschung
_____

Salts as Highly Diverse Porogens:

Functional Ionic Liquid-Derived Carbons and Carbon-Based Composites for Energy-Related Applications

Dissertation

zur Erlangung des akademischen Grades
"doctor rerum naturalis"
(Dr. rer. nat.)
in der Wissenschaftsdisziplin „Kolloidchemie"

Eingereicht an der
Mathematisch-Naturwissenschaftlichen Fakultät
der Universität Potsdam

von

Nina Fechler

Geboren am 11.10.1985 in Kassel

Potsdam, den 28.11.2012

Table of contents

1. Introduction

1.1. Motivation

Nanotechnology In recent years the terms "Nanoscience" and "Nanotechnology" became ubiquitous in science, industry as well as everyday life. However, it is quite challenging to give a general definition due to the wide variety of different disciplines which have been pooled. Focusing on the actual fundamental principles instead of certain examples, nanoscience may be summarized as investigation, manipulation and application of everything which deals with structures that are at least in one dimension smaller than 100 nm. While in the past research was separated into classical fields such as chemistry, physics, biology and mathematics it turned out that for natural phenomena in the sub-micrometer range classical schemes are not applicable anymore but rather requires interdisciplinary approaches. This opened the way into a barely explored world which was already envisioned by Noble laureate Richard Feynman in his lecture "There is plenty of room at the bottom" from 1959 which is often considered as a seminal inspiration for future research.[1] Another prominent and revolutionary invention was the scanning tunneling microscope in 1981 which enabled the visualization of the world on the atomic scale for the first time. By down-scaling dimensions, material surface properties gain major relevance and the manipulation of matter on the molecular level enables exciting new material properties which are different from the bulk.

Economy The tremendous impact of Nanotechnology on the world's economy may be illustrated by the massive investments by government in this research. According to the 2007 nanotechnology White Paper by the U.S. Environmental Protection Agency (EPA) 1.3 billion $ were invested on nanotechnology-related activities in 2006. These were coordinated by the National Nanotechnology Initiative (NNI) who support nanotechnology-based fundamental research as well as the development of respective devices and systems.[2] In a press release of the German Bundesministerium für Bildung und Forschung from 2007 a total of 1.5 billion € is earmarked for nanotechnology under the 7th EU Research Framework Program up to 2013.[3] One of the most famous forecasts of future nanotechnology world market by the National Science Foundation (NSF) of the United States predicts an continuously increasing market share for nanotechnology-related products (*Figure 1-1*).
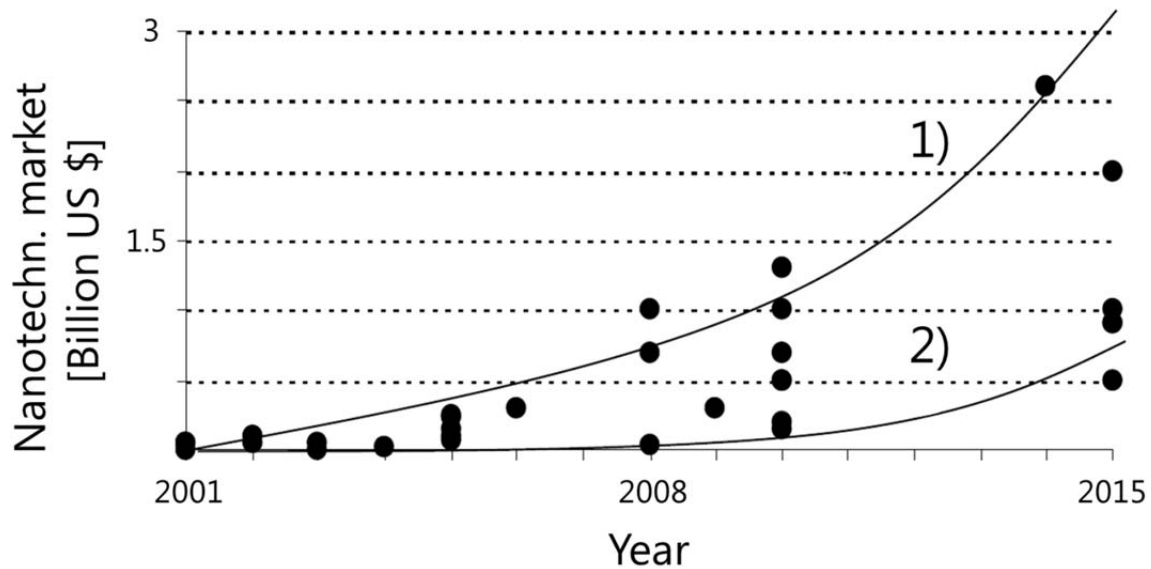
Figure 1-1 Forecast for Nanotechnology: World market, 1) optimistic 2) pessimistic scenario.[4]

For the largest shares of nanotechnology-based materials, electronics, pharmaceuticals and chemical processing are forecasted to be responsible.[4] The potential of nanotechnology can be illustrated by the diversity of already existing products. Nowadays, *e.g.* consumer electronics, vehicle industry, sports equipment and grooming items are just a few examples that experienced influx from nanotechnology. However, regarding a steady growing population and as a consequence thereof increased environmental impacts and resource consumption, more efficient and sustainable technologies are inevitable.

Carbon Facing the challenge to maintain current living standards while sparing the environment, carbon, "the sixth element",[5] in particular has become the material of choice in many fields.[6] Some major advantages of carbon include its almost ubiquitous availability, low cost, safety and its multifaceted properties such as high electrical conductivity, thermal and chemical stability which can be influenced by a range of different approaches. In the past half-century, *e.g.* communication, computing or sensors were based on semiconductor technologies. Those materials were mainly silicon-based which even coined the famous term "Silicon Valley" for the high-tech business San Francisco bay area. However, in the course of an exponential growth of computing power and miniaturization for cost reduction, silicon technology is expected to reach its fundamental limits. Thus, revolutionary new approaches as well as device designs are required. Among others the discovery of new nanostructured carbon allotropes such as graphene, fullerenes or nanotubes let to an increased interest in carbon-based materials sometimes even referred to "the new carbon age".[7] Here, the enormous impact of nanostructure on material properties again becomes visible since

all those allotropes reveal completely different properties. Besides the new carbon allotropes, a further very prominent class is nanoporous carbon. It already found application *e.g.* in waste water treatment, catalysis, filters and gas storage. Furthermore, a highly relevant utilization of porous carbon materials is dedicated to energy-related applications such as cathode material for the oxygen reduction reaction (ORR) in fuel cells or for energy-storage in supercapacitor and battery electrodes.[8-15]

In spite of the already accomplished progress, one major challenge in developing new materials for certain applications includes the understanding of the structure-property relation. Here, not only the actual composition but also the morphology of a material influences its properties which accentuates the essence of Nanotechnology. Therefore, much effort has been expended on the synthesis and investigation of nanostructured carbon and carbon-based materials.

Composition In this context, it is a well-known concept that the introduction of heteroatoms *i.e.* nitrogen, boron, sulfur or phosphor can amplify the carbon material properties. Here, it has to be distinguished between surface and structural functionalities. For example while surface amine groups cause Brønsted-basicity, the introduction of structural nitrogen affects *e.g.* the electrical conductivity and chemical stability.[16-19] Common techniques for the synthesis of nitrogen-doped carbons (N-doped carbons) include the thermolysis or chemical vapor deposition of nitrogen-rich precursors[20, 21] as well as the post-functionalization of carbon materials in a nitrogen-containing atmosphere.[22-24] Recently, our group and others presented ionic liquids as versatile precursors for the synthesis of nitrogen- and nitrogen-boron-co-doped carbons (N-B-co-doped carbons).[25-38] Since ionic liquids are salts which are liquid below 100 °C with a negligible vapor pressure, simple handling and processing is possible while no special technical equipment is required. Furthermore, the liquid state also enables for casting, molding or printing. Thereby, the introduction of surface area, which is inevitable for a range of applications, is facilitated as such. First examples of structured ionic liquid-derived N-doped carbons by employing hard-templates were reported by Paraknowitsch *et al.* and imply the enormous potential of ionic liquids in materials science.[27]

In addition, the properties of carbon materials can be complemented by the introduction of other species such as metals or metal compounds through composite formation. Thereby, the benefits of different materials may be combined by synergistic interactions which results in superior performance also on the device level. For example, a carbon support possesses high conductivity and porosity while a metal species may add properties such as catalytic or redox activity. Current state-of-the-art systems are

composed of precious metal nanoparticles *e.g.* platinum or palladium deposited on porous carbons.[39] However, this comprises high costs whereas the performances are still moderate. Therefore, the research on the development of alternative nonprecious metal-based systems, preferentially within a scalable one-step procedure, has gained much attention.[40, 41]

Morphology The material properties do not only depend on the actual composition but also on the morphology. For example, a highly porous material is able to absorb a considerable amount of a gas species while its bulk counterpart would not be suitable at all. In addition to the surface area, the pore size and pore connectivity is crucial which might be best illustrated with two actual applications: while for gas or energy storage small pores with a very narrow size distribution are important, for catalytic applications a hierarchical and interconnected pore structure is essential. At present, for the introduction of an adequate porosity state-of-the-art techniques are templating or activation methods.[42-46] However, these procedures bring along certain drawbacks such as multiple time- and energy-consuming synthesis steps, low yield or the utilization of hazardous chemicals prohibiting industrial applications. Therefore, it is safe to state that additional, simple and sustainable techniques to address high surface area materials with controllable porosity are highly welcomed.

Thesis approaches Within the present work different approaches will be introduced to address the mentioned issues regarding the need for alternative, facile and sustainable methods for the production of carbon and carbon-based composite materials which are suitable for energy-related applications. Special focus is set on alternative strategies to synthesize porous materials with tunable composition and morphology on exactly the required length scale so that each material can be tailor-made for a certain application. All materials have in common that they are based on ionic liquids as versatile precursors for the formation of nanostructured materials.
An overview of the present thesis is given in *Figure 1-2*.

Functional carbons

Salt templating		Template-free
N-dC	N-B-dC	N-S-dC

Eutectics – high T
- micropores
- mesopores
- macropores
  (globule, aerogel-like monolithic)

ZnAc/CsAc
- micropores (CsAc)
- mesopores (ZnAc/CsAc)
- sheets (high ZnAc)

Eutectics – low T
- polymeric networks
- CO$_2$-utilization

Functional carbons – MN composites

Salt templating	Template-free
N-dC	

| VN | TiN | VN | TiVN |

CsAc - synthesis
- micropores
- small mesopores
- bigger nanoparticles

ZnAc - synthesis
- mesopores
- small nanoparticles

ZnAc/CsAc
- tunable pores
- tunable particle size

CsAc - application
- supercapacitors

- metal nitrides@N-dC
- binary and ternary nitrides
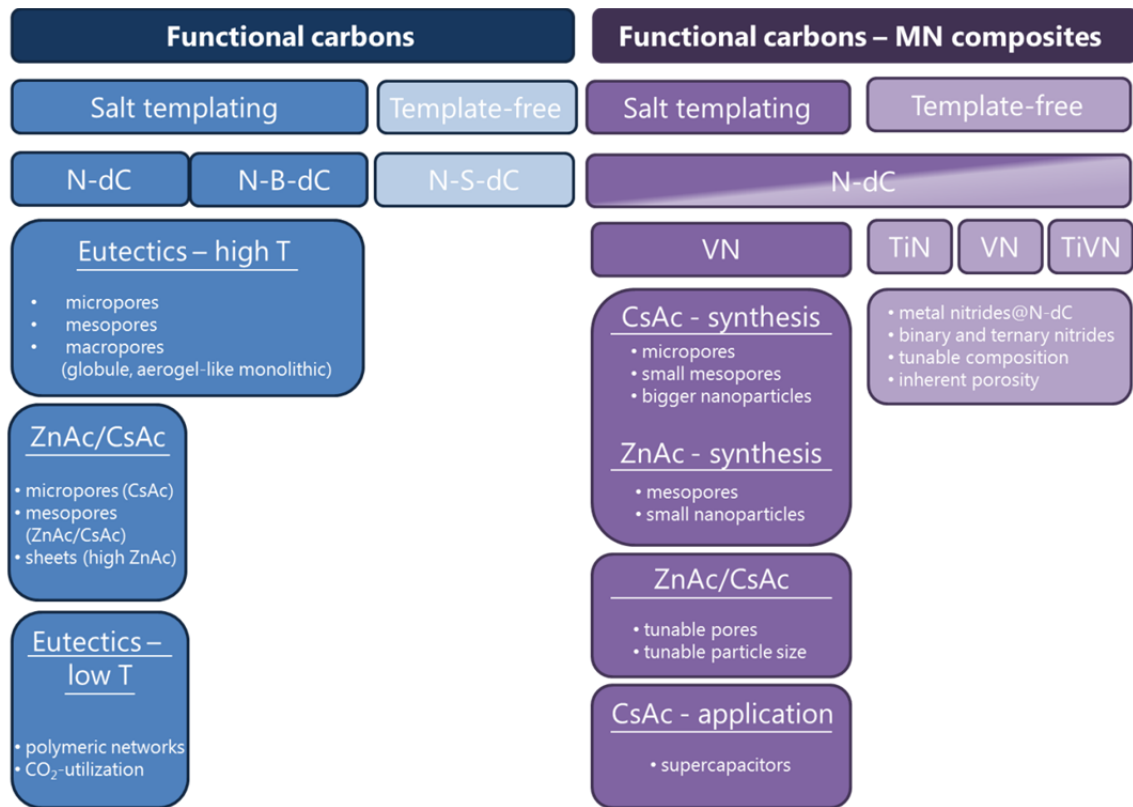- tunable composition
- inherent porosity

Figure 1-2 Overview of topics and approaches covered within this thesis.

The second chapter focusses on heteroatom-containing carbon materials. A new method we call "salt templating" will be introduced as alternative, simple and sustainable tool to control the materials' morphology especially on the nanometer scale. In more detail, through the synthesis of ionic liquid-derived highly porous N- and N-B-co-doped carbons, the applicability of ordinary salts as diverse porogens is presented. Here, the ionic liquid is mixed with a non-carbonizable inorganic salt prior to the heat-treatment in an inert gas-atmosphere. After the carbon formation through condensation and scaffolding in the presence of the molten inorganic salt at elevated temperatures, the porogen phase can easily be removed by simple washing with water. Ensuring a homogeneous mixture of both, the carbonizing and porogen salt during the main reaction process leads to highly porous functional carbons in high yield. The avoidance of hazardous chemicals and the possibility of porogen salt recycling render this approach a sustainable closed-loop process. Different salts *i.e.* eutectic mixtures (LiCl/ZnCl$_2$, NaCl/ZnCl$_2$ and KCl/ZnCl$_2$), zinc acetate dihydrate (ZnAc) and cesium acetate (CsAc), will be applied for the synthesis of functional carbons with morphologies ranging from micro- to mesoporous. While for some materials even globule- and aerogel-like monolithic structures can be obtained, others show unusually high surface areas and pore volumes of up to 2000 m^{2}g^{-1} and 2.75 mlg^{-1}, respectively. In general, the composition of the materials can be tuned by the heat-treatment

procedure. Thus, N-containing carbons synthesized at lower temperatures (450 °C) still reveal a polymer-like structure with a high amount of functional groups. This renders these networks suitable for CO_2-utilization. Indeed, preliminary CO_2-sorption measurements reveal the materials to show promising properties and performance. To expand the range of functional carbons based on ionic liquids, the ionic liquid 1-Ethyl-3-methyl thiocyanate (Emim-scn) is introduced as versatile precursor for the synthesis of nitrogen-sulfur-co-doped carbon (N-S-co-doped carbon).

The third chapter is concerned with the synthesis and characterization of composite materials constituted of metal nitride nanoparticles and N-doped carbon. Here, metal nitrides just recently arouse interest as supplement for precious metals because of their outstanding properties such as high temperature and chemical stability, wear resistance, hardness and tunable properties in ternary compounds. Yet, their utilization is far from being established. In the present thesis, titanium and vanadium nitride were chosen because their electronic properties are of additional interest. Through simple mixing of metal precursors with an ionic liquid followed by heat-treatment, the respective metal nitride composites can be generated which possess an inherent porosity. The metal nitride amount as well as the metal ratio in ternary nitrides are easily controllable by the initial metal precursor amount and ratio, respectively. Hence, compared to conventional energy-consuming and barely controllable routes, this one-pot approach offers a simple and effective alternative towards porous composites of metal nitrides without the need for any template.

In the fourth chapter both concepts presented in chapter two and three will be combined, *i.e.* salt templating and the one-pot synthesis of metal nitride containing N-doped carbons. This offers the opportunity not only to generate composite materials with tunable composition within a one-pot approach, but also allows for the precise control over the porosity and morphology. Thus, the two crucial adjusting parameters *composition* and *morphology* are addressable individually while keeping synthesis steps, energy-consumption and costs comparatively low. Here, access to adjustability granted by salt templating will also be delineated on the device level by employing the composites as electrodes for supercapacitors.

1.2. Basic concepts

1.2.1. Functional carbons from ionic liquids

In general, the term ionic liquid describes a salt which is liquid below a temperature of 100 °C. Compared to common salts *e.g.* sodium chloride, ionic liquids usually consist of organic and bulky ions which hamper the formation of a crystal lattice, eventually expanding the liquid state. Thus, as opposed to aqueous solutions, they are solvents which solely consist of ions resulting in a variety of differences in chemical and physical properties.

The first report on ionic liquids dates back to 1914, when P. Walden described ethylammonium nitrate.[47] However, except for a few further examples in the past decades, research on ionic liquids became prominent just recently.[48, 49] Some of their outstanding properties beside the wide range of liquidus include low vapor pressure due to the ionic character, thermal stability, high ionic conductivity, a large electrochemical window, non-flammability and a high solvation potential for a range of substances. Furthermore, through the modification and combination of the ions the properties of an ionic liquid can carefully be adjusted. Nowadays, ionic liquids are ubiquitous in fundamental research as well as industry with their applications ranging from electrolytes in commercial batteries or supercapacitors over reaction solvents to protein stabilization agents.[50]

Just recently, the application potential of ionic liquids was extended to their successful use as precursors for functional carbon materials. [25-38] It is generally known that the introduction of secondary elements *e.g.* nitrogen,[51-53] boron,[28, 29, 54-57] sulfur[58-62] or phosphor[63-65] in the structure of carbon can modify and enhance certain properties of the materials. In this regard, most research has been done on N-doped carbons and it was shown that the introduction of structural nitrogen into the carbon matrix affects and often improves electrical conductivity, basicity and oxidation stability. This eventually increases the material's performance in catalysis, gas or energy storage, just to mention some examples.

Commonly, N-doped carbon materials are synthesized either *via* a post-treatment of carbon materials in a N-containing atmosphere, *e.g.* ammonia,[22-24] or by *in situ* processes such as thermolysis or chemical vapor deposition of Nn-rich precursors. Frequently used precursors are melamine,[20, 21] N-containing heterocyclic compounds[66] or acetonitrile.[67] However, all these methods suffer from multiple and thus time- as well as energy-consuming processing steps, restrictions due to solvent evaporation and heterogeneous products within solid state reactions.

1 Introduction

In this regard, especially the liquid state accompanied by negligible vapor pressure and the enormous structural diversity render ionic liquids highly suitable precursors for heteroatom-doped carbon materials. Here, the ionic character is a key property compared to common precursors since it hinders the evaporation loss during the initial heating-process and thus promotes the solid-formation. Furthermore, decomposition products might be trapped by Coulomb interaction for further reactions which results in an efficient implementation of the precursor components in the final product. This is supported by experiments with the respective uncharged relatives of the ionic liquids, which did not yield any char formation.[25]

However, the ionic liquids need to fulfill certain prerequisites for the successful generation of carbon materials without *e.g.* high pressure or confined carbonization.[68] Within careful mechanistic studies on the product formation of ionic liquid derived N-doped carbons by Paraknowitsch *et al.* and Fellinger *et al.*, it was shown that functional groups which are capable to perform polymerization reactions at comparable low temperatures are required to avoid complete evaporation. It turned out that cyano functionalities meet this condition and should be present either in the anion or in the cation, as they undergo trimerization reactions in the course of heat-treatment.[31] Additionally, the cation needs to contain structural nitrogen. Recently, Fellinger *et al.* further revealed detailed insights into the formation mechanism of ionic liquid-derived N-B -containing carbons.[28, 29]

Some ionic liquids which were already applied as precursors for the formation of heteroatom-containing carbon materials are shown in *Figure 1-3*.
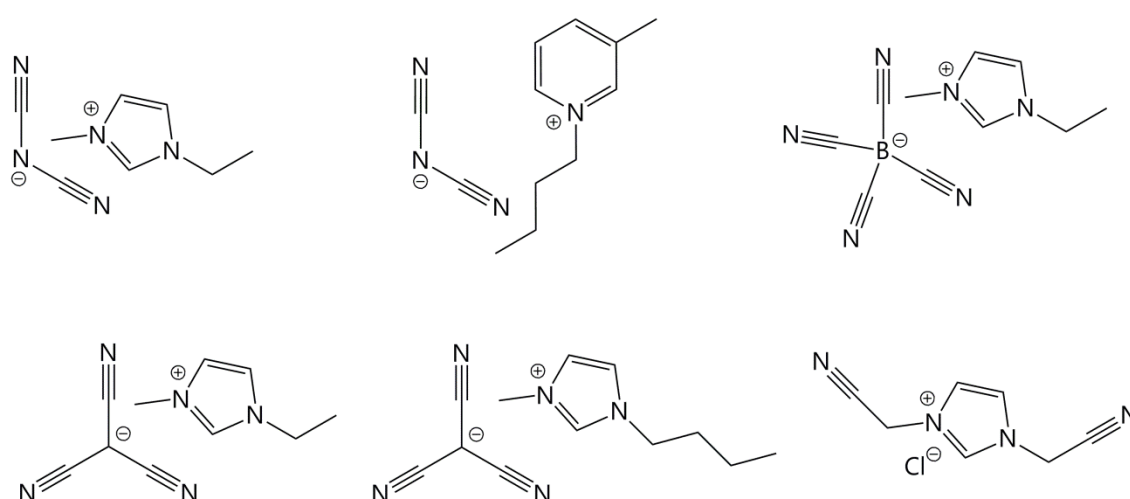

Figure 1-3 Chemical structures of some ionic liquids suitable as carbon precursors.[29, 31, 35]

1 Introduction

In the present thesis, most studies were carried out with the three ionic liquids 1-Butyl-3-methyl-pyridinium dicyanamide (Bmp-dca), 1-Ethyl-3-methyl-imidazolium dicyanamide (Emim-dca) and 1-Ethyl-3-methyl-imidazolium tetracyanoborate (Emim-tcb) because they allow for a systematic comparison. Here, Bmp-dca and Emim-tcb possess either identical cations or anions with regard to Emim-dca. Thus, in the following passages the processes occurring during the thermolysis of the N-(1.2.1.1.) and N-B-containing (1.2.1.2.) ionic liquids will be described in more detail.

1.2.1.1. Product formation pathways – N-doped carbons

Since the research exploring ionic liquids as precursors for heteroatom-containing carbons started just recently, only few is known and reported.

Some hints for possible reactions occurring during the heat-treatment of ionic liquids can be found in a study of Wooster *et al.* who investigated the thermal stability of ionic liquids.[69] They recognized an incomplete decomposition in an inert gas atmosphere and proposed a reverse Menschutkin reaction to take place resulting in an alkyl dicyanamide and the respective cation derivate. This was also described by Ohtani *et al.* for the heat-treatment of imidazolium-based ionic liquids (*Figure 1-4*).[69, 70]
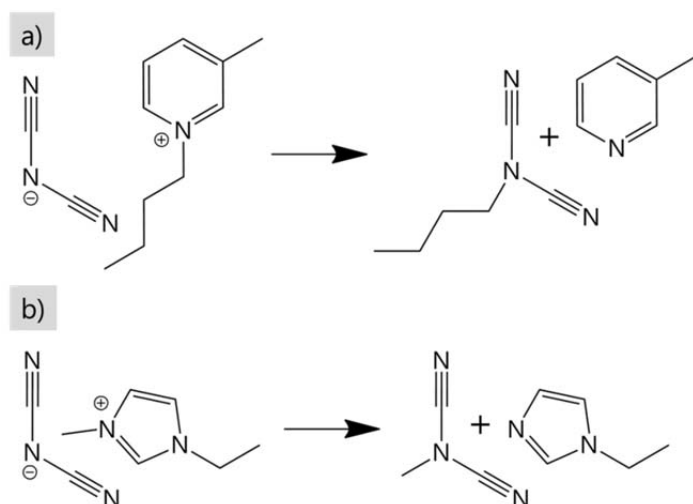

Figure 1-4 Reverse Menschutkin reaction occurring during thermolysis of **a)** Bmp-dca and **b)** Emim-dca.

Besides alkyl fragmentation, the condensation of cyano groups also known from other materials is a further reaction which may occur during the thermally induced decomposition of ionic liquids (*Figure 1-5*).[25, 69-71]
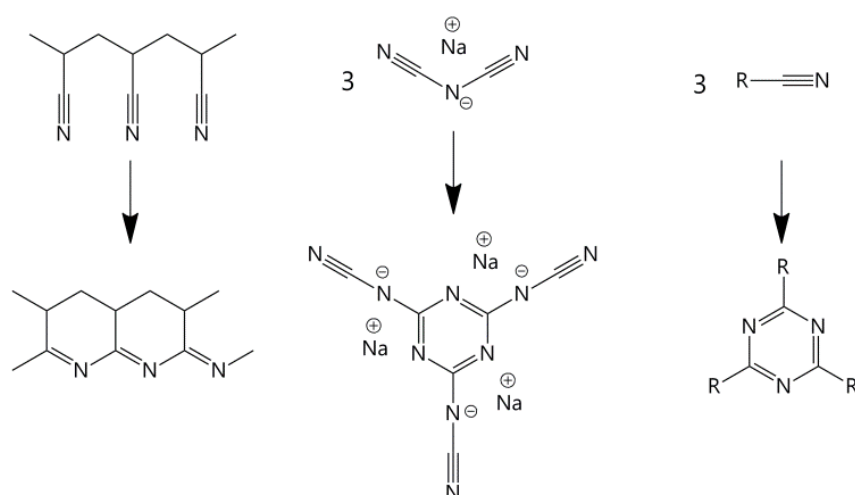
Figure 1-5 Examples for the condensation of different cyano groups.

However, it can be excluded that only the polymerization of the anion contributes to the carbon formation since the products derived from thermal treatment at moderate temperatures show different compositions. The incorporation of the cation structure was also revealed within detailed investigations by Paraknowitsch and co-workers.[25, 26] An overview of the different reaction pathways occurring during carbonization of the ionic liquids up to 500 – 600 °C is exemplarily given for Emim-dca in *Figure 1-6*.
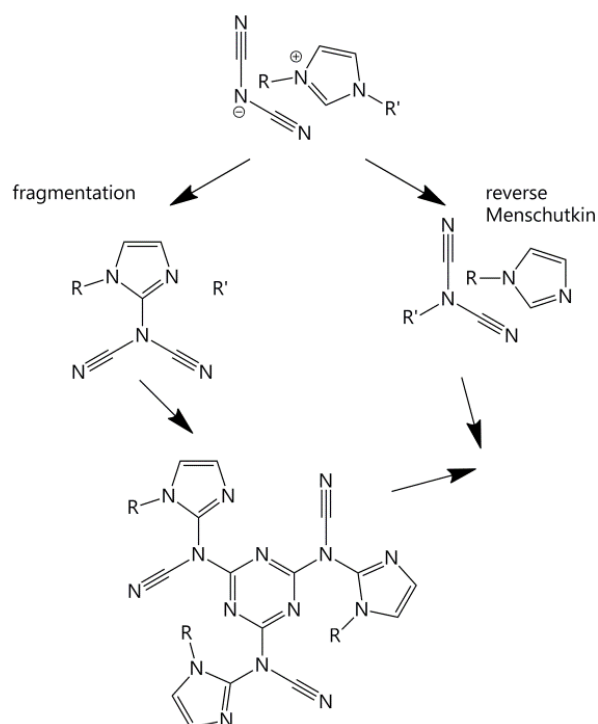
Figure 1-6 Possible reaction pathways of a dicyanamide-based ionic liquid, here exemplified with Emim-dca, during thermal treatment leading to carbon formation.[25, 28]

1 Introduction

At temperatures of around 300 °C the product formation sets in for both Emim-dca and Bmp-dca. Induced through the reverse Menschutkin reaction and alkyl fragmentation which may also be accompanied by elimination of ammonia, the nucleophilic dicyanamide can attack on the aromatic cations. Further cycloaddition is expected to generate branched polymer-like triazine-networks which can rearrange in the ongoing condensation process of the aromatic system. At around 400 - 500 °C, insoluble chars are formed. Upon a temperature increase up to 1000 °C graphitic carbon materials are generated through elimination of nitrogen and hydrogen.

1.2.1.2. Product formation pathways
– N-B-co-doped carbons

Besides N-doped carbons, practical and theoretical studies on N-B-co-containing carbons already suggested their promising properties.[54, 55, 57, 72] However, research on heteroatom-doped carbons containing heteroatoms other than nitrogen is just at its beginning. Thus, relatively few is known about possible synthesis strategies or the physicochemical properties of the respective materials. On that account, much room is left for investigations in this wide field.

Taking into account the findings for N-doped carbons derived from Bmp-dca and Emim-dca, among others,[36, 73] our group aimed to continue the story of carbons from ionic liquid precursors towards different dopants. Here, Fellinger *et al.* were recently able to obtain N-B-co-containing carbons *via* thermolysis of the ionic liquid Emim-tcb (*Figure 1-7*).[28, 29]
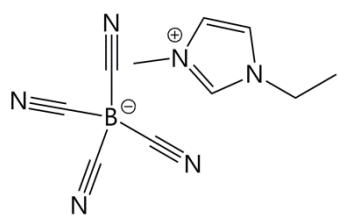
Figure 1-7 Chemical structure of Emim-tcb.

The processes which occur during carbonization of Emim-tcb eventually leading to char formation were also conducted within detailed mechanistic studies.[28, 29] Since the thermal decomposition of Emim-dca which structurally differs from Emim-tcb only in the anion was already investigated,[26] it is reasonable to compare the characteristics of both ionic liquids. Here, the most striking differences are the nucleophilicity, stability and basicity of the anion. While the dca anion is rather nucleophilic, possesses Lewis basic character and is thermally less stable, the tcb anion is fully coordinated, thus has

low nucleophilicity, low basicity and high thermal stability. Regarding the product formation process this causes a higher decomposition onset temperature of Emim-tcb (416 °C) compared to Emim-dca (321 °C).

As mentioned above for dca-containing IL, alkyl fragmentation and reverse Menschutkin reaction play major roles in the decomposition process. Within thermal stability investigations of imidazolium-based ionic liquids, Ohtani *et al.* proposed the dealkylation of N,N'-dialkylimidazolium which indeed occurs through Hofmann elimination and a reverse Menschutkin reaction for nucleophilic anions.[28, 70] For non-nucleophilic anions the reactions have to be initiated by their decomposition. This explains the higher reaction onset temperature of Emim-tcb compared to Emim-dca. At those elevated temperatures the decomposition of the stable imidazolium ion (thermal stability up to 550 °C) already sets in. Since the decomposition of the anion and cation occur in a narrow temperature range, both ions can effectively be incorporated. This may be the reason for the higher yield of Emim-tcb-derived materials compared to Emim-dca. The processes occurring at moderate temperatures *i.e.* below 600 °C were summarized by Fellinger *et al.* as follows (*Figure 1-8*).
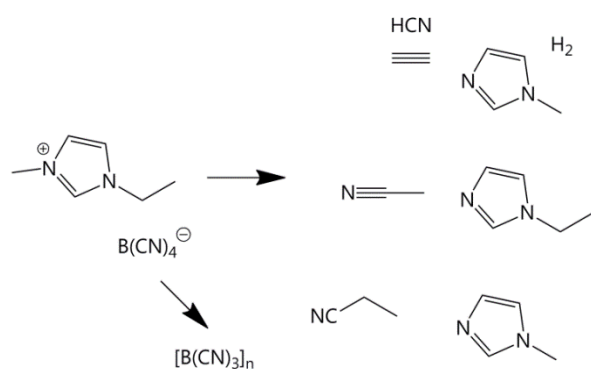

Figure 1-8 Proposed decomposition scheme for the thermolysis of Emim-tcb at lower temperatures (< 600 °C).[28, 29]

In general, the char formation is assumed to be based on the formation of polyimidazole-type networks and cycloaddition of cyanides which introduces triazine-motifs. Furthermore, aromatic substitution or addition reactions may cause cross-linked intermixed networks which finally contain parts of both the cation and anion. At higher temperatures the network further condenses and rearranges, accompanied by the loss of functional groups. Because boron is very oxophilic, the materials synthesized at temperatures up to 1000 °C contain a reasonable amount of oxygen and are better described as BCN(O). Only when the temperature is raised up to 1400 °C, the strong B-O bonds break and oxygen is released in the form of CO and CO_2. Finally, this results in a graphitic carbon material that contains structural boron

and nitrogen with an almost one-to-one ratio of boron and nitrogen. This reflects the isoelectric character of the C and BN bond.

Consolidating the previously discussed observations, an ionic liquid needs to possess at least the following prerequisites to be suitable as precursor for carbon materials:

- polymerizable functional group present either in the cation or in the anion
- nucleophilic ions (optionally generated through thermal decomposition)
- structural nitrogen in the cation
- high temperature stability

1.2.1.3. Further development

Besides the obvious inherent advantages of the liquid state in combination with negligible vapor pressure, the ionic liquid precursors are also very easy to process. For example, techniques like dip-coating, printing, electro spinning or spin coating can be envisioned. Furthermore, the ionic liquids possess good interaction with inorganic templates, thus they can easily be infiltrated which was already presented *e.g.* for porous silica or aluminum oxide.[27]

These techniques allow the application of the materials *e.g.* as electrocatalysts for the ORR in PEM fuel cells,[30, 74] hydrogen peroxide production,[75] supercapacitor electrodes or in gas sorption implementations such as CO_2-storage.[36] This already demonstrates the impressive potential of ionic liquids not only for scientific but also application purposes.

However, as ionic liquids possess exceptional dissolution capabilities for a wide range of substances, the ionic liquid-based route is not limited to standard processing techniques such as hard-templating or pure carbon systems but can be extended through the addition of further additives or precursor substances. This approach is, besides the application of the materials, central purpose of the present thesis. It will be presented in the following chapters throughout the generation of highly porous carbons and carbon-based composites by the combination of ionic liquids with salts and metal precursors.

1.2.2.   Porous carbons: standard preparation techniques

Porous materials are of key importance in many different areas. Several examples can be found in nature *e.g.* the water transportation system in trees or channel proteins in cell membranes. Due to their massive potential, research has focused on the discovery and synthesis of porous materials which gave rise to a wide variety of different material classes such as sol-gel-derived oxides, molecular sieves, porous coordination solids or porous polymers. However, special emphasis is put on porous carbon materials because of their exceptional properties like electrical conductivity, high chemical as well as physical stability and processability while production costs can be kept low.[76] A closer look on the porosities of the different material classes clearly reveals the constantly high and still increasing surface areas of carbon materials (*Figure 1-9*).[77] As can be seen from this graphic, materials with ultrahigh surface areas do exist. However, most of them possess only low gas selectivity.
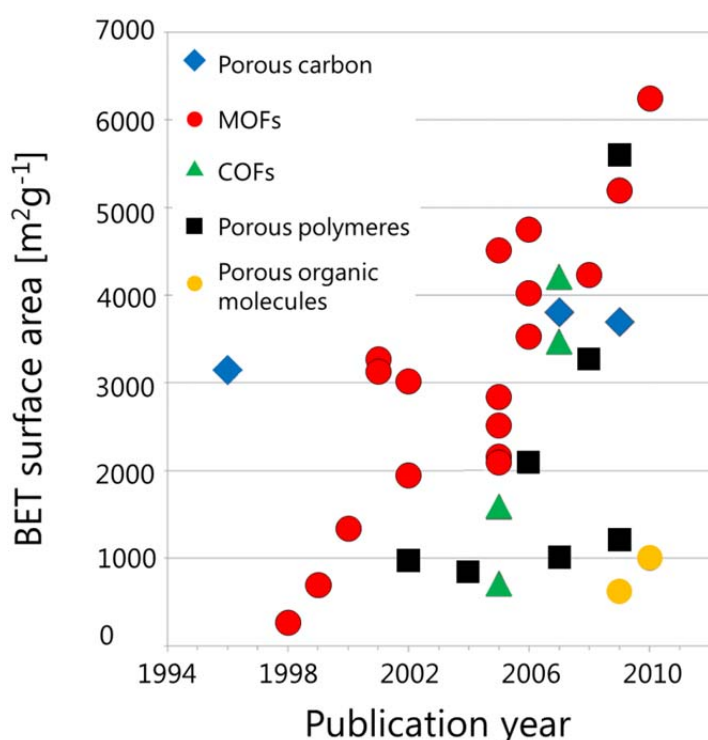
Figure 1-9 Course of the discovery of materials with exceptionally high surface areas in dependence on their publication year. Adapted from Holst and Cooper.[77]

Furthermore, carbon materials are highly suitable as supports, thus the properties of porous carbons can be complemented by those of other material classes, *e. g.* metals or polymers. In most cases, this is realized by impregnation or coating which is easy to perform and allows for additional cost reduction since the amount of precious materials can be minimized. In general, carbon as well as carbon-based composite or hybrid

materials can be found in a range of applications such as catalysts, energy generation and storage devices, adsorption and separation.[78-87] Here, the suitability of a material strongly depends on the match of pore size, pore shape, pore connectivity, surface area as well as the material's morphology with the requirements of a certain application. For example, a material which is supposed to be used for gas storage needs to possess small pores with a narrow size distribution. In contrast, for applications where diffusion and mass transport are essential *e.g.* in catalysis, bigger pores or hierarchical structures with in an interconnected pore system are of advantage. Therefore, the precise control over porosity is crucial and much effort has been expended on the development of the respective techniques.

Following IUPAC conventions,[88] pores can be classified according to their pore diameter d:

> *Microporous materials* : d < 2 nm
> *Mesoporous materials* : 2 nm < d < 50 nm
> *Macroporous materials* : d > 50 nm

Nowadays, suitable methods to tailor the porosity in these dimensions exist for many material classes. However, for carbon materials activation and templating techniques are probably the most important ones.

1.2.2.1.　　**Activation**

Carbon materials in which small pores are introduced to increase the surface area and as a consequence also the adsorption capability are called activated carbons. These mainly microporous carbons with surface areas up to 2500 m^2g^{-1} are commonly prepared from coal, wood, peat or vegetable waste *e.g.* fruit shells by heat-treatment in an inert atmosphere.[46] Recently, much effort has been made to utilize waste materials because it is cheap, abundant and otherwise mass produced occupying waste can be converted into valid products.[89] Sherwood *et al.* used paper mill sludge and Graham *et al.* employed sewage sludge for the successful production of activated carbon.[90, 91] Commonly, activated carbons are applied in water purification, gas separation, sensors, sequestration or energy storage.[45, 92-96] Because microporous carbons are typically highly disordered revealing bent aromatic sheets which are cross-linked by aliphatic bridging groups (*Figure 1-10*), they cannot be tailored by the control over the crystal structure as it is possible for zeolites.[76] However, much is known about the processability of carbon materials, thus they can still be tailored.

Figure 1-10 Schematic illustration of the structure motives occurring in activated carbon. Adapted from reference 97.[97]

In general, carbonaceous materials can be distinguished into graphitizable and non-graphitizable carbons.[76] During the carbonization process of graphitizable carbons, a liquid-crystalline phase occurs where the precursor can transform into stacked parallel sheets. Therefore, graphitizable carbons possess low specific surface areas. In contrast, non-graphitizable carbons undergo crosslinking without the formation of a liquid phase. For this reason, non-graphitizable carbons possess inherent microporosity. However, most of the pores are closed and have to be opened up by activation techniques *i.e.* physical or chemical activation. The former case involves a two-step-process where first the carbon precursor has to be carbonized and second the activation of the formed product can be conducted by exposure to oxidizing gases such as H_2O or CO_2.[45, 76] Here, the fact that some parts of the carbon react faster than others is used to open up closed pores. While in the initial stage new open micropores are created due to removal of secondary carbon from pore entrances, later on pore widening is the main process. Because the activation agent is cheap and gaseous which does not produce any water pollution, physical activation is considered as environmentally benign technique. However, the process is time- and energy-consuming while only low yields are achieved, thus the application of this method is limited. Depending on the precursor, the process of chemical activation can either be performed in one or two steps. In general, a precursor or preformed carbon material is mixed or impregnated with an inorganic chemical activating agent such as H_3PO_4, $ZnCl_2$ or KOH.[98-100] Porous materials are formed by subsequent heat-treatment in an inert atmosphere. Here, the porosity can be influenced by the ratio of activation agent and carbon precursor as well as the temperature. Compared to the physical

activation only few is known about the mechanism of chemical activation. It is assumed that the chemicals act as dehydration agents, thus tar formation is hindered and cross-linking reactions are promoted.[100, 101] Therefore, otherwise volatile species are bonded which leads not only to porous materials but also an increased carbon yield. In the case of activation with potassium hydroxide which was first described by Wennerberg and O'Grady in 1978, another effect has to be taken into account *i.e.* the intercalation of elemental potassium between the as-formed graphene sheets. Simplistically, the chemical activation of carbon with KOH can be summarized with the following reaction.

$$4\ KOH + C \rightarrow K_2CO_3 + K_2O + 2\ H_2$$
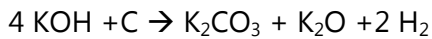
Upon the reaction of amorphous carbon with KOH, potassium carbonate and potassium oxide are formed accompanied by hydrogen evolution.[45] The process of activation was described in more detail by Otowa *et al.* with the following reactions.[102]

Table 1-a Reactions during activation of carbons with KOH.

Below 700 °C		Above 700 °C	
$2\ KOH \rightarrow K_2O + H_2O$	A		
		$K_2O + H_2 \rightarrow 2\ K + H_2O$	E
$C + H_2O \rightarrow CO + H_2$	B		
$CO + H_2O \rightarrow CO_2 + H_2$	C		
		$K_2O + C \rightarrow 2\ K + CO$	F
$CO_2 + K_2O \rightarrow K_2CO_3$	D		

At lower temperatures (*Table 1-a, A-D*), pores are formed through carbon consumption *via* the dehydration of KOH to K_2O and the subsequent formation of K_2CO_3 with *in situ* produced CO_2 which is generally catalyzed by alkali metals. At temperatures higher than 700 °C (*Table 1-a, E, F*), compared to other chemical activation agents, KOH has the special inherent ability to form intercalation compounds of elemental potassium with adjacent graphene planes.[103] After removal of potassium, the pores and voids left by separated carbon planes contribute additional porosity to pores formed by chemical reactions.[45]

Since within the chemical activation generally lower temperatures and shorter reaction times are applied, this method is preferred over physical activation.

Over the last years, activation methods have been improved which led to new approaches such as carbide derived carbons (CDC). Here, very narrow pore size distributions and high specific surface areas can be generated *via* selective removal of metals by reaction with halogen gases from carbides, which serve as carbon source.[104] Activation methods mainly allow for the introduction of small pores which do not allow

for high mass transport, or only broad mesopore size distribution. Additionally, the morphology of a material cannot be influenced in a controlled manner, electrical conductivities are low due to the high amount of surface functional groups as well as defects and the structures often collapse upon high-temperature-treatment. Furthermore, within the process of activation, structural heteroatoms such as nitrogen are released from the carbon material in order to form graphitic domains and networks. As a consequence, access to porous carbons with structural rather than surface functionalities is limited eventually restricting the applicability of the activated materials. Thus, if bigger pores, other geometries or functionalities are required, other methods have to be applied. In this regard, templating strategies have proven to be highly suitable to overcome limitations of activation protocols.

1.2.2.2.   **Template-assisted synthesis**

The synthesis of a structured materials on the nanometer scale *via* templating may be illustrated with the macroscopic analogue *i.e.* bronze casting using a mold made out of wax or other materials.[105] True templating is strictly the formation of a one-to-one inverse copy of the template. However, the template-assisted approach can generally be described as the synthesis of a material in the presence of a structure-directing agent which after template removal results in a patterned porous material. In cases where a real templating process takes place, the structural information of a template can be directly transcribed into the final product.

Tremendous research activities in the field of template-derived porous materials were accomplished since the discovery of the M41S family by the Mobil Corporation researchers Beck and Kresge et al. in 1992.[106] The probably most prominent examples of this aluminosilicate family are MCM-41 (Mobil Composition of Matter, hexagonally packed rod-shaped micelle structure), MCM-48 (cubic) and MCM-50 (lamellar). These materials were synthesized from a synergistic precipitation of a surfactant – silicate ions solution to form a condensed silica framework.[107]

In general, templating approaches can be distinguished into endo- and exotemplating (*Figure 1-11*).[105] In the former, case the material to be templated is formed around the template *e.g.* a single molecule or a supramolecular aggregate, thus pores are created within the final material. In the latter case, the material to be templated is formed inside the channels or pores of the template. If the template pores are not connected to each other, separated structures such as rods or nanoparticles are obtained after template-removal whereas porous material scaffolds result from interconnected template pores.
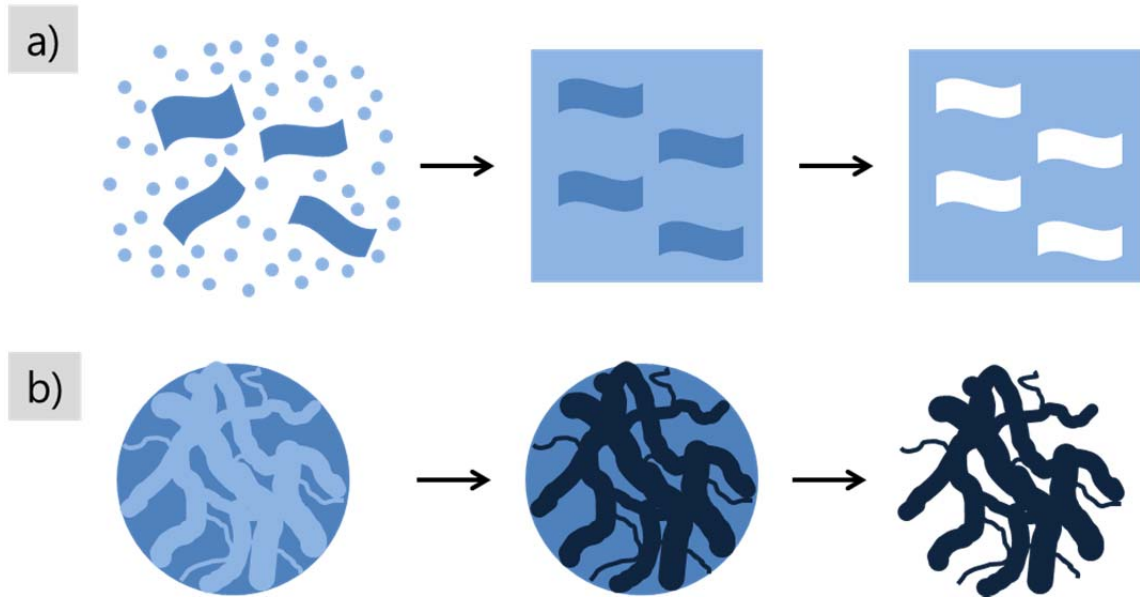
Figure 1-11 Schematic representation of **a)** endo- and **b)** exotemplating for the generation of high surface area materials.

If within the endotemplating approach single molecules are used, this more specific method is called molecular imprinting. Here, the shape information of a molecule is directly transferred into a surrounding material *e.g.* a polymer *via* polymerization of a mixture containing the molecule and the monomers. One of the first reports date back to 1949 when F. Dickey discovered a preferred uptake of a dye molecule from silica that was synthesized in the presence of the respective dye molecule.[108] In contrast, the process is described as nanocasting if the material to be templated is filled and processed in a mold with structures in the nanometer regime which correlate to the porosity of the final product as one-to-one inverse replicate.

Nowadays, a variety of different material classes can be processed *via* templating strategies *e.g.* silicates, metal oxides, polymers or carbons.[105, 109] However, in order to obtain porous materials, the right combination of precursor and template is crucial. Here, the interaction of the precursor and the template (*i.e.* the wettability or miscibility) is mostly provided through van der Waals and Coulombic interaction or hydrogen bonds. Furthermore, template stability needs to be provided at least until the precursor reactions lead to an adequate solidification without pore collapse, and the template pores should not be blocked. Additionally, for the successful synthesis of nanostructured materials, some concerns need to be applied regarding the synthesis strategy, too. Today, a range of different synthesis techniques for tailored porous materials through templating are available.[110]

Sol-gel deposition: The gelation (hydrolysis and condensation reactions) of a precursor sol in the presence of a template is initiated *via* adjustment of *e.g.* the temperature or pH value. Here, either discrete particles or networks can be formed.

Electrodeposition: The template surface needs to be electrical conductive, thus it is coated with a metal film serving as cathode for electroplating of the precursor. The growth of the nanostructure is controllable *via* the applied voltage and time.

Electroless *i.e.* chemical deposition: Compared to electrodeposition the template surface does not have to be electrically conductive but the material is rather deposited by the utilization of a chemical agent. Here, the structure dimension is preset by the template but through adjustment of the reaction time either hollow (short reaction time) or solid (longer reaction time) structures are produced.

Chemical polymerization: The template is immersed in a solution containing a monomer and a polymerization agent. The polymerization preferentially takes place on the template surface, thus the polymer adapts the template morphology.

Chemical vapor deposition: The volatile precursor is solidified on the template surface. This technique is useful for the production of thin films and highly pure materials.

Regarding the template species, two different approaches *i.e.* hard- and soft-templating can be distinguished. Even though a strict classification is not always appropriate due to the existence of many borderline cases, it is still suitable to group the currently applied methods, including their merits and drawbacks:

Soft-templating This approach is based on the utilization of amphiphilic molecules such as surfactants (*e.g.* cetyltrimethylammonium bromide, CTAB) or block copolymers (*e.g.* poly(ethylene oxide)- or poly(styrene)-based block copolymers) as template phase. These structures are very interesting since they are able to self-assemble into a variety of macromolecular architectures and their properties are easily tunable.[44, 111]

The probably most prominent examples for soft-templating are the above-mentioned silica materials MCM-41 and MCM-48 as well as SBA-15 (Santa Barbara Amorphous Type Material).[112] First assumptions about the formation mechanism suggested a so called true liquid crystal templating (TLCT, *Figure 1-12 a*) which occurs only at very high surfactant concentrations. This process was later elaborated by Göltner and G. Attard and represents a borderline case since liquid crystals are formed which then act as template.[43, 113-116] For templating at lower surfactant concentrations, it turned out that the material is rather formed *via* a cooperative mechanism where the surfactant and inorganic phase assemble without replicating a preformed template/surfactant structure (*Figure 1-12 a*).[117, 118] With this model the generation of meso- as well as micropores by single amphiphiles can be explained. As schematically shown with an

amphiphile containing a hydrophilic poly(ethyleneoxid)-block (blue), the hydrophobic (yellow), and parts of the hydrophilic block contribute to the mesoporous core while the rest of the hydrophilic part creates micropores in the walls (*Figure 1-12 b*).[105, 117]
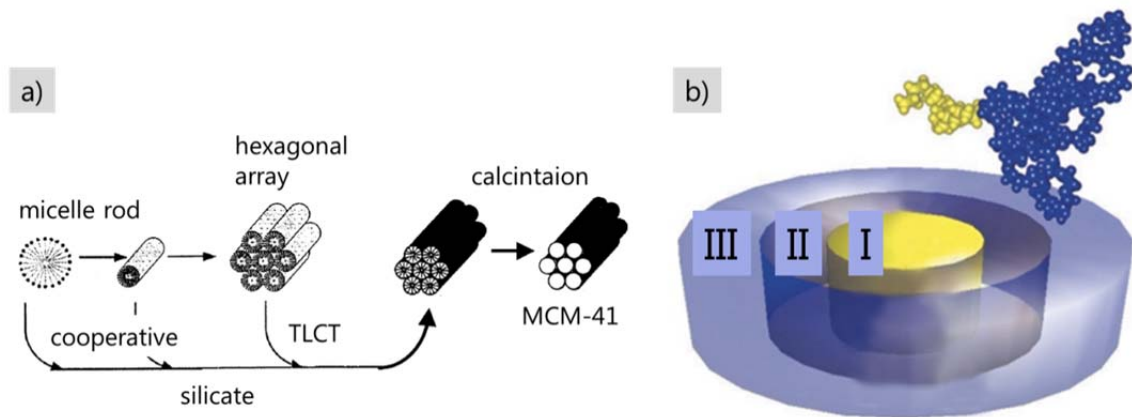

Figure 1-12 a) Simplified formation pathway of surfactant templated silica. At low surfactant concentrations, a cooperative mechanism occurs while at high concentrations the surfactant liquid crystals serve as template (TLCT). Adapted from Beck *et al.*[106] **b)** Detailed schematic representation of the cooperative pore construction in silica through surfactants denoted as "three-phase model". The amphiphilic molecules form a hydrophobic core (yellow, I), a depletion zone which contributes to the mesopore volume (II), and a hydrophilic outer shell (blue, III). The latter is mixed with the silica phase and contributes to the micropores. Adapted from Antonietti.[117]

Carbon materials are more difficult to prepare *via* soft-templating since several prerequisites have to be fulfilled:[111]

- the precursors have to self-assemble into nanostructures
- pore-forming and carbon-forming components have to be miscible
- the pore-forming component has to be sufficiently stable to serve as template *i.e.* until onset of carbon formation but favorably decomposes for template removal afterwards
- a sufficiently stable carbon network has to form during template removal

A major drawback is the often susceptible self-assembly process of the amphiphilic molecules which may be disturbed by the presence of the precursor species. Another issue is the pore collapse of the templated material either during solidification of the precursor or after template-removal. A report of Moriguchi *et al.* showed that it was possible to form different mesophases *i.e.* lamella, hexagonal and disordered phases in the precursor system containing CTAB as surfactant and phenolic resin as carbon precursor.[119] However, after aging at elevated temperatures the obtained carbons did not possess any porosity.

Furthermore, alkyl chain-based surfactants do not decompose completely but leave carbon residue. In the case of *e.g.* oxides this can be overcome by pyrolysis in oxygen containing atmosphere which is, however, not possible for templated carbon materials. Thus, the replication efficiency is limited which may result in blocked pores. Consequently, the soft-template either needs to decompose solely in gaseous components, possess low carbon yield or has to be removable by solvent extraction.

Since block copolymers show a rich phase behavior, research also focuses on their direct conversion into nanostructured carbons, *i.e.* the polymer is template as well as carbon precursor at the same time. Very recently Matyjaszewski *et al.* reported the synthesis of copolymer-templated N-rich porous carbons (CTNC) through the utilization of well-defined block copolymers of polyacrylonitrile and poly(n-butyl acrylate) as nitrogen/carbon precursor and porosity source, respectively.[120]

However, many factors have to be considered but are barely controllable especially in the case of carbon materials which often possess a sensible and complex structure evolution. Therefore, soft-templating approaches are in most cases less suitable compared to hard-templating methods.

Hard-templating Here, as the term already implies, rigid templates with a fixed structure are employed. Compared to soft-templating, this approach has the great advantage of a relatively easy control over the synthesis and final structure of the templated material. This is due to the fixed template structure which does not change throughout the process. In pioneering work by Knox and co-workers in 1980s, the synthesis of mesoporous carbons *via* templating of a phenol-hexamine mixture with spherical solid gels is reported.[121] This route was very successful and the carbon material was later commercialized as "Hypercarb".[111] However, the first mesoporous carbon with an ordered structure was described by Ryoo and co-workers in 1999 when they replicated MCM-48 to generate the new carbon material CMK-1.[122]

In general, the hard-templating process includes four main steps:

1) template synthesis
2) impregnation or infiltration with the precursor
3) network formation of the precursor
4) template removal

This is not only suitable to produce porous materials with a defined structure but also provides further insights into the structural characteristics of the host template material.

Nowadays, many different template classes are available with silica (Ludox, SBA-15), aluminosilicate minerals (Zeolites, M41S family) and aluminium oxides (AAO) as the most prominent examples. Porous materials with unusual and complex structures were also derived from biotemplates such as bacterial threads, eggshell membranes, plant leaves or spider silk.[123-125]

Through hard-templating many pore sizes, pore shapes and morphologies including hollow structures are addressable. With regard to optical and electrochemical applications, materials with large ordered pores or monolithic character are very suitable. Using colloidal crystals with particle sizes of 0.1-1 µm as templates, inverse opals with a tunable optical band gap *i.e.* photonic materials, are producible.[126, 127] For electrode material *e.g.* in catalysis, monolithic structures revealed to be highly suitable since they can be directly used as electrodes eventually minimizing contact resistance and enabling efficient mass transport. A standard synthesis method for carbon monolith is the templating of silica monoliths.[128] Nevertheless, it is still very challenging to obtain the aforementioned materials because the structures are very fragile and silica monoliths tend to crack during fabrication.

Of essential importance is the compatibility of the precursor and product with the template surface which has to be provided throughout the entire process. Otherwise, the limits of nanocasting are reached if either the interface energy or the network formation of the precursor cannot sufficiently be controlled.[105, 117] The former becomes increasingly important at small scales due to an increased surface proportion. It is sometimes reported that the replicated carbon structures can differ from the original template structure which is ascribed to structural shrinkage and preferred positioning of the carbon material in the template, respectively.[111] Other issues represent template degradation and reactions with the precursor.

As for the soft-templating, the precursors for hard-templating also have to fulfill certain requirements:[43]

- the precursor needs to be gaseous, liquid or soluble in a compatible solvent for an efficient coverage of the template
- the template needs to be stable/inert against precursor reactions
- simple conversion of the precursor with low volume shrinkage is favored

In some cases, it was reported that nanostructured products could also be obtained from precursors which otherwise would not form any solid residue without being trapped in a template.[68] This so-called confined carbonization approach extends the range of possible precursors but is not universally valid. Thus, depending on the

material system, the replication of a template structure into the final product may vary and is often accompanied by serious restrictions.

Compared to the soft-templating approach, hard-templating enables the replication of numerous morphologies. However, it is conducted in a multitude of time-, material- and energy consuming steps not least because of the template generation and destruction during removal. Furthermore, since the templates are inorganic and robust structures, harsh conditions *e.g.* application of hazardous chemicals are necessary for their removal. This is neither applicable for industrial scale nor environmentally friendly. Within the approaches for porosity generation and control available to date, including the methods presented above, some are unique but still not ready to be applied in large scale or industry whereas others are of practical use. In order to achieve the ultimate goal of structure control eventually resulting in the control over materials properties, further improvement of existing and development of new strategies are required. An ideal pathway would also take into account the demand for low costs and sustainability. This is clearly one of the most challenging but also fascinating tasks in the synthesis of porous materials and will be addressed in the present thesis.

2. Heteroatom-doped carbon materials

- Porosity control through salts as porogen

2.1. Background and current research

Carbon materials are one of the most present materials due to their outstanding properties as well as comparably facile manufacturing. However, introduction of heteroatoms such as nitrogen results in modifications of the chemical as well as physical properties. One can distinguish between surface and structural modifications. In the former case, functional groups are covalently attached to the carbon surface *e.g.* nitrogen can be present as amine, while the properties of the original carbon structure as such are maintained (*Figure 2-1*).[31]
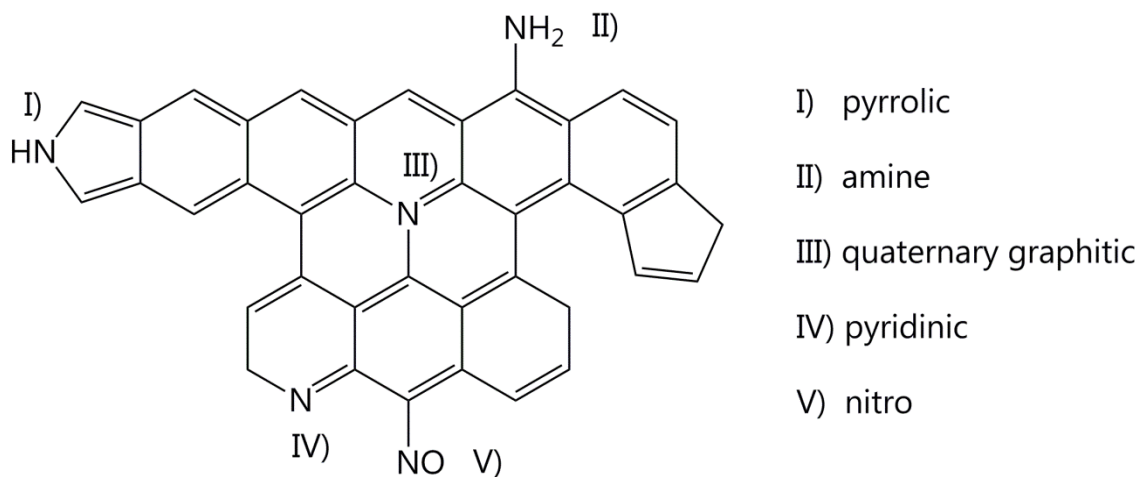

I)   pyrrolic

II) amine

III) quaternary graphitic

IV) pyridinic

V) nitro

Figure 2-1 Schematic representation of possible incorporation of nitrogen into carbon materials.[31]

In the case of layered edge chemical nitrogen this leads to a Brønsted-basicity. In contrast, if the heteroatoms are structurally incorporated into the carbon, the physical properties of the material drastically change. Structural nitrogen is reported to modify the band structure by lowering the valence band and increasing the electron density at the Fermi-level. Thus, the material becomes chemically more stable and it is sometimes referred to "noble carbons".[16, 129] Another prominent example is the increased electrical conductivity achieved by doping carbon materials with the electron-rich nitrogen which was shown to introduce metallic character in N-doped carbon nano tubes (CNTs).[18] In contrast to surface-bound nitrogen functionalities which introduce Brønsted-basicity, structural nitrogen adds Lewis-basicity to the carbon material. This is of special interest

for catalytic applications and among others it was indeed already shown that N-doped carbon possesses superior catalytic activity *e.g.* for the ORR.[30, 51] Besides catalysis, the incorporation of both surface and structural nitrogen in carbon materials increases the performance of the materials for the application as electrodes for supercapacitors. Here, the functional groups add a pseudocapacitance where energy is stored by Faradaic reactions, thus the overall energy storage is increased.[15] To demonstrate the vast potential of N-doped carbons but also with respect to the application of the synthesized materials described in this chapter, the utilization for CO_2-capture and separation is important to mention.[36, 93] However, the nature of the heteroatom is not restricted to nitrogen but other elements such as boron,[28, 29, 54-57] sulfur[58-61] or phosphor[62-65] were also reported to be suitable for tuning carbon material properties. For instance, by doping of graphitic carbon with either nitrogen or boron or co-doping with the isoelectric boron-nitrogen motif, the physical properties of the material should be switchable between those of graphite, N-doped and B-doped carbon (*Figure 2-2*).[57] Carbon materials containing boron and nitrogen were already reported to possess good performance in hydrogen storage, supercapacitors, as phosphors and in CO_2-capture.[35, 53-55]
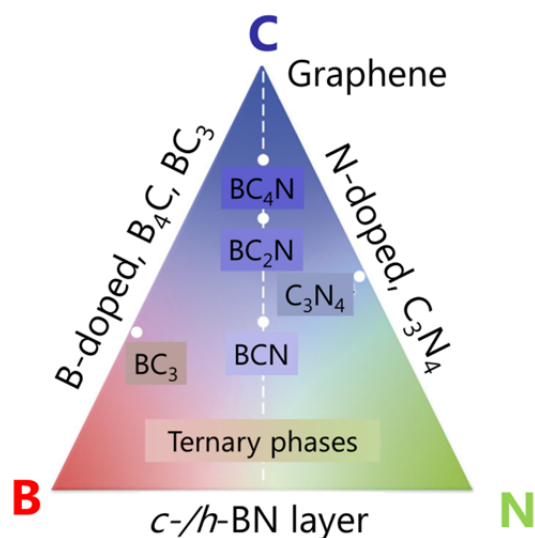

Figure 2-2 Schematic representation of possible materials formed from carbon, nitrogen or boron within a ternary phase diagram.[57]

As stated in the introduction, heteroatom-doped materials are commonly generated through thermolysis or chemical vapor deposition of heteroatom-containing precursors,[20-24, 66, 67] and post-modification of carbons in a heteroatom-containing atmosphere, respectively.[22-24] However, all these methods reveal certain drawbacks such as low yield, multi-step synthesis, difficult shaping and processing as well as problematic and inhomogeneous incorporation of heteroatoms.

Therefore, as recently shown by our group[30, 38, 75] and others,[27, 31, 36] the approach of employing ionic liquids as alternative and highly suitable precursors for the synthesis of heteroatom-doped carbons is extremely attractive. Detailed information on this methodology is described in the first chapter of the present thesis.

The utilization of relatively expensive ionic liquids as precursors for carbon materials may appear contradicting at the first sight. However, they are regarded as green and sustainable solvents not least because of the negligible vapor pressure and reagent economy, thus their processability and handling are very user-friendly.[31, 130] Furthermore, ionic liquid-derived materials show impressive performance in many different applications, hence compared to standard precursors very high-quality products are obtainable. Additionally, it is not always necessary that a material is solely composed of ionic liquids but cheaper supports *e.g.* porous carbons from sugars may be coated with a thin film of ionic liquid-derived material. Finally, the research field of ionic liquids as precursor materials is just beginning and it is foreseeable that the costs for established ionic liquids will be massively reduced in the future. Concomitant, much effort is made on the synthesis of ionic liquid species solely from biomaterials and the number of successful routes towards "bio-ionic liquids" increases constantly.[131, 132] These deep eutectic solvents (DES), firstly reported in 2003 by Abbott *et al.*, are generally composed of a mixture of hydrogen bond donors *e.g.* acids, amines or alcohols with halide salts (commonly quaternary ammonium salts *e.g.* choline chloride) which produce eutectics.[133, 134]

Each application demands for certain and sometimes very specific material properties For this reason, not only precise control over the materials composition but also over the morphology is essential for an improved performance. In this regard tunability of the porosity plays a key role, and much effort has been made to develop suitable methods. Of special interest are micro- and mesoporous as well as hierarchically structured materials. As shown in the basic concepts, different activation and templating methods can be applied to produce a variety of structured materials. However, they suffer from restriction to low temperature regime, several time- and energy-consuming synthesis steps, insufficient self-organization of the surfactant phase, miscibility or wettability, the application of hazardous chemicals for template removal and low product yields. Thus, even though the chemical design of porous carbons has made enormous progress,[135-138] additional and sustainable tools for the rational pore design are still highly welcomed.

In this chapter it will be demonstrated that ordinary salt can be successfully applied as porogens for the fabrication of high surface area ionic liquid-derived heteroatom-doped carbons with tunable porosity and morphology. We refer to this approach as "salt templating". The porogen *i.e.* the non-carbonizable salt phase is easily removed by simple washing with water. In this way, drawbacks of conventional template systems can be overcome eventually resulting in high surface area carbons with structural and chemical functionality through a facile and scalable closed-loop process.

Within first results of our salt templating, microporous boron carbon (oxy)nitrides with moderate surface areas (373 m^2g^{-1} for LiCl/KCl, 817 m^2g^{-1} for CsAc) were successfully obtained.[28] This enabled the application of this material as electrocatalysts for the ORR for the first time.[28]

It is to mention that "salt templating" was also introduced for the synthesis of macroporous polymers, by using salts (*e.g.* NaCl) in a non-solvent in the form of freshly ground crystals (crystallite size 0.2 to 500 µm).[139, 140] The synthesis of low surface area inorganic scaffolds *via* salt-inclusion was also reported.[141] This is however not to be mixed up with the present approach where a salt melt enables the generation of a factor of 1000 smaller pores and much higher surface areas. Here, the appropriate choice of cation size and counterion controls the minimal pore size as well as miscibility with the reaction medium *via* adjustment of the polarizability.

In general, the main focus will be on N- and N-B-co-doped carbon materials. Through variation of the synthesis temperature, the material properties can be adjusted from polymeric (low temperature) to graphitic (high temperature) products. The CO_2-sorption measurements reveal the materials as promising candidates for CO_2-conversion. At the end of this chapter, preliminary results on the synthesis of N-S-co-doped materials by using a mixture of N- and S-containing ionic liquids will be presented. This further amplifies the ambit of the convenient ionic liquid based route towards heteroatom-doped carbon materials.

2.2. Eutectics – N- and N-B-co-doped carbons

The carbon materials which are formed through the thermal treatment of carbonizable ionic liquids under inert atmosphere normally do not possess any porosity in the absence of templates which is, however, crucial for many applications.

Recently, Dai and co-workers showed that the utilization of certain ionic liquids resulted in porous carbon materials. Here, a porogen effect is attributed to the ion which does not crosslink but decomposes during the thermal treatment.[32, 33] They also employed mixtures of different ionic liquids to adjust the porosity.[35] However, only moderate surface areas of around 600 m^2g^{-1} could be generated and the approach offered limited tunability.

Already in 1965, Sundermeyer presented molten salts as alternative solvents and emphasized the good solubility of nitrides, cyanides, cyanates and thiocyantes. [142, 143] In 2004, Cooper *et al.* and Morris *et al.* reported on the so-called ionothermal synthesis *i.e.* reactions which are conducted in an ionic liquid or deep eutectic solvent (DES) as both solvent and structure directing agent.[144, 145] In these papers, they opened an alternative route towards zeolite materials which crystallinity can be varied by the salt. Recently, the formation of covalent triazine-based frameworks using zinc chloride[71, 146, 147] or the eutectic mixture lithium chloride/potassium chloride[148] was described. The molecular precursors were mixed with the salt and heated in quartz ampules under inert atmosphere. However, for zinc chloride the presence of nitrile functionalities was crucial, the precursors were uncharged molecules and the porosity was found to originate solely from a phase separation. In the case of the eutectic mixture, the focus was on the formation of crystalline species of graphitic carbon nitrides.

The synthesis of carbon materials based on DES as all-in-one precursor *i.e.* solvent, structure directing agent and precursor was reported by del Monte *et al.*.[130, 149-151] Briefly, the polycondensation of a DES based on resorcinol and choline chloride with formaldehyde resulted in the formation of a carbon monolith. Bimodal porosity was developed through DES rupture due to resorcinol-formaldehyde polycondensation. However, the class of DES cannot be regarded as true ionic liquids since DES are not solely composed of ions but are also obtained from non-ionic species.[133] Furthermore, as DES are eutectic mixtures, the melting point and thus the liquid state depend on the component ratio which might be rather sensitive to the addition of further reactants such as (metal)salts. This probably causes the imbalance of the thermodynamic equilibrium and eventually the loss of the homogenous liquid state. In the case of DES, the melting point depression is caused by the charge delocalization due to hydrogen bonding between the components *i.e.* the halide anion and the hydrogen bond donor.[130, 134] In contrast, the melting point of ionic liquids depends on the charge

distribution in the ions, *e.g.* strong charge delocalization causes a lower melting point, thus they can be regarded as true single phase system or solvent which are entirely composed of ionic species. As a consequence, ionic liquids present a less sensitive medium and offer a wider variety as precursors for carbon-based materials.

Nowadays, many materials *e.g.* metal-organic frameworks (MOFs), covalent-organic frameworks (COFs), polymer-organic frameworks (POFs),[71, 152-154] or porous silica[155] can be prepared *via* ionothermal synthesis.

However, to the best of our knowledge, the combination of an ionic liquid as carbon and heteroatom source with a non-carbonizable salt as porogen for the generation of high surface are functional carbons with tunable porosity as well as morphology was not reported so far.

In this chapter, eutectic mixtures will be presented as versatile *in situ* porogens with template character for the synthesis of porous N- and N-B-co-doped carbons from ionic liquids.[38] In this regard, eutectics offer many advantages such as high temperature stability, good solubility of small molecules and melting points below onset of polycondensation of the ionic liquid. Reaction kinetics may also be accelerated since the reaction occurs in the molten state eventually increasing structure ordering and yields. Furthermore, as the system solely consists of ions, favorable miscibility is ensured *via* Coulombic interactions. Again, special emphasis is to put on the fact that the porogen *i.e.* the salt phase is easily removed by simple washing with water, thus overcoming drawbacks of conventional template systems.

The N-doped carbons (N-dC) were synthesized from the ILs Bmp-dca and Emim-dca as carbon and nitrogen source.

For the N-B-co-doped carbons (N-B-dC), the IL Emim-tcb was chosen as precursor.

In the present chapter the porogen salts are eutectic mixtures of lithium chloride/zinc chloride (LiZ, melting point 294 °C), sodium chloride/zinc chloride (SZ, melting point 270 °C) and potassium chloride/zinc chloride (PZ, melting point 230 °C).

In a typical synthesis, varying concentrations of the eutectics were mixed with one of the ILs (*Scheme S2-1, 1.*). The carbonization under nitrogen atmosphere (*Scheme S2-1, 2.*) followed by aqueous removal of the salt porogen (*Scheme S2-1, 3.*) yields highly porous heteroatom-doped carbons which appear as voluminous, black powders (*Scheme S2-1, 4.*). Throughout this thesis, the precursor solutions from the eutectics are named IL_XZ_r while the N- and N-B-dC are denoted as N(-B)-dC_IL_XZ_r_T. Here, IL is the respective ionic liquid used as precursor, XZ is the eutectic made from zinc chloride (Z) with X being lithium chloride (Li),

sodium chloride (S) or potassium chloride (P), r represents the mass ratio eutectic/IL in the precursor mixture and T is the synthesis temperature.

The N-dC and N-B-dC were synthesized at high temperatures *i.e.* 1000 °C and 1400 °C, respectively as opposed to the low temperature materials (450 °C) which will be presented in part 2.4.

Scheme S2-1 Description of product and surface area formation using the salt templating approach.
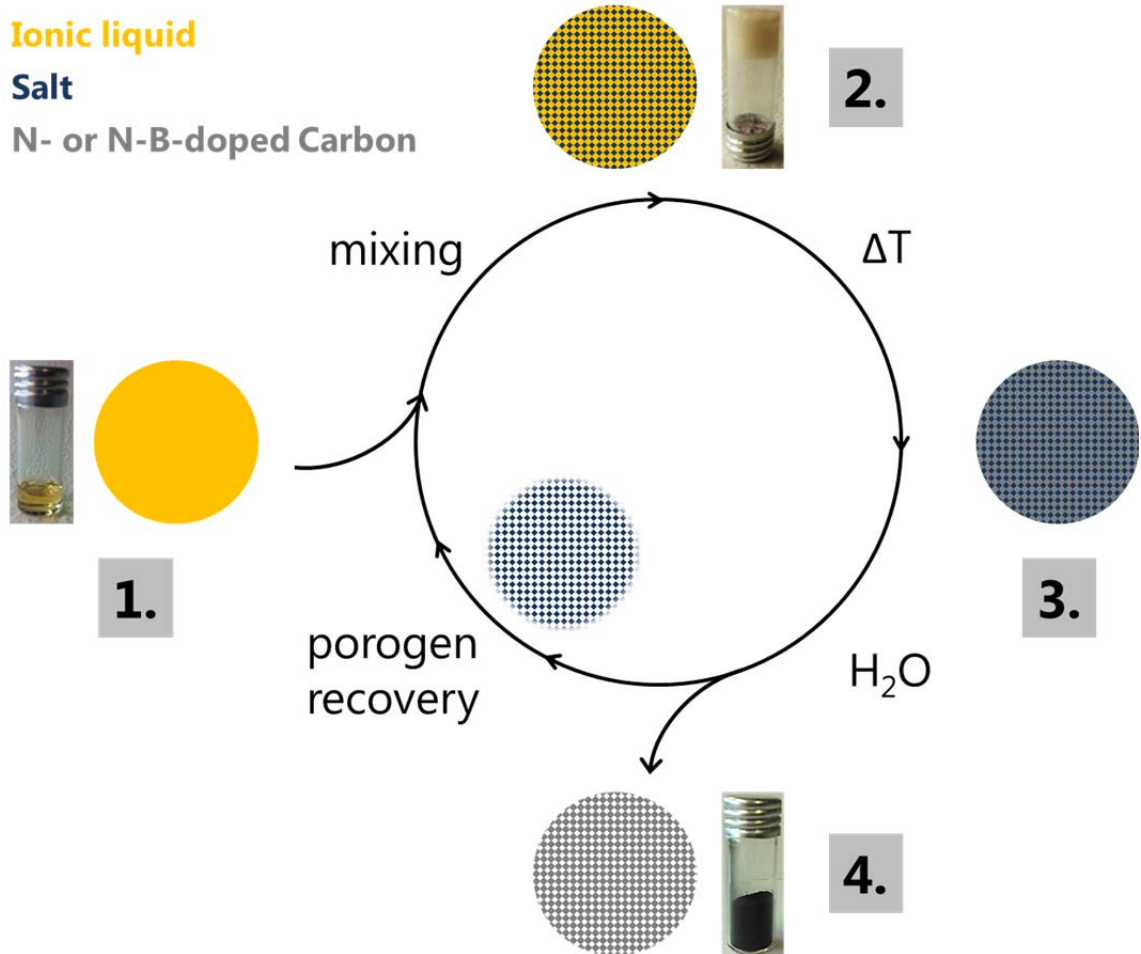
The IL (yellow, 1.) is mixed with the porogen salt (blue) forming a glassy beige solid (2.). During carbonization the heteroatom-doped carbon forms in the presence of the molten salt, thus space between the carbon layers is generated by delamination (3.). The aqueous removal of the salt phase eventually results in highly porous carbon materials (4.) while the porogen could be recovered afterwards.

The mixing of the ILs with each of the eutectics is an exothermic process which indicates the good miscibility of the substances prior to carbonization. The homogeneity of the precursor mixtures (*Scheme S2-1, 2.*) during the heat treatment can be assumed because the melting points of the eutectics are below the onset of crosslinking of the IL units (around 300 °C).[26, 27]

The representatively shown crude product of N-dC_Emim-dca_SZ_3_1000 (*Figure 2-3 a*) supports this assumption since it reveals a homogeneous solid. As the washing solutions are neutral, etching processes during carbon formation can be excluded.

The washed and dried products (*Figure 2-3 b-d*) appear as shiny and relatively hard rough-grained (N-dC_Emim-dca_LiZ_3_1000), slightly shiny fine (N-dC_Emim-dca_SZ_3_1000) and matt black voluminous (N-dC_Emim-dca_PZ_3_1000) powders. Already this optical inspection suggests even without any further analysis that the materials reveal different properties *i.e.* different porosity and morphology. Here, it must be underlined that regardless of the ionic liquid precursor, all materials can be received in remarkable yields of about 35 wt%. On the one hand this demonstrates the suitability of salt templating for the large scale synthesis of porous functional carbons. On the other hand, compared to the lower carbon yields obtained from the pure ionic liquids,[27] it also suggests an increased crosslinking efficiency of the ionic liquid. This may be due to a trapping effect *via* Coulombic interaction between the ionic liquid and the porogen salt.
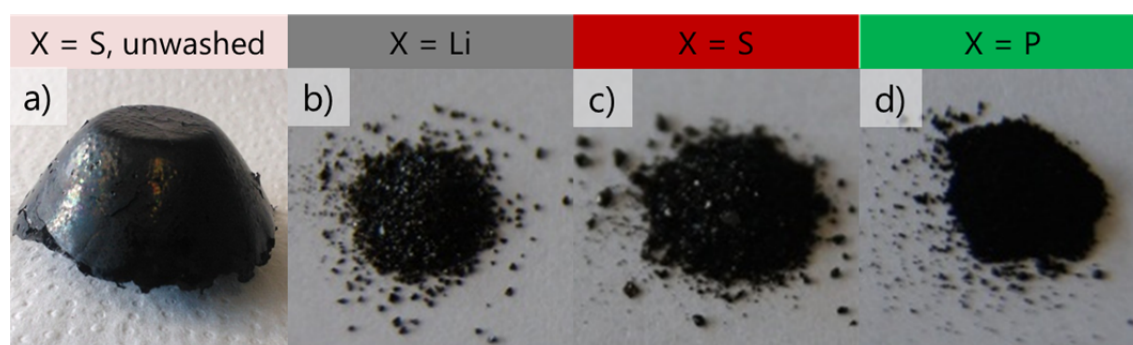

Figure 2-3 a) Unwashed and **b-d)** washed products of N-dC_Emim-dca_XZ_3_1000 with X = Li, S and P.

The representative wide angle X-ray scattering (WAXS *Figure 2-4 a*) of the unwashed product N-dC_Emim-dca_PZ_3_1000 shows sharp diffraction peaks which can be assigned to KCl. The second eutectic compound $ZnCl_2$ is highly hygroscopic and therefore not detectable due to the lack of crystallinity. This confirms the presence of the porogen phase in the carbon-salt-composite after heat-treatment at elevated temperature.
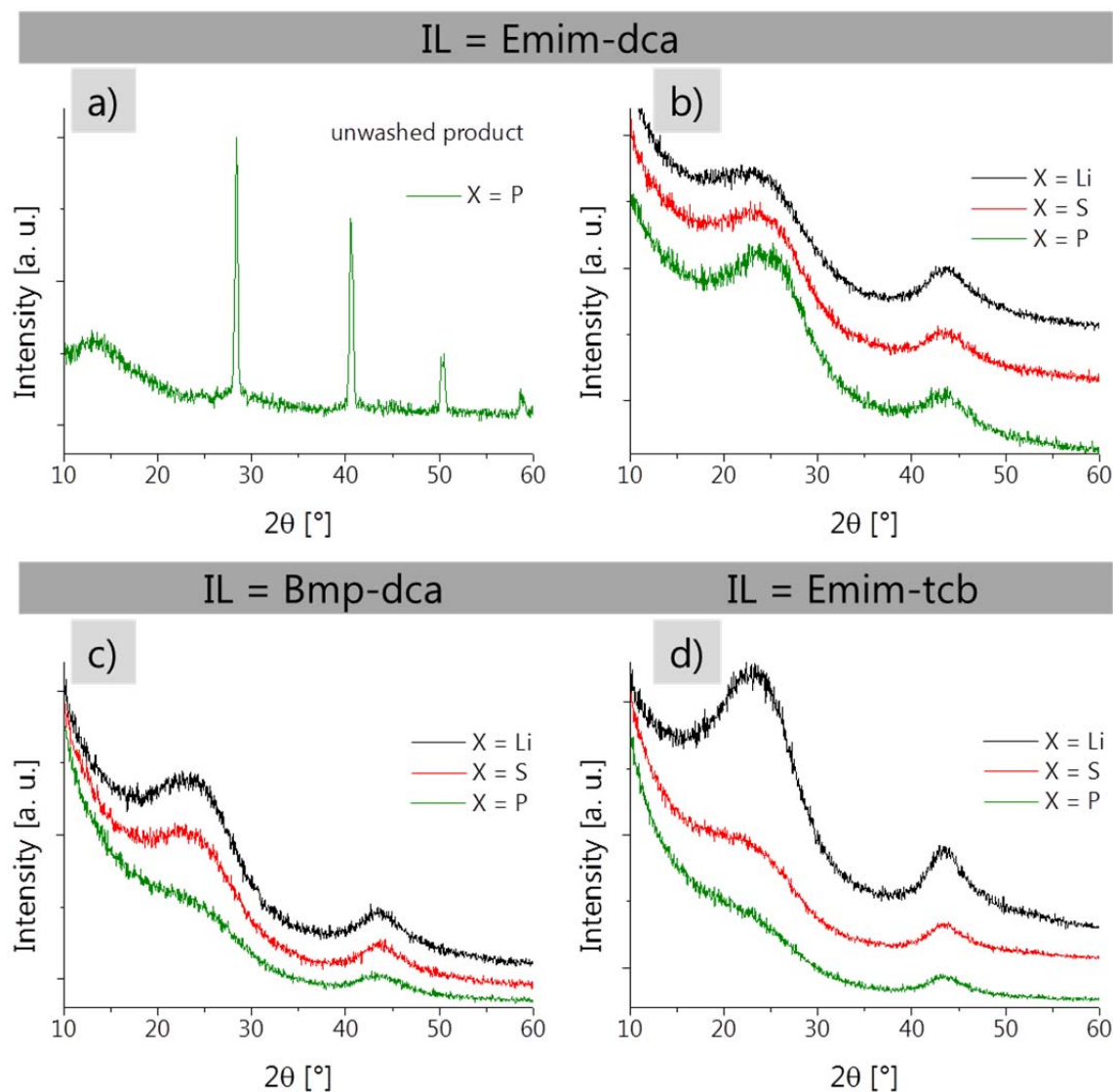

Figure 2-4 WAXS patterns of **a)** unwashed N-dC_Emim-dca_PZ_3_1000 and washed N-(B) dC_IL_XZ_3_1000/1400 with X=Li, S and P derived from **b)** Emim-dca, **c)** Bmp-dca and **d)** Emim-tcb.

The WAXS patterns (*Figure 2-4 b-d*) of the washed products show the typical peaks of slightly disordered, porous graphitic carbon at 2θ 25° (002) and 44° (100). The absence of additional peaks indicates the about complete removal of the salt phases which was also confirmed by Energy-dispersive X-ray spectroscopy (*EDX, Supplementary information Figure C-1*).

2 Heteroatom-doped carbon materials

Bulk elemental analysis reveal the N-dCs to be constituted of 85 wt% carbon and 5 wt% nitrogen and the N-B-dCs to be constituted of 70 wt% carbon, 6 wt% nitrogen and 6 wt% boron (*Table 2-a*). Residual mass can be ascribed to oxygen content or incomplete combustion of the samples.

Table 2-a Composition and nitrogen sorption data of N-(B-)-dC_IL_XZ_3_1000/1400 with X= Li, S and P derived from Bmp-dca, Emim-dca and Emim-tcb.

Sample N-(B-)-dC	Elemental analysis [wt%]								S_{BET}[i] $[m^2g^{-1}]$	Pore volume[i] $[mlg^{-1}]$		
	Combustion			XPS				ICP OES				
	N	C	H	N	C	O	B	B		Total	Micro	Meso
Bmp-dca_ LiZ_3_1000	5.7	85.3	1.1	5.1	83.0	10.4	-	-	1497	0.81	0.47	0.34
Bmp-dca_ SZ_3_1000	5.0	80.5	1.2	5.6	84.5	8.5	-	-	1685	1.18	0.42	0.76
Bmp-dca_ PZ_3_1000	4.7	80.1	1.3	4.0	89.7	4.3	-	-	2013	1.70	0.48	1.22
Emim-dca_ LiZ_3_1000	6.1	84.5	1.1	-	-	-	-	-	1490	0.68	0.53	0.15
Emim-dca_ SZ_3_1000	5.7	84.2	1.0	-	-	-	-	-	1715	0.99	0.49	0.5
Emim-dca_ PZ_3_1000	5.1	82.3	1.1	-	-	-	-	-	1485	0.78	0.5	0.28
Emim-tcb_ LiZ_3_1400	7.5	70.3	2.0	-	-	-	-	6.1	1168	0.57	0.41	0.16
Emim-tcb_ SZ_3_1400	6.3	72.7	1.8	-	-	-	-	5.5	1728	0.96	0.51	0.45
Emim-tcb_ PZ_3_1400	5.6	72.3	2.1	4.2	87.7	5.6	1.8	5.6	1784	1.04	0.56	0.48

i Determination described in A Nitrogen sorption measurements.

For reasons of clarity, further information on the material properties *i.e.* elemental analysis from X-ray photoelectron spectroscopy (XPS) and porosity evaluation are also included in the table.

Regarding fundamental discussions on principles and applicability of the gas sorption data evaluation, it is referred to section A Nitrogen sorption measurements.

34

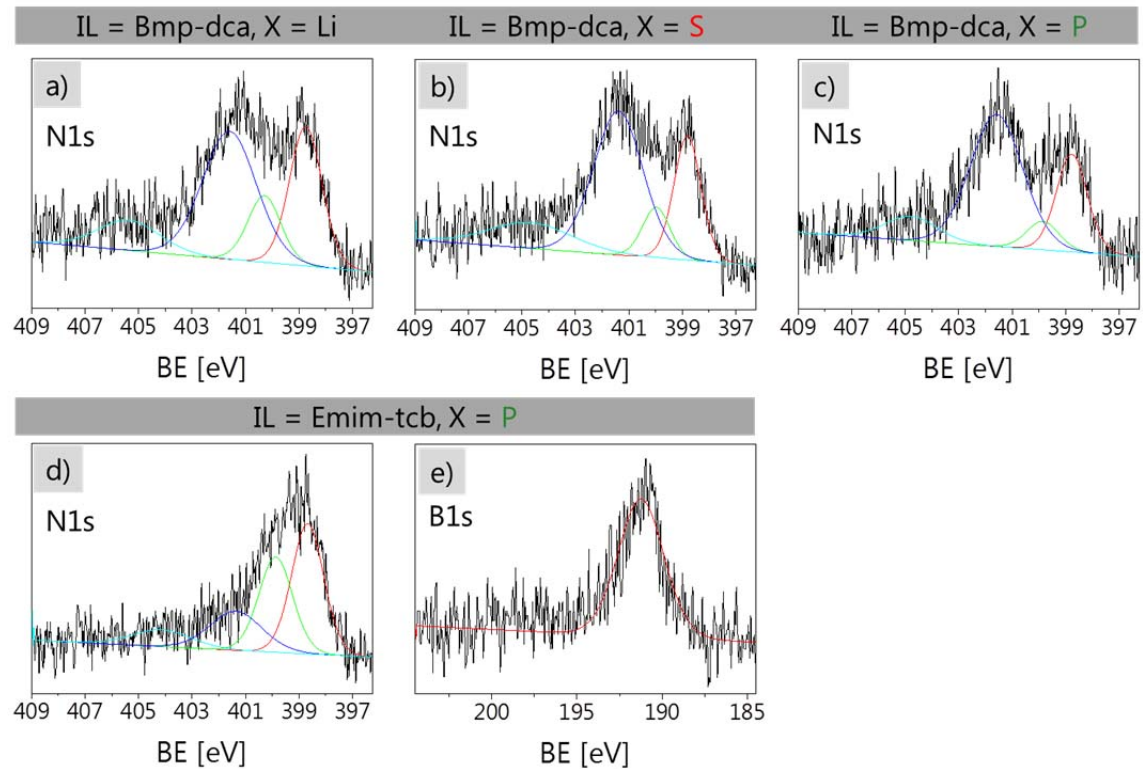The presence of structural nitrogen and boron was confirmed by XPS measurements (*Figure 2-5*).

Figure 2-5 XPS spectra (N1s orbitals) of N-dC_Bmp-dca_XZ_3_1000 with X= Li (**a**), S (**b**) and P (**c**). XPS spectra (**a)** N1s orbital and **b)** B1s orbital) of N-dC_Emim-tcb_PZ_3_1400.

Regarding the N1s spectra, the nature of the nitrogen-carbon bonds is found to be pyridinic (398.7 eV), pyrrolic (400.1 eV) quaternary-graphitic (401.4 eV), oxidic-nitrogen species within graphitic micro domains (404.5 eV) and for N-B-dCs also C-N-B (399.9 eV), respectively.[24, 27, 28, 156, 157] The B1s spectrum of N-B-dCs shows a peak at 191.25 eV (B-N, BC$_3$) approving structural boron.[28, 53] The deconvoluted C1s spectra can be found in *Figure C-2*. With respect to the boron carbon (oxy)nitride material already described in our group obtained from templating with CsAc,[28] the oxygen content is dramatically decreased by the utilization of the eutectic mixture, shifting the material property towards a N-B-co-doped carbon. This, however, nicely demonstrates the tunability of the composition *via* the choice of porogen. Compared to combustion elemental analysis, XPS reveals slightly higher carbon contents for the N-dCs (*Table 2-a*). For the N-B-dC, exemplarily performed for N-B-dC_Emim-tcb_PZ_3_1400, the carbon (boron) content is 87.7 wt% (1.8 wt%) as compared to 72 wt% (5.6 wt%) from combustion elemental analysis which supports the assumption of incomplete combustion. Since XPS is a surface sensitive technique, an enrichment of boron inside the material is also possible. The oxygen content decreases from

10.4 wt% (N-dC_Bmp-dca_LiZ_3_1000) over 8.5 wt% (N-dC_Bmp-dca_SZ_3_1000) to 4.3 wt% (N-dC_Bmp-dca_PZ_3_1000) which shows an additional tuning of surface functionality by the choice of salt. However, oxygen content due to adsorbed water molecules should also be taken into account.

Transmission and Scanning Electron Microscopy (TEM and SEM) pictures of the washed products reveal the morphology of the materials to be dependent on the nature of the eutectic salt which is exemplarily shown for the Bmp-dca derived carbons (*Figure 2-6*).
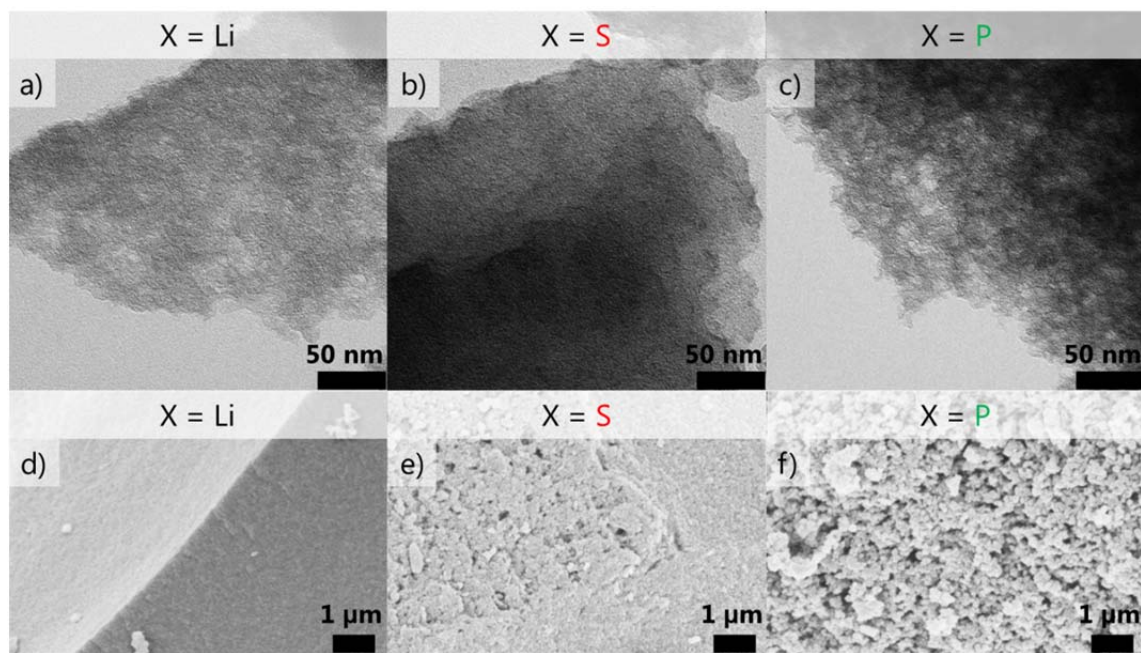

Figure 2-6 TEM (**a-c**) and SEM pictures (**d-f**) of N-dC_Bmp-dca_XZ_3_1000 with X= Li (**a, d**), S (**b, e**) and P (**c, f**).

Comparable morphologies are also obtained for the carbon materials derived from Emim-dca and Emim-tcb and the respective eutectics (*Figure 2-7*). This indicates that the morphology of the carbon materials mainly depends on the nature of the porogen salt whereas the nature of the IL plays a minor role, thus a main part of the pore formation indeed results from a templating mechanism by the salt.

For the sake of clarity, the SEM pictures of the Bmp-dca-derived materials N-dC_Bmp-dca_XZ_3_1000 are also included in the following graphic which summarizes the salt impact on the carbon structure (*Figure 2-7*). Thus, the direct comparison of the material morphologies obtained from all three ionic liquids *i.e.* Bmp-dca, Emim-dca and Emim-tcb is facilitated and further reveals the generality of the salt templating approach.
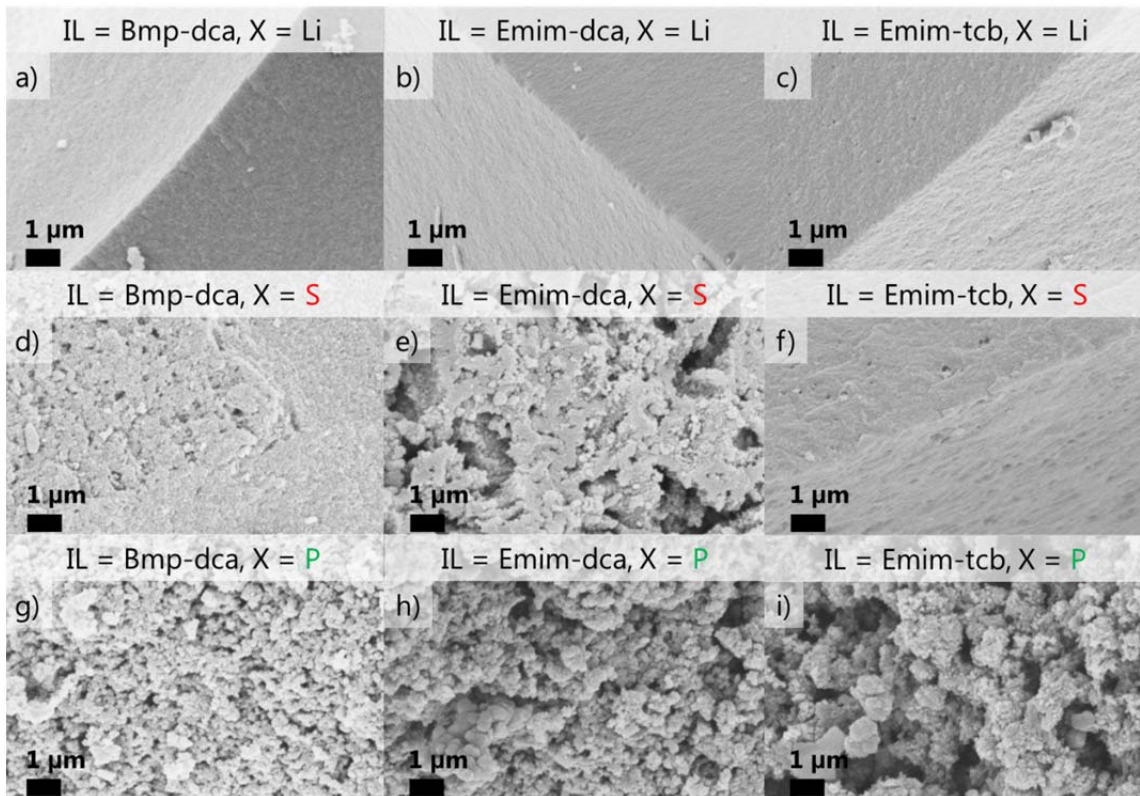
Figure 2-7 SEM pictures of N-(B-)-dC_IL_XZ_3_1000/1400 with X= Li, S and P derived from Bmp-dca (**a, d, g**), Emim-dca (**b, e, h**) and Emim-tcb (**c, f, i**).

The TEM and SEM pictures already show that the surface roughness of the carbons increases from LiZ over SZ to PZ, indicating the presence of larger mesopores or small macropores. Furthermore, in the latter case spherical carbon globules are observed to constitute all PZ-derived materials, again independent of the nature of the ionic liquid.

The nitrogen sorption isotherms (*Figure 2-8*), the apparent surface areas (*Table 2-a*) and pore size distributions (*Figure 2-9*) were determined through nitrogen sorption measurements by applying the Brunauer-Emmett-Teller (BET) model and the nonlocal density functional theory (NLDFT) equilibrium model method for slit pores, respectively.
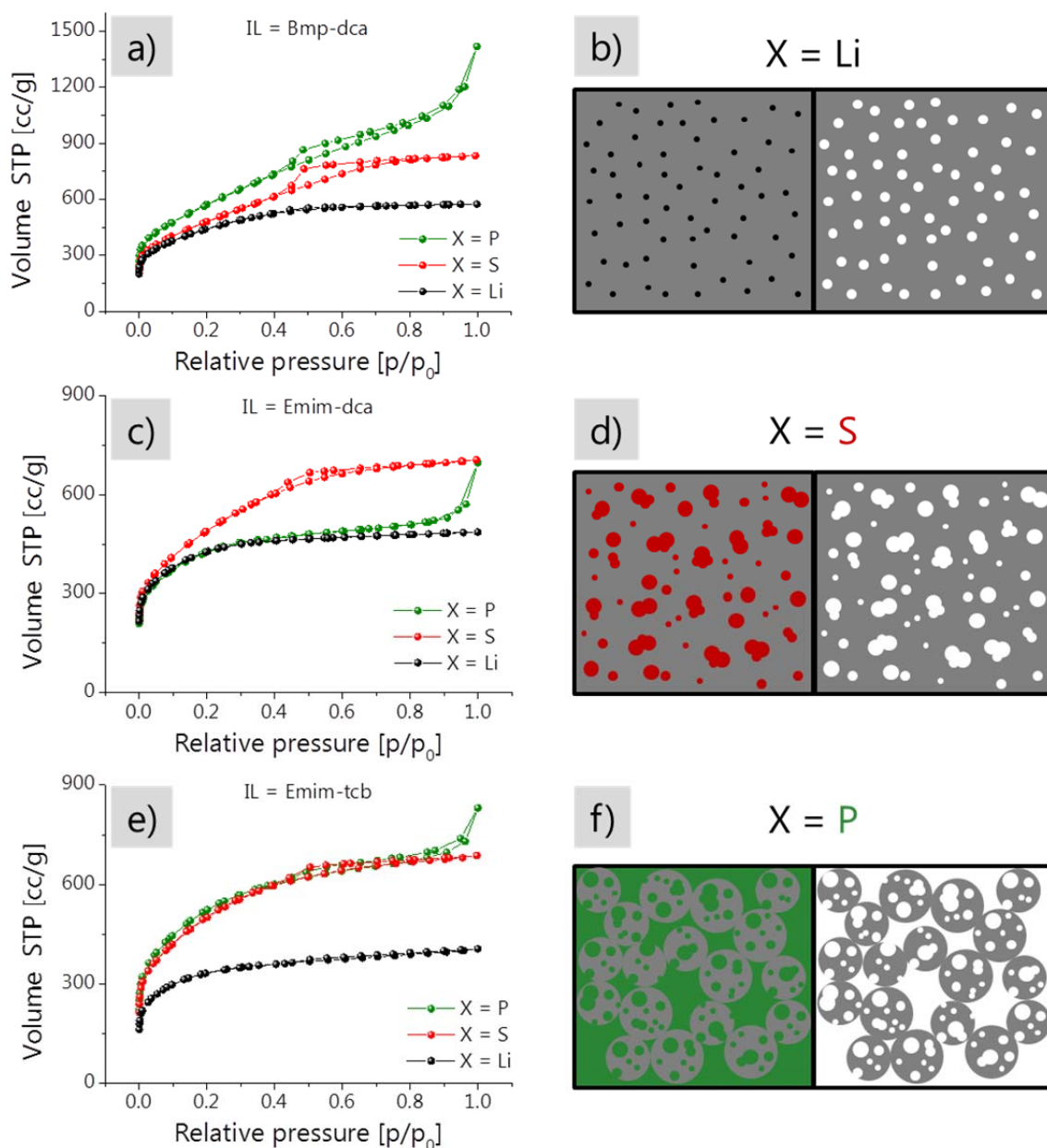
Figure 2-8 Left: Nitrogen sorption isotherms of N-(B-)-dC_IL_XZ_3_1000/1400 with X= Li, S and P derived from Bmp-dca (**a**), Emim-dca (**c**) and Emim-tcb (**e**). **Right**: Schematic representation of pore formation for carbons templated with LiZ (**b**), SZ (**d**) and PZ (**f**) at equal mass ratios. Each left image depictures the carbon (grey)/salt (black, red, green) composite and each left the carbon after washing.
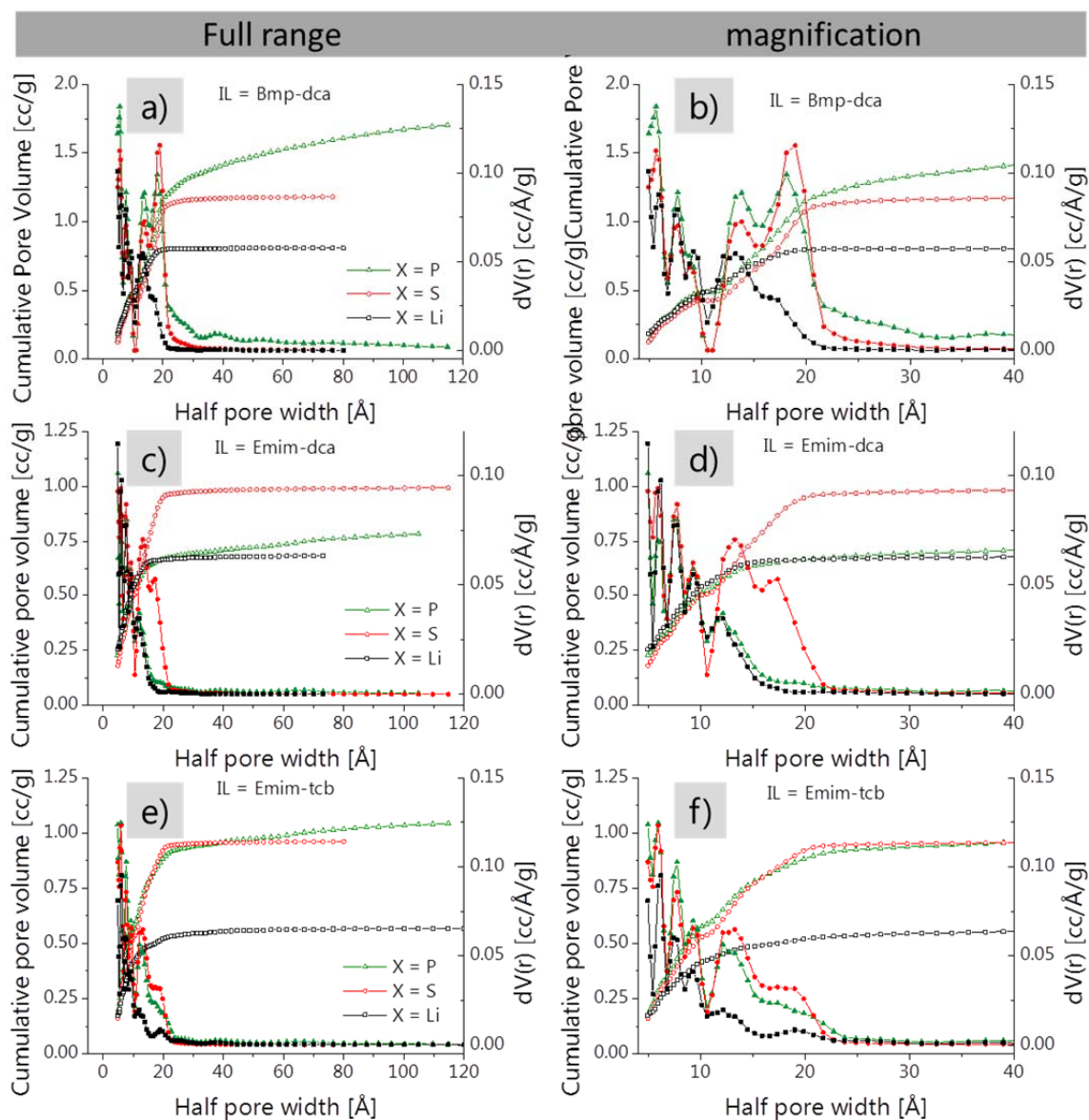
Figure 2-9 Pore size distribution of N-(B-)-dC_IL_XZ_3_1000/1400 with X= Li, S and P derived from Bmp-dca (**a, b**), Emim-dca (**c, d**) and Emim-tcb (**e, f**).

In all cases a high nitrogen uptake is observed and, compared to the carbons derived from the pure ILs,[27] the apparent surface areas significantly increase due to salt templating ranging from 1100 m^2g^{-1} up to 2000 m^2g^{-1} (*Table 2-a*). Here, it must be emphasized that an apparent specific surface area of 2000 m^2g^{-1} is much higher than that of any zeolite, activated carbons and few-layer graphenes, even approaching the theoretical value of single-layer graphene.[72, 156, 158] Furthermore, to the best of our knowledge we also obtained the highest surface area for a boron carbon nitride *i.e.* 1784 m^2g^{-1}.[54] In spite of the simplicity of the applied one step process, this is a notable result. In accordance with the TEM and SEM images, the materials templated with the same salt mixture also show a comparable shape of the isotherms independent of the nature of the IL used as precursor. This further supports the template character of the

salts which enables the easy control of the materials' morphology. In more detail, by the addition of the eutectic LiZ, the isotherms are of type I which implies a mainly microporous structure of the carbons, *i.e.* the salt presumably acts as a "molecular template", either forming ion pairs or little salt clusters of minimal free energy (*Fig. 2-8 a, b*). For carbons templated with SZ the sorption isotherms of the materials show a further uptake of N_2 in the medium relative pressure region as well as a small hysteresis, reflecting a substantial contribution of additional supermicropores and small mesopores. We attribute this to a lower melting point of SZ and bigger salt clusters due to an onset of phase demixing in the later stages of condensation towards salt nanodroplets in the 4 nm range which now act as template (*Fig. 2-8 c, d*). Finally, for materials templated with PZ which has the lowest melting point of the used eutectics, an additional uptake in the high relative pressure region is observed. This is typical for macroporous materials and is here in accordance with the formation of spherical particles of the carbon phase and their interstitial pores, as observed in SEM. The particle formation is ascribed to a more pronounced demixing in even earlier phases of the crosslinking reaction which results in a continuous salt phase (*Fig. 2-8 e, f*). Thereby, interstitial voids between the micro- and mesoporous particles become visible, reminding on the Nakanishi process for polymer templated silica.[159, 160]

For comparison, the ionic liquid Emim-dca was mixed with equal amounts of each single salt *i.e.* LiCl, NaCl, KCl and $ZnCl_2$. The products are named N-dC_Emim-dca_X_3_1000 with X (Li, S, P, Z) denoting the respective salt cation. Only the mixing with $ZnCl_2$ was an exothermic process which indicates the complexation of the ionic liquid ions with the zinc ions. The other mixtures were also homogeneous but not molecularly dissolved at ambient temperature. After heat-treatment and washing the carbons were submitted to nitrogen sorption measurements in order to get further insights into the influence of the salt nature on templating and pore formation.
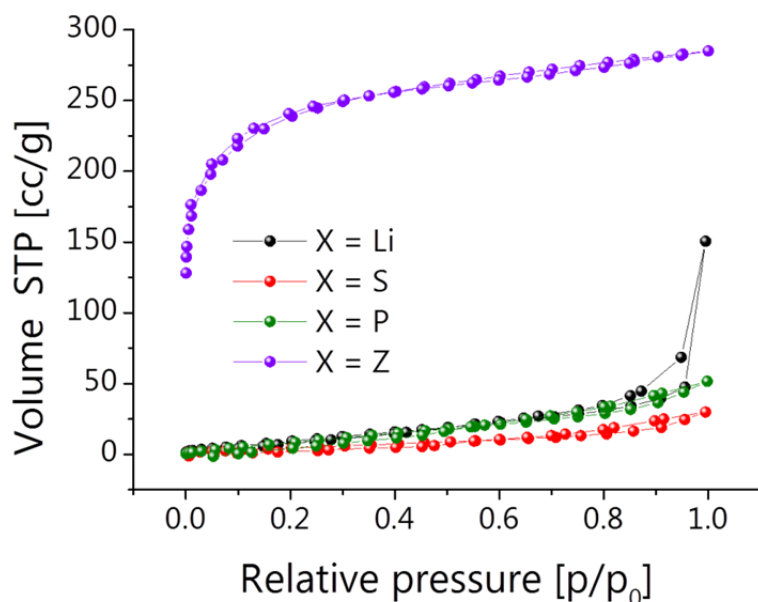
Figure 2-10 Nitrogen sorption isotherms of N-dC_Emim-dca_X_3_1000 with X = Li, S, P, Z.

Except for N-dC_Emim-dca_Z_3_1000, none of the products reveal any porosity. Furthermore, this carbon "only" possesses a surface area of 856 m^{2}g^{-1}. Thus, the porosities of the eutectic mixture-derived carbons presumably not only originate from one salt component but from a cooperative effect of different salts.

In order to investigate the influence of varying salt concentrations on the morphology and pore formation of the carbon materials, the ionic liquid Emim-dca was templated with different amounts of each eutectic mixture, *i.e.* N-dC_Emim-dca_LiZ_x_1000, N-dC_Emim-dca_SZ_x_1000 and N-dC_Emim-dca_PZ_x_1000.
The impact of the eutectics on the product properties can already nicely be observed through a direct comparison of equal amounts of the non-templated material with the washed and dried carbons produced with the highest amount of salts, *i.e.* N-dC_Emim-dca_LiZ_15_1000, N-dC_Emim-dca_SZ_13_1000 and N-dC_Emim-dca_PZ_14_1000 (*Figure 2-11*). While the untemplated product is a silver shiny and hard material, the salt templated carbons appear as highly voluminous black powders. The most voluminous powder is N-dC_Emim-dca_PZ_14_1000 which suggests a significant difference compared to N-dC_Emim-dca_LiZ_15_1000, and N-dC_Emim-dca_SZ_13_1000. Here, it is also to be emphasized, that all materials are still obtained in high yields of around 35 wt%. Therefore, a structural effect of the porogen rather than activation can be assumed.
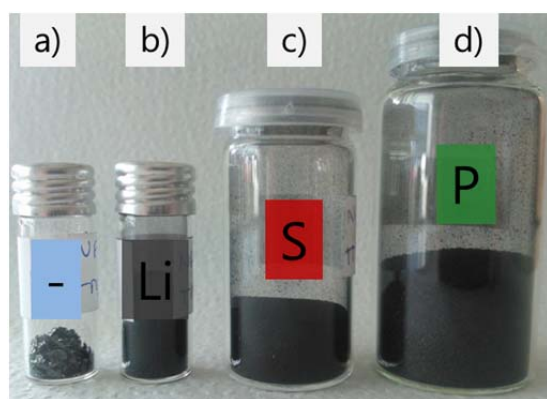
Figure 2-11 Comparison of **a)** N-dC_Emim-dca_0_0_1000 with **b)** N-dC_Emim-dca_LiZ_15_1000, **c)** N-dC_Emim-dca_SZ_13_1000 and **d)** N-dC_Emim-dca_PZ_14_1000.

The WAXS pattern of N-dC_Emim-dca_LiZ_x_1000, N-dC_Emim-dca_SZ_x_1000 and N-dC_Emim-dca_PZ_x_1000 also show the typical peaks of slightly disordered graphitic carbon at 2θ 25° (002) and 44° (100) (*Figure 2-12*). The absence of any further peaks reveals the removal of any crystalline species. However, for N-dC_Emim-dca_LiZ_7.5_1000 and N-dC_Emim-dca_SZ_6_1000 diffraction pattern different from the residual diffractograms are observed revealing sharper instead of broad peaks. This suggests that the respective carbon materials possess a structure with larger extension of ordered domains.
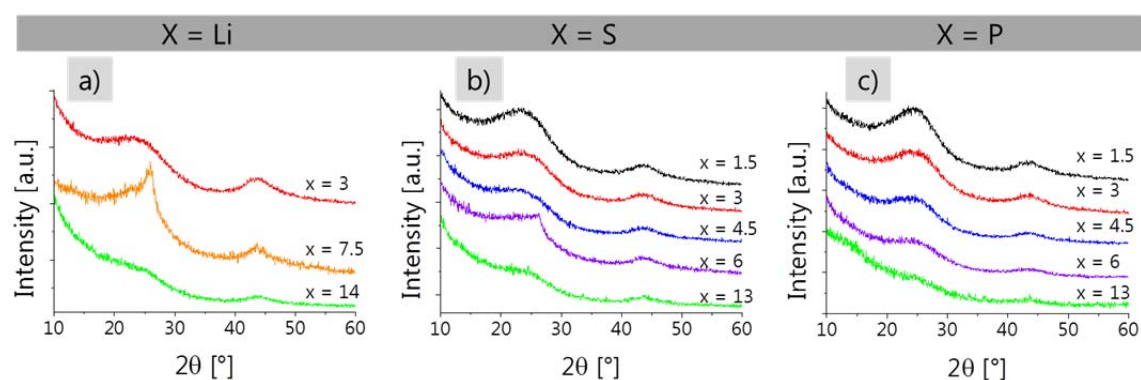

Figure 2-12 WAXS patterns of N-dC_Emim-dca_XZ_x_1000 with X=Li (**a**), S (**b**) and P (**c**) at varying salt concentrations x.

This is potentially due to an ionic liquid-to-porogen ratio in the precursor mixture which passes through a mesophase *i.e.* a highly ordered phase which is retained in the final product.[6] The WAXS pattern of the carbons templated with the highest salt amount show very broad diffraction peaks which points to a decreased order of the structure. This is in accordance with the low-density materials with thin carbon tectonics observed in TEM, which are commonly less ordered. The carbons derived from templating with LiZ still possess a smoother surface while carbons derived from

SZ reveal a rougher structure (*Figure 2-13 a, b*). As already assumed from the product appearance, the carbon material N-dC_Emim-dca_PZ_14_1000 shows a fundamentally different morphology compared to N-dC_Emim-dca_LiZ_15_1000 and N-dC_Emim-dca_SZ_13_1000. As in the case of N-dC_Emim-dca_PZ_3_1000 a globule structure is observed. However, at very high potassium chloride amounts, it is even possible to obtain aerogel-like, monolithic structures which are composed of agglomerated particles (*Figure 2-13 c*).
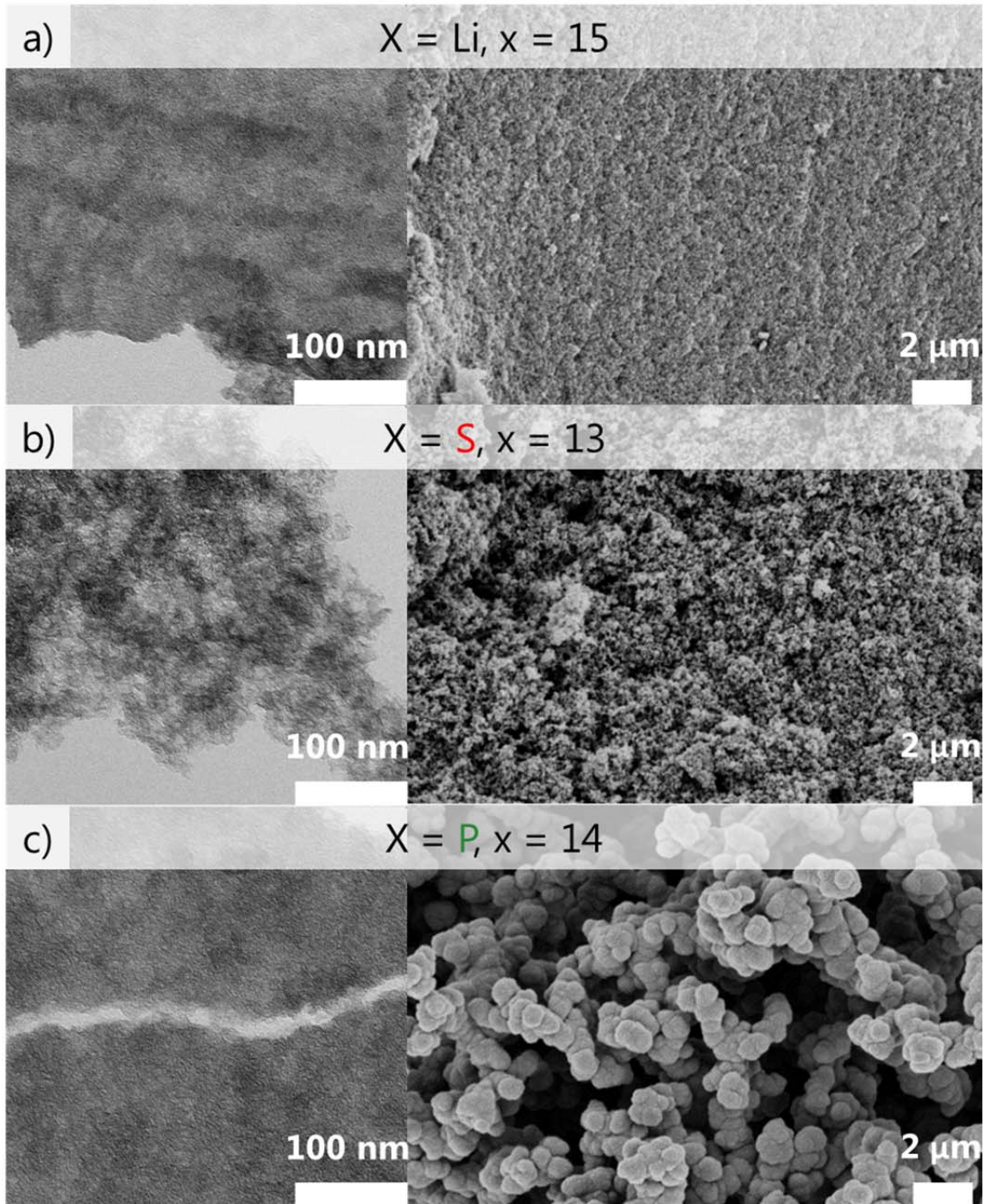

Figure 2-13 TEM (**left**) and SEM (**right**) images of **a)** N-dC_Emim-dca_LiZ_15_1000, **b)** N-dC_Emim-dca_SZ_13_1000 and **c)** N-dC_Emim-dca_PZ_14_1000.

Since visual powder appearance, TEM and SEM already reveal differences compared to the carbons prepared at lower ionic liquid-to-porogen ratios, high salt concentrations were assumed to have a peculiar influence on the porosities (*Figure 2-14*).

In general, from nitrogen sorption measurements no considerable changes of the isotherms are observed in the lower relative pressure range. However, for N-dC_Emim-dca_LiZ_15_1000 and N-dC_Emim-dca_SZ_13_1000, an additional nitrogen uptake occurs at high relative pressures with increasing amount of salt. This is due to the development of a macropore texture between the sheets, in addition to the otherwise unaltered micro and mesopore structure.
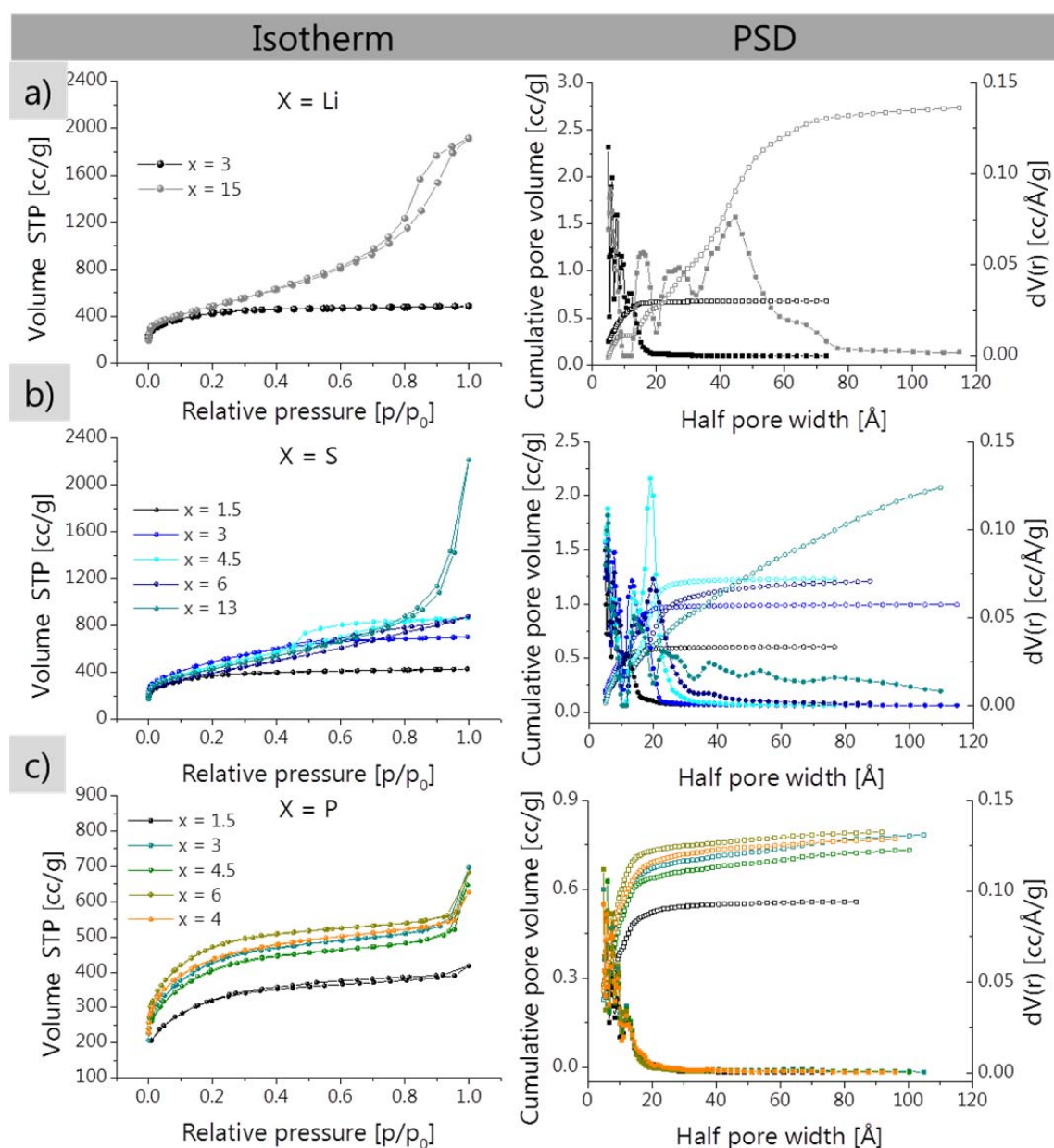

Figure 2-14 Nitrogen sorption isotherms (**left column**) and pore size distributions (**right column**) for Emim-dca_XZ_x_1000 with X=Li (**a**), S (**b**) and P (**c**) at varying salt concentrations x.

Because of that, the mesopore volume increases with salt amount for LiZ and SZ derived materials while the micropore volume and the surface area are relatively constant (*Table 2-b*).

Table 2-b Composition and nitrogen sorption data of N-dC_Emim-dca_XZ_x_1000 with X = Li, S and P at varying salt concentrations x.

Sample N-dC	Elemental analysis [wt%] Combustion			S_{BET}[i] $[m^2g^{-1}]$	Pore volume[i] $[mlg^{-1}]$		
	N	C	H		Total	Micro	Meso
Emim-dca_LiZ_3_1000	6.1	84.5	1.1	1705	0.68	0.53	0.15
Emim-dca_LiZ_15_1000	4.3	77.6	1.9	1715	2.75	0.31	2.44
Emim-dca_SZ_1.5_1000	4.8	71.9	2.3	1248	0.60	0.45	0.15
Emim-dca_SZ_3_1000	5.7	84.2	1.0	1715	0.99	0.49	0.5
Emim-dca_SZ_4.5_1000	4.1	75.4	2.0	1678	1.23	0.37	0.86
Emim-dca_SZ_6_1000	4.5	73.3	2.0	1403	1.21	0.33	0.88
Emim-dca_SZ_13_1000	4.0	77.1	1.8	1511	2.07	0.34	1.73
Emim-dca_PZ_1.5_1000	4.4	75.2	2.1	1135	0.56	0.38	0.18
Emim-dca_PZ_3_1000	5.1	82.3	1.1	1485	0.78	0.5	0.28
Emim-dca_PZ_4.5_1000	3.9	74.5	2.1	1403	0.73	0.48	0.25
Emim-dca_PZ_6_1000	4.4	73.8	2.4	1629	0.79	0.57	0.22
Emim-dca_PZ_14_1000	3.5	69.7	2.5	1504	0.77	0.53	0.24

i Determination described in A Nitrogen sorption measurements.

Here, a notable pore size of 12 nm in diameter and a pore volume of 2.75 mlg^{-1} are obtained for LiZ and SZ templated materials, respectively. In contrast, the carbons templated with varying amounts of PZ show overall constant porosity values which can again be attributed to the formation of particles. Importantly, the particle formation as such is not influenced at higher salt concentrations, but an intergrowth to globule, aerogel-like monolithic structures is observed (*Figure 2-15*). Here, the particle size and connectivity can be adjusted through the salt amount.
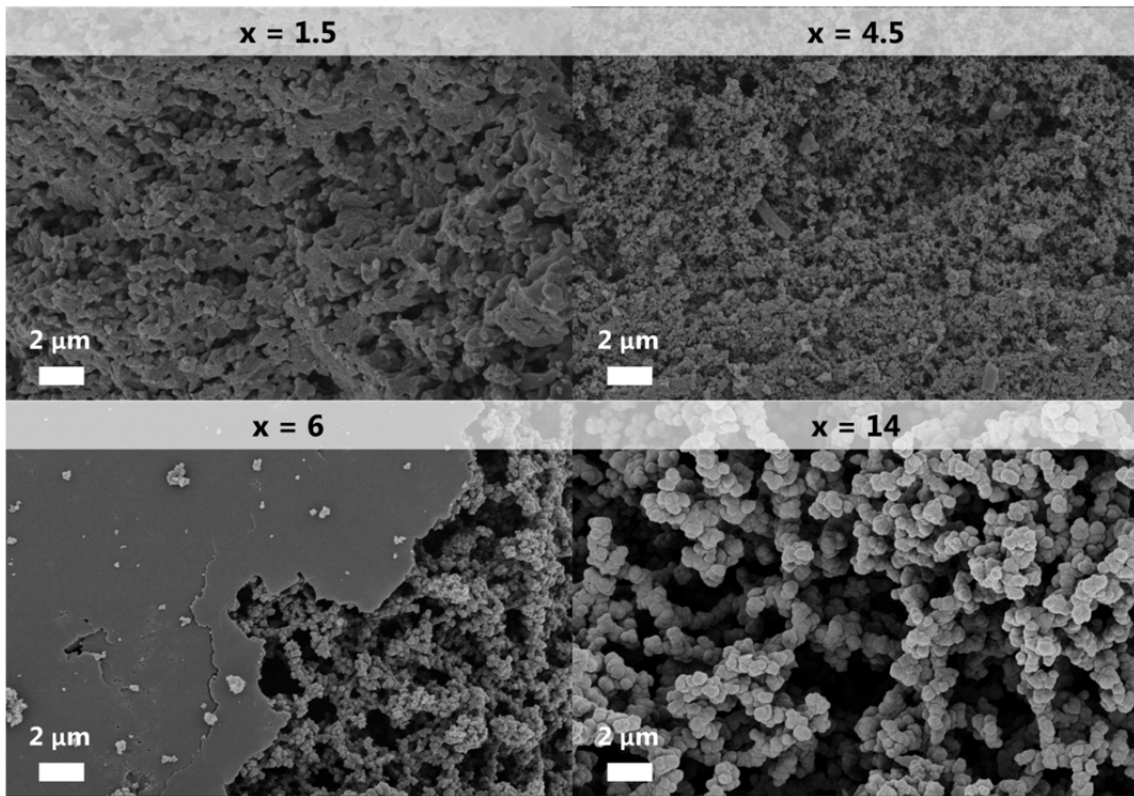
Figure 2-15 SEM images of N-dC_Emim-dca_PZ_x_1000 at varying PZ concentrations x.

This is comparable to classical sol-gel chemistry where the particle size can be adjusted, beside other factors, through the precursor and solvent concentration.

The nucleation and growth of nanoparticles was extensively studied by La Mer *et al.* in sulfur sols.[161, 162] The requirements to obtain monodisperse particles can be described using the La Mer diagram (*Figure 2-16*).
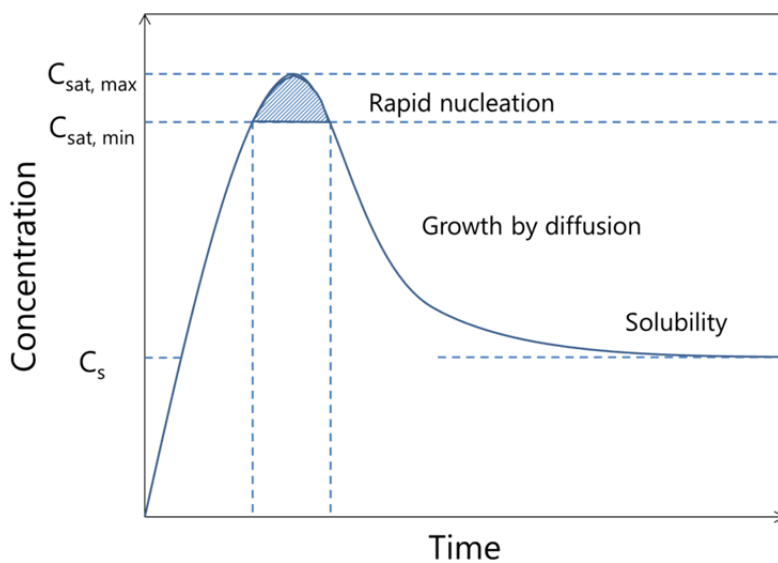
Figure 2-16 La Mer diagram.

In order to obtain monodisperse colloidal particles, the initial monomer concentration has to exceed the minimal saturation concentration $C_{sat,min}$ rapidly. In this supersaturated regime, burst nucleation occurs which reduces the monomer concentration. If the latter falls below $C_{sat,min}$, the nucleation process is terminated and the particles grow further until the solubility concentration C_s is reached. This mechanism is not applicable for every system, but the general idea of separating the nucleation and growth processes is a widely accepted approach to obtain nanoparticles.

Drawing parallels to the herein presented system, the ionic liquid is the precursor, while the salt melt, here PZ, acts as solvent. Note that the zinc chloride is a known catalyst for triazine formation,[163, 164] therefore the salt melt is also catalytic which may accelerate nuclei and particle formation.

At low salt concentrations (*Figure 2-15, x=1.5*), a porous material is already formed, yet without distinct particle shaping. This is attributed to the very high monomer concentration, *i.e.* the concentration of the ionic liquid in the salt, thus agglomeration and intergrowth of the particles takes place. Increasing the salt amount to medium concentrations (*Figure 2-15, x=3, 4.5, 6*) dilutes the ionic liquid eventually enabling the formation of a high nuclei amount which further grow into small particles. If the particles are not stabilized, agglomeration occurs due to the domination of attractive interaction which results in a monolithic material. This is a general behavior which can be described with the Lennard-Jones potential (*Figure 2-17*). Here, $1/r^{12}$ represents the repulsion caused by Pauli repulsion at short ranges and $1/r^6$ the attraction mainly caused by van der Waals force at longer ranges with r_0 as separation r at which the inter-particle potential is zero and r_m as separation r at which the potential reaches its minimum. This is also observed for other systems such as resorcinol-formaldehyde (RF-gels) and silica with the latter also known as the Nakanishi process.[159, 160, 165]

Figure 2-17 Lennard-Jones (12, 6) potential.

If the ionic liquid is highly diluted (*Figure 2-15, x=14*), only few nuclei are generated. Consequently, a high monomer amount is still left eventually causing the growth of big particles.

It can be concluded that the PZ templated system will always reveal a globule-like, monolithic structure where the partic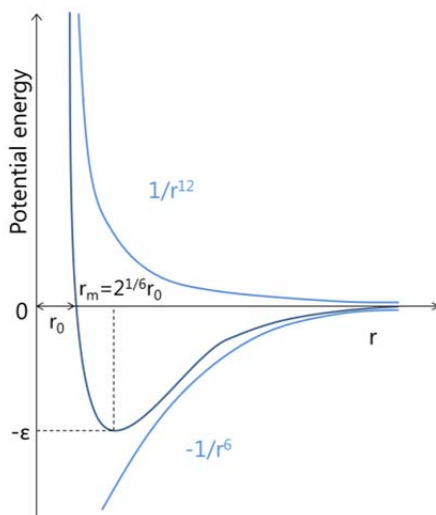le size and connectivity can be tuned by the porogen amount. Concerning bulk elemental analysis (*Table 2-b*), the materials have comparable compositions, which support the structural effect of the porogen rather than activation.

2.3. Single- and binary-salt-systems: N-doped carbons

2.3.1. Single-salt systems

In 2.2 eutectic mixtures each composed of two different salts *i.e.* $LiCl/ZnCl_2$, $NaCl/ZnCl_2$ and $KCl/ZnCl_2$ with each salts composed of two different inorganic ions *i.e.* Li^+, Na^+, K^+ and Zn^{2+} combined with Cl^-, respectively, were used as a porogen phase. It was found, that besides the melting point also the ion species and their combination has an influence on the porosity as well as morphology of the carbon material. In order to gain further insights into the impact of the inorganic cation and different porogens, in the following "single-salt-systems" were investigated. Here, zinc acetate dihydrate (ZnAc) and cesium acetate (CsAc) were chosen since they are miscible with the representatively employed ionic liquid Emim-dca and both possess melting points below the onset of ionic liquid polymerization (ZnAc: 237 °C, CsAc: 194 °C). Furthermore, cesium has a very large ion radius, thus it may serve as molecular template while zinc is known to catalyze the triazine-formation.[71, 163, 164] The acetate ion is believed to have a minor influence since it is at least partially released during the precursor mixing and carbonization process. The incorporation into the carbon structure cannot be excluded but is not regarded as main process because even at high CsAc concentrations no increase in carbon content was observed.

The functional carbons were synthesized in the same way as in the case of the eutectic mixtures by mixing the ionic liquid Emim-dca with varying amounts of ZnAc and CsAc, respectively. For reasons of comparison, the molar ratio of acetate cation and ionic liquid was kept identical for both porogens. After subsequent heat-treatment under nitrogen atmosphere and washing, black voluminous powders were obtained. In the case of CsAc the template was also removed with water while for ZnAc diluted HCl was employed.

Throughout this thesis, the precursor solutions derived from ZnAc and CsAc are named IL_YAc_r while the N-dCs are denoted as N-dC_IL_YAc_r_T. Here, IL is the respective ionic liquid used as precursor, YAc is the acetate (Ac) with Y being zinc (Zn) or cesium (Cs), r represents the mass ratio acetate/IL in the precursor mixture and T is the synthesis temperature. Here, the N-dCs were synthesized at 800 °C.

Already the precursor mixtures reveal a fundamentally different behavior (*Figure 2-18*). For mixtures of Emim-dca with ZnAc clear gels are obtained which viscosity/strength increases with the ZnAc amount added. In the case of CsAc opaque and solid mixtures are formed which can reversibly be liquified through heating. This is presumably due to the different valence and coordination ability of the metal ions so that for the ZnAc system gelation occurs because of coordination of Zn^{2+} with the dicyanamide anions of the ionic liquid.
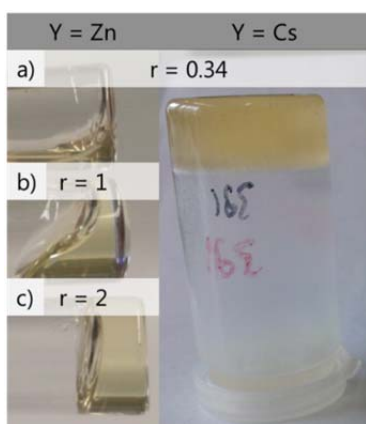
Figure 2-18 Left: Emim-dca_ZnAc_r with r= 0.34 (**a**), 1 (**b**) and 2 (**c**). **Right**: Emim-dca_CsAc_0.34.

WAXS diffractogram of the unwashed products were measured in order to gain more insights into the porogen behavior throughout the heat-treatment (*Figure 2-19 a*). This was, however, only possible for the ZnAc system since CsAc forms hygroscopic compounds.
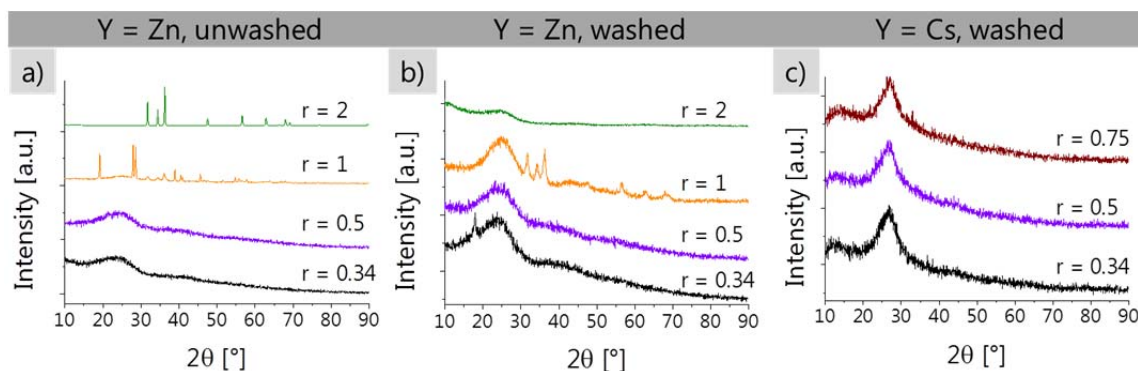
Figure 2-19 WAXS pattern of **a)** unwashed, **b)** washed N-dC_Emim-dca_ZnAc_r_800 and **c)** washed N-dC_Emim-dca_CsAc_r_800 at varying acetate concentrations r.

At low ZnAc amounts (*Figure 2-19 b*), typical peaks for slightly disordered graphitic carbon are already visible. Increasing ZnAc amounts results in the additional formation of zinc cyanamide for N-dC_Emim-dca_ZnAc_1_800 and zinc oxide for N-dC_Emim-dca_ZnAc_2_800. After washing, all carbon materials show a broadened 2θ 25° (002) peak revealing graphitic stacking of the carbon materials. However, the 44° (100) peak is not visible and consequently the intralayer organization is still relatively low. It is to mention that the materials synthesized at 1000 °C exhibit the (100) peak because of a higher degree of graphitization. Furthermore, for N-dC_Emim-dca_ZnAc_1_800 additional peaks assigned to zinc oxide are found which remain even after several washing steps. Thus, at this zinc acetate-to-ionic liquid ratio, composite materials with stable enwrapped zinc oxide nanoparticles can be obtained. In comparison, templating with the eutectics (2.2) did not reveal any zinc oxide species even though the zinc ion concentrations were higher. Additionally, carbons derived from ZnAc (without zinc oxide *i.e.* at high salt amounts) are obtained in higher yields than from CsAc. This may be due to a less efficient ion trapping by Cs^+ and the ability of Zn^{2+} to catalyze the triazine formation. The WAXS pattern of the carbons derived from CsAc as porogen (*Figure 2-19 c*) reveal the (002) peak sharper and shifted to slightly higher values of 2θ 26.8° compared to the carbons made in ZnAc. This indicates a higher degree of ordering and smaller interlayer distance, respectively.

The TEM and SEM images of N-dC_Emim-dca_CsAc_0.34_800 (*Figure 2-20*) reveal rolled up sheets which are in accordance with the WAXS pattern. The materials derived from ZnAc also show sheet-like structures (*Figure 2-21*), however, more crumbled than in the case of CsAc. This goes well with the broader peaks obtained from WAXS. Furthermore, the structures become thinner with increasing ZnAc concentration, finally yielding separate flakes for N-dC_Emim-dca_ZnAc_2_800. Again, none of those morphologies was observed for the eutectic salt mixtures, which suggests a specific influence of the counter-ion on the carbon structure.
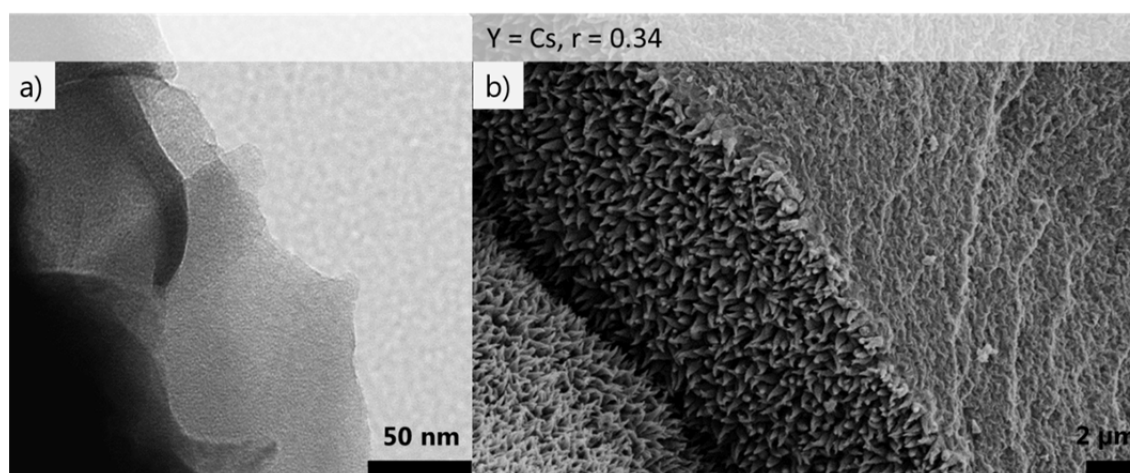
Figure 2-20 a) TEM and **b)** SEM images of N-dC_Emim-dca_CsAc_0.34_800.
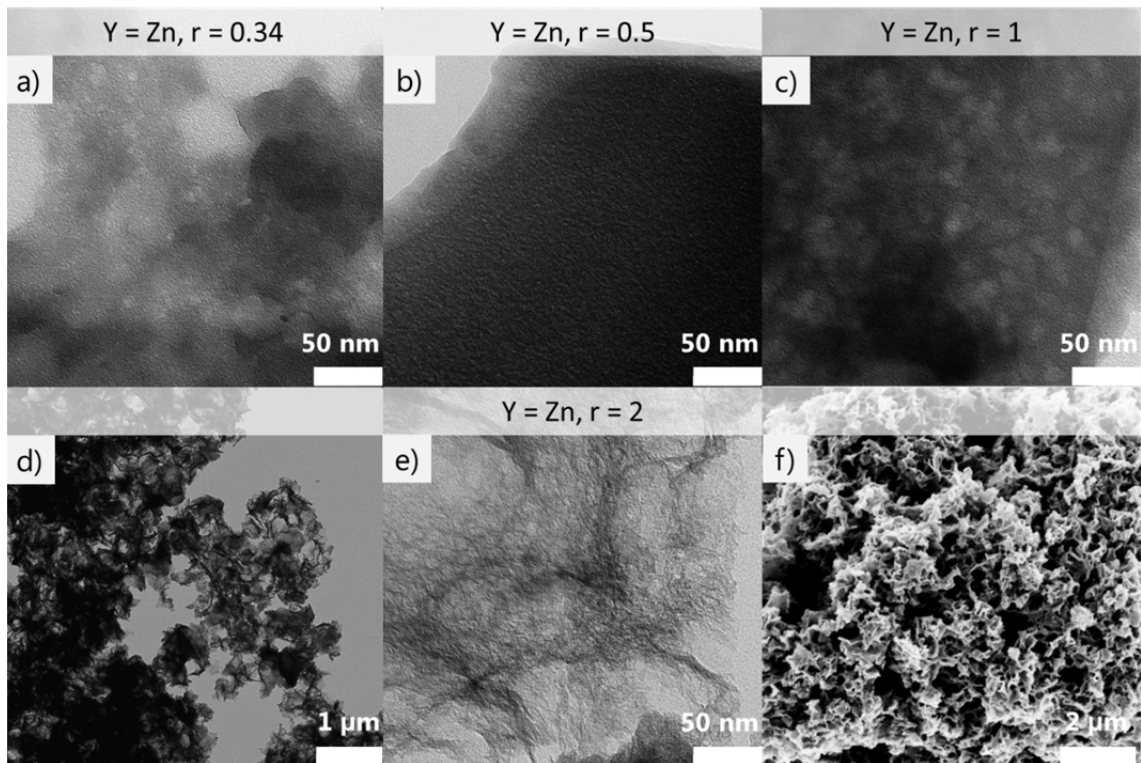
Figure 2-21 a-e) TEM and **f)** SEM images of N-dC_Emim-dca_ZnAc_r_800.

The nitrogen sorption measurements show a significant nitrogen uptake for all CsAc-derived carbon materials (*Figure 2-22 a*). The highest surface area of 515 m^2g^{-1} is obtained for N-dC_Emim-dca_CsAc_0.5_800 while higher salt amounts presumably promote structure collapse (N-dC_Emim-dca_CsAc_0.34_800: 287 m^2g^{-1}, N-dC_Emim-dca_CsAc_0.75_800: 151 m^2g^{-1}). For the materials derived from ZnAc (*Figure 2-22 b*), the surface area increases with increasing salt amount up to 1000 m^2g^{-1} for N-dC_Emim-dca_ZnAc_2_800 (N-dC_Emim-dca_ZnAc_0.5_800: 23 m^2g^{-1}, N-dC_Emim-dca_ZnAc_1_800: 140 m^2g^{-1}). The shape of the isotherm indicates multilayer adsorption on sheet-like structures which is in accordance with the TEM and SEM observations.
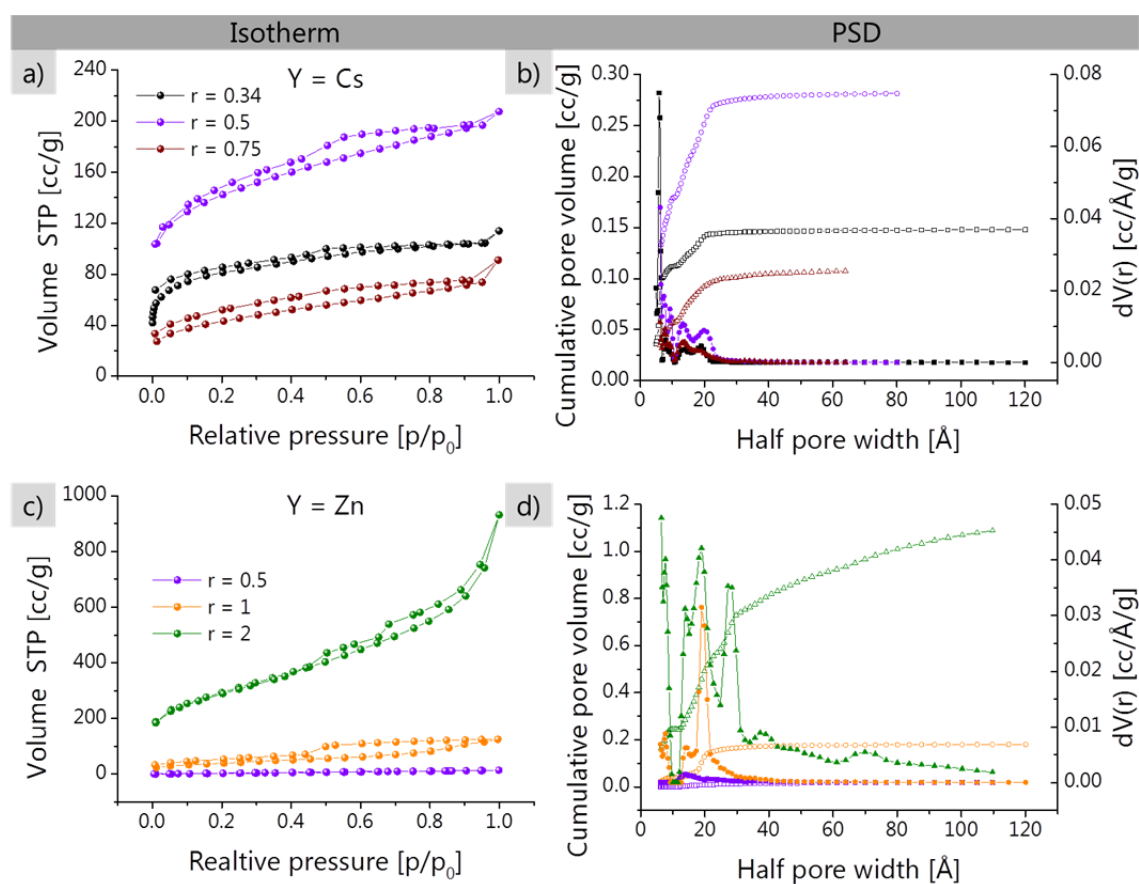
Figure 2-22 Nitrogen sorption isotherms (**left**) and PSDs (**right**) of N-dC_Emim-dca_YAc_r_800 with Y = Cs (**a, b**) or Zn (**c, d**) at varying salt concentrations r.

For the acetates, the templating presumably rather relies on the metal ion binding, ion clusters and in the case of zinc also on oxide structures than on a liquid salt melt as the acetates are less stable and convert into the corresponding oxides and hydroxides.

2.3.2. Binary-salt system

In 2.3.1 single-salt-systems of Emim-dca with either ZnAc or CsAc were investigated. To support the results of part 2.2 that not only the melting point but also the cooperative interplay of different ion species can be a parameter to control the carbon porosity and morphology, in this part the binary system ZnAc and CsAc as templates for Emim-dca condensation is presented.

The carbon material was synthesized according to the procedure described before. Here, a carbon material templated with equal molar ratio of ZnAc and CsAc and a total mass corresponding to 1000 mg CsAc was synthesized (notation according to the previous nomenclature N-dC_Emim-dca_ZnAcCsAc1:1_1_800).

In contrast to the WAXS of the single-salt systems, for the binary-salt system both the 2θ 25° (002) and the 44° (100) peak are visible, thus, pointing to a higher interlayer organization (*Figure 2-23 a*). Furthermore, no zinc oxide phase is present which already suggests a different formation pathway. The TEM image reveals a highly porous light-weight material with spherical pores which is also observed in the SEM (*Figure 2-23 b, c*).
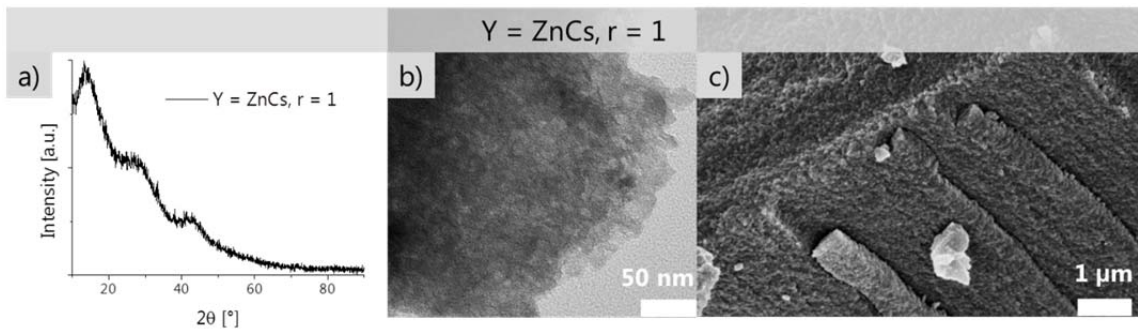
Figure 2-23 a) WAXS pattern, **b)** TEM and **c)** SEM images of N-dC_Emim-dca_ZnAcCsAc1:1_1_800.

In order to evaluate whether the two salts affect the carbon morphology in a synergistic manner, nitrogen sorption measurements were conducted (*Figure 2-24*). Here, N-dC_Emim-dca_ZnAcCsAc1:1_1_800 (1555 m^2g^{-1}) was compared to the material solely derived from ZnAc (N-dC_Emim-dca_ZnAc_1_800, 140 m^2g^{-1}) at the corresponding molar ratio of salt to ionic liquid. The synthesis of N-dC_Emim-dca_CsAc_1_800 did not yield a sufficient amount of sample and is therefore not included. To exclude that the porosity in the binary system originates only from one component, the carbons N-dC_Emim-dca_ZnAc_0.5_800 (23 m^2g^{-1}) and N-dC_Emim-dca_CsAc_0.5_800 (515 m^2g^{-1}) were also measured (*Figure 2-24*).
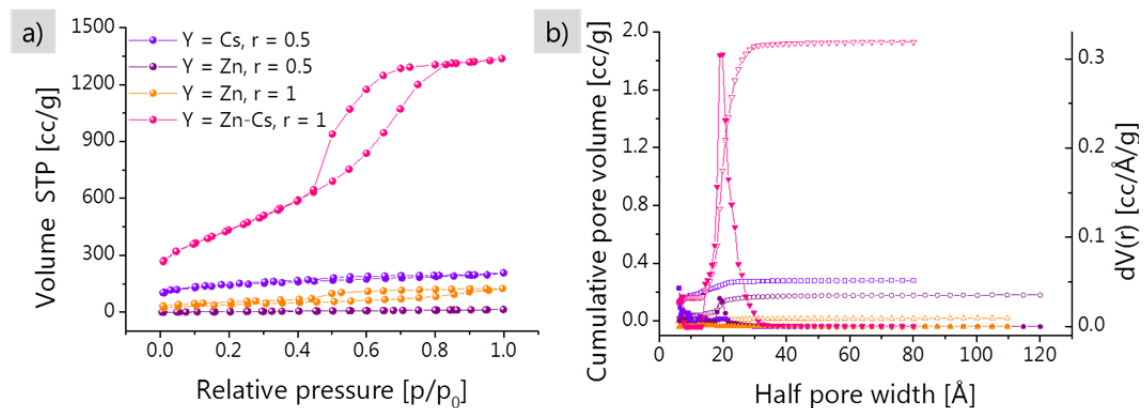
Figure 2-24 Nitrogen sorption isotherms (**a**) and PSD (**b**) of the single- and binary-salt-systems N-dC_Emim-dca_YAc_r_800 with Y=Cs or/and Zn at varying salt concentrations r.

From the nitrogen sorption measurements it is clearly visible that the porosity of the carbon material N-dC_Emim-dca_ZnAcCsAc_1_800 is completely different from the other systems. The porosity is not only generated because of the presence of a salt since N-dC_Emim-dca_ZnAc_1_800 reveals a very different nitrogen uptake. Furthermore, the pores are also not only due to the presence of one of the salts because N-dC_Emim-dca_ZnAc_0.5_800 and N-dC_Emim-dca_CsAc_0.5_800 do not resemble the nitrogen sorption behavior of the binary-salt-system. Additionally, by combining ZnAc and CsAc, the zinc ions presumably trap the ionic liquid as well as Cs ions, thus higher yield, surface area, and pore volume are accessible. All results point to a cooperative template effect by the different salts offering a further possibility to fine-tune the porosity of carbons by salt templating.

The porosity of materials derived from salt templated ionic liquids is mainly influenced by the following variables:

- miscibility of the phases
- trapping effect due to coulombic interaction of the salts
- melting point of porogen salt
- ion radius
- amount of porogen
- counter anion

The carbon morphologies presumably originate from demixing of the salt phases which varies on many scales in dependence on the above listed constraints. Here, it is to mention that the eutectic behavior is influenced by the ionic liquid itself. However, because of the "all-ionic" reaction environment, the electrostatic interactions of the ionic liquids with each porogen are comparable. Thus, the term "salt templating" is reasonable, it is just that different salt structures are templated. Furthermore, we propose the possibility to adjust the morphology smoothly between different states just through the right combination of the nature and amount of the porogen salt. Even the combination of different porosities can be envisioned, *e.g.* the generation of hierarchical structures.

2.4. Application in CO$_2$-utilization

To date, most energy and fuel production still relies on CO$_2$-generating techniques. However, given a constant rate, the CO$_2$ concentration is estimated to exceed the level which can be balanced by the natural carbon cycle within the next decades.[166] Therefore, alternative energy sources such as wind and solar energy possess high potential but still need to be improved. One of the current attempts to counteract the greenhouse effect is CO$_2$-sequestration (carbon capture and storage CCS) and separation of CO$_2$ from flue gas.[166, 167] Nevertheless, one step further would not only include the storage of CO$_2$ but also its utilization[168] to produce valuable compounds.
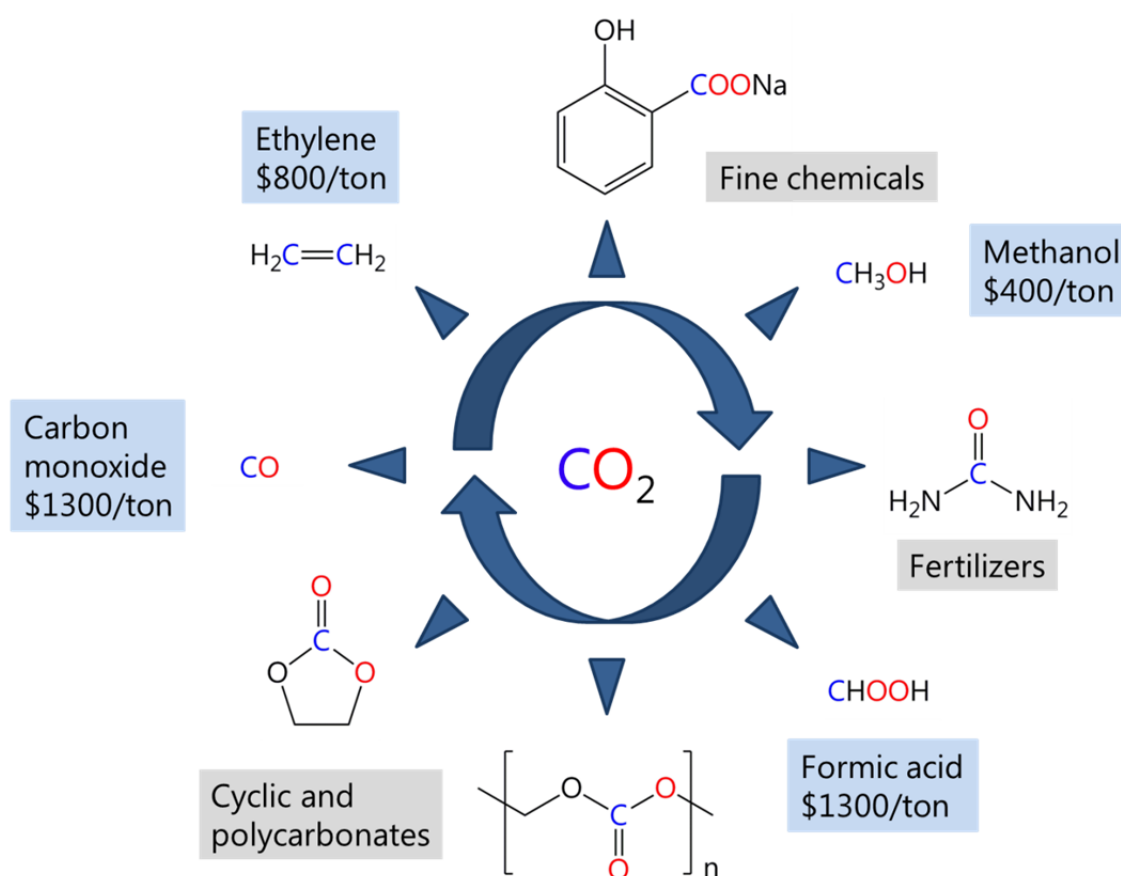
Figure 2-25 Examples for CO$_2$-conversion into more valuable compounds.[166]

Indeed, a range of compounds is obtained from CO$_2$ as feedstock (*Figure 2-25*). In this regard, the golden goal is the synthesis of hydrocarbons or alcohols *e.g.* methanol from CO$_2$,[169] preferably through electrochemical conversion since electrocatalysis is very efficient because it is not limited by the Carnot cycle. Furthermore, electrochemical conversion is simple and can be performed at ambient operation conditions.[170] However, carbon dioxide is a non-polar, linear molecule which is thermodynamically very stable. Consequently, the conversion *i.e.* the rearrangement from a linear molecule

to a bent radical anion has a high overpotential of -1.9 V $vs.$ NHE for the single electron reduction.[171] In order to lower the reduction potential and to increase the selectivity, appropriate catalysts are required. In this regard, proton coupled multi electron steps are thermodynamically favored ($Table~2\text{-}c$).

Table 2-c Pathways of electrochemical reduction of CO_2 in a proton-containing environment.[171]

Reaction	Potential [V][i]	
$CO_2 + 2H^+ + 2e^- \rightarrow CO + H_2O$	$E^0 = -0.53$	(1)
$CO_2 + 2H^+ + 2e^- \rightarrow HCO_2H$	$E^0 = -0.61$	(2)
$CO_2 + 4H^+ + 4e^- \rightarrow HCHO + H_2O$	$E^0 = -0.48$	(3)
$CO_2 + 6H^+ + 6e^- \rightarrow CH_3OH + H_2O$	$E^0 = -0.38$	(4)
$CO_2 + 8H^+ + 8e^- \rightarrow CH_4 + 2H_2O$	$E^0 = -0.24$	(5)
$CO_2 + e^- \rightarrow CO_2^{\bullet-}$	$E^0 = -1.90$	(6)

i Aqueous solution, pH7, $vs.$ NHE at room temperature.

State-of-the-art systems seek to follow biological systems $e.g.$ enzymes and are mainly based on metal complexes and metals such as copper.[166, 171]

However, current systems are either unstable or possess low selectivity and mainly catalyze two-electron processes. The production of further-reduced species is highly desirable, but already reveals difficulties in the oxygen reduction yet being less complex compared to CO_2 reduction. Nevertheless, studies by Bocarsly $et~al.$ showed that pyridinium cations at certain metal electrodes are capable to selectively catalyze the CO_2 reduction to methanol.[172] This finding is very surprising since the pyridinium can only transfer one electron contradicting the present assumption that multi-electron charge-transfer reagents are necessary.[173-175] Mechanistic studies suggest multiple electron transfers between various species and intermediates through a coordinative interaction.

Other promising candidates are porous N-doped carbon materials since they possess an increased ability for CO_2-adsorption.[35, 36] Much effort has been made to synthesize porous carbons with a high amount of functional groups, however, the fundamental phenomena which are responsible for the superior sorption properties of these materials are still not fully understood. Besides high surface areas and microporosity, some possible processes are currently discussed in the literature: acid-base interaction between N-containing basic functional groups and acidic CO_2,[176-178] interaction between net positive charge on carbon atoms adjacent to the nitrogen and CO_2,[35] interaction with polarizable CO_2 through dipol-quadrupol interaction[179] or hydrogen-bonding interaction between hydrogen atoms from CH and NH on the

carbon surface and CO_2 molecules.[180] In this context, it is to mention that within a mechanistic study, also Bocarsly and co-workers assumed an increased Lewis-basicity of the pyridyl-nitrogen and the stabilization of carbon-based radicals on the electrode surface to increase reaction kinetics.[181] In general the presence of nitrogen favors CO_2 uptake and results in increased heat of adsorption.[149] Thus, the pyridinium motive is assumed to play a key role in the course of CO_2 reduction.

In order to evaluate potential electrode materials for electrochemical CO_2-reduction, in the present study preliminary CO_2 sorption measurements were performed with N-doped carbons templated with eutectic salt mixtures. Here, the eutectics were chosen as porogen since this system offers the possibility to screen and compare different morphologies *i.e.* microporosity, mesoporosity and globule, aerogel-like monolithic structures made out of the same material.

The materials presented in part 2.2 were produced at high temperatures *i.e.* 1000 °C and 1400 °C, respectively. However, as mentioned before, for an increased CO_2-uptake/interaction a high amount of nitrogen and surface functional groups is advantageous. Therefore, the carbon materials were produced according to the previous carbons but at a lower temperature of 450 °C using Emim-dca and Bmp-dca as precursor. This yields polymeric networks with a high amount of functional groups and consequently higher nitrogen content. The precursor mixtures and carbon materials are named following the nomenclature described in 2.2.

In *Figure 2-26*, the aqueous washing solutions of N-dC_Emim-dca_XZ_3_450, with X=Li, S and P are shown representatively. While N-dC_Emim-dca_LiZ_3_450 precipitates relatively fast, the precipitation of N-dC_Emim-dca_SZ_3_450 takes several minutes and N-dC_Emim-dca_PZ_3_450 shows a dispersion which does not completely precipitate completely even after several hours. This suggests already without any further analysis that the materials reveal different properties *i.e.* different interaction with water probably caused by a different porosity and morphology as well as surface chemistry, respectively.
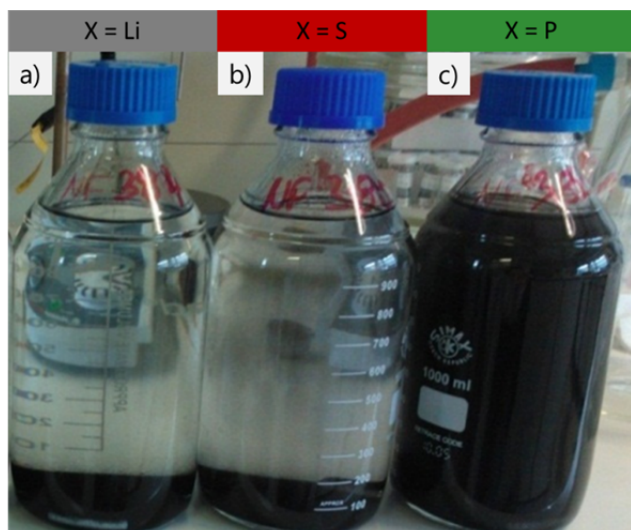
Figure 2-26 Aqueous washing solutions of N-dC_Emim-dca_XZ_3_450 with X=Li (**a**), S (**b**) and P (**c**).

The WAXS patterns (*Figure 2-27*) of the washed products show a broadened 2θ ~ 25° (002) peak which reflects the graphitic stacking of the carbon materials. However, the 2θ ~ 44° (100) peak is not visible and consequently the intralayer organization is relatively low. This is a comprehensible observation since the carbon materials are produced at a relatively low temperature of 450 °C which results in less in-plane order. The absence of additional peaks indicates the near complete removal of the salt phases.
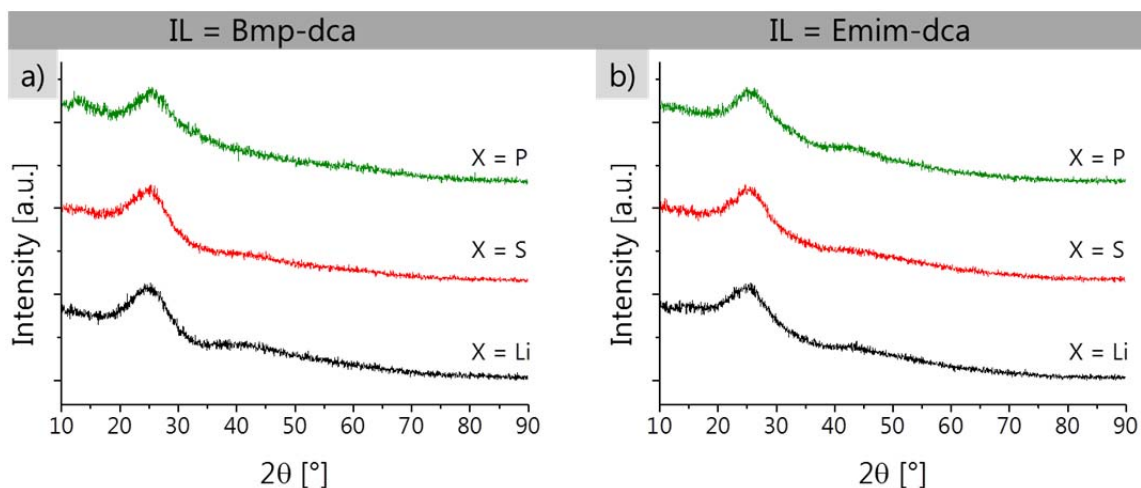
Figure 2-27 WAXS patterns of **a)** N-dC_Bmp-dca_XZ_3_450 and **b)** N-dC_Emim-dca_XZ_3_450 with X=Li (**black**), S (**red**) and P (**green**).

The TEM and SEM pictures of the washed products N-dC_Bmp-dca_XZ_3_450 and N-dC_Emim-dca_XZ_3_450 with X= Li, S and P reveal morphologies comparable to the respective high-temperature materials presented in 2.2 (*Figure 2-28*). This is an

important observation since it further supports the previous statements that a main part of the pore formation indeed results from a templating mechanism by the salt. Essentially, the desired morphology can be obtained over a wider temperature range independent of the nature of the IL. This indicates the generality of the route not only towards tunable porous functional carbons but also porous polymeric materials.
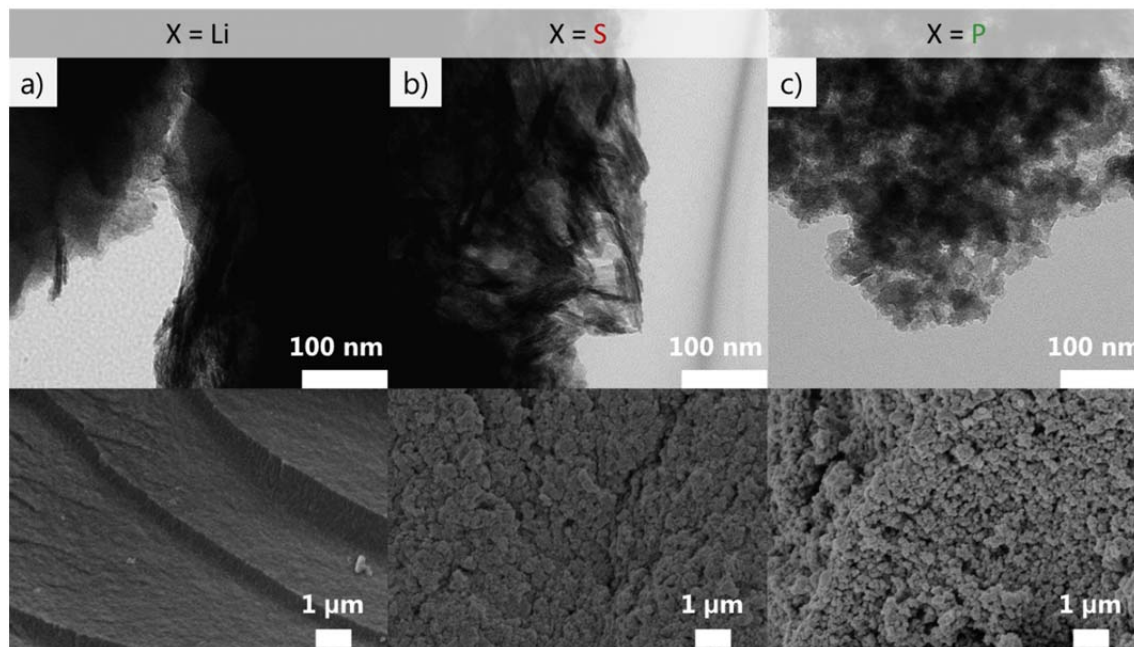
Figure 2-28 TEM (**top**) and SEM (**bottom**) pictures of N-dC_Bmp-dca_XZ_3_450 with X=Li (**a**), S (**b**) and P (**c**).
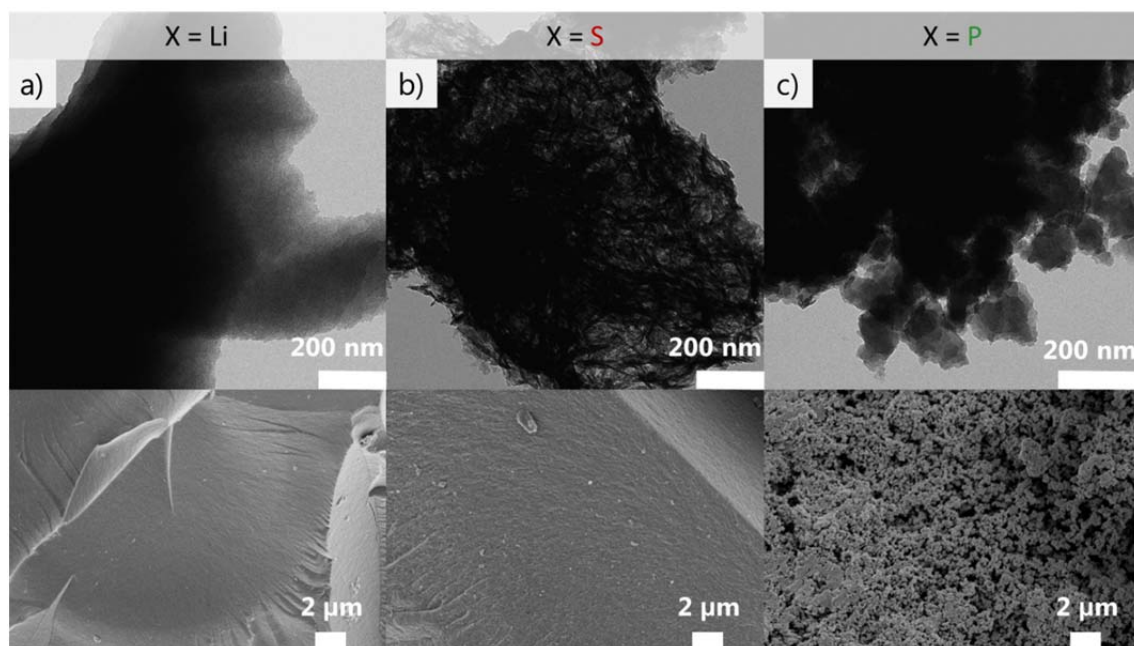
Figure 2-29 TEM (**top**) and SEM (**bottom**) pictures of N-dC_Emim-dca_XZ_3_450 with X=Li (**a**), S (**b**) and P (**c**).

In order to gain further insights into the structure of the low-temperature materials, infrared spectroscopy measurements (IR) were conducted (*Figure 2-30*). The CN stretch vibration at ~2200 cm^{-1} of the untreated ionic liquid almost disappeared for all materials after heat-treatment at 450 °C which indicates the polymerization of the cyano groups during product formation.[26] The observation of strong and broadened absorption bands at ~1250 cm^{-1} and ~1556 cm^{-1} points to the formation of aromatic CN structures, *e*.g. triazine rings. Additionally, NH stretching bands appear at ~3300 cm^{-1} as an indication of amino groups. However, the very broad absorption band can also be due to adsorbed water molecules. The IR results support the assumption of functional polymeric structures.
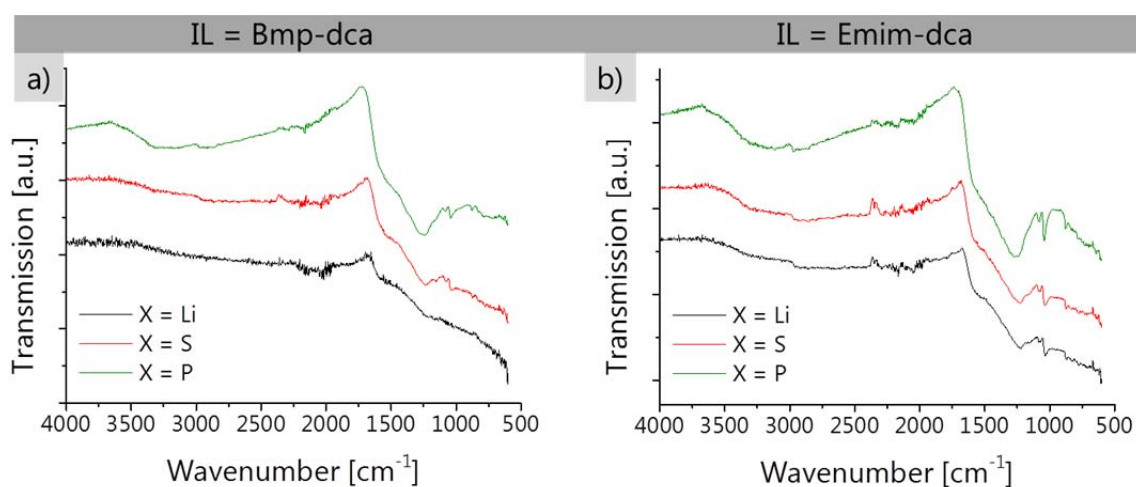
Figure 2-30 IR spectra of **a)** N-dC_Bmp-dca_XZ_3_450 and **b)** N-dC_Emim-dca_XZ_3_450 with X=Li (**black**), S (**red**) and P (**green**).

Besides the similar morphologies of the high and low temperature salt templated carbons observed by TEM and SEM images, the nitrogen sorption isotherms and PSDs of the washed products N-dC_Bmp-dca_XZ_3_450 and N-dC_Emim-dca_XZ_3_450 also reveal comparable porosities (*Figure 2-31*).

In comparison to the high temperature products presented in 2.2., the nitrogen sorption isotherms and PSDs indeed reveal similar shapes and pore sizes, respectively.
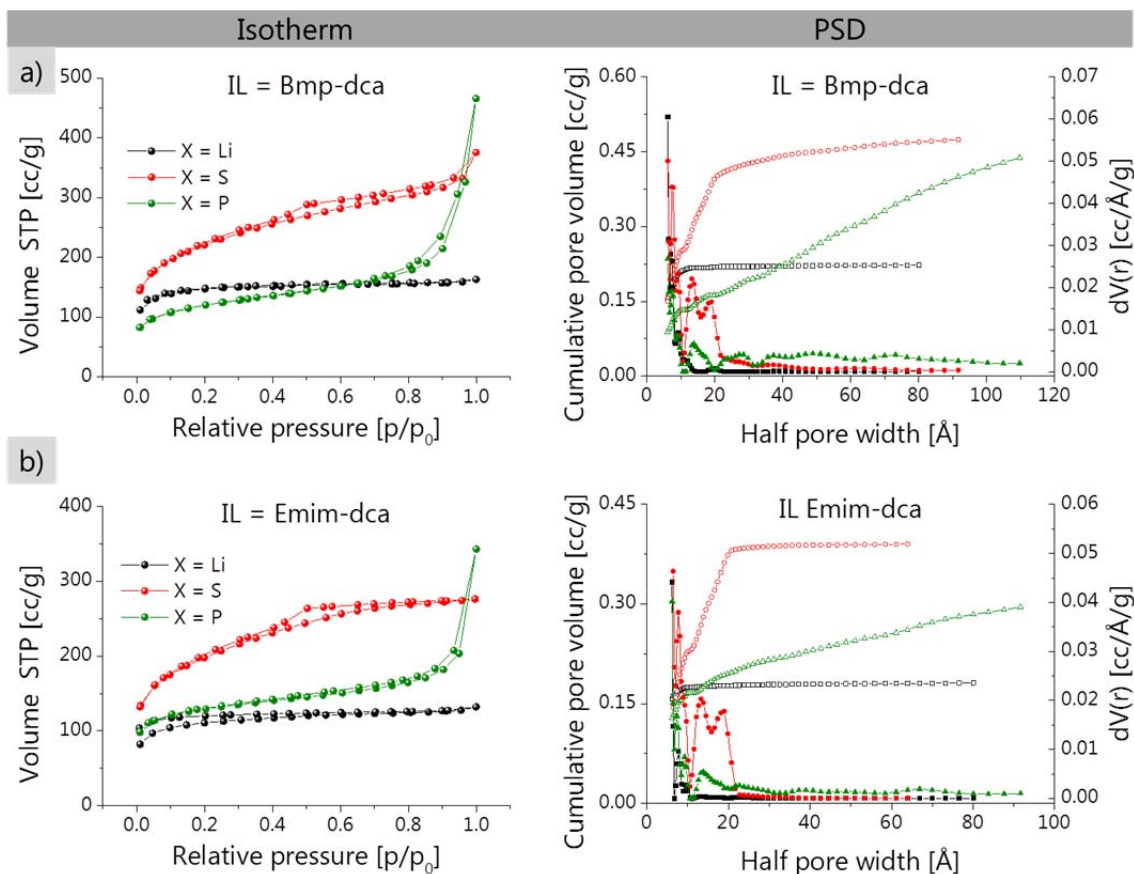
Figure 2-31 Nitrogen sorption isotherms (**left**) and PSD (**right**) of **a)** N-dC_Bmp-dca_XZ_3_450 and **b)** N-dC_Emim-dca_XZ_3_450 with X=Li, S and P.

Compared to the carbon materials produced at 1000 °C, the materials made at 450 °C reveal lower surface areas, yet with qualitatively comparable morphology and porosity (*Table 2-d*). One might attribute this also to the presence of residual salt in closed pores, but no corresponding diffraction peaks were observed in the WAXS diffractogram (*Figure 2-27*). Thus, the salt is either present as amorphous species or only in low amounts. It is also a well-known process that with increasing reaction temperature the surface area of carbon materials increases due to enhanced release of volatile compounds during structure rearrangement. This is naturally accompanied by a decrease of product yields at higher temperatures. Most likely, the materials produced at 450 °C are still flexible and the pores collapse during the drying step as known from other polymers. This is supported by the fact that for different drying methods *i.e.* vacuum-drying and freeze-drying, different porosities were obtained which, however, are not shown.

Bulk elemental analysis reveals the N-dCs to contain a higher nitrogen amount than the respective materials synthesized at higher temperatures (*Table 2-d*). Residual mass can be ascribed to oxygen content or incomplete salt removal, respectively. Furthermore, the results may also be influenced by adsorbed water.

Table 2-d Composition and nitrogen sorption data of the washed products N-dC_Bmp-dca_XZ_3_450 and N-dC_Emim-dca_XZ_3_450 with X=Li, S and P.

Sample **N-dC**	Elemental analysis [wt%]			S_{BET}[i]	Pore volume[i]		
	Combustion			$[m^2g^{-1}]$	$[mlg^{-1}]$		
	N	C	H		Total	Micro	Meso
Bmp-dca_LiZ_3_450	15.6	52.8	3.2	551	0.22	0.21	0.01
Bmp-dca_SZ_3_450	17.3	45.4	3.1	767	0.47	0.25	0.22
Bmp-dca_PZ_3_450	20.4	36.5	2.7	430	0.44	0.13	0.31
Emim-dca_LiZ_3_450	16.1	42.8	3.3	416	0.18	0.17	0.01
Emim-dca_SZ_3_450	17.2	40.8	3.1	687	0.39	0.23	0.16
Emim-dca_PZ_3_450	17.8	40.5	3.1	478	0.3	0.17	0.13

i Determination described in A Nitrogen sorption measurements

Here, it is to mention that the carbon yield derived from N-dC_Emim-dca_ZX_3_450 is twice the amount of the one derived from N-dC_Bmp-dca_XZ_3_450. Thermogravimetric analysis (TGA) of the pure ionic liquids under inert atmosphere on the other hand indicate, that both Emim-dca and Bmp-dca yield comparable amounts of product at 450 °C.[25, 26] This discrepancy gives evidence that the interaction of the ionic liquid with the template salt influences the crosslinking efficiency and the yield *via* specific ionic interactions. Taking account of the TEM, SEM and nitrogen sorption measurements, strong evidence is given that the porosity and morphology are an inherent character of the salt porogen which also supports a real template effect as already stated in 2.2. Here, the salt template structure is shown to be not only independent of the nature of the ionic liquid but also the temperature.

In order to reduce CO_2 with the help of a heterogeneous catalyst *e.g.* on a porous functional carbon electrode the catalyst surface has to interact with the CO_2 molecule. Here, two processes can be distinguished: 1) Adsorption caused by comparably weak interaction (up to 50 kJmol^{-1}) between a surface and an adsorbate *e.g.* through van der Waals force are categorized as physisorption. 2) Stronger adsorption (> 80 kJmol^{-1}) which involves chemical interaction between a surface and an adsorbate is called chemisorption. However, it is to mention that the interaction phenomenon cannot strictly be categorized by binding energies. For example, it is referred to chemisorption if a chemical modification of the adsorbate and the surface occurs, respectively. Thus, depending on the process, chemisorption can exist already at comparably low binding energies. In general, for heterogeneous catalysis the chemisorption is important. The so called isosteric heat of adsorption Q_{st} represents the strength of the adsorbate-adsorbent interaction and can be derived from CO_2 sorption measurements

(see A Applied methods). Thus, a high heat of adsorption indicates among other factors a promising material for heterogeneous catalysis, as the adsorbate is activated.

The CO_2 sorption isotherms were recorded at 273 K and 283 K (*Figure 2-32, a, c, e*) and further used for the calculation of the isosteric heat of adsorption based on the Clausius-Clapeyron equation as a function of the adsorbed CO_2 amount using the adsorption branch (*Figure 2-32, b, d, f*).
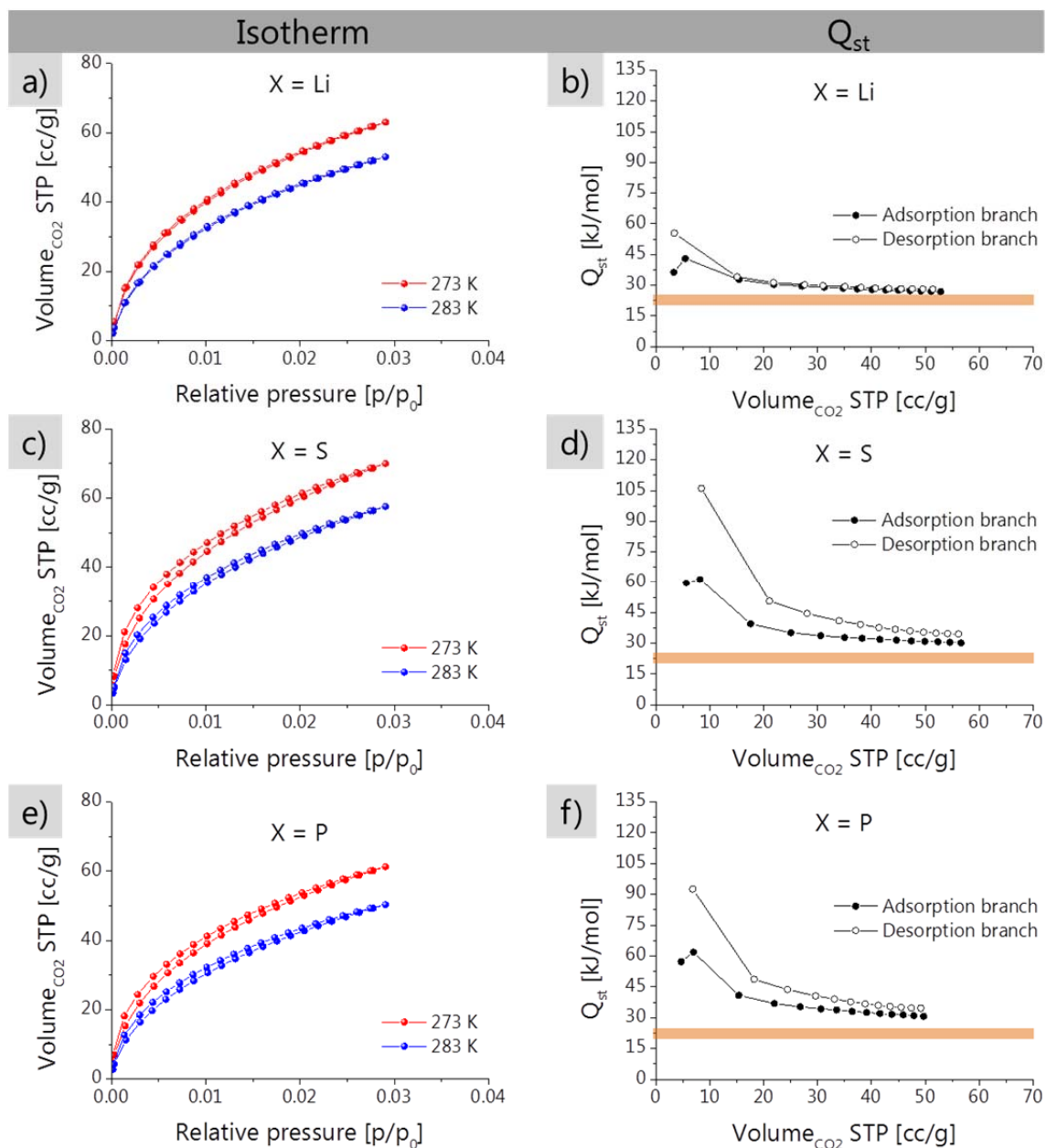
Figure 2-32 CO_2 sorption isotherms (**a, c, e**) measured at 237 K (red) and 283 K (blue) and heat of adsorption (**b, d, f**) of N-dC_Bmp-dca_XZ_3_450 calculated from the adsorption branch (**solid**) and desorption branch (**circles**). Orange bar: Average range of Q_{st} for microporous carbon.
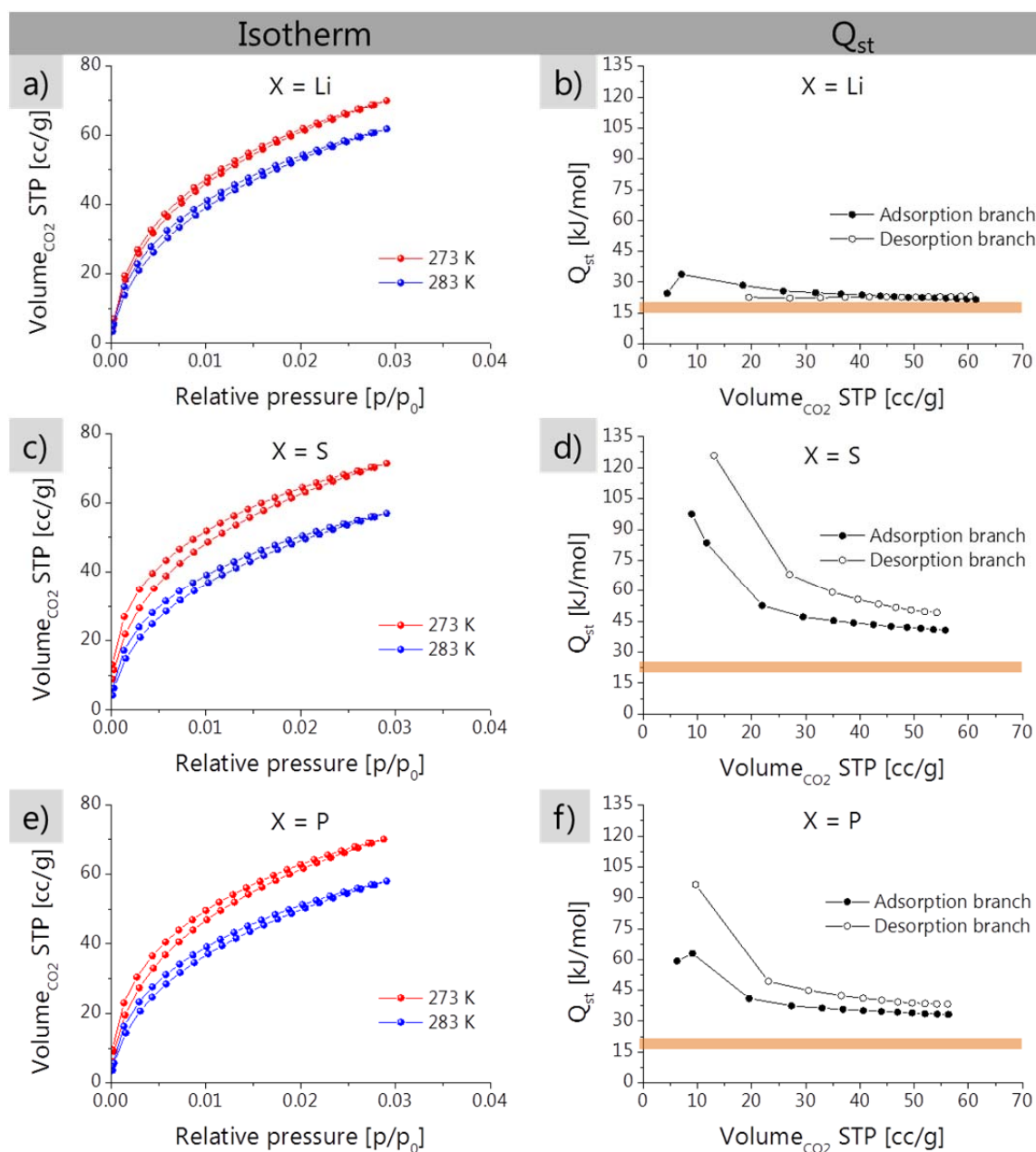
Figure 2-33 CO$_2$ sorption isotherms (**a, c, e**) measured at 237 K (red) and 283 K (blue) and heat of adsorption (**b, d, f**) of N-dC_Emim-dca_XZ_3_450 calculated from the adsorption branch (**solid**) and desorption branch (**circles**). Orange bar: Average range of Q$_{st}$ for microporous carbon.

For each material, the CO$_2$ sorption isotherms at 273 K resemble the ones at 283 K which reveal a lower uptake. In every case a small hysteresis occurs, which has to be taken into account for the calculation of Q$_{st}$ since it assumes an equilibrium.

The decrease of the isosteric heat of adsorption with increasing CO$_2$ loading is due to two different CO$_2$ adsorption mechanisms. At low coverage specific sites *e.g.* nitrogen functionalities are responsible for an increased CO$_2$ uptake while after their saturation at higher loadings unspecific sites such as a microporous carbon surface are the

determining factor.[80, 149] Consequently, solely microporous carbons possess a relatively constant isosteric heat of adsorption with an average value between 20 and 25 kJmol^{-1} (*Figure 2-32, 2-33* orange bars).[79, 80]

Because all materials in the present study reveal an increased isosteric heat of adsorption which decreases with loading, the presence of specific strong adsorption sites *i.e.* with accessible nitrogen functionalities can be assumed. If the isosteric heats of adsorption is calculated from the desorption branch, even higher values are obtained for most materials. This indicates that the hysteresis is presumably due to binding of CO_2.[182]

Because of the comparable nitrogen content of the Emim-dca and Bmp-dca samples of about 17 wt%, it is not only the amount of the nitrogen but presumably also the binding state and morphology which influences the CO_2 sorption. Here, it was shown that the carbon material with the highest mesoporosity *i.e.* N-dC_Emim-dca_NaZ_3_450 also possesses the highest heat of adsorption with 100 kJmol^{-1} at low coverage. Thus, this functional carbon is a promising candidate for further investigation in electrochemical CO_2 reduction. Again, it is to mention that residual salt cannot be excluded. However, since the heat of adsorption values are obtained from a surface related measurement technique *i.e.* CO_2 sorption, only minor influence is ascribed to possible enclosed salt.

In comparison with the isosteric heat of adsorption at low coverage of other porous materials such as MOFs (~35 kJmol^{-1}, BET surface area ~1600 m^{2}g^{-1}), zeolites (~50 kJmol^{-1}), activated carbons (~25 kJmol^{-1}) or amine-functionalized MOFs and silicas (~90-100 kJmol^{-1})[80] the functional polymeric carbons presented herein keep up or even outperform most of the other material classes. In spite of the comparatively moderate surface areas and the simple synthesis, this is a remarkable result.

2.5. Synthesis of N-S-co-doped carbons

The introduction of nitrogen into carbon structures is known to enhance properties such as electrical conductivity as well as stability. N-doped carbons were already shown to be highly active materials for a variety of applications such as ORR, H_2O_2-production and CO_2-storage.[30, 36, 75, 93, 120, 178] Recently, N-S-co-doped carbon materials were synthesized hydrothermally and presented as efficient catalysts for ORR.[58-60, 183] The results suggest a synergistic interaction of the N- and S-dopants presumably due to an easier polarizability. Thus, sulfur is a further promising element for doping of carbon materials. This is supported by DFT calculations conducted by Qiao *et al.* which reveal the synergistic interaction of N- and S-co-doping to result from the redistribution of

spin and charge densities in the HOMO structure.[60] In the time of writing the present thesis, Paraknowitsch *et al.* reported on the synthesis of N- and S-co-doped carbons from thiazolium salts.[73] The materials possess high N- and S-content even at high temperatures, yet the precursor salts first have to be synthesized in several steps.

For proof of principle and also to extend the class of materials producible from ionic liquids, the ionic liquid 1-Ethyl-3-methyl imidazolium thiocyanate (Emim-scn, inset *Figure 2-34*) was chosen as precursor for N-S-co-doped functional carbons (N-S-dC). This ionic liquid was employed because the cation was already successfully proven for the synthesis of the N-doped carbons. Furthermore, the sulfur is present in form of the thiocyanate anion which can undergo cyclization, the ionic liquid possesses high temperature stability (*Figure 2-34*) and the compound is readily available. Thus, the ionic liquid can be purchased and used without further treatment.
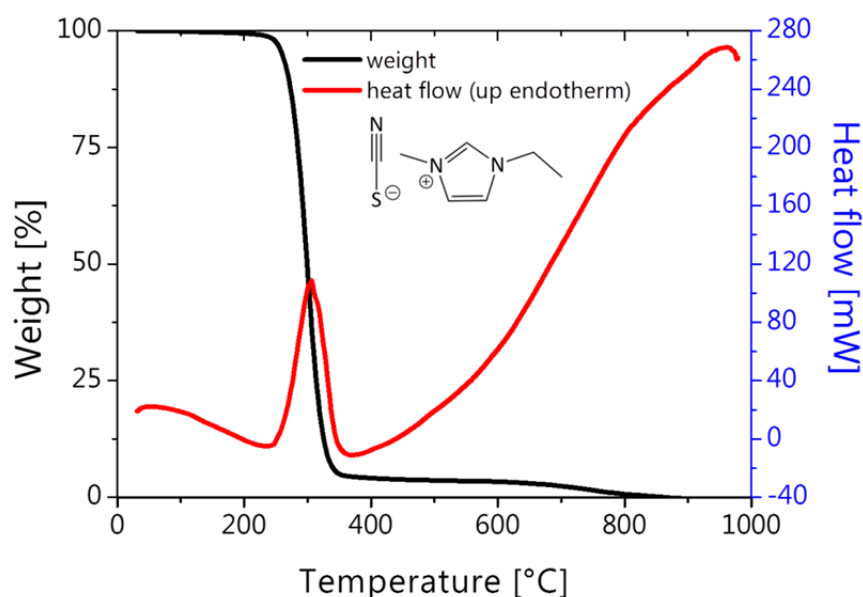
Figure 2-34 TGA-DSC of Emim-scn (inset: chemical structure).

As can be seen from TGA-DSC measurement, carbonization under inert atmosphere of Emim-scn results only in low yields. This was, however, to be expected since the thiocyanate presumably undergoes cycloaddition but does not form extended polymer networks. However, the reaction onset is in the range of the ones obtained for the ionic liquids Emim-dca and Bmp-dca. Thus, a combination of Emim-scn with the two latter might lead to the incorporation of sulfur into the carbon structure.

In order to verify the assumption, mixtures of Emim-scn with Emim-dca and Bmp-dca, respectively, were carbonized in flowing nitrogen at 800 °C in a 2:1 weight ratio.

Concerning the bulk-elemental-analysis, besides a N-content of 24 wt% (N-S-dC_Emim-dca:Emim-scn_1:2_800) and

20 wt% (N-S-dC_Bmp-dca:Emim-scn_1:2_800), an increased S-content of about 2 wt% was indeed obtained in both cases. Here, the reverse Menschutkin reaction can be initiated by the nucleophilic dicyanamide anion as shown in chapter 1.2.1.1 while in the course of cyclization reactions also the thiocyanate anion participates and is incorporated into the polymer network.

The WAXS patterns still reveal the $2\theta \sim 26°$ (002) peaks of slightly disordered graphitic carbon and the in-plane 43° (100) peak (*Figure 2-35*). The (100) peak is slightly shifted towards a lower angles which, compared to undoped carbons, indicates a larger distance between the carbon layers. This eventually reveals the structural incorporation of sulfur heteroatoms. However, the ordering of the functional carbon as such is not hindered.
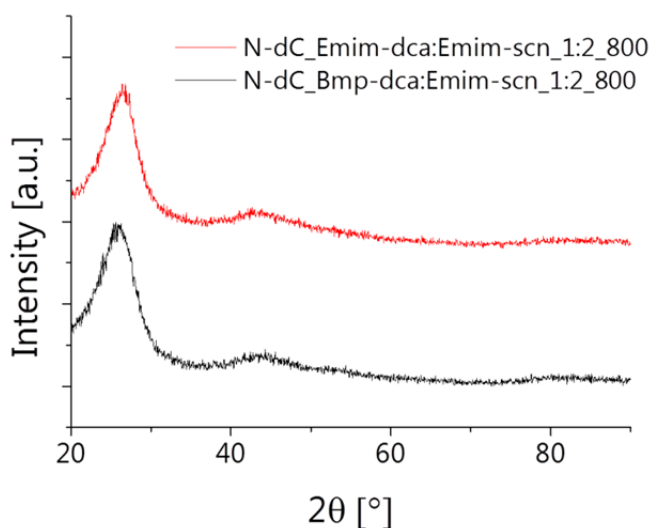
Figure 2-35 WAXS patterns patterns of N-S-dC_Emim-dca:Emim-scn_1:2_800 (red) and N-S-dC_Bmp-dca:Emim-dca_1:2_800 (black).

Essentially, the composition of the carbons should be tunable between the properties of a purely N-doped carbon and different amounts of incorporated sulfur simply by the ratio of the ILs in the initial precursor solution.

For a decisive confirmation of the sulfur binding state, XPS has to be measured, which could not be performed within the timeframe of this thesis but is subject of ongoing research.

These preliminary results suggest the ionic liquid Emim-scn to be suitable for the synthesis of N-S-co-doped carbons with tunable sulfur content. Furthermore, the salt templating approach described in 2.2. for N- and N-B-co-doped carbons should easily be applicable also for the N-S-co-doped carbons.

3. Composite materials - template-free

- Porous metal nitride containing N-doped carbons

3.1. Background and current research

So far, functional materials solely constituted of heteroatom-doped carbons were presented. The carbons were shown to possess different properties which, among others, can be tuned by their composition. However, the properties of carbon-based materials can only be altered within a certain range. Thus, the combination of different material classes into composites or hybrids is a well-known concept to complement carbon properties. Classical examples are the deposition of noble metal nano particles on porous carbon supports. These catalysts combine the high catalytic activity of the metal species with a high accessible surface area and electrical conductivity of carbon.[39] Commonly, activated carbons are decorated with pre-formed particles or impregnated with precursor solutions for the *in situ* particle formation on the surface. Just recently, Hasché *et al.* presented the high suitability of N-doped carbon from ionic liquids as highly efficient support material for polymer electrolyte membrane (PEM) fuel cell electrocatalysts.[74] In this context, Tuaev *et al.* demonstrated the increased stability of an ionic liquid-derived N-doped carbon nanotube material decorated with platinum nanoparticles to result from the influence of the N-doping on the platinum adsorption.[184] Furthermore, ionic liquid-derived N-doped carbon with palladium nano particles was shown as promising catalyst for biofuel upgrade.[185] This demonstrates the superior potential of these heteroatom-doped carbons also within the composite class. However, facts such as high cost of noble metals and lack of sustainability whilst offering still relatively low efficiencies demand for alternative approaches.[40] Here, nonprecious metal based composites, ideally synthesized in an easily scalable and single-step pathway, are the systems of choice.

In this regard, transition metal nitrides (MN) have attracted much attention due to their unique characteristics and potential applications. Typical features include extremely high melting points, very high chemical stability, hardness and wear as well as corrosion resistance.[186-191] Relative to their parent transition metals they behave like noble metals for some chemical and electrochemical reactions.[190] This may be attributed to the fact that with respect to the band structure and their relative ordering, transition metal nitrides are similar to face-centered cubic (fcc) transition.[190, 192]

Commonly, metal nitrides are synthesized by chemical vapor deposition[193] or by conversion of metals and metal oxides in the presence of nitrogen sources like

ammonia,[194] hydrazine,[195] or urea.[196] However, these methods often employ hazardous chemicals and complicated procedures while large-scale synthesis is difficult. Additionally, due to conversion and recrystallization of the starting materials, the control over the metal nitrides morphologies is lost in most cases. Recently, it was reported that mesoporous carbon nitride can be used as both nitrogen source and exotemplate to prepare different metal nitrides.[197] This approach of reactive templating enables the synthesis of metal nitride nanoparticles with flexible composition in a surrounding amorphous carbon matrix. These composites containing TiVN were successfully tested as battery electrodes, showing the beneficial combination of metal nitrides and carbon.[198] In this context, Domen *et al.* also demonstrated composites of TiN nanoparticles on porous carbon as efficient catalyst for the ORR.[41] Here, the heterojunctions between the particles and the support material are believed to play an important role. Just recently, TiN was also presented as bifunctional catalyst for non-aqueous Li-O$_2$ batteries with an additional activity as oxygen evolution reaction (OER) catalyst.[199] Furthermore, VN was found to be a promising electrode material for supercapacitors.[191] These are just a few examples which demonstrate the high potential of TiN and VN composites. However, the syntheses still involve several energy- and time-consuming steps which render the approaches less attractive.

In recent years, much effort has been conducted to the ionothermal synthesis of inorganic materials.[200, 201] In particular, the utilization of ionic liquids as environmentally benign solvents not only allows for the transfer of reactions commonly conducted in molecular solvents but also offers access to new nanostructures.[202] For example, besides zeolite structures,[144, 145] Smarsly *et al.* and Zhou *et al.* presented the facile synthesis of different titanium dioxide modifications and morphologies in ionic liquids.[203-205] Dai and co-workers reported on hierarchically structured zinc oxides[206] and various studies are concerned with the control over the nanoparticle formation.[207] However, the ionothermal synthesis of composite materials is in its infancy, and only sporadic reports are available, thus only few is known about the materials synthesis and property control.[68, 208, 209]

Based on the aforementioned facts, it is reasonable to search for facile and one-step routes towards porous composite system. Thereby, the benefits of two worlds, *i.e.* N-doped carbon and metal nitrides can be combined, which will be the focus of this chapter.

3.2. One-pot template-free synthesis of metal nitride nanoparticles in N-doped carbon

With respect to both, research and industry, an ideal pathway for material synthesis is a one-step approach. However, this poses one of the biggest challenges since parallel occurring processes should not influence each other and the whole system has to be controlled at the same time. As mentioned above, ionic liquids provide a fascinating synthesis environment which may enable new strategies.

In the following, a simple one-pot synthesis approach toward composites of metal nitride nanoparticles supported at N-doped carbon (MN@N-dC) is presented.[37]

The method relies on the miscibility of ionic liquids with a wide range of substances, here metal precursors, the liquid state at ambient temperature and the ability to produce N-doped carbons through heat-treatment of certain ionic liquids. The focus will be on composites containing titanium nitride, vanadium nitride and titanium-vanadium nitride since these metal nitrides are highly attractive as noble metal replacements as mentioned above.

In general, the nanocomposites are generated by mixing varying amounts of a metal precursor(mixture) (50 mg – 250 mg) with the ionic liquid Bmp-dca (1 g) followed by carbonization in inert atmosphere (400 °C - 1000 °C). The ionic liquid acts first as nitrogen source for the *in situ* formation of the corresponding metal nitrides and second as nitrogen and carbon source for the *in situ* constitution of a N-doped carbon matrix. The metal precursors were chosen as titanium tetrachloride ($TiCl_4$) and vanadium oxytrichloride ($VOCl_3$) since they can be homogeneously mixed with the ionic liquid, while the corresponding nitrides TiN and VN are highly functional and therefore interesting. Furthermore, the properties of metal nitrides can be tuned by the introduction of a second metal, yielding ternary metal nitrides. For example, vanadium nitride exhibits a high redox capacity but only a poor electrical conductivity,[191, 198] whereas titanium nitride is known to possess a low redox capacity but good electrical conductivity, making it suitable as a metallic current collector.[210, 211] Combining both metals in a ternary metal nitride can add up those properties, having high redox activity and electrical conductivity at the same time.

The precursor mixtures are named IL_M_m while the resulting composites consisting of TiN, VN, or TiVN nanoparticles within a N-doped carbon matrix are named, TiN@N-dC_IL_M_m_T, VN@N-dC_IL_M_m_T and TiVN@N-dC_IL_M_m_T, respectively.

By mixing $TiCl_4$ and $VOCl_3$ with the ionic liquid Bmp-dca, red and green viscous solutions are obtained, respectively (*Figure 3-1*).
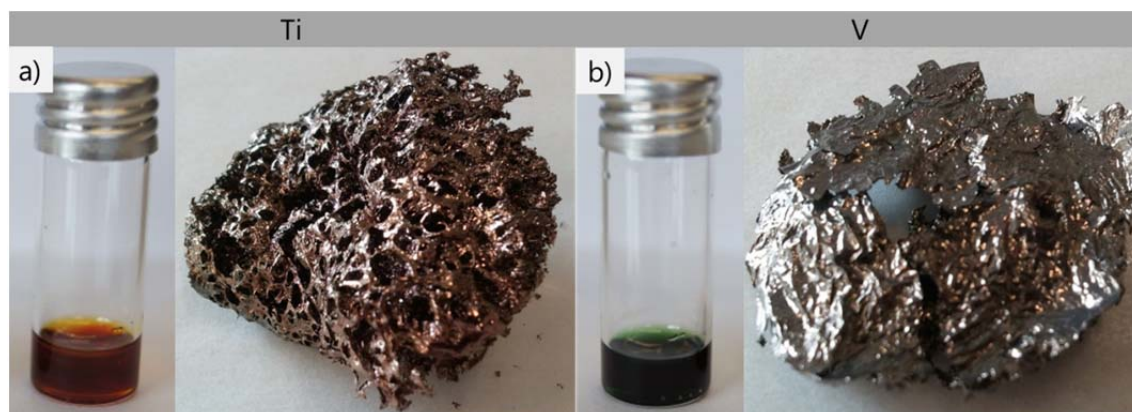
Figure 3-1 Precursor solutions and products of **a)** (TiN@N-dC_)Bmp-dca_TiCl$_4$_0.05_1000 and **b)** (VN@N-dC_)Bmp-dca_VOCl$_3$_0.05_1000.

This indicates that the initial oxidation states Ti^{4+} and V^{5+} are not stable in the precursor solutions but that the metals are reduced to Ti^{3+} and V^{3+} already before the heat-treatment, thus facilitating the formation of the corresponding nitrides. The solutions become more viscous with increasing amount of metal precursor forming a hard gel at the highest concentration. The gels can reversibly be liquified by gentle heating. Most probably, the metal ions cross-link the IL solvent clusters *via* coordination with the dicyanamide anion of the IL.[212] This somewhat reminds on cyanogels described by Bocarsly and co-workers.[213] Cyanogels are formed through the reaction of an aqueous solution of a cyanometalate $[M'(CN)_n]^{2-/3-}$ (n=4, 6) and a chlorometalate $[MCl_4]^{2-}$ which results in amorphous Prussian Blue-like polymers *via* the substitution of two *trans* chloride ligands on $[MCl_4]^{2-}$ by the nitrogen end of $[M'(CN)_n]^{2-/3-}$. In contrast, in the present approach there is no limitation to cyano- or chlorometalate, and the reaction environment is not a molecular solvent but all-ionic. The reaction process of the pure ionic liquid has been described by Paraknowitsch *et al.* and was already presented in chapter 1.2.1.1..[25, 26] Briefly, the thermolysis starts at around 300 °C, yielding a glassy solid. In a second mass loss step at around 450 °C a cross-linked material is formed. Finally, a metallic looking solid is obtained at 1000 °C, composed of N-doped carbon with about 10 wt% of nitrogen. The introduction of the metal ions into the precursor solution accelerates these steps yielding the corresponding metal nitride nanoparticles within a N-doped carbon matrix.

The TEM pictures show a homogeneous incorporation of the nanoparticles with a narrow size distribution of around 7 nm in diameter (*Figure 3-2*). The homogeneity of the composites is further supported by SEM pictures (*Figure C-3*).
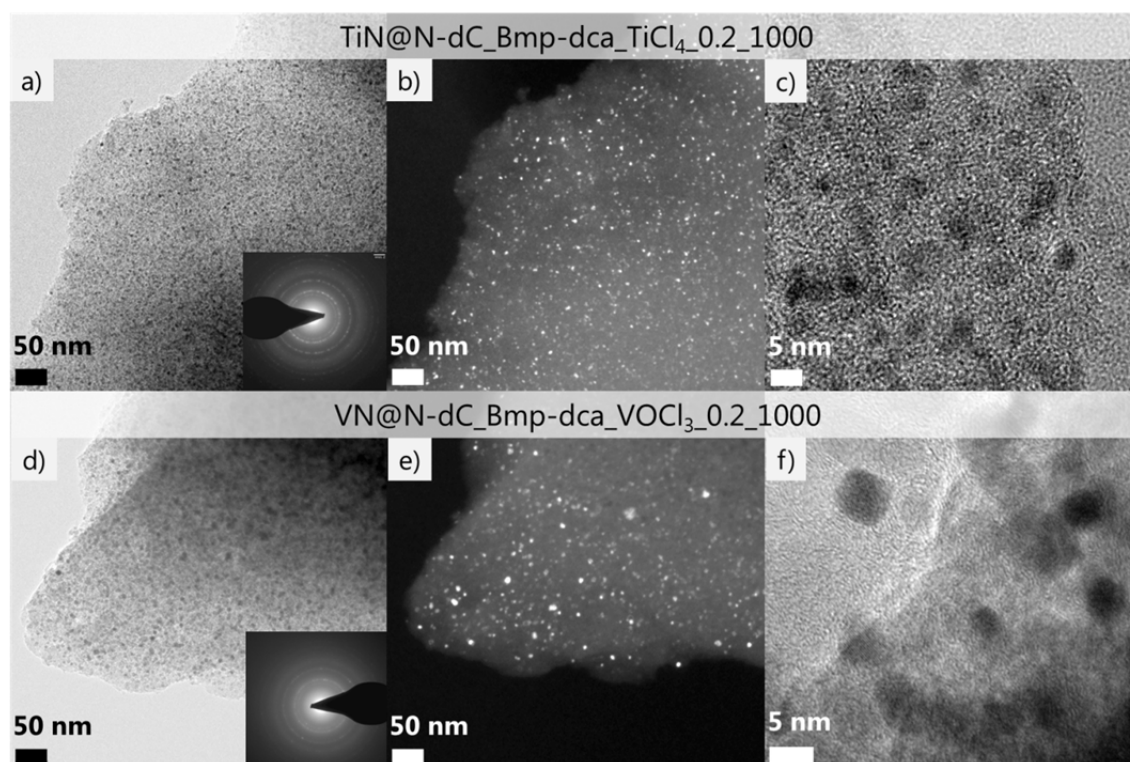
Figure 3-2 Bright- (**a, d**), dark-field (**b, e**) and high-resolution TEM images (**c, f**) of TiN@N-dC_Bmp-dca_TiCl$_4$_0.2_1000 and VN@N-dC_Bmp-dca_VOCl$_3$_0.2_1000. Inserts show SAED patterns for TiN and VN, respectively.

The metal nitride nanoparticles are highly crystalline, thus they become visible in discriminating dark-field TEM. Selected area electron diffraction (SAED) patterns enable the identification of the particles as TiN and VN. The presence of well-defined lattice fringes in the high-resolution transmission electron microscopy (HRTEM, *Figure 3-2 c, f*) also confirms the single crystalline character of the metal nitride nanoparticles. With HRTEM, the carbon phase can be analyzed, too, and a bent layer structure avoiding edge termination is found, which is typical for N-doped carbon derived from Bmp-dca.[26, 27] The homogeneity of the nanoparticles in size and distribution is presumably caused by the confinement of the metal precursor in the ionic liquid. It is known that ionic liquids with longer alkyl chains (C > 12) or fluorine containing anions are able to possess an organization between the molecules so that they can be viewed as ionic liquid crystals.[214, 215] An ordered structure may also be obtained for ionic liquids with shorter alkyl chains through the introduction of metal ions eventually resulting in microphase segregation with polar and less polar regions.[216]

The properties of the binary metal nitrides within the N-doped carbon composite in dependence on the metal precursor concentration and synthesis temperature were further characterized *via* WAXS (*Figure 3-3*).
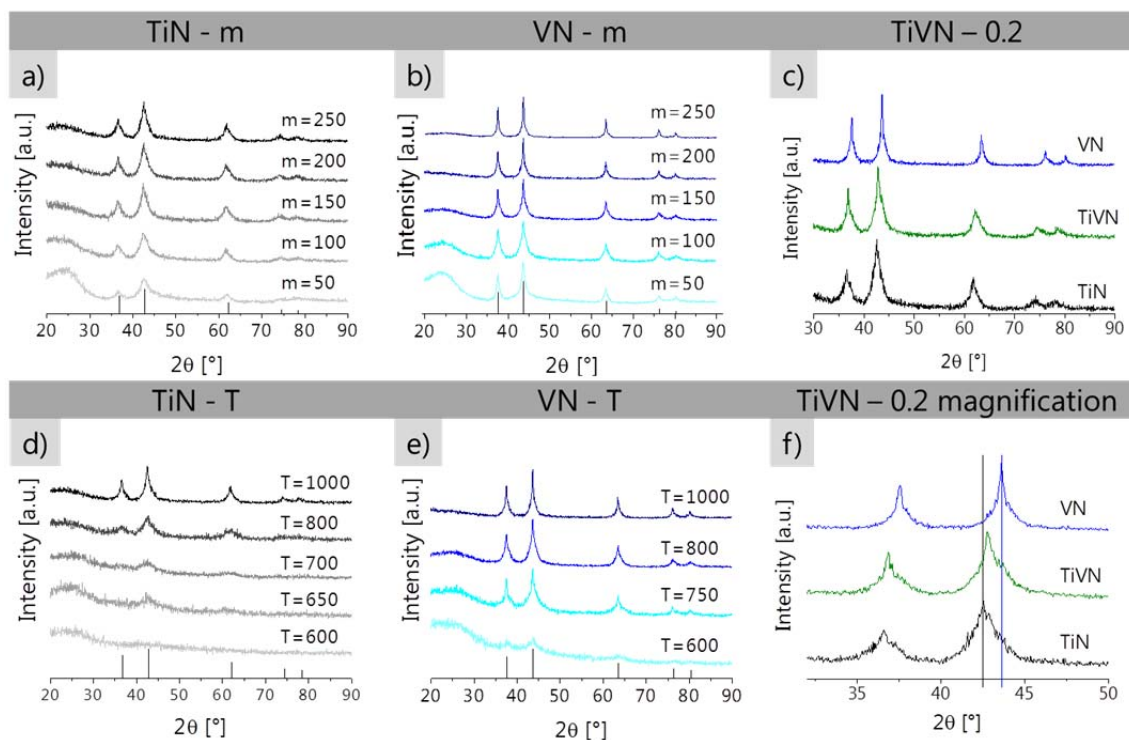
Figure 3-3 WAXS patterns of TiN@N-dC_Bmp-dca_TiCl₄_m_T (**a, d**) and VN@N-dC_Bmp-dca_VOCl₃_m_T (**b, e**) in dependence on the metal precursor concentration m and synthesis temperature T. Comparison of WAXS patterns (**c, f**) of TiN@N-dC_Bmp-dca_TiCl₄_0.2_1000 (black), TiVN@N-dC_Bmp-dca_VOCl₃-TiCl₄0.43_0.2_1000 (green), and VN@N-dC_Bmp-dca_VOCl₃_0.2_1000 (red).

For both systems the diffraction peaks become narrower with increasing amount of metal precursor, implying that the nanoparticles become larger. The comparison of the diffraction patterns for TiN@N-dC_Bmp-dca_TiCl₄_m_1000 and VN@N-dC_Bmp-dca_VOCl₃_m_1000 reveals broader peaks for the former at every metal precursor concentration m, indicative for generally smaller nanoparticles. A similar trend is observed in the case of Emim-dca as precursor (*Figure C-4*). However, the diffraction peaks are narrower and the particles are bigger which is attributed to a different solubility or complexation of the metal precursors in the two ionic liquids. Regarding the temperature dependence, it is found that for both ILs the metal nitride formation sets in at around 650 °C for the TiN and 600 °C for the VN composites, respectively, which is possibly due to the higher reduction efficiency of the cyano groups at higher temperatures. To confirm the successful synthesis of ternary metal nitrides, WAXS patterns of pure TiN@N-dC_Bmp-dca_TiCl₄_0.2_1000 and VN@N-dC_Bmp-dca_VOCl₃_0.2_1000 were compared with TiVN@N-dC_Bmp-dca_VOCl₃-TiCl₄ 0.43_0.2_1000 (*Figure 3-3, c, f*). The peak positions of the TiVN@N-dC composite are in between the respective peaks of the binary compounds, indicative for the formation of a homogeneous Ti-V-N solid solution.[211, 217, 218] Furthermore, the peak

positions of the TiVN@N-dC composite are closer to the peaks of the TiN@N-dC composite, revealing the structure of the ternary metal nitride to be more dense and closer to TiN, which is in accordance with the utilized metal precursor ratio and beneficial for electrical conductivity. Thus, it is also possible to determine the composition of the nitride nanoparticles within the composite by the initial ratio of the metal precursors used in the starting solution.

The composition of the materials was additionally investigated by elemental analysis. The development of the nitrogen, carbon, and hydrogen content in dependence on the amount of metal precursor and synthesis temperature are presented for the TiN and VN containing composites (*Figure 3-4*).
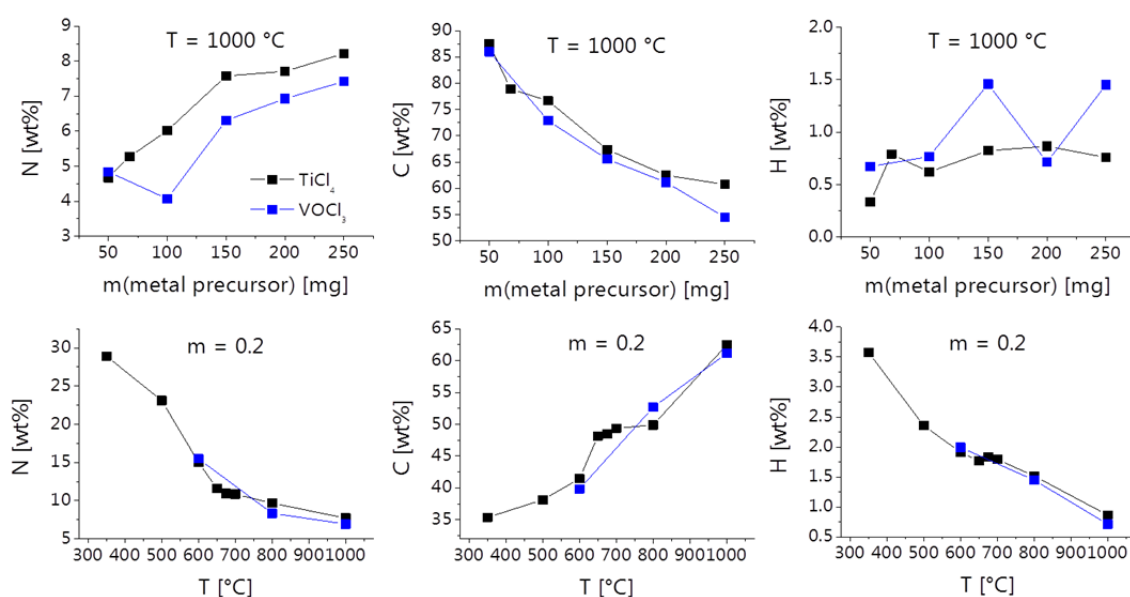
Figure 3-4 Course of elemental composition of TiN@N-dC_Bmp-dca_TiCl$_4$_m_T (black) and VN@N-dC_Bmp-dca_VOCl$_3$_m_T (blue) at different metal precursor concentrations m with T=1000 (**top**) and at different reaction temperatures T produced with m=0.2 (**bottom**).

For both systems as well as for the composites from Emim-dca (*Figure C-5*) the trends are similar, indicating a similar formation process of the respective products. The nitrogen content increases with increasing metal precursor amount. This can be attributed to the higher amount of metal nitride formed, showing that the metals fix the nitrogen originating from the surrounding IL. At the same time the carbon content decreases with increasing metal content, indicating a constant carbon formation while the metal nitride phase is increasing. No considerable change of the hydrogen content can be observed. Regarding the dependence of the compositions on the synthesis temperature, the nitrogen content decreases at higher temperatures; that is, denitrification of the carbon matrix takes place. This behavior is expected and well-known from other N-doped carbons at higher temperatures. The relative carbon

content increases with higher temperature due to the aforementioned release of heteroatoms. The loss of hydrogen is here more pronounced, showing that the nitrogen also leaves as ammonia. The amount of the metals was determined by ICP-OES. The compositions of the composites produced at 1000 °C and 200 mg metal precursor are shown in *Table 3-a*.

Table 3-a Composition of TiN@N-dC_Bmp-dca_TiCl$_4$_0.2_1000, VN@N-dC_Bmp-dca_VOCl$_3$_0.2_1000, and TiVN@N-dC_Bmp-dca_VOCl$_3$-TiCl$_4$0.43_0.2_1000 obtained from ICP-OES and XPS.

Composite	Element	[wt%]	
		XPS	**ICP-OES**
TiN@N-dC	O1s	10.1	-
	C1s	51.9	-
	N1s	8.8	-
	Ti2p	29.3	18.3
VN@N-dC	O1s	8.4	-
	C1s	54.3	-
	N1s	6.5	-
	V2p	30.8	21.1
TiVN@N-dC	O1s	9.7	-
	C1s	55.2	-
	N1s	7.8	-
	Ti2p	19.1	12.6
	V2p	8.2	6.5

The results obtained from ICP-OES reveal an average metal content of 20 wt % at 200 mg metal precursor concentration for all hybrid materials. However, the elemental analysis derived from the XPS spectra show an increased average metal content for all composites of around 30 wt%. Nevertheless, the ratio of vanadium and titanium in the ternary compound obtained from XPS is comparable to the initial precursor ratio and the results from ICP-OES. Because XPS gives information about the surface properties, it can be concluded that there exists slight but homogeneous metal nitride enrichment on the composite surface.

The ICP-OES measurements of titanium and vanadium nitride composites produced with varying precursor amounts reveal an almost linear increase of the metal content in the final product. Since the metal content in the product is directly proportional to the initial metal precursor amount, the composition of the hybrids can be easily varied (*Figure 3-5*).
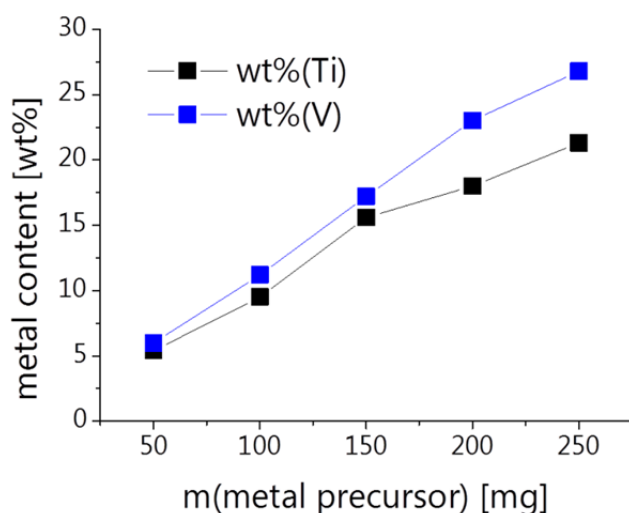
Figure 3-5 Course of metal content obtained from ICP-OES of TiN@N-dC_Bmp-dca_TiCl$_4$_0.2_1000 (**black**) and VN@N-dC_Bmp-dca_VOCl$_3$_0.2_1000 (**blue**) in dependence on the metal precursor amount m.

Furthermore, the initial metal ratio of the ternary precursor solution closely resembles the one found in the composite (*Table 3-a*). This indicates the ability to control the composition of TiVN@N-dC_Bmp-dca_VOCl$_3$-TiCl$_4$_m_T by the ratio of the precursors in the starting solution.

To gain more insight into the structural nature of the composites, Raman spectroscopy was applied (*Figure 3-6*).
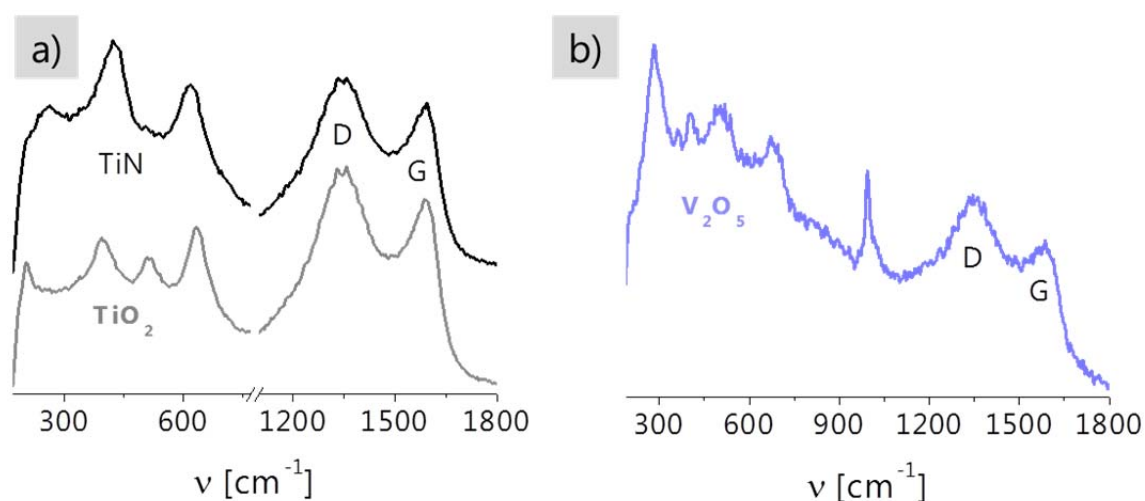
Figure 3-6 Raman spectra of **a)** TiN@N-dC_Bmp-dca_TiCl$_4$_0.2_1000 and **b)** VN@N-dC_Bmp-dca_VOCl$_3$_0.2_1000.

Among the most important variables, the Raman spectrum depends on the composition, defects, short-range order and crystallinity of a material. This is especially helpful for the investigation of the carbon matrix of the composite since this is not

clearly visible in the WAXS patterns due to the high intensities of the metal nitrides. In both cases the Raman resonances of the metal nitrides are located at lower frequencies whereas the carbon signals appear in the upper range. For TiN@N-dC_Bmp-dca_TiCl$_4$_0.2_1000 two different spectra could be obtained (*Figure 3-6 a*). The upper spectrum reveals Raman vibrations at 260 cm^{-1}, 423 cm^{-1}, and 616 cm^{-1} corresponding to TiN.[219, 220] The resonances at 1346 cm^{-1} and 1592 cm^{-1} can be assigned to the D- and G-bands, respectively, which are characteristic for slightly disordered and heteroatom-doped graphitic materials.[26] The intensity of the D-band is higher than the one of the G-band, which, besides defects, can be attributed to the N-doping, disrupting local symmetry. In the lower spectrum, apart from the D- and G-band signals, distinct resonances are obtained at 204 cm^{-1}, 395 cm^{-1}, 512 cm^{-1}, and 633 cm^{-1}, matching with TiO$_2$.[219] This is also true for VN@N-dC_Bmp-dca_VOCl$_3$_0.2_1000 (*Figure 3-6 a*), where resonances at 282 cm^{-1}, 405 cm^{-1}, 482 cm^{-1}, 531 cm^{-1}, 685 cm^{-1}, and 993 cm^{-1} solely corresponding to the oxide can be found.[221] Here, the intensity ratio of the D- and G-band is slightly higher than for the TiN composite. Regarding the WAXS patterns of both composites, no signals corresponding to the oxides could be observed, and according to elemental analysis, the overall amount of oxygen within the samples is relatively low. The oxide signals in the Raman spectra can therefore be attributed to a thin oxide layer on the nitrides. However, the oxide signals for VN@N-dC_Bmp-dca_VOCl$_3$_0.2_1000 are too pronounced. A signal enhancement due to plasmon resonances on the surface of the VN can be considered, since VN is regarded as metallic.

For a decisive confirmation of structural nitrogen and for further investigation of the chemical nature of the composites, XPS was performed. The survey and deconvoluted N1s, Ti2p and V2p, (*C1s and O1s Figure C-6*) peaks are shown for TiN@N-dC_Bmp-dca_TiCl$_4$_0.2_1000, VN@N-dC_Bmp-dca_VOCl$_3$_0.2_1000, and TiVN@N-dC_Bmp-dca_VOCl$_3$-TiCl$_4$0.43_0.2_1000, respectively (*Figure 3-7*).
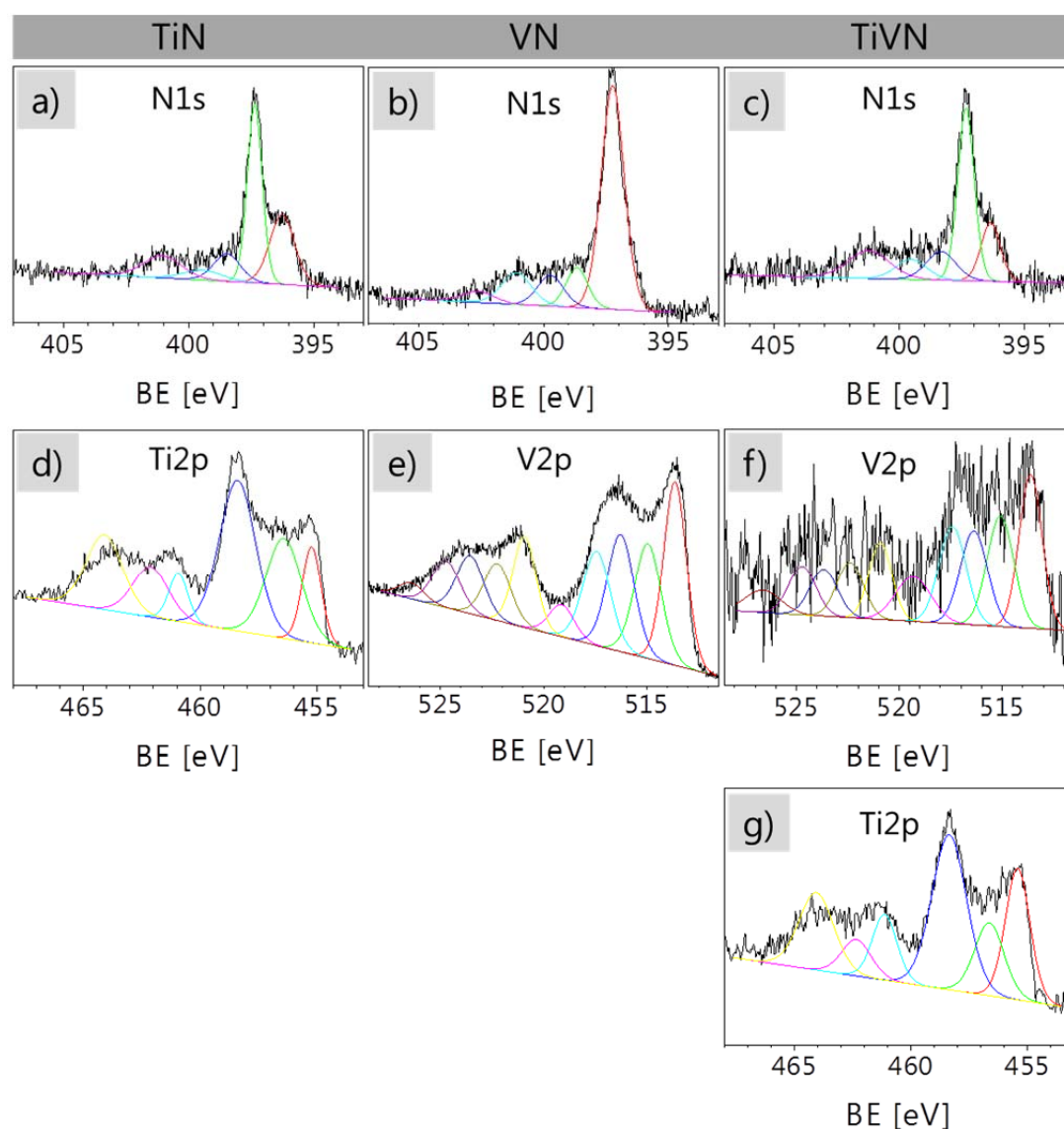
Figure 3-7 XPS-spectra: N1s, Ti2p, and V2p orbitals of TiN@N-dC_Bmp-dca_TiCl$_4$_0.2_1000 (**a, d**), VN@N-dC_Bmp-dca_VOCl$_3$_0.2_1000 (**b, e**), and TiVN@N-dC_Bmp-dca_VOCl$_3$-TiCl$_4$0.43_0.2_1000 (**c, f, g**).

While in the high-resolution N1s spectra the titanium and vanadium compounds are located at lower binding energies, the carbon bonded species can be found in the upper region. For all materials, the peaks at around 397.3 eV can be assigned to the corresponding metal nitrides.[191, 211, 218, 221-223] In the TiN based composite approximately 41 atom% and for VN 63 atom% of nitrogen are bound to Ti and V, respectively. In the ternary TiVN based composite approximately 43 atom% of N is bound to the corresponding metals. Additional peaks at around 396.3 eV ascribed to metal oxynitrides were found for the TiN and TiVN based composites.[222, 223]

The corresponding binding energies are summarized in *Table 3-b*.

Table 3-b Assignment of XPS binding energies to the corresponding component with m=0.2 and T=1000.

Peak	Binding energy [eV]			Assignment
	TiN@N-dC_Bmp-dca_TiCl$_4$_m_T	VN@N-dC_Bmp-dca_VOCl$_3$_m_T	TiVN@N-dC_Bmp-dca_VOCl$_3$-TiCl$_4$0.43_m_T	
N1s	396.25	-	396.35	TiO$_x$N$_y$
	397.35	397.24	397.32	Ti/VN
	398.45	398.66	398.32	pyridinic
	399.45	399.72	399.52	pyrrolic
	401.05	401.09	401.23	quaternary-graphitic
	-	402.62	-	oxidized nitrogen
Ti2p$_{3/2}$	455.25	-	455.45	TiN
	456.40	-	456.65	TiO$_x$N$_y$
	458.40	-	458.35	TiO$_2$
V2P$_{3/2}$	-	513.62	513.60	VN
	-	514.94	515.10	V$_x$O$_y$
	-	516.26	516.40	
	-	517.42	517.40	
	-	519.12	519.30	

For all materials nitrogen is also bound to carbon, showing the characteristic peaks which confirm the abundance of structural nitrogen. The nitrogen-carbon bonds can be further distinguished into different species. The peaks at around 398.5 eV, 399.7 eV, 401.1, and 402.2 eV can be assigned to pyridinic, pyrrolic, quaternary-graphitic, and oxidized nitrogen species within graphitic microdomains, respectively.[24, 27, 157, 224] For the TiN composite 11.6 atom%, the VN composite 10.7 atom% and the TiVN composite 13 atom% of nitrogen atoms are pyridinic. This is highly interesting, since pyridine-type nitrogen-bonding at the edge of graphitic domains has been considered as a potential catalytic active site.[225] The chemical nature of the metals could further be analyzed with the help of the high-resolution Ti2p and V2p spectra. For the TiN and TiVN composite, the peaks in the Ti2p spectrum at around 455.3, 456.5, and 458.5 eV can be assigned to TiN, TiO$_x$N$_y$, and TiO$_2$, respectively.[218, 222, 223] For the VN and also the TiVN composite the peaks in the V2p spectra at around 513.6 eV and 515 eV to 519.3 eV can be ascribed to VN and V$_x$O$_y$.[191, 211, 221] The simultaneous presence of the Ti2p and the

V2p peaks for the TiVN composite further supports the successful formation of the ternary metal nitride.

The porosity of the binary composites TiN@N-dC and VN@N-dC in dependence on the respective metal precursor concentration was investigated by nitrogen sorption measurements (*Figure 3-8*). Here, the focus was on the general question whether the composites possess any porosity as well as the influencing parameters, thus the discussion is based on the nitrogen uptake of the materials obtained from standard measurements.
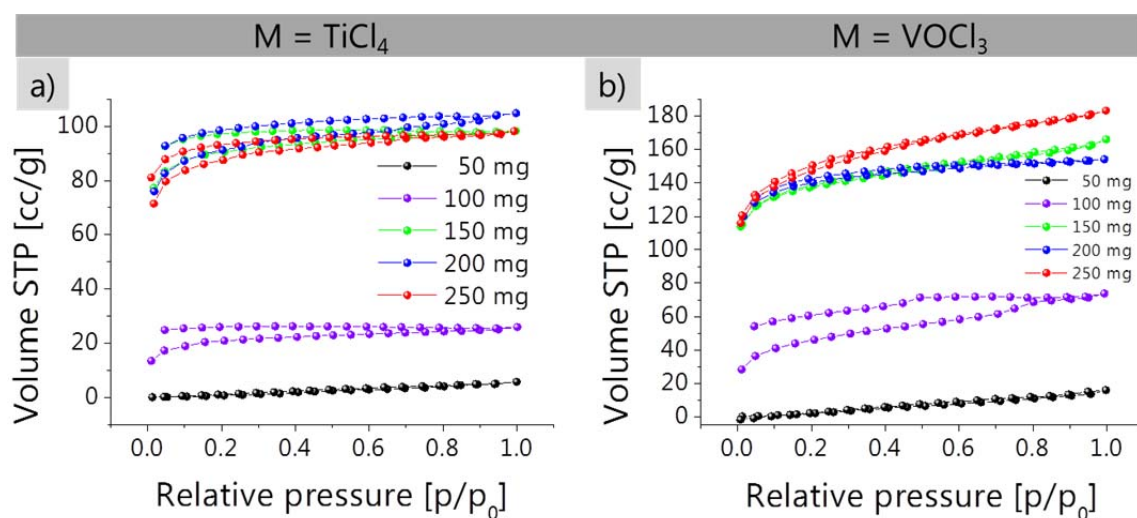
Figure 3-8 Nitrogen sorption isotherms of **a)** TiN@N-dC_Bmp-dca_$TiCl_4$_m_T and **b)** VN@N-dC_Bmp-dca_$VOCl_3$_m_1000 at different metal precursor concentrations m.

In every case the isotherms can be classified as type I hysteresis, which implies that the materials possess a microporous structure. This is supported by the micropore analysis exemplarily conducted for N-dC_Bmp-dca_$TiCl_4$_0.25_1000 (*Figure C-7*). At low metal concentrations the materials are practically nonporous, resembling the pure pyrolyzed ionic liquid. A further increase of metal precursor causes a stepwise surface area increase whereby a plateau is reached at around 150 mg of metal precursor. For both systems it is found that the surface area increases with increasing metal precursor concentration (*Figure 3-9*).
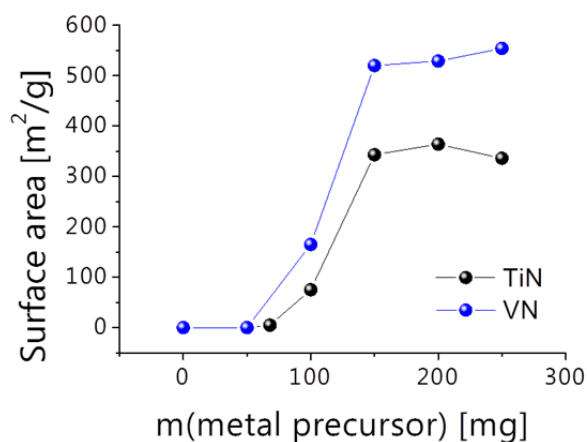
Figure 3-9 Course of the surface areas of TiN@N-dC_Bmp-dca_TiCl$_4$_m_1000 (black) and VN@N-dC_Bmp-dca_VOCl$_3$_m_1000 (blue) at different metal precursor concentrations m.

Evaluating the data according to Brunauer−Emmett−Teller (BET), specific surface areas up to 350 m^{2}g^{-1} and 550 m^{2}g^{-1} for TiN@N-dC_Bmp-dca_TiCl$_4$_0.25_1000 and VN@N-dC_Bmp-dca_VOCl$_3$_0.25_1000, respectively, are reached. This behavior of surface development suggests that the porosity results from a cohesive delamination at the materials interfaces, which can percolate exceeding a critical content of nanoparticles. At metal precursor concentrations higher than 100 mg, the cracks between the graphitic carbon and the metal nitride nanoparticles start to form a pore system accessible to nitrogen from the outside. Further increase of the metal precursor concentration leads to larger metal nitride nanoparticles, and the specific surface stagnates. The nature of the metal precursor also has an influence on the surface areas, yielding higher values for VOCl$_3$ compared to TiCl$_4$. We attribute this to a more efficient delamination and pore formation at the corresponding inner surfaces.

The composites presented in this chapter fulfill important aspects of material design and synthesis since they can be obtained within a one-step process without the need for any further treatment. Furthermore, the synthesis procedure is facile and can be conducted without special instrument equipment or safety concerns. The system already possesses a variety of desirable advantages including an inherent porosity, conductivity as well as tunability of the metal content, the metal nitride particle composition and the surface area. Since the metal species can be varied, this approach offers a general synthesis platform for the generation of porous mental nitride composites already revealing interesting properties also with regard to potential applications *e.g.* energy-storage.

However, for the utilization as electrodes for supercapacitors, even higher surface areas and pore volumes would lead to a highly increased performance. Thus, finding a method for the introduction of additional porosity into the present one-pot synthesis approach is highly desirable and will be addressed in the following chapter.

4. Composite materials – salt-templated

- Porous metal nitride containing N-doped carbons

4.1. Background and current research

In the previous chapters salt templating (2.) and the one-pot synthesis of metal nitride containing N-doped carbons (3.) were presented. As mentioned earlier, depending on the application composite materials are often superior to carbons, yet the simultaneous introduction of a foreign species and high surface area into a carbon system is usually challenging. Mostly, this is due to an incompatibility of one of the composite components and templating procedures *e.g.* template removal. The composite materials from metal precursor-containing ionic liquids described in chapter 3 possess an inherent porosity which is reasonable considering the absence of any template.[37] However, the surface area is solely tunable in dependence on the metal amount. Thus, with this approach it is not possible to generate high surface area composites with lower metal nitride content. The method of choice for the synthesis of high-surface area composite materials is still the post-impregnation of ordinary porous carbons, which however we want to avoid. Yet, major drawbacks of impregnation are several synthesis steps, the limitation to certain support structures, inhomogeneous coverage of the surface and loose contact of the components which is of disadvantage especially for electrochemical applications. In the view of the aforementioned facts, it is not far to seek for the combination of both thesis approaches *i.e.* salt templating of the one-pot composites which should enable for independent tunability of composition and porosity.

With regard to applications, porous composites became prominent in the field of energy storage in recent years.[191] High-power energy sources have attracted much attention since they are indispensable for numerous applications *e.g.* portable electronics or hybrid electric vehicles.[226-228] Electrochemical capacitors (EC), also known as supercapacitors or ultracapacitors, possess high specific power, fast charge and discharge rates, excellent reversibility and long cycle life.[229, 230] This makes them suitable as an alternative or supplement to batteries, which up to today still reveal higher energy density (Ragone Plot, *Figure 4-1 a*).[104] Just in the very recent September Energy Quarterly issue of MRS Bulletin, publishing state-of-the-art contributions of the leading materials scientists dedicated to present challenges and progress in the energy field, an article about the employment of supercapacitors in Germany appeared. This illustrates the high significance of this device also for general public (*Figure 4-1 b*).
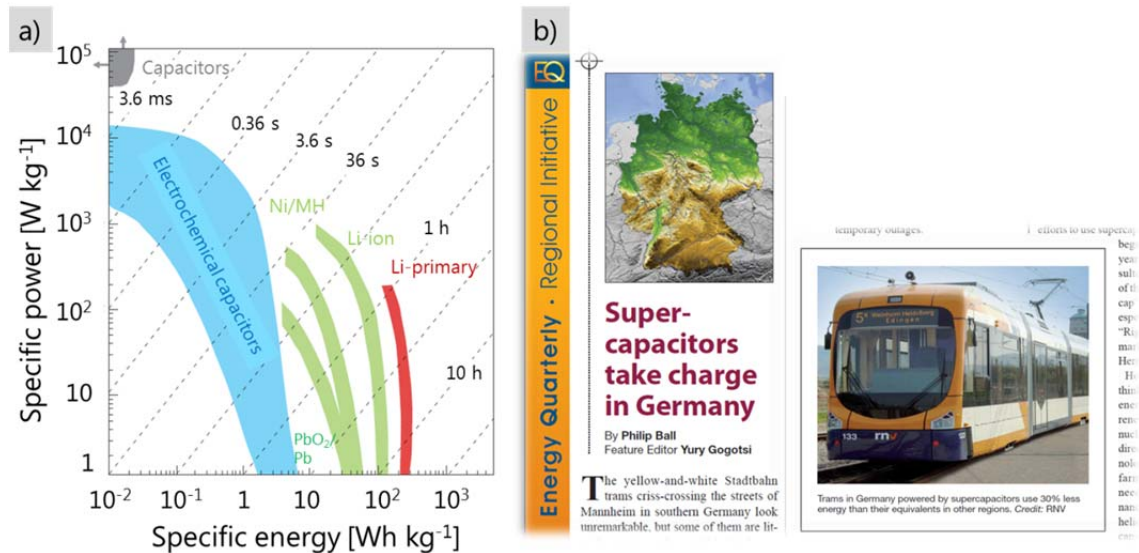
Figure 4-1 a) Ragone plot[231] and **b)** Excerpt from September Energy Quarterly issue of MRS Bulletin.[232]

In the simplest configuration, a supercapacitor consists of two electrodes which are in contact with an electrolyte and electrically separated by an ion conducting membrane (*Figure 4-2 a*). Depending on the charge-storage mechanism, supercapacitors can be classified into electrical double layer capacitors (EDLC) and pseudocapacitors (*Figure 4-2 b*).[226, 227, 233]
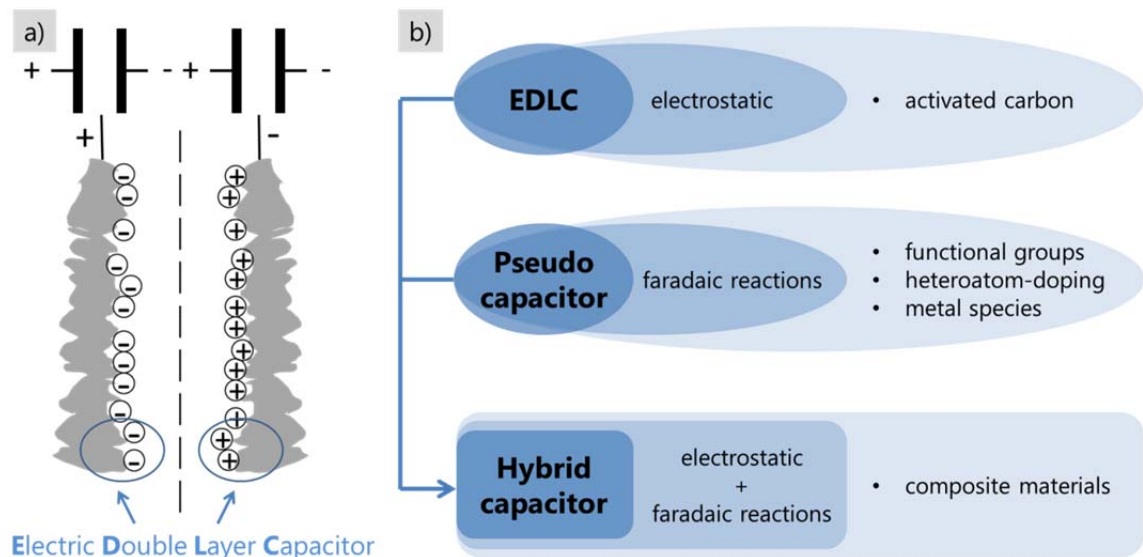
Figure 4-2 a) Schematic representation of an EDLC and **b)** overview of different supercapacitor classes.

In EDLCs, the capacitance is of electrostatic nature and nanoporous carbons are commonly used.[96, 229, 234] Pseudocapacitors involve Faradaic reactions *e.g.* reversible reduction/oxidation processes between the surface of the electroactive electrode material and the electrolyte.[235] Here, metal oxides (RuO_2, MnO_2 and V_2O_5), conductive polymers (polyaniline, polypyrrole) and heteroatom-containing carbons are widely used.[221, 233, 236-240] Carbon based electrodes nowadays commonly exhibit capacitances of around 100 Fg^{-1} due to electrostatic interactions. However, improved performances are reported ranging from 300 up to 500 Fg^{-1} which are due to pseudocapacitive contributions.[241] Still, one of the most promising electrode material is RuO_2[242] but its high costs essentially shun commercial application.[226, 233] Vanadium oxides (V_xO_y) also exhibit a variety of oxidation states,[191, 236] potentially advantageous for the performance of pseudocapacitors, but the poor electrical conductivity of V_2O_5 is a prohibitive drawback.[236] Recently, VN was found to be a promising electrode material due to its low cost and enhanced electrical conductivity, as compared to V_2O_5.[191] The high capacities were attributed to a thin oxide layer on top of the surface of the VN.[191] However, the rate capability is still rather limited which can be ascribed to still insufficient electrical conductivity. In order to further improve the electrochemical performance of ECs, hybrid electrodes combining electrostatic attraction (EDLC) and Faradaic reactions (pseudocapacitor) are the system of choice (*Figure 4-2 b*).[233, 236] Hierarchical pore structures are certainly favorable for supercapacitors,[136, 243] but not the only paradigm in this community. It was recently shown that micropores smaller than the size of the solvated electrolyte ions led to a dramatic increase in capacitance,[104, 244] pointing to a new energy storage mechanism.

The capacitance can be determined by different methods *i.e.* from charge-discharge measurements within a two-electrode setup or from cyclic voltammograms (CV) within a three-electrode setup. The values obtained with the former more resemble the performance in a real device. However, the latter is suitable for both, a quantitative and qualitative evaluation of the charge storage processes.[245] Thus, the three-electrode setup is used within this thesis. The capacitances are calculated from the CVs using following equation.

$$C = \frac{\int_{V_1}^{V_2} I(V)dV}{2mv\Delta V}$$

Eq. 4-1

Here, I(V) represents the instantaneous current, V_1 and V_2 are the cutoff potentials in the CV defining the potential window ΔV, m is the sample mass and v is the scan rate.[211, 246]

It is to mention that capacitances obtained from the three-electrode setup are commonly slightly higher than in the two-electrode setup. Nevertheless, the relative values are identical, thus, trends can be determined from both methods.

In the present chapter, salt templating (chapter 2.) will be applied to the one-pot synthesis approach (chapter 3.) in order to generate high surface area vanadium nitride nanoparticle containing N-doped composites. It will be shown, that the porosity as well as the particle size is tunable through the nature, amount and combination of different salts, *i.e.* CsAc and ZnAc. Finally, the materials are applied as electrodes for supercapacitors.

4.2. Single-salt systems

With respect to the results obtained for salt templating of the pure heteroatom-doped carbons, first the single-salt systems CsAc and ZnAc are applied to the precursor mixture of Emim-dca and $VOCl_3$. In order to get insights into the influence of the metal source, the synthesis was also conducted with ammonium metavanadate (NH_4VO_3), a polymeric vanadium oxide, as vanadium precursor.

The composites were synthesized by dissolving equal molar amounts of $VOCl_3$ (50 mg or 200 mg) or NH_4VO_3 (35 mg or 135 mg) in the IL Emim-dca (1 g). Varying concentrations of CsAc (max. 1 g) or ZnAc (notation expressed in amount CsAc) were subsequently added. For reasons of comparison, the molar ratio of acetate cation and ionic liquid was kept identical for both porogens. Pure N-dC were produced according to chapter 2. The composite precursor mixtures are denoted as IL_YAc_r_M_m. Here, IL is the respective ionic liquid used as precursor, YAc is the acetate (Ac) with Y being zinc (Zn) or cesium (Cs), r represents the mass ratio salt/IL in the precursor mixture, M the metal precursor species and m the mass ratio metal precursor/IL. After pyrolysis at T=800 °C and aqueous removal of the salt porogen, highly porous carbons/composites are formed, appearing as voluminous black powders.

The resulting composites are named MN@N-dC_IL_YAc_r_M_m_T where MN denotes the respective metal nitride.

Similar to the single-salt system in 2.3. and the one-pot precursors in 3.2., the present precursor mixtures reveal different behaviors (*Figure 4-3*). The addition of CsAc to Emim-dca_$VOCl_3$_0.05 results in the green mixture Emim-dca_CsAc_0.34_$VOCl_3$_0.05 indicating the presence of V^{3+} ions. The mixtures become more solid with increasing salt amounts (*Figure 4-3 a, b*). In contrast, the mixture Emim-dca_NH_4VO_3_0.035 appears as black liquid presumably due to the presence of V_2O_3 (*Figure 4-3 c*). Here, CsAc addition leads to a brown solid at low and beige solids at high salt concentrations

which can be ascribed to $[V(O_2)]^{3+}$ and $H_3[VO_2(O_2)]$ species (*Figure 4-3 d, e*).[247] However, mixing the black precursor solution of Emim-dca-NH_4VO_3 with ZnAc forms a green gel Emim-dca_ZnAc_1_NH_4VO_3_0.035, again indicative for V^{3+} ions (*Figure 4-3 f*). All precursors can be reversibly liquified by gentle heating which also points to a coordination of the metal and ionic liquid ions influenced by the porogen salts, however, still forming homogeneous mixtures.
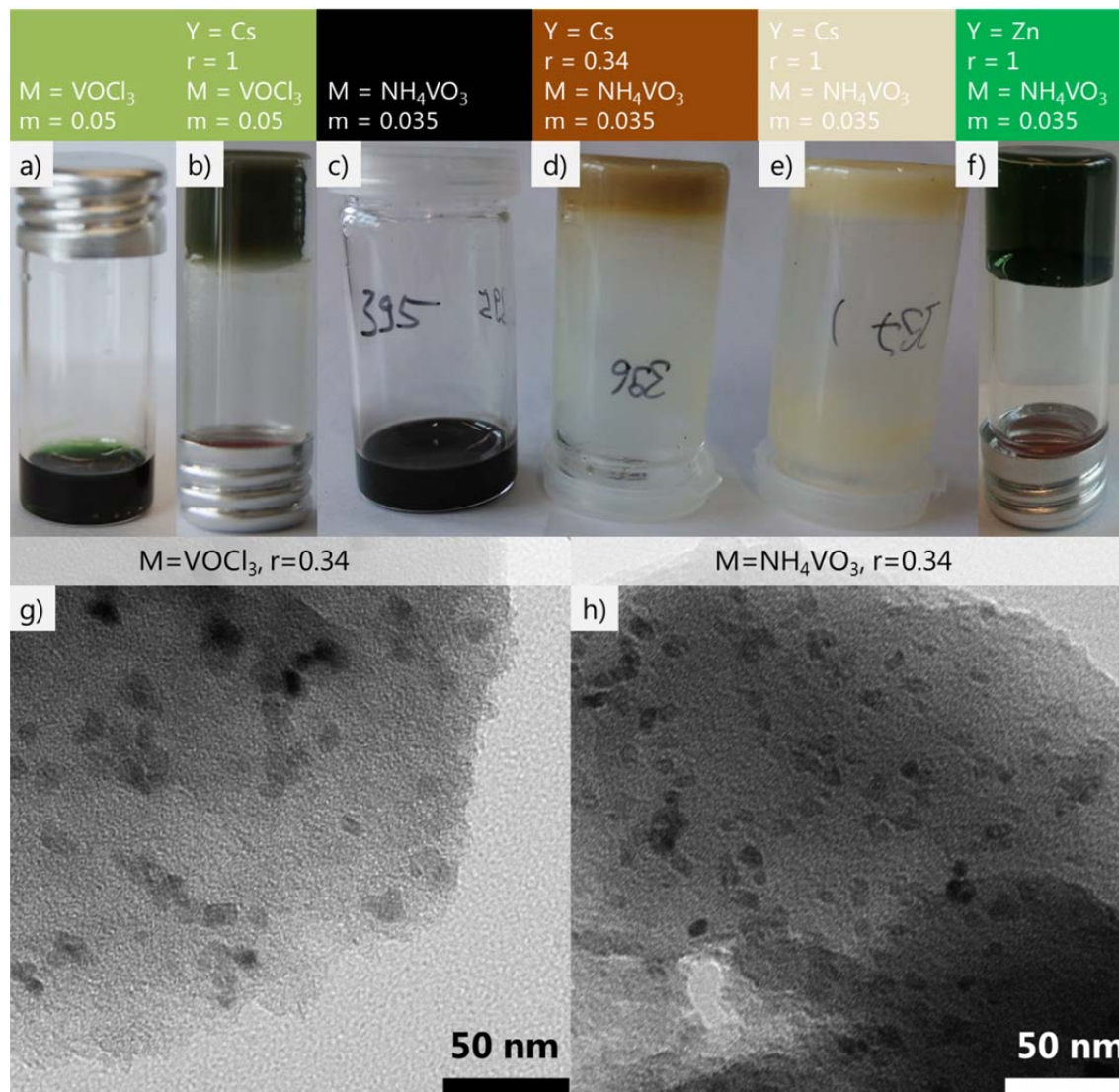
Figure 4-3 a-f) Photographs of the precursor mixtures Emim-dca_YAc_r_M_m. TEM pictures of the composites VN@N-dC_Emim-dca_CsAc_0.34_$VOCl_3$_0.05_800 (**g**) and VN@N-dC_Emim-dca_CsAc_0.34_NH_4VO_3_0.035_800 (**h**).

The subsequent heat-treatment of the precursor mixtures followed by aqueous template removal results in black and voluminous powders. TEM pictures of the formed composites reveal spherical nanoparticles embedded in a carbon matrix for both metal precursors (*Figure 4-3 g, h*).

To reveal the nature and size of the nanoparticles, WAXS diffractograms were recorded for varying CsAc amounts (*Figure 4-4 a, b*).
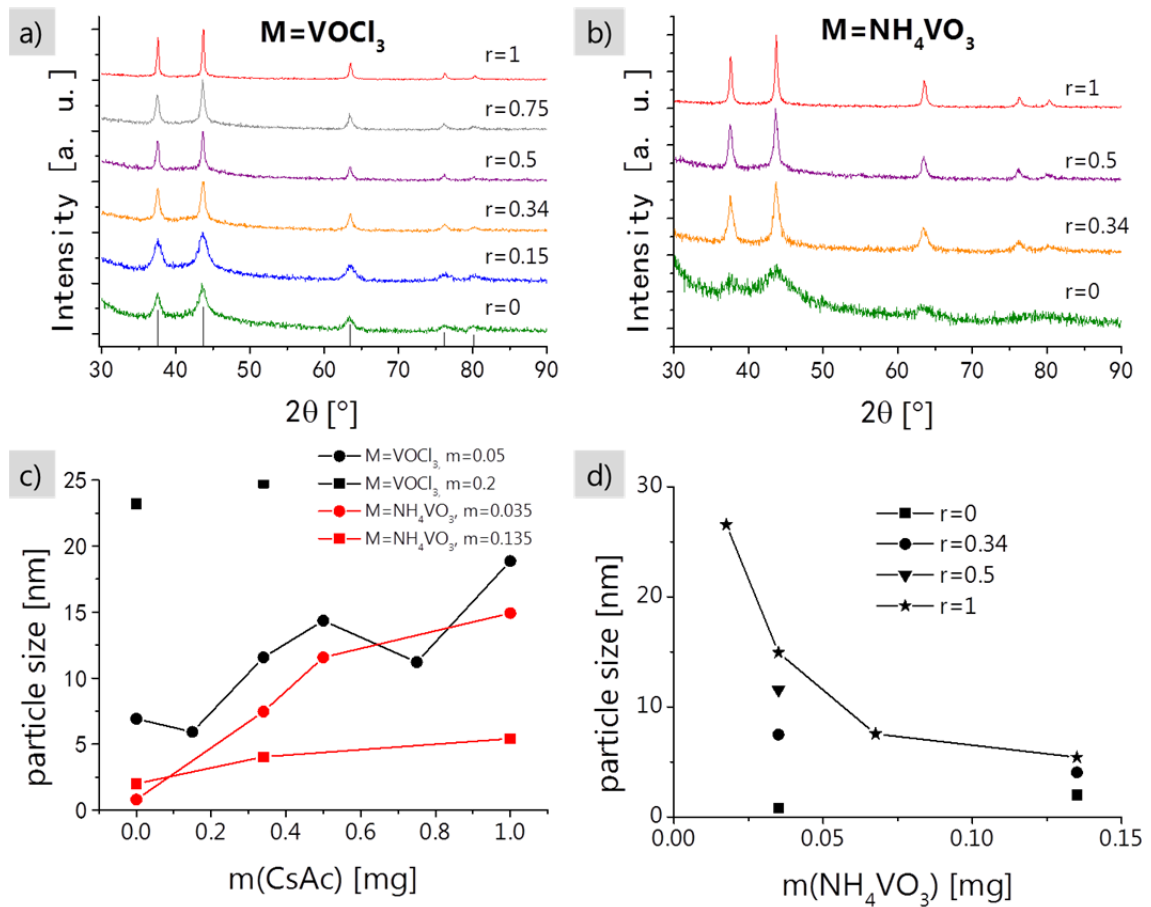
Figure 4-4 WAXS patterns of the composites **a)** VN@N-dC_Emim-dca_CsAc_r_VOCl$_3$_0.05_800 and **b)** VN@N-dC_Emim-dca_CsAc_r_NH$_4$VO$_3$_0.035_800 at varying CsAc amounts r. Course of particle size calculated from Scherrer equation in dependence of **c)** the CsAc amount for both VOCl$_3$ and NH$_4$VO$_3$ and **d)** of the metal precursor amount for NH$_4$VO$_3$.

The WAXS patterns of the washed products can be ascribed to VN. At fixed vanadium concentrations, the diffraction peaks become narrower with increasing CsAc concentration. This, quantified by the crystallite sizes calculated by the Scherrer equation (*Figure 4-4 c, d and Eq. A-2*), shows that the nanoparticles become larger. On the one hand, this probably arises from a decrease in viscosity at the reaction temperature. On the other hand, high amounts of salt diminish the miscibility of the metal precursor and the pre-ordered structure within the precursor solution at the reaction temperature. This also leads to the formation of large nitride particles as coexisting species in the final material (*Figure 4-5*).
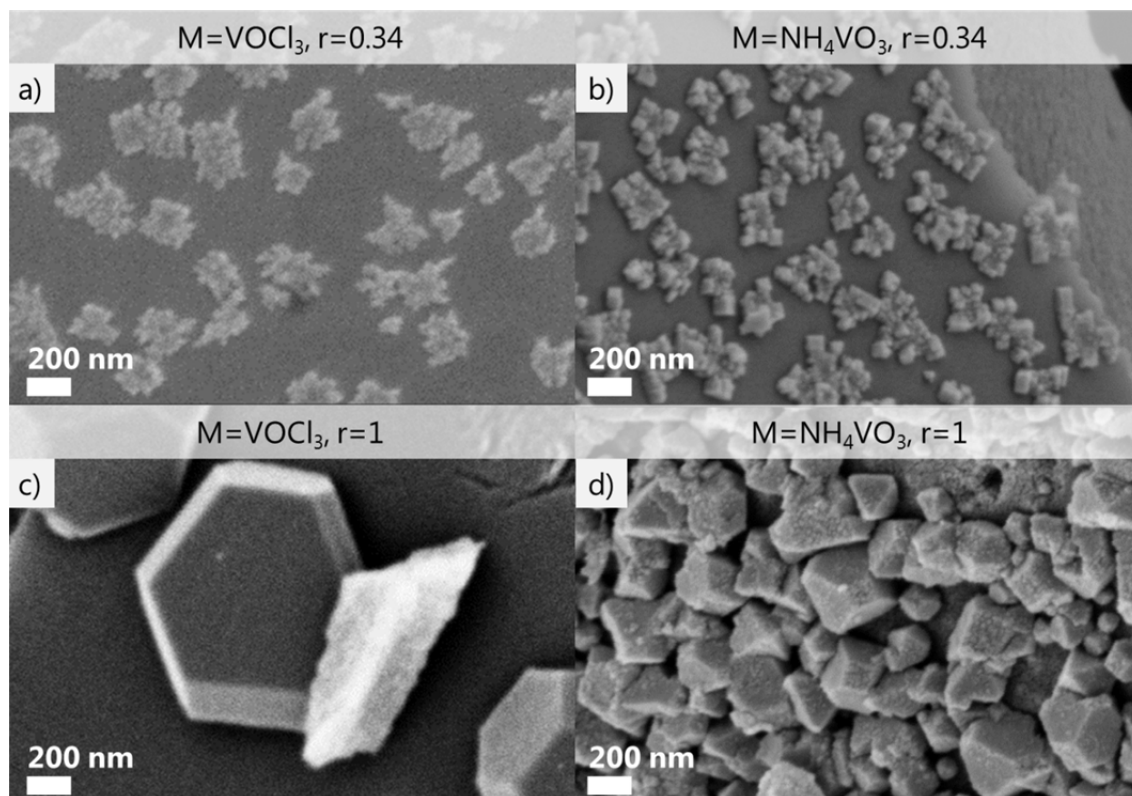
Figure 4-5 SEM pictures of the composites VN@N-dC_Emim-dca_CsAc_r_VOCl₃_0.05_800 (**a, c**) and VN@N-dC_Emim-dca_CsAc_r_NH₄VO₃_0.035_800 (**b, d**) templated with low (**a, b**) and high CsAc amounts r (**c, d**).

The additional larger particles are found on top of the materials which supports the assumption of reduced miscibility. For the precursor $VOCl_3$ these particles possess a flat, plate-like morphology while for NH_4VO_3 three-dimensional and comparably smaller cubes are obtained. However, the particle sizes calculated from the WAXS diffractograms reveal only small particles. Here, it is to mention that the Scherrer equation is only applicable for spherical particles, thus the results from TEM/SEM and WAXS can deviate. Furthermore, the equation only determines the crystallite size and eventually particle sizes may be underestimated. Additionally, it is also possible that at least for the composites at lower salt concentrations, the large particles are constituted of agglomerated small particles. On the other hand, the proportion of the large particles may be low and the signals are overlaid. Since the TEM pictures reveal the coexistence of many small particles, the latter is likely to be the case.

It has to be noted that for $VOCl_3$ the particles become larger with increasing metal precursor amount whereas for NH_4VO_3 they become smaller (*Figure 4-4 c, d*). This is attributed to a better solubility of NH_4VO_3 and a higher ordering within the precursor for higher NH_4VO_3 amounts possibly due to the polymeric structure.

It is known that carbonized Emim-dca in the absence of any template[26, 27] or with only small amounts of a metal precursor possesses no porosity as was shown in chapter 3.

However, the addition of porogen salts, here CsAc and ZnAc, increases the surface area of the carbon and carbon composites significantly as revealed by nitrogen sorption measurements (*Figure 4-6*).
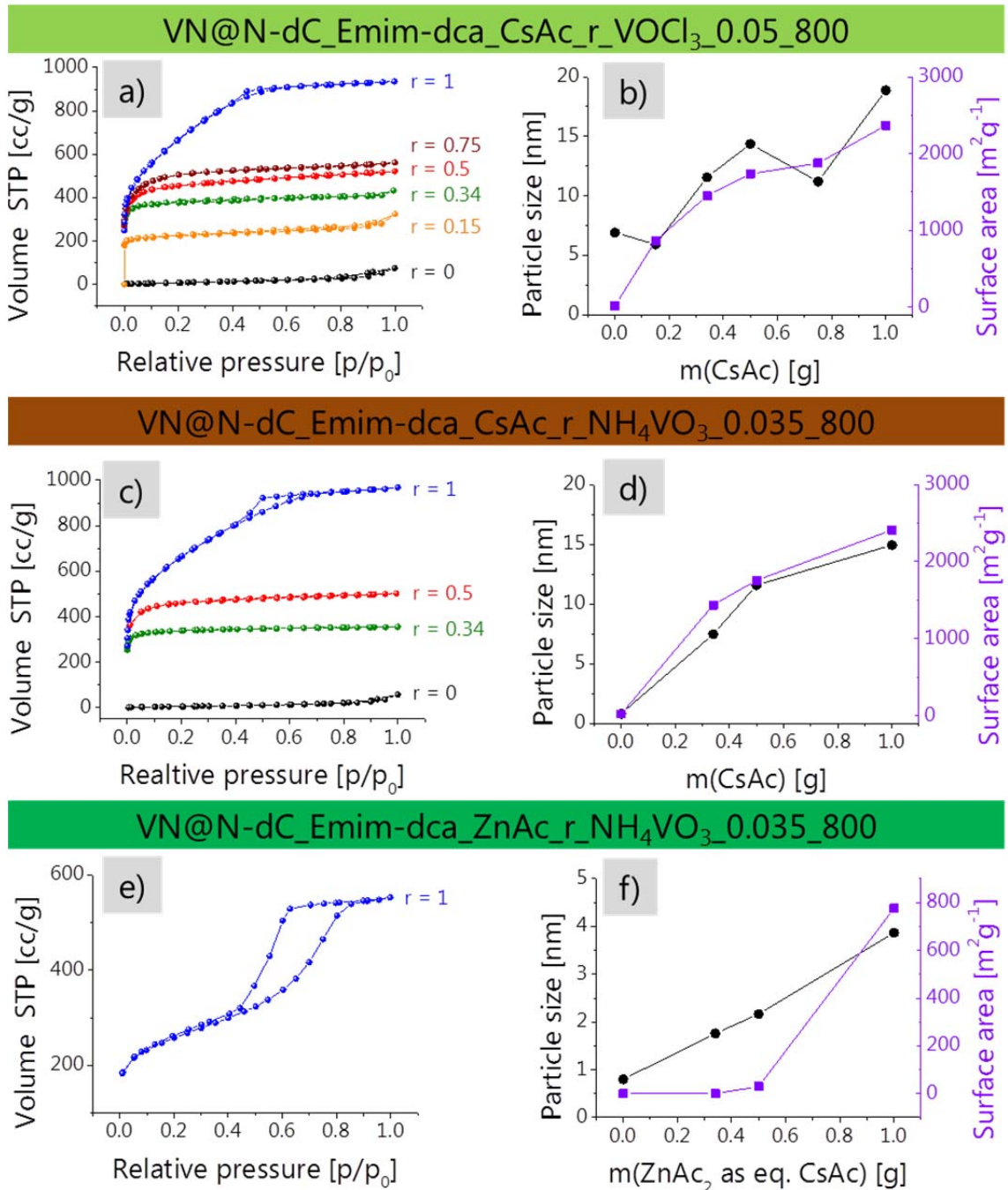
Figure 4-6 Nitrogen sorption isotherms (**left**) and respective course of particle size and surface area (**right**) for VN@N-dC_Emim-dca_YAc_r_M_m_800 with **a,b)** Y=CsAc, M=VOCl$_3$, m= 0.05 **c, d)** Y=CsAc, M=NH$_4$VO$_3$, m=0.035 and **e, f)** Y=ZnAc, M=NH$_4$VO$_3$, m=0.035 in dependence on the salt concentration r.

Regardless the metal precursor, similar isotherms and surface areas are obtained in the case of CsAc with slightly smaller particles for the composites derived from NH_4VO_3 which is in accordance with the TEM pictures (*Figure 4-6 a-d*). Here, the surface areas increase about linearly with CsAc amount which means that the salt indeed mainly acts as a molecular or clustered template with pore percolation effects setting in at high salt concentrations. At a fixed vanadium amount, the isotherms are of type I for 0 to 500 mg CsAc which implies a mainly microporous structure of the composites, *i.e.* the salt presumably acts as a "molecular template". At 750 mg CsAc the sorption isotherms show a further uptake of N_2 in the medium relative pressure region, reflecting a contribution of additional supermicropores and small mesopores. We attribute this to little salt clusters in the 2 nm range which now act as template. Finally, for the highest CsAc concentration, a small hysteresis is observed in the isotherms, underlining that the content of small mesopores has significantly been increased. While for VN@N dC_Emim-dca_CsAc_0.34_VOCl$_3$(NH$_4$VO$_3$_)_0.05(0.035_)_800 a high contribution of pores around 1 nm in diameter can be observed, additional pores of around 3 nm are found for VN@N-dC_Emim-dca_CsAc_1_VOCl$_3$(NH$_4$VO$_3$_)_0.05(0.035_)_800 (*Figure C-9*). It must be underlined that an apparent specific surface area of 2400 m^2g^{-1} is much higher than of any zeolite,[156] higher than of few-layer graphenes approaching the theoretical value of molecularly dispersed single layer graphene[72] and of the order of the highest surface areas found for activated carbons.[158] In spite of the simplicity of the applied one-step process, this is a remarkable result especially taking into account the presence of elements which are heavier than carbon. With the same salt templating approach, microporous TiN@N-dC_Emim-dca_CsAc_0.34_TiCl$_4$_0.05_800 and TiVN@N-dC_Emim-dca_CsAc_0.34_TiCl$_4$-VOCl$_3$_0.035-0.015_800 were also synthesized (*Figure C-9*). The results support the assumption of a templating effect, because different metals at comparable amounts lead to similar porosities. The pore size, the pore volume and specific surface area are controlled by the salt amount with deviations pointing to entrapped salt.

For the composite templated with ZnAc *i.e.* VN@N-dC_Emim-dca_ZnAc_1_NH$_4$VO$_3$_0.035_800, the isotherm is of type IV (*Figure 4-6 e*) with a more pronounced hysteresis than observed for the respective composite from CsAc indicating the presence of a substantial amount of mesopores (*Figure C-10*). Compared to the respective N-doped carbon without the vanadium nitride component in chapter 3, the surface area is much higher due to the additional delamination caused by the VN particles. Here, for surface area development a higher amount of salt is needed than for CsAc-derived composites, which is attributed to the smaller VN particles (*Figure 4-6 f*) and thus a decreased ability for delamination. The very small particle sizes of the ZnAc-derived composites are believed to result from a more ordered precursor structure

because of the higher coordination/complexation *via* the zinc ions.[207, 214] The contribution of zinc oxide structures to the porosity cannot be excluded. However, mainly a different arrangement in the precursor solution, also including different clustering of the metal ions, is believed to be responsible for the larger pore sizes.

Taking into account all results, the ongoing structural processes during salt templating are illustrated within a first reaction scheme (*Scheme S4-1*).

Scheme S4-1 Description of product and surface area formation for the combination of salt templating and one-pot synthesis of porous metal nitride composites.
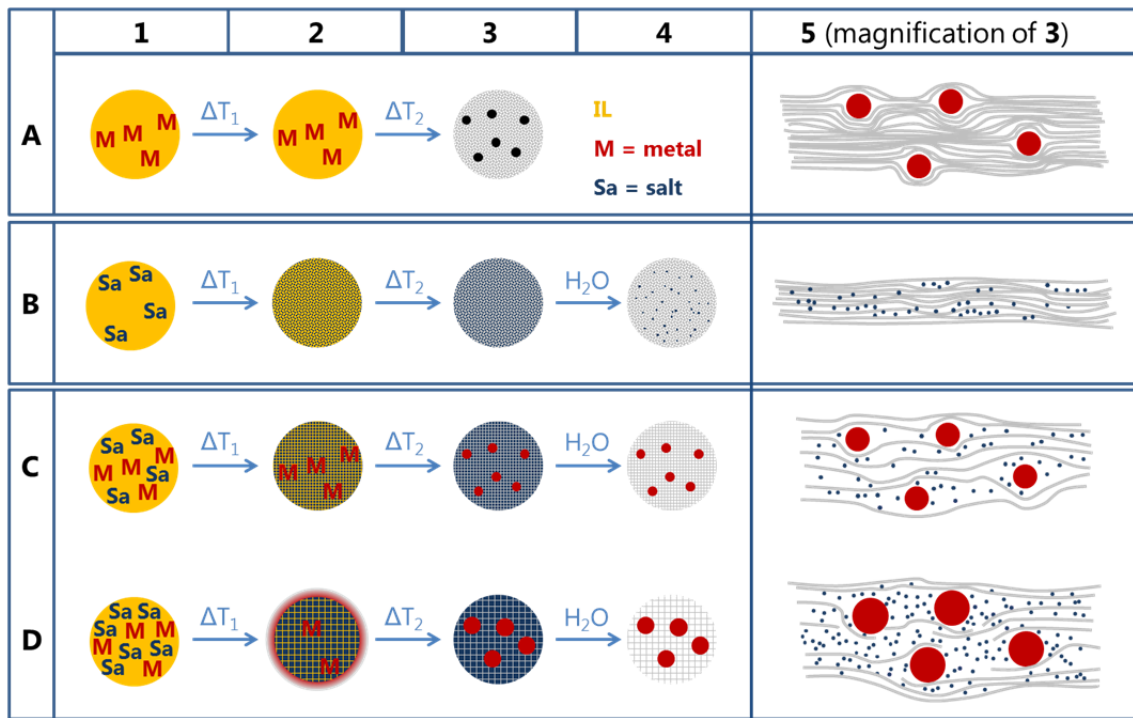
The letters M (red) and Sa (blue) correspond to the dissolved metal precursor and salt in the IL (yellow), respectively. In **column 1** the precursor solutions are shown at room temperature, in **column 2** the solution states at intermediate temperature T_1 during heat-treatment and in **column 3** the products after pyrolysis at $T_2 > T_1$. The final products after aqueous removal of the porogen are depicted in **column 4**. The pictures in **column 5** represent the magnifications of column 3 illustrating the pore formation by delamination/percolation without (A5) and in the presence of the salt (B5 to D5). **Row A** pictures the pure hybrid. The metal precursor is well dissolved during the whole heat-treatment (A2) and small MN nanoparticles form in between the carbon layers resulting in a composite with moderate surface area and microporosity (A3, A5). **Row B** shows the pure salt system. During the calcination process the salt is well dissolved in the IL (B2) but is partly entrapped in inaccessible pores (B3, B5) generating a moderate microporosity (B4). By the addition of a small amount of metal precursor (**Row C**) a good miscibility of the components is maintained (C2) and small MN nanoparticles are

formed (C3). Those nanoparticles promote access to the salt pores by delamination (C5) creating a highly microporous composite (C4). A high amount of salt (**Row D**) causes a lowered solubility of the metal precursor during the heating process (D2), thus larger MN particles are formed (D3, D4). However, high surface area products with small mesopores are generated (D5) since little salt clusters act as template.

As after the dissolution of the salt the washing solution turns alkaline for higher CsAc concentrations (150 mg CsAc pH8, 1000 mg CsAc pH14), it can be assumed that cesium hydroxide (CsOH) is formed. The formation of Cs_2O is unlikely to occur as the dehydration of CsOH is energetically disfavored even under extreme thermal conditions.[248] The activation through CsOH cannot be excluded but is not believed to be the main pore forming process.

The vanadium amount within the composites of both metal precursors derived from CsAc_0.34 determined by ICP-OES was found to be around 7 wt%. This value corresponds to the one obtained for the template-free composites described in 3.2.. Thus, the addition of the salt has thereby (as expected) a negligible influence on the metal content, *i.e.* the metal nitride content is simply controlled by the amount of initial metal precursor, and the salt is an orthogonal template.

Furthermore, elemental analysis obtained from XPS (*Figures C-11, C-12*) reveal the materials VN@N-dC_Emim-dca_CsAc_0.34_VOCl$_3$_0.05_800 and VN@N-dC_Emim-dca_CsAc_0.34_NH$_4$VO$_3$_0.035_800 to be constituted of around 73 wt% carbon, around 7 wt% nitrogen and 10 wt% oxygen which is in agreement with the bulk elemental analysis. The composition of the materials is given in *Table C-a*. A little residue of oxygen is beneficial for the desired application as supercapacitor electrode: V_xO_y was reported to be responsible for high capacitances observed for VN in form of a thin oxide layer on top of the nitride.[191] Additional oxygen within the carbon can also facilitate the wettability of the composite and thus enhance the electrolyte access to the pores, which further increases the capacitance.[249] However, the vanadium amount obtained from XPS reveals more V-N bonds (397.6 eV) and less nitrogen-carbon bonds for VN@N-dC_Emim-dca_CsAc_0.34_NH$_4$VO$_3$_0.035_800 (approx. 398.0 to 402 eV) compared to VN@N-dC_Emim-dca_CsAc_0.34_VOCl$_3$_0.05_800. Again, since XPS is a surface sensitive method and the results obtained from ICP are almost identical, the amount of VN close to the surface is presumably higher for the composites from NH$_4$VO$_3$.

Regarding the N1s spectra, the nature of the nitrogen-carbon bonds is found to be pyridinic (398.6 eV), pyrrolic or quaternary-graphitic (400.4 eV) and oxidic nitrogen species within graphitic micro domains (402.2 eV), respectively.[24, 27, 157] This is relevant, since heteroatom-doping in nanocarbons introduces additional pseudocapacitance, enhancing their supercapacitor performance.[233, 238] As also shown by Raman
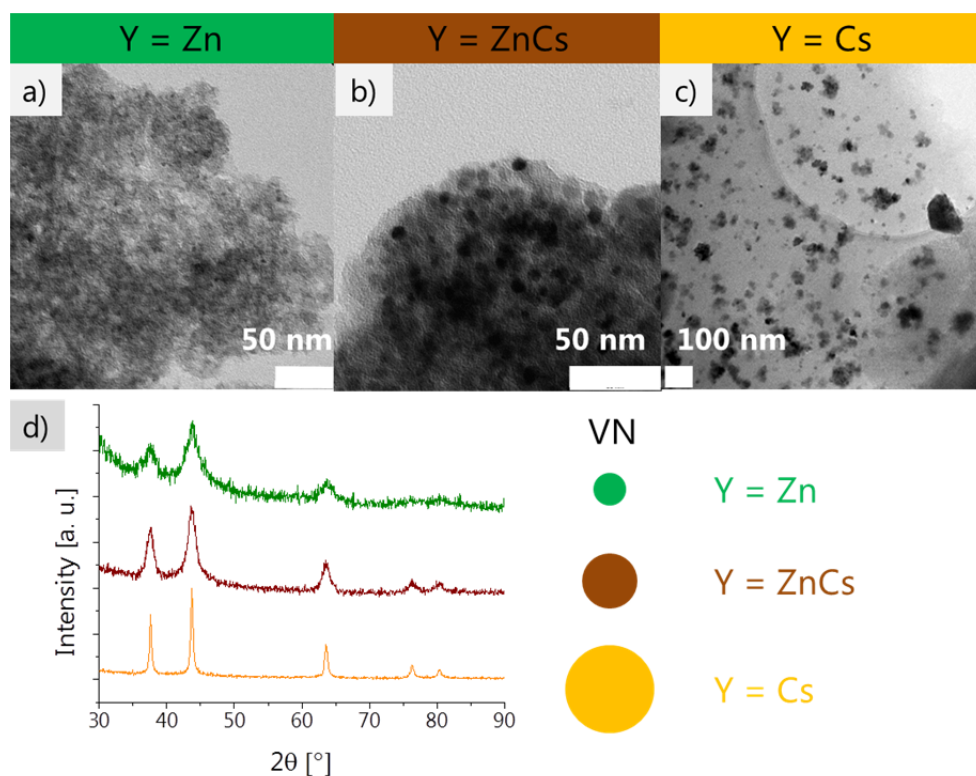
spectroscopy (*Figure C-13*), the V2p peaks of the XPS spectrum reveal, in addition to signals assigned to VN (513.6 eV), the presence of V_xO_y (514.9 to 518.9 eV).[191, 211, 221] All results shown in this part illustrate that salt templating can successfully be applied to different one-pot precursors eventually expanding the relevance of this technique to guarantee access to a wide range of hybrid materials with tunable porosity.

4.3.   Binary-salt system

In the previous part, high surface area composites with tailored pores were generated using the single salt systems CsAc or ZnAc. Here, the surface area and the particle size can be tuned depending on the salt nature and amount. However, both properties are connected and cannot be tuned independently from each other. Furthermore, with ZnAc bigger pores and smaller nanoparticles are achievable while the opposite behavior is true for CsAc. Eventually, the question arises if through a mixture of both salts intermediate states can be obtained, as it was already indicated for the N-doped carbons in chapter 2.3.2.Thus, in the following, the combination of both salts into a binary-salt system is shown to be suitable for a more flexible adjustment of the VN composites. Essentially, through different amounts and ratios of the salts, it is possible to adjust the particle size independently of a given pore size and *vice versa*.

For proof of principle, a composite was synthesized (following the default case of the single-salt systems in 4.2.) with Emim-dca (1 g) and NH_4VO_3 (35 mg), except for employing a molar 1:1 mixture of both salts *i.e.* ZnAc and CsAc (ZnAcCsAc1:1, 1 g). The precursor solution is named Emim-dca_ZnAcCsAc1:1_1_NH$_4$VO$_3$_0.035 while the composite is named VN@N-dC_Emim-dca_ZnAcCsAc1:1_1_NH$_4$VO$_3$_0.035_800.

In order to exclude that only one of the salts is responsible for the porosity, composites with the pure single salts *i.e.* VN@N-dC_Emim-dca_CsAc_0.5_NH$_4$VO$_3$_0.035_800 and VN@N-dC_Emim-dca_ZnAc_0.5_NH$_4$VO$_3$_0.035_800 were also generated.

The comparison of the TEM pictures of three composites produced with pure ZnAc, CsAc and the mixture ZnAc1:1 at equal salt mass ratios with respect to the IL-metal precursor reveals different particles sizes for each material (*Figure 4-7 a-c*). Here, the particle size increases from a) VN@N-dC_Emim-dca_ZnAc_1_NH$_4$VO$_3$_0.035_800 over b) VN@N-dC_Emim-dca_ZnAcCsAc1:1_1_NH$_4$VO$_3$_0.035_800   to c) VN@N-dC_Emim-dca_CsAc_1_NH$_4$VO$_3$_0.035_800.   This   already   shows   an intermediate behavior of the composite templated with the salt mixture.

To evaluate the nature of the particles and to confirm the tunability of the nanoparticle size, WAXS diffractograms of all three materials were recorded (*Figure 4-7 d*).

Figure 4-7 TEM pictures (**a-c**) and WAXS patterns (**d**) of VN@N-dC_Emim-dca_YAc_1_NH$_4$VO$_3$_0.035_800 with Y = Zn (green), ZnCs (brown) and Cs (yellow).

All peaks can be assigned to VN, thus the salt mixture has no influence on the formation of the nitride as such. Furthermore, broad peaks are obtained for the pure ZnAc system followed by the ZnAcCsAc and CsAc systems. The particle sizes are calculated with the Scherrer equation as 4 nm, 7 nm and 17 nm, respectively. Therefore, the WAXS data support the results from TEM and confirm the ability to adjust the particle size by mixing ZnAc and CsAc in different rations.

To address the question of tunability also of the surface area and porosity, nitrogen sorption measurements were performed with all composites from above (*Figure 4-8*).
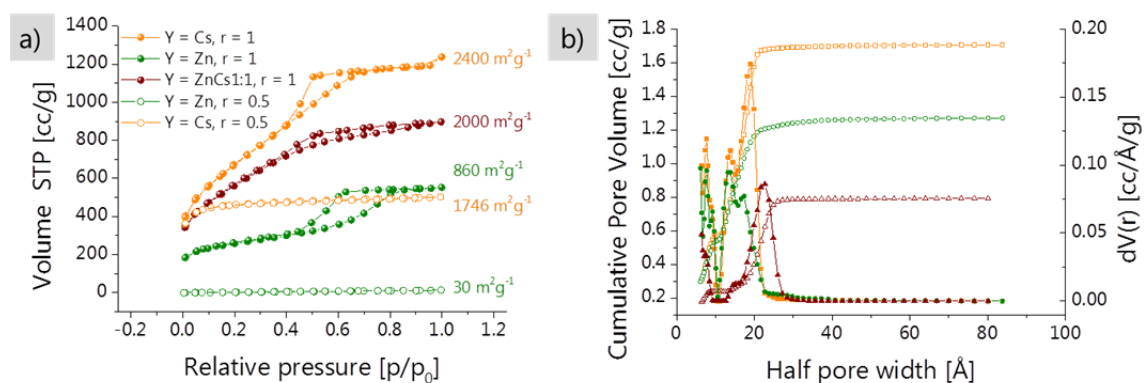

Figure 4-8 Nitrogen sorption isotherms (**a**) and PSD calculated based on NLDFT model for slit pores (**b**) of VN@N-dC_Emim-dca_YAc_r_NH$_4$VO$_3$_0.035_800.

The nitrogen sorption isotherm (*Figure 4-8 a*) of the composite VN@N-dC_Emim-dca_ZnAcCsAc1:1_1_NH$_4$VO$_3$_0.035_800 derived from the salt mixture shows a different shape compared to the materials of the pure salts at equal mass ratio. The hysteresis is less pronounced than for VN@N-dC_Emim-dca_ZnAc_1_NH$_4$VO$_3$_0.035_800 but distributed over a larger relative pressure range. Thus, the pore size distribution is relatively broad but includes several pore sizes from micro- to mesoporous. This is also visible in the plot of the respective pore size distributions (*Figure 4-8 b*). Eventually, not only the simple presence of a porogen but the nature of the salt has an impact on the pore formation as was also observed for the pure N-doped carbons as well presented in in chapter 2.3.2.. To exclude that the porosity only results from one salt component, nitrogen sorption measurements were also conducted with the composites VN@N-dC_Emim-dca_YAc_0.5_NH$_4$VO$_3$_0.035_800 with Y=Zn and Cs (*Figure 4-8 a*). The composite templated with half the amount of ZnAc reveals almost no porosity while the composite with half the amount of CsAc shows a type I isotherm indicative for a microporous material. Therefore, also for the composites a cooperative templating effect is found when different salts are mixed.

In general, this should offer the opportunity to tune the particle as well as pore size independently from each other by using different salt ratios and salt amounts of the mixture which enables a finer tuning of the composite properties.

4.4. Application as electrodes for supercapacitors

Even though the current literature is often controversial concerning optimal material properties for the utilization as supercapacitor electrodes, some general prerequisites can be extracted. Here, a high surface area, match of pore size and electrolyte size, the contribution of pseudocapacitance and high conductivity are of advantage to obtain a high energy storage capacity.

For the evaluation of the performance as supercapacitor electrode, the CsAc-based materials were chosen due to the absence of alkali chlorides. Thereby, a transient reactive liquid-sintering process and eventually metal densification can be avoided which was observed by Bocarsly *et al.* for the calcination of cyanogels.[250] Additionally, the highest surface area of 2400 m^{2}g^{-1} was obtained for the materials templated with CsAc while crucial parameters such as surface area, pore size and particle size are almost linearly tunable. For the sake of completeness, the one-pot composites were also templated with the eutectics, which will, however, not be discussed herein but it is referred to the appendix (*Figure C-14 to C-20*). In order to determine the influence of the VN nanoparticles and the CsAc addition on the capacitance, CVs of the salt

templated N-doped carbon N-dC_Emim-dca_CsAc_0.34_800 (*Figure 4-9, red*), the template-free composite VN@N-dC_Emim-dca_VOCl$_3$_0.05_800 (*Figure 4-9, green*) and the salt templated composite VN@N-dC_Emim-dca_CsAc_0.34_VOCl$_3$_0.05_800 (*Figure 4-9, black*) were recorded. The measurements were performed in 2 M HCl at different scan rates (2 - 500 mVs^{-1}) using a three electrode setup. Exemplarily, the CVs at the lowest and highest scan rates are shown (*Figure 4-9*).
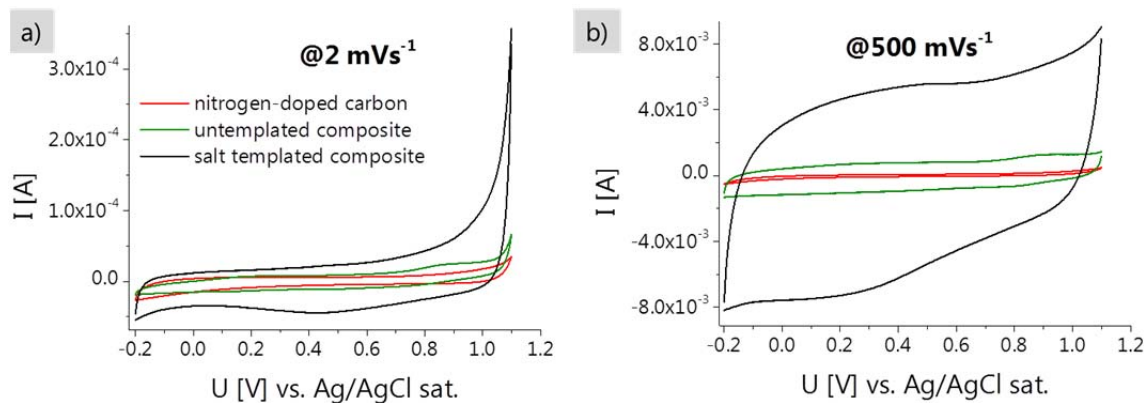

Figure 4-9 CVs at **a)** 2 mVs^{-1} and **b)** 500 mVs^{-1} of N-dC_Emim-dca_CsAc_0.34_800 (red), VN@N-dC_Emim-dca_VOCl$_3$_0.05_800 (green) and VN@N-dC_Emim-dca_CsAc_0.34_VOCl$_3$_0.05_800 (black). All measurements were conducted in in 2M HCl vs. Ag/AgCl (sat.).

In the CVs of the materials which contain VN, relatively broad peaks are observed which arise from reversible redox reactions on the VN/V$_x$O$_y$ surface responsible for the pseudocapacitance contribution. The N-doping revealed through XPS also contributes to an additional pseudocapacitance which is, however, not detectable as a defined peak but rather as a general widening of the CV curve. This is due to presence of different structural nitrogen motifs which undergo diverse reactions. For the CV of the salt templated composite, a sharp current increase is observed in the high potential region at the lowest scan rate (*Figure 4-9 a*). Since electrolyte or electrode degradation were excluded and a dependence on the porosity was observed, this is assumed to arise from a distortion or partial loss of the hydrate shell of the electrolyte ions within the small micropores.[104, 244] At the highest scan rate, an almost rectangular shaped CV is observed (*Figure 4-9 b*), revealing a nearly ideal capacitive behavior. Regarding the energy storage performance, the larger the enclosed area of the CV, the higher is the capacitance since both are proportional to each other (*Eq.-1*). Even though VN@N dC_Emim-dca_VOCl$_3$_0.05_800 possesses a very low apparent surface area compared to N-dC_Emim-dca_CsAc_0.34_800 (20 *vs.* 287 m^{2}g^{-1}), its capacitance is higher. This can be attributed to a significant contribution of the VN nanoparticles. However, the influence of variations of the pore morphology can neither be excluded, since the pores are formed *via* cohesive interface delamination and salt templating,

respectively. For VN@N-dC_Emim-dca_CsAc_0.34_VOCl$_3$_0.05_800, the area enclosed by the CV curve and eventually C, calculated from CVs according to *Eq.-1*, are always higher than the sum of C of the untemplated composite and the salt templated N-dC at the respective scan rate (*Figure 4-10 a*). This is indicative of a synergistic interaction within the hybrid structure, as already discussed in the porosity data, and strongly supports the central premises of the present doctoral thesis.
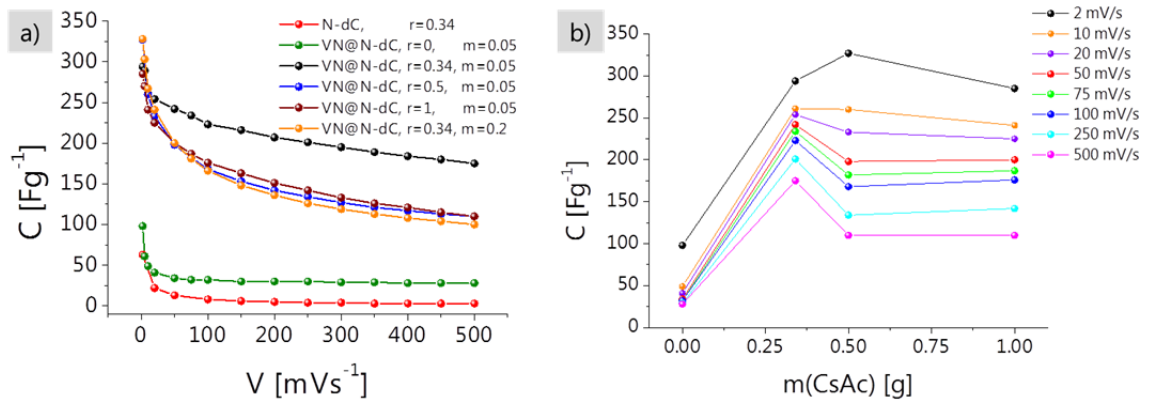

Figure 4-10 a) Scan rate dependence of the specific capacitance C for VN@N-dC_Emim-dca_CsAc_r_VOCl$_3$_m_800 in the range from 2 to 500 mVs^{-1}. **b)** Specific capacitance C in dependence on the CsAc amount r for VN@N-dC_Emim-dca_CsAc_r_VOCl$_3$_m_800 at different scan rates. All measurements were conducted in in 2M HCl *vs.* Ag/AgCl (sat.).

In order to evaluate the impact of the salt concentration and eventually the pore structure on the capacitance, the performances of the composites VN@N-dC_Emim-dca_CsAc_r_VOCl$_3$_0.05_800 were tested in dependence on the CsAc amount (*Figure 4-10 b*). High capacitances are observed for VN@N-dC_Emim-dca_CsAc_0.34_VOCl$_3$_0.05_800 at all scan rates since this material offers a good compromise between a high surface area, good electrical conductivity (*Table C-b*) and small VN nanoparticles.

To also assess the influence of the VN amount, the capacitance of the composite VN@N-dC_Emim-dca_CsAc_0.34_VOCl$_3$_0.2_800 synthesized with a higher VOCl$_3$ concentration was also investigated (*Figure 4-10 a*). Overall high values are still obtained for VN@N-dC_Emim-dca_CsAc_0.34_VOCl$_3$_0.05_800 and maintained even at scan rates as high as 500 mVs^{-1}. However, at low scan rates VN@N-dC_Emim-dca_CsAc_0.5_VOCl$_3$_0.05_800 and VN@N-dC_Emim-dca_CsAc_0.34_VOCl$_3$_0.2_800 possess a slightly increased capacitance compared to VN@N-dC_Emim-dca_CsAc_0.34_VOCl$_3$_0.05_800, concomitant with a higher surface area and a higher number of VN nanoparticles, respectively. With increasing scan rate, the contribution of the electrical conductivity becomes more important. In this measurement range, the capacitance of the higher surface area materials in fact

decreases, explained by a reduced electrical conductivity of thin pore walls, reaching the thickness of a single, distorted carbon layer. Also the increased amount of VN nanoparticles in VN@N-dC_Emim-dca_CsAc_0.34_VOCl$_3$_0.2_800 lowers the electrical conductivity of the composite, thus the capacitance decreases dramatically with the scan rate. The superiority of VN@N-dC_Emim-dca_CsAc_0.34_VOCl$_3$_0.05_800 is due to the combination of several aspects. At high energies, a sufficiently high surface area as well as a pore size in the micropore range enables a high amount of charge to be adsorbed at the electrode/electrolyte interface. At the same time, the remaining wall thickness is large enough to provide the system with adequate electrical conductivity for good rate performance. Regarding the VN nanoparticles, smaller nanoparticles possess a higher surface area and thus a faster redox response. This causes a higher pseudocapacitance, which however contributes to the overall capacitance in our case only at low scan rates.

Taking into account all these aspects, it is interesting to state that the pore volume and the surface area as the commonly lead properties have only a minor influence on the capacitance of the composites. Here, VN@N-dC_Emim-dca_CsAc_0.34_VOCl$_3$_0.05_800 shows an overall better performance compared to VN@N-dC_Emim-dca_CsAc_1_VOCl$_3$_0.05_800 in spite of the fact that the latter possesses a more than doubled surface area and a three times higher pore volume. The new lead properties seem to be the pore size and the nanoparticle size as well as the electrical conductivity on the nanoscale, which is inversely related to the surface area.

Finally, the impact of different vanadium precursors *i.e.* VOCl$_3$ and NH$_4$VO$_3$, on the storage capacitance of the CsAc-templated composites is evaluated. The capacitances were determined according to the previous measurements (*Figure 4-11*).
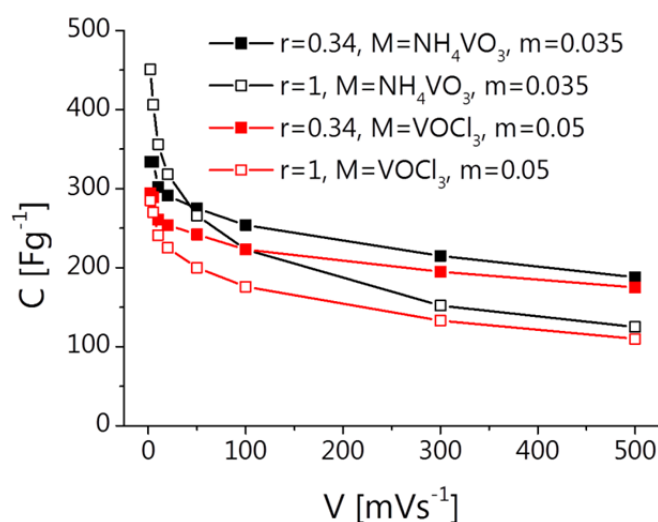

Figure 4-11 Scan rate dependence of the specific capacitance C for VN@N-dC_Emim-dca_CsAc_r_M_m_800 in the range from 2 to 500 mVs^{-1}. All measurements were conducted in 2 M HCl vs. Ag/AgCl (sat.).

At all scan rates, the composites from NH_4VO_3 possess a better performance than the ones from $VOCl_3$. However, with increasing scan rates, the capacitances converge resulting in similar values at 500 mVs^{-1} for both metal precursors. Both systems reveal the same trends *i.e.* high but rapidly decreasing capacitances for the composites templated with a high CsAc amount. The materials templated with a lower salt amount possess an overall relatively constant performance even at high scan rates. Here, we have to emphasize that a specific capacitance of around 450 Fg^{-1} is a remarkably high value outperforming all available commercial systems ($\sim$ 150 – 250 Fg^{-1}), which is valuable especially considering the straightforward synthesis approach. The difference between $VOCl_3$ and NH_4VO_3 as vanadium precursor is presumably due to a different distribution and size of the VN nanoparticles since all other properties are similar. As was shown in part 4.2., the XPS spectra of VN@N-dC_Emim-dca_CsAc_0.34_NH$_4$VO$_3$_0.035_800 reveals less N-C bonds but a higher VN amount compared to VN@N-dC_Emim-dca_CsAc_0.34_VOCl$_3$_0.05_800. However, the vanadium amounts obtained from ICP are almost identical. Therefore, the amount of VN present on the surface is higher for the composites from NH_4VO_3. Additionally, the coexisting big VN particles are smaller and possess a three-dimensional shape for NH_4VO_3. This eventually increases the accessible surface of the pseudocapacitive metal compound for NH_4VO_3 compared to $VOCl_3$. Because the processes occurring in a supercapacitor are surface-related, it is reasonable to consider the differences in the surface properties of the composites as the main explanation for an improved performance.

The herein presented preliminary results obtained from the composites VN@N-dC_Emim-dca_CsAc_0.34_M_m_800 (M=VOCl$_3$, m=0.05 and M=NH$_4$VO$_3$,m=0.035), are further promising examples of microporous materials capable of storing a high amount of energy even at high scan rates, especially suited for applications where very fast charge/discharge processes are required.

5 Conclusions and outlook

The present thesis is concerned with the challenge to develop alternative and sustainable approaches toward energy conversion materials and aims to contribute to the current fundamental and practical understanding of the corresponding systems and devices.

In this regard, carbon-based materials have become very prominent and also constitute the compositional basis of this work. All experiments have in common that ionic liquids are employed as versatile precursors.

The main aspects covered within this thesis can be summarized in three areas *i.e.* salt templating of heteroatom-doped carbons, the synthesis of metal nitride containing N-doped carbon composites and the combination of both approaches. This also defines the outline of the thesis (*Figure 5-1*).
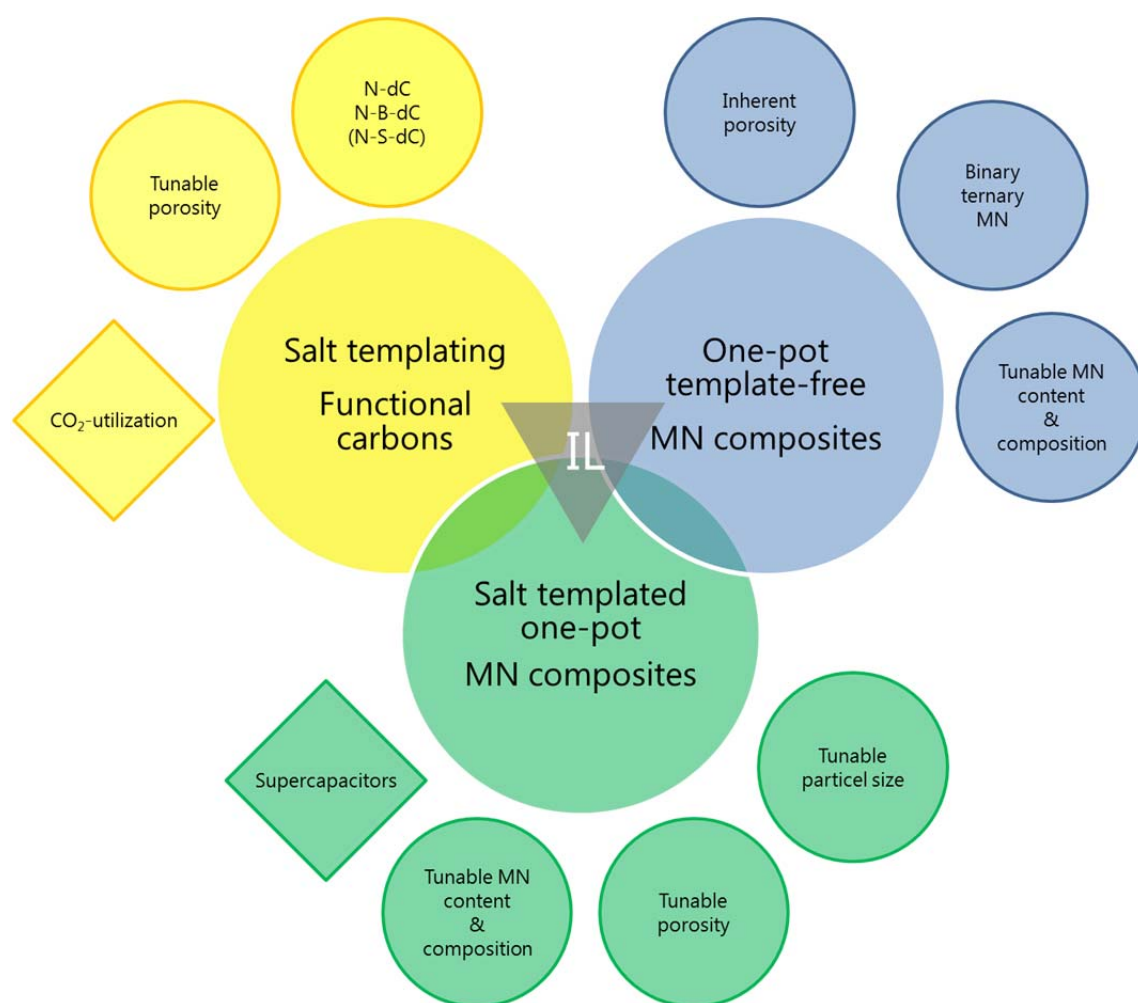

Figure 5-1 Graphical summary of the present thesis.

5 Conclusions and outlook

In the second chapter (yellow), salt templating was introduced as a new, alternative and sustainable method for the generation of high surface area functional carbons with tunable porosity. The utilization of ionic liquids as precursors for carbon materials brings along several advantages such as liquid state, negligible vapor pressure and improved dissolution properties enabling simple functionalization. The ionic liquids were chosen to be Bmp-dca, Emim-dca and Emim-tcb since careful mechanistic studies by Paraknowitsch *et al.* as well as Fellinger *et al.* already revealed their suitability for the generation of N- and N-B-containing carbons, respectively. However, the materials do not possess any porosity in the absence of a template which is crucial for a range of application such as energy storage and conversion.

In order to overcome certain drawbacks of hard-templating *i.e.* multiple synthesis steps, the need for the compatibility of the templating procedure with the product, and the utilization of usually hazardous chemicals for the template removal, the salt templating approach was developed. Here, it was shown that ordinary salts can be used as *in situ* diverse porogens. The carbons were generally synthesized by mixing an ionic liquid with a non-carbonizable salt, followed by heat-treatment where the carbon is scaffolded in the presence of the homogeneously distributed salt. The porogen phase was easily removed through simple washing with water. Thus, *e.g.* hydrogen fluoride commonly used to remove silica hard-templates can be avoided. Furthermore, the salt template is in principle recyclable eventually rendering salt templating as a closed, sustainable approach towards high surface area materials design. In more detail, through the employment of eutectic mixtures, porous N- and N-B-co-doped carbons with surface areas and pore volumes up to 2000 m^2g^{-1} and 2.75 ml g^{-1} were obtained, respectively. This surface area is higher than of any zeolite, activated carbons and few layer graphenes. It was shown that by applying different eutectics the porosity of the functional carbons could be tuned from micro- ($LiCl/ZnCl_2$) to mesoporous ($NaCl/ZnCl_2$) and even globular, aerogel-like monolithic materials ($KCl/ZnCl_2$) were generated. Besides the introduction of porosity, the salt templating presumably also results in increased yields due to Coulombic interactions in the "all-ionic" systems. The porosity could further be controlled by the salt amount leading to particulate carbons at very high concentrations which was discussed in the context of common sol-gel chemistry. Since the templating with just one of the eutectic components only yielded a moderate surface area for $ZnCl_2$ and no porosity for the others, it was concluded that the salt templating is not just due to the simple presence of a salt and space filling but rather a cooperative effect. The factors which probably influence the porosity were summarized and cross-tested through the investigation of two single-salt systems *i.e.* ZnAc and CsAc and their combination in a binary-salt system. Here, even sheet-like

structures could be obtained which already illustrates the high structural diversity of the salt templating approach.

For the eutectic mixtures, the templating occurs in a salt melt presumably with microphase separation while for the single salt systems ZnAc and CsAc a molecular or ion cluster templating is believed to occur. However, because of the "all-ionic" systems the electrostatic interactions of the ionic liquids with each porogen are comparable and the demixing proceeds in a similar fashion. Thus, different ionic liquids templated with the same salt reveal comparable porosity and morphology since the templating is mainly dependent on the salt nature.

The composition of the products can be adjusted through the heat-treatment procedure, therefore salt templated polymeric carbonaceous materials using eutectic mixtures were obtained at lower temperatures (450 °C) compared to the aforementioned graphitic carbons (1000 °C and 1400 °C). Here, it could be shown that the pore size and morphology is identical to the high-temperature carbon which supports the assumption of a real template effect. Furthermore, first results obtained from CO_2-sorption measurements revealed these systems to be potentially suitable for CO_2-binding and subsequent utilization. The highest heat of adsorption with 100 kJ mol^{-1} at low coverage was found for the product of Emim-dca templated with SZ. Compared to other material classes such as MOFs or zeolites, this is a remarkable value. This carbon is therefore a promising candidate for further investigation in electrochemical CO_2 reduction.

At the end of this chapter, to extend the range of materials which can be obtained from ionic liquids as precursors, a N-S-co-doped carbon was synthesized. Here, the ionic liquid Emim-scn was presented as a suitable precursor in combination with Emim-dca and Bmp-dca.

In the third chapter (blue), a one-pot and template-free synthesis approach of inherently porous metal nitride nanoparticle containing N-doped carbons was delineated. Metal nitrides offer favorable properties such as high mechanical, chemical and thermal stability and catalytic activity. Furthermore, the properties of ternary metal nitrides can be adjusted through their composition. Thus, they are an interesting material class to substitute commonly used precious metal based materials *e.g.* for catalysis or energy storage.

The composites are generated through the heat-treatment of precursor solutions consisting of Bmp-dca, TiCl$_4$ and/or VOCl$_3$ to obtain titanium nitride and vanadium nitride nanoparticle containing N-doped carbons, respectively. The ionic liquid serves as both, the precursor for the nitrogen-doped carbon matrix and as nitrogen source for *in situ* formation of the metal nitrides. This approach enables to circumvent standard

synthesis techniques of metal nitrides which are mostly hardly scalable or controllable. The composites reveal a homogeneous distribution of around 7 nm small nanoparticles which size slightly increases with metal precursor amount. The narrow size distribution of the particles is believed to be based on a high degree of pre-organization in the precursor gel due to the coordination of the ionic liquid ions to the metal ions. It was shown, that the metal nitride amount and composition in ternary nitrides is tunable simply through the amount of metal precursor. Furthermore, the composites possess an inherent porosity starting from a distinct metal nitride concentration, reaching surface areas of up to 550 m^2g^{-1}. This behavior was attributed to a percolation mechanism caused by the growing nanoparticles which led to the delamination of the carbon and eventually to the formation of accessible pores. Since the ionic liquid or metal precursor can be varied, this approach offers a general platform for the generation of porous composites within a scalable energy- and time-efficient one-step synthesis.

In the fourth chapter (green), both approaches *i.e.* salt templating and the one-pot synthesis of metal nitride composites are combined. This opens the route towards the generation of metal nitride composites with tunable composition, porosity and particle size within a one-step synthesis pathway.

Besides the metal precursors $TiCl_4$ and $VOCl_3$ which were already used in the third chapter, ammonium metavanadate NH_4VO_3 was employed as a second vanadium precursor. For the introduction of porosity the single-salt systems ZnAc and CsAc from chapter 2 were employed and were shown to be highly suitable for the introduction of very high surface areas. In the case of CsAc the surface area was almost linearly adjustable for both vanadium precursors simply by the porogen amount, reaching values of 2400 m^2g^{-1} at the highest salt concentrations. The activation through CsOH etching cannot be excluded but is not believed to be the main pore forming process. While the composites produced with a lower CsAc amount reveal microporosity which is attributed to molecular templating, higher salt concentrations cause the formation of supermicropores and small mesopores presumably due to salt cluster formation which then serves as template. In the case of ZnAc, smaller nanoparticles and lower surface areas were obtained presumably caused by a higher pre-organization in the precursor solution than in the case of CsAc. However, the composites possessed bigger pores, thus real mesopores are accessible which is possibly due to different clustering of the ions. Within this thesis, a pore formation mechanism is proposed and depicted in an overview scheme. Generally, the salt further enhances the pore percolation caused by the metal nitride nanoparticles and thus facilitates the delamination process which results in high surface area composites. The generality of the salt templating approach

was demonstrated by the synthesis not only of vanadium nitride but also titanium and titanium vanadium nitride nanoparticle containing composites which possess comparable porosities and morphologies.

Finally, the CsAc templated VN composites were applied and tested as highly efficient supercapacitor electrodes, and the influence of several parameters such as porosity and particle size on the performance was investigated within a three-electrode setup. Here, the salt templated composites possess a performance superior to both the salt templated carbon and the untemplated composite, revealing a maximum capacitance of 450 Fg^{-1} at a scan rate of 2 mV s^{-1} which is a remarkably high result. It has to be mentioned that the values calculated from a three-electrode setup are higher than from a two-electrode setup which gives values closer to the practical performance in the actual device. However, the three-electrode setup enables for a better qualitative evaluation on the processes and is therefore more suitable in terms of fundamental investigations especially if pseudocapacities are involved. Furthermore, it still allows for the relative comparison of the performance of different materials. While general trends were identical for the composites from the two different vanadium precursors, the materials synthesized with NH_4VO_3 revealed a higher energy storage capacity which was attributed to a more favorable distribution of the VN phase. Generally, besides a high surface area and matching pore size and electrolyte size, lead properties were found to be the pore and the nanoparticle size as well as the electrical conductivity on the nanoscale.

Since various combinations between different ionic liquids, metal precursors and salts can be envisioned, the salt templating presents a general platform for the simple generation of high surface area carbons and carbon-based composites. Here, we want to make the conjecture that through the right combination of nature and amount of salt, both the porosity and for composites also the particle size is smoothly and individually adjustable. Consequently, this approach is believed to provide a helpful tool for future materials design not only in fundamental research but also on the practical device level.

The implementation of salt templating may be facilitated by the development of other research fields, such as the synthesis of biomass derived ionic liquids, which would additionally result in lower costs and a more sustainable system. With respect to cost reduction, alternative methods to high temperature carbonization such as microwave-assisted synthesis offer possibly additional opportunities.

On the material level the extension of salt templating also to poly-ionic liquids could enable to take advantage not only of the unique properties of ionic liquids but also of

polymers. Thus processing methods such as spin coating or electro spinning may be applicable, guaranteeing access to porous films or fibers, respectively. Furthermore, through the utilization of *e.g.* block copolymers or functionalized polymers, the dissolution and phase behavior of the precursor solution with respect to additional metal precursors and salts might be tunable and open the way to different morphologies not obtainable by single molecules.

On the device level, a fascinating potential application of the low-temperature polymeric carbon materials is for electrochemical CO_2-conversion. In our case, an extra electrical conductivity is crucial. This may be realized through coating of a conductive core structure, *e.g.* the ionic liquid-derived functional carbons synthesized at high temperatures with the salt templated porous polymeric low-temperature carbon material. This again demonstrates the multifaceted material structures and coupled properties which can be obtained based on ionic liquids.

With regard to the application of the composites as supercapacitor electrodes, the ZnAcCsAc system is believed to offer the opportunity to determine the optimal combination of properties since the porosity and particle size can be tuned independently.

In any case, detailed investigations of the processes behind the product formation of salt templated carbons, the one-pot synthesis of metal nitride composites and salt templated composites offers important key parameters for understanding and improving energy storage and conversion materials. In this context, the present thesis can be understood as a first step toward this direction and to reveal the high potential of the salt templating approach in general.

A Applied methods

Wide angle X-Ray scattering (WAXS)

From the interaction of electromagnetic radiation with matter, different informations can be obtained which depend on the wavelength. If X-Ray is employed, it is possible to analyze the structure of sub-micrometer objects since the wavelength λ of the radiation (1 to 10^{-5}) nm is in the same range. Here, the Cu-K$_\alpha$ radiation (wavelength of 0.154 nm) is commonly used. The measurement technique is based on the coherent (Rayleigh or elastic) scattering of the incident beam on lattice planes of matter. If the material possesses ordered structures with planes in the distance d *i.e.* it possesses crystallinity, constructive interference occurs for reflected waves which phase shift is an integer multiple n of the incoming wavelength. In dependence on the angle θ, defined by the incident beam and the lattice planes, the connectedness is given by Bragg's law (*Eq. A-1*).

$$n\lambda = 2d \sin(\theta)$$

(A-1)

A diffraction pattern is obtained through measuring the scattering intensity $I(\vec{s})$ with $\vec{s}$ being the scattering vector in dependence on the scattering angle θ. For conditions which satisfy the Bragg equation, constructive interference causes very strong diffraction peaks. Here, the diffraction lines become broader with decreasing structure size and increasing lattice imperfection. The lattice planes can be classified by the Miller Indices (*hkl*) which are defined as the reciprocal points of intersection of the planes with the unit cell. As can be seen from the Bragg equation, bigger structures cause reflections at smaller angles while the peaks due to smaller structures are located at higher angles. The former is called Small Angle X-Ray Scattering (SAXS, 2θ < 5°) where colloidal structures in the range of 1 to 100 nm can be investigated (*Figure A-1*). The latter is denoted as Wide Angle X-Ray Scattering (WAXS, 2θ > 5°) and enables the analysis of atomic structures (*Figure A-1*).
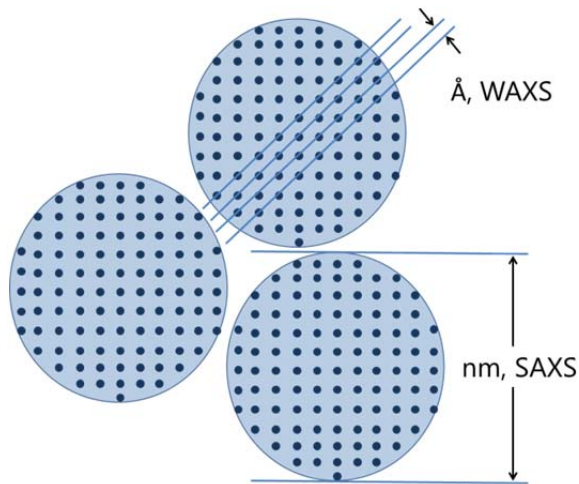
A Applied methods

Figure A-1 Illustration of structure dimensions detectable through SAXS and WAXS.

The crystallite size Δd can be estimated with the Scherrer equation

$$\Delta d = \frac{K\lambda}{(FWHM)\cos\theta}$$

(A-2)

where K is a dimensionless shape factor with a typical value of 0.9, FWHM is the full width at half maximum in radian measure and θ is the Bragg (angle in radian measure). This, however, only provides a lower bound of the particle size since other factors than the particle size may have an influence on the peak broadening. Furthermore, it only determines the mean size of the ordered (crystalline) domains. Thus, the results should always be interpreted in combination with further characterization methods.

WAXS-patterns were measured on a Bruker D8 Advance instrument using Cu-K$_\alpha$-radiation.

Nitrogen sorption measurements

One of the most widely used techniques for the characterization of porous materials is the gas sorption. This method allows for the qualitative and quantitative determination of the surface area, pore volume and pore size distribution of porous materials. Here, the gas amount *i.e.* the adsorbate, which is adsorbed by a sample *i.e.* the adsorbent, which is commonly a solid, is measured in dependence on the relative pressure p/p_0. The measurement is conducted at a constant temperature and at the equilibrium vapor pressure p_0 of the gas. Commonly, nitrogen is employed as adsorbate, thus it is measured at 77 K and atmospheric pressure. This ensures solely weak interaction through van der Waals interaction of the adsorbent and adsorbate which is called physisorption and enables multilayer formation. In a typical measurement, the

adsorbate is dosed into a sample cell and the gas uptake is recorded in dependence on the relative pressure which is increased up to $p/p_0=1$ yielding the adsorption branch of the isotherm. Afterwards, the pressure is lowered again and the desorption branch is obtained. The final isotherm results from the overlay of several sorption phenomenons and provides crucial informations on the porosity of a material.

In general, it is distinguished between the external and internal surface. The former includes surface roughness and slits which are wider than deep while the latter describes cracks, slits and pores which are deeper than wide and are accessible by the adsorbate. With regard to the different sorption effects caused by different pore sizes, porous materials are classified by the IUPAC into three categories

microporous (< 2 nm) < mesoporous (2 nm to 50 nm) < macroporous (> 50 nm)

The classification is based on the different isotherms mentioned above which are characteristic for each pore regime. They can further be classified in different types (*Figure A-2*).
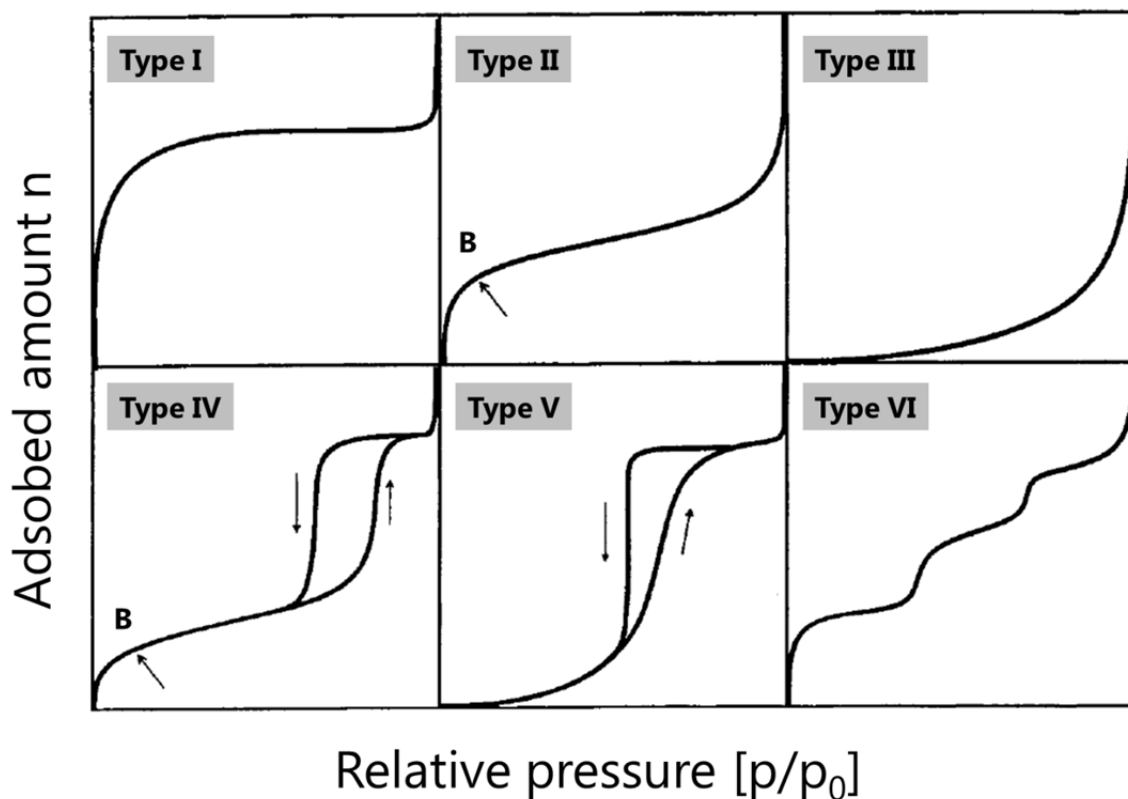

Figure A-2 Classification of sorption isotherms by the IUPAC.[88]

A Applied methods

Isotherms of class I are characteristic for microporous materials which only possess a low external surface. Because the small pores are already filled at low relative pressures (p/p$_0$ < 0.1) due to micropore filling, the nitrogen uptake reaches a plateau.

Systems which reveal isotherms of type II are typically obtained for macro- or non-porous materials with a continuous monolayer-multilayer formation. The point B indicates the complete coverage with the first layer after which solely multilayer formation occurs. Type III isotherms are uncommon and are observed when the adsorbate-adsorbent interaction is important.

Isotherms of type IV are characteristic for mesoporous materials. Here, the nitrogen uptake is typically limited at high relative pressures. Furthermore, a steep increase of the adsorption branch at higher relative pressures can be attributed to capillary condensation in mesopores where the pore size and form govern the isotherm shape. Additionally, a hysteresis is observed which is influenced also by the pore connectivity and occurs only at a certain pore size. A separate hysteresis classification is established, too.[88]

Type V isotherms are also uncommon but are obtained in the case of porous materials with a weak adsorbate-adsorbent interaction.

Finally, uniformly non-porous materials which possess a stepwise multilayer formation reveal isotherms of type VI.

If an isotherm reveals an unclosed hysteresis in the low relative pressure range, this may be attributed to flexibility of the porous material or pores in the molecular regime.

The determination of the surface area is based on the relation of the adsorbed volume to the thickness of mono- and multilayer formation on the pore walls. The original theory based on the kinetics of gas sorption was developed by Langmuir which, however, did not include multilayer formation. Nowadays, the BET method which was established by Brunauer, Emmett and Teller, is commonly applied.

$$\frac{p/p_0}{n_a(1-p/p_0)} = \frac{1}{n_m C} + \frac{C-1}{n_m C} p/p_0$$

(A-3)

Here, n_a is the adsorbed gas amount at p/p$_0$, n_m is the monolayer capacity and C is exponentially related to the net molar energy of adsorption (E$_1$-E$_L$)

$$C \approx \exp[(E_1 - E_L)/RT]$$

(A-4)

with E$_1$ as energy of adsorption for the first layer and E$_L$ the liquefaction energy.

A Applied methods

If the plot of the left side of equation A-3 in the range of 0.05 < p/p$_0$ < 0.3 against p/p$_0$ results in a straight line, access is provided to n_m and C. With the Avogadro constant N$_A$ and the area occupied by an adsorbate molecule a_m, the specific surface area S of the material is obtained *via* the following equation.

$$S = n_m a_m N_A$$

(A-5)

As mentioned above, the BET analysis is normally performed in the range 0.05 < p/p$_0$ < 0.3 and monolayer formation is assumed. However, for microporous materials this may vary due to the fact that different mechanisms *i.e.* micropore filling and monolayer adsorption overlap and the appropriate relative pressure range has to be chosen. Two criteria were established for the selection (1) the adsorbed N$_2$ amount has to increase with increasing p/p$_0$ and (2) the linear region has to reveal a positive intercept in order to result in a positive C value.[251] The BET method requires at least three points in the appropriate relative pressures range[88] which is restricted to p/p$_0$ < 0.12 for graphitized carbon black and many activated carbons. Furthermore, the inapplicability of the BET method is mainly valid for ultramicroporous materials (pore sizes smaller than 0.8 nm) while supermicroporous systems (pore size 0.8 nm to 2 nm) can still be analyzed.[252] The materials presented in this thesis can be count among the latter class and in principle the BET analysis can be applied in the range of linearity of the BET plot.[88] Furthermore, we attempt to determine general trends by relative comparison of different materials and we provide and discuss our results always in combination with detailed information on the gas adsorption-desorption isotherms and calculated pore volumes.[77]

Besides the surface area it is also possible to determine the pore size and pore size distribution. Regarding capillary condensation which can be described with the Young-Laplace equation, the saturation pressure above the meniscus of a condensed gas is lowered due to the curvature of the pores. Thus, the condensation occurs already at p/p$_0$ < 1 which decreases for smaller pores. The relation of the maximum radius r$_p$ where all pores are filled and the relative pressure where capillary condensation sets in, can be expressed through the modified Kelvin equation (*Eq. A-6*).

$$r_p(p/p_0) = -\frac{2\sigma V_L}{RT\ln(p/p_0)} + t(p/p_0)$$

(A-6)

Here, σ is the surface tension and V$_L$ the molar volume of the liquid condensed in the pores. The fact that before pore filling first an adsorbate film of the thickness t is formed is taken into account by the addition of the last term in equation A-6. One of

the commonly used methods was developed by Barrett, Joyner and Halenda (BJH). However, since this model is based on the Kelvin equation, it is not applicable for non-cylindrical pores and pores smaller than 2.5 nm. For smaller pores, the Kelvin equation is not valid anymore because of the increased interaction of the adsorbate and adsorbent due to the smaller pore wall distances. Here, the sorption mechanism is believed to occur without the formation of an adsorbate film but through volume filling. In the past, the semi empirical Dubinin-Radushkevich or Horvath-Kawazoe method were applied for the determination of micropore size and distribution. Yet, they are not applicable if also mesopores are present. An alternative strategy is the t-plot method where the adsorbed volume is plotted as a function of the film thickness $t(p/p_0)$. Every deviation from the point of origin is ascribed to the presence of microporosity. The further developed α_s-method uses the adsorbed amount on a non-porous reference material. A more recently developed method is based on the density functional theory (DFT) which was shown to be suitable for the determination of micro- and mesoporous materials. We chose the non-local DFT (NLDFT) method, since it describes the confined fluid better than the macroscopic purely thermodynamic BJH model.[253]

Again, it is to mention that all gas sorption results are derived from idealized theoretical models and may eventually lead to values containing errors. Here, attention is also to be paid on the fact, that the composites presented in this thesis contain species other than carbon, silica or zeolites which is, however, not covered by the methods available at present.

Nitrogen sorption measurements were accomplished with N_2 at 77 K after degassing the samples at 150 °C under vacuum for 20 hours using a Quantachrome Quadrasorb SI porosimeter. The apparent surface area was calculated by applying the BET model to the isotherm data points of the adsorption branch in the relative pressure range $p/p_0 < 0.11$ for the microporous [QuadraWin Version 5.05 User manual] and $p/p_0 < 0.3$ for the mesoporous materials. This is in accordance with the linear regions determined with the software-implemented "Micropore BET Assistant". The pore size distribution and total pore volume (meso pore volume by subtraction of the micro pore volume from the total pore volume) were calculated from N_2 sorption data using the nonlocal density functional theory (NLDFT) equilibrium model method for carbons with slit pores provided by Quantachrome data reduction software QuadraWin Version 5.05.

A Applied methods

CO$_2$ sorption measurements

The utilization of CO$_2$ instead of N$_2$ in gas sorption measurements *i.e.* CO$_2$ sorption is a further suitable method for the characterization of porous materials. The different physicochemical properties of the two gases bring along the possibility to determine porosities in different size regimes. The nitrogen sorption is suitable for the characterization of micro-, meso- and macroporous materials, yet revealing difficulties for the determination of very small micropores *i.e.* ultramicropores (pore size < 0.8 nm). This is where CO$_2$ sorption becomes important which enables also the characterization of the lower micropore regime. This is mainly due to the fact that the CO$_2$ sorption is conducted at 273 K or 298 K and ambient pressure. Therefore, the gas has a much higher thermal energy than N$_2$ at 77 K and diffusion is facilitated also in micropores. The high saturation pressure of CO$_2$ at 273 K and 1 atm restricts the pore analysis to pores smaller than 1.5 nm but also enables a simpler setup and a faster measurement compared to N$_2$ sorption. Applying the NLDFT or Grand Canonical Monte Carlo (GCMC) method gives access to the specific surface area and pore size distribution. Further information on the isosteric heat of adsorption Q$_{st}$, which represents the strength of the adsorbat-adsorbent interaction, can be obtained by CO$_2$ sorption measurements at 273 K and 283 K and application of the Clausius-Clapeyron equation

$$\ln p = -\frac{Q_{st}}{R}\frac{1}{T} + c$$

(A-7)

where p is the pressure, R the universal gas constant, T the temperature and c is a constant. This equation gives the relation between the pressure and temperature along the phase boundaries in the phase diagram. The plot of the left side of equation A-7 against 1/T gives access to Q$_{st}$. Nowadays, the determination of Q$_{st}$ in dependence on the gas loading is facilitated through software provided by the suppliers.

With respect to industrial applications, it is also useful to determine the gas selectivity of a porous material *e.g.* CO$_2$ vs. N$_2$. This can be achieved through an additional N$_2$ sorption measurement at 273 K where, compared to the measurement at 77 K, diffusion problems are supposed to be absent. The selectivity is then determined by the comparison of the gas uptake at identical temperature and pressure, which is, however, not the scope of the present thesis.

Prior to the sorption measurement, the samples were degassed at 150 °C under vacuum. The CO$_2$ sorption measurements at 273 K and 283 K were accomplished with an Autosorb 1-MP machine from Quantachrome Instruments. The isosteric heats of adsorption were calculated with the AS1 Win software provided by Quantachrome Instruments using the adsorption and desorption branch, respectively.

A Applied methods

Transmission electron microscopy (TEM)

This microscopy technique uses the wave-particle dualism of electrons to enable the imaging of object sizes down to 1 nm. This is possible since the resolution is proportional to the wavelength. Thus, electrons with a very short wavelength, which can be expressed with the de Broglie relation, can visualize structures which would not be detectable with a visible light source. Here, an electron beam is focused on a very thin prepared sample and the transmitted electrons are detected. The image results from the differing transmittance due to varying sample thickness and more important due to interaction of the electrons with the specimen such as absorption, elastic and inelastic scattering and diffraction. Thereby, sample regions appear as contrast richer areas which also depends on the electron density *e.g.* heavier elements appear darker while sample-free regions or lighter elements appear brighter. Therefore, this mode which is commonly used is also called bright-field imaging mode. At very high resolution (HRTEM) even structures on the atomic scale can be visualized. In modern microscopes it is also possible to switch to the so-called dark-field mode which is suitable for crystalline or crystalline-part containing samples which occur as bright spots due to Bragg scattering.

TEM images were obtained using a Zeiss EM 912Ω instrument.
HRTEM was accomplished on a FEI Tecnai G2n20 S-TWIN device.

Scanning electron microscopy (SEM)

This method is a further microscopy technique which utilizes an electron beam as was already described in the case of TEM. However, SEM is suitable for imaging of the sample surface topology. Here, commonly secondary electrons are detected which result from the interaction of the electron beam with the specimen. The contrast is due to varying probabilities of electrons to be released from different sample areas. Thus, SEM gives a three-dimensional image of the surface topology. In order to guarantee an efficient electron release, the samples either have to be conductive or the surface is sputtered with a metal such as gold or platinum. This technique also enables the visualization of structures on the nanometer scale.

SEM images were obtained on a LEO 1550-Gemini instrument after sputtering with platinum.

A Applied methods

Energy Dispersive X-Ray Spectroscopy (EDX)

This analytical method is suitable for the determination of the elemental composition. Here, the sample is irradiated with an electron beam which may excite electrons from inner orbitals eventually creating holes. These holes are then filled by electrons from orbitals of higher energy while X-Ray photons are released with an energy corresponding to the energy difference between the two electron states. In the emission spectrum the spikes at a distinct energy are also called characteristic lines while the broad background is the continuous Bremsstrahlung. Since the spectral lines, which notation corresponds to the shell the electron was originally released from *e.g.* K- or L-line, are characteristic for each element and the number of emitted photons can be correlated to the atom content, the EDX allows for the qualitative and quantitative elemental analysis. Commonly, the measurement is conducted with the electron source of an SEM or TEM and determines the composition on or near the surface due to the low penetration depth. However, in the case of SEM a broader sample area is detected because of the beam dissipation whereas in a TEM the sample is very thin, thus giving a higher local resolution. Additionally, through coupling EDX with a SEM enables for elemental mapping which gives information about the elemental distribution.

EDX was taken on the SEM with an EDX spectrometer.

Fourier Transform Infrared spectroscopy (FTIR)

The investigation of material properties by infrared spectroscopy is based on the absorption of specific wavelengths by molecules if they are irradiated with electromagnetic radiation (here in the mid-IR, *i.e.* the range of 4000 to 400 cm^{-1}) which frequency matches the energy required for a transition. The vibrational and vibrational-rotational transitions of a molecule, which depend on the bond strength and atom mass can be detected if the requirement of a change in dipole is fulfilled. However, IR-inactive substances can be detected with Raman spectroscopy, thus both techniques complement each other. The IR technique can be used for structural clarification but also for quantitative evaluation. Commonly, IR-spectra are shown as transmission of the radiation in dependence on the wavenumber and signals occur if the substance absorbs light due to the mentioned transitions. Within a FTIR setup, a beam of many frequencies is coupled into a Michelson interferometer which enables the generation of different sets of frequencies and generates an interferogram. The actual spectrum is obtained by data processing through applying the Fourier Transformation.Here, it has to be mentioned that the Attenuated Total Reflection (ATR) setup was employed where

an evanescent wave is used for analysis. Thus, only surface informations of a material are obtained.

FTIR was conducted with a Varian 600 FTIR spectrometer with an ATR support.

Raman spectroscopy

As mentioned in the FTIR section, Raman spectroscopy is the complementing technique. Here, a monochromatic laser is used as light source and the method is based on inelastic scattering which causes rotational and vibrational transitions of molecules or vibrational transitions of the crystal lattice. The elastic scattered photons only cause Rayleigh scattering which is, however, the dominant effect. The small portion of inelastic scattered photons possesses a higher (Anti-Stokes) or lower (Stokes) energy compared to the incident radiation and the relative frequency shift is detected. In contrast to IR, a material is Raman-active if a change in polarizability occurs.

With respect to carbon materials, a characteristic G-band between 1500 and 1600 cm^{-1} is obtained for graphitic carbon while disordered carbon reveals the so-called D-band at around 1350 cm^{-1} attributed to a breathing-mode of a six-membered carbon ring. The ratio of both bands can be used to determine the doping of carbons with heteroatoms, which commonly causes an increased D-band due to local disruption of structural order.

Raman spectra were taken with a confocal Raman microscope (Witec Alpha300R) equipped with a 532 nm laser.

X-Ray photoelectron spectroscopy (XPS)

This non-destructive technique is based on the photoelectric effect which occurs through the irradiation of matter with high-energy photons *i.e.* X-ray photons. The photons are capable to release electrons from the irradiated material which are then detected. Here, the energies of the released electrons are characteristic for each element and their number correlates to the element content. Thus, this method enables the qualitative and quantitative determination of the composition except for the elements hydrogen and helium because their orbitals are too small. However, XPS is a surface sensitive technique since the energy of the X-Ray photons (which may penetrate the sample to some microns but are recaptured or trapped within the

sample) and the mean free path are the limiting factors which results in photoelectrons from a maximal depth of around 5 to 10 nm. Therefore, the measurement needs to be carried out in ultra-high vacuum. Since the energy of the released electrons also depends on their chemical and electronic environment, XPS further reveals information of the binding states of each element through recording and deconvolution of high-resolution spectra of the respective element. In a typical spectrum, the signal intensity is plotted in dependence on the binding energy of the emitted electron calculated from its kinetic energy. In order to release electrons efficiently and to avoid charging of the sample, the material has to be conductive. Otherwise an electron flood gun is employed for charge compensation. The peak-fitting is conducted with special software and peak identification is possible with the help of experimentally determined binding-energy tables.

XPS-measurements were made with a Kratos Axis165 system using Al-K_α-radiation.

Elemental analysis (EA)

Most commonly, the quantitative determination of the elemental composition with regard to the elements nitrogen, carbon, hydrogen and sulfur is accomplished by combustion analysis. Within this technique, a sample is burned in an oxygen atmosphere and the decomposition products such as CO_2, NO, H_2O, SO_2 and N_2 are detected.
For the determination of other elements such as metals, the Inductively Coupled Plasma-Optical Emission Spectroscopy (ICP-OES) method, an atomic spectroscopy, is applied. Here, argon plasma is used to induce atom and ion emission which is characteristic for the respective element and enables for the quantitative analysis of the composition.

Elemental analysis was accomplished as combustion analysis using a Vario Micro device.
ICP OES analysis was carried out using an ICP OES Optima 2100 DV (Perkin Elmer).

A Applied methods

Thermo gravimetric Analysis (TGA) – Differential Scanning Calorimetry (DSC)

The TGA is a further combustion method which is employed to follow the decomposition of a material in either inert or oxygen atmosphere in dependence on the temperature. Thus, the stability and transitions can be detected.

The calorimetric method DSC enables for a precise investigation of state transitions by measuring the heat flow compared to a reference sample, thus revealing endothermal or exothermal reactions.

Both techniques complement each other and are therefore often used within a coupled TGA-DSC setup.

TGA was conducted with a Perkin-Elmer STA 6000 in air using a heating rate of 10 $Kmin^{-1}$.

Conductivity measurements:

The electrical conductivity σ was calculated using the following equation

$$\sigma = \frac{1}{\rho}$$

(A-8)

where ρ is the specific electrical resistance

$$\rho = R_{el} \frac{A}{l}$$

(A-9)

R_{el} is the electrical resistance, A is the cross section and l is the length of the measured sample, respectively.

The electrical resistance R_{el} was measured in a two electrode setup using a Gamry Potentiostat Reference 600 (Gamry Instruments) and Gamry EIS 300/Physical Electrochemistry software. The electrical resistance was obtained from potentiostatic impedance spectroscopy at 1-1000 Hz by applying the R-model.

A Applied methods

Electrochemistry

The cyclic voltammetry (CV) is commonly used for the investigation of electrochemical processes. Here, within a defined potential window, the current is measured in dependence on an applied potential which varies with time *i.e.* the scan rate. Thus, electrochemical reactions such as redox reactions can be identified by current changes. Furthermore, adsorption phenomena such as double layer charging are detectable which enables the determination of a capacitive behavior.

In the present thesis, the capacitance is determined within the three-electrode setup since it is suitable for both, a quantitative and qualitative evaluation of the charge storage processes. The capacitances are calculated from the CVs using the following equation

$$C = \frac{\int_{V_1}^{V_2} I(V)dV}{2mv\Delta V}$$

(A-10)

where $I(V)$ represents the instantaneous current, V_1 and V_2 are the cutoff potentials in the CV defining the potential window ΔV, m is the sample mass and v is the scan rate. The factor 2 occurs due to the fact, that the electrodes in a real device are connected in series and because of the relation $C_{total}=C_1^{-1}+C_2^{-1}+...$ the total capacitance is half in case of two equal electrodes.

It is to mention that capacitances obtained from the three-electrode setup are commonly slightly higher than in the two-electrode setup which more resembles the performance in an actual device. However, the focus is more on the qualitative investigation and trends can be determined from both methods.

Three-electrode setup: The charge storage capacity was evaluated by CV on a Gamry Potentiostat Reference 3000 using a standard half-cell three-electrode configuration. The working electrode was prepared by mixing 5 mg of the respective composite with Nafion (95 µl) and ethanol (350 µl). After sonicating the slurry for 30 min, 5 µl were coated on a glassy carbon electrode and dried for 30 min at 50 °C. A platinum wire served as counter electrode and a saturated Ag/AgCl electrode was used as reference electrode. CV was conducted in 2 M HCl electrolyte over a potential range from -0.2 to 1.1 V employing scan rates from 2 to 500 mV s^{-1}. The electrolyte was degassed with nitrogen 30 min prior to measurements. The specific capacitance was determined from the CV with Eq. A-10.

B Experimental part

B.2: Heteroatom-doped carbon materials

– Porosity control through salts as porogen

B.2.2. Eutectics – N- and N-B-co-doped carbons

Bmp-dca and Emim-tcb were purchased from Merck, Emim-dca was purchased from IoLiTec with purities of > 98%. Lithium chloride, sodium chloride, potassium chloride and zinc chloride (all 99%) were acquired from Sigma Aldrich. All chemicals were used without further purification.

The eutectic salt mixtures were freshly prepared prior to the synthesis by grinding and mixing the respective salts in the ratio required for the eutectic: lithium chloride/zinc chloride (LiZ 23 mol% lithium chloride), sodium chloride/zinc chloride (SZ 42 mol% sodium chloride) and potassium chloride/zinc chloride (PZ 51 mol% potassiuim chloride).

In a typical synthesis of the N-dCs, the carbon precursor, Bmp-dca (1 g) or Emim-dca (1 g) was thoroughly mixed with the respective eutectic salt mixture (1.5 - 15 g) prior to the calcination process. For the synthesis of N-B-dC, Emim-tcb (1 g) was used as carbon precursor and mixed with the eutectics in the same way. The resulting mixtures were placed in a ceramic crucible and heated to 1000 °C for N-dC and to 1400 °C for N-B-dC with a heating rate of 2.5 Kmin^{-1} in a Nabertherm N7/H Chamber Oven. After holding this temperature for 1 h, the samples were allowed to cool to room temperature. All steps were carried out under a constant flow of nitrogen. In order to remove the residual salt porogen, the materials were grinded and washed in water for several hours and finally filtrated and dried in vacuum.

The precursor solutions from the eutectics are named IL_XZ_r while the resulting carbons are denoted as N(-B)-dC_IL_XZ_r_T. Here, IL is the respective ionic liquid used as precursor, XZ is the eutectic made from zinc chloride (Z) with X being lithium chloride (Li), sodium chloride (S) or potassium chloride (P), r represents the mass ratio eutectic/IL in the precursor mixture and T is the synthesis temperature.

B.2.3.1. Single-salt systems

Zinc acetate dihydrate (ZnAc) and cesium acetate (CsAc) were purchased from Merck with purities of > 99 % and 99.9%, respectively. All chemicals were used without further purification.

The functional carbons were synthesized in the same way as in the case of the eutectic mixtures by mixing the ionic liquid Emim-dca (1 g) with varying amounts of ZnAc (390 - 2289 mg, notation expressed in amount CsAc) and CsAc (340 – 750 mg), respectively. For reasons of comparison, the molar ratio of acetate cation and ionic liquid was kept identical for both porogens.

The resulting mixtures were placed in a ceramic crucible and heated to 800 °C with a heating rate of 10 Kmin^{-1} in a Nabertherm N7/H Chamber Oven. After holding this temperature for 1 h the samples were allowed to cool to room temperature. All steps were carried out under a constant flow of nitrogen. In order to remove the residual salt porogen, the materials were grinded and washed in water (CsAc) or 2 M HCl (ZnAc) for several hours and finally filtrated and dried in vacuum.

Throughout this thesis, the precursor solutions from ZnAc and CsAc are named IL_YAc_r while the N-dC derived from ZnAc and CsAc are denoted as N-dC_IL_YAc_r_T. Here, IL is the respective ionic liquid used as precursor, YAc is the acetate (Ac) with Y being zinc (Zn) or cesium (Cs), r represents the mass ratio acetate/IL in the precursor mixture and T is the synthesis temperature.

B.2.3.2. Binary-salt systems

The carbon material was synthesized according to the procedure described for the single-salt system. Here, a carbon material templated with an equal molar ratio mixture of ZnAc and CsAc (ZnAcCsAc1:1) was synthesized at 800 °C by mixing Emim-dca (1 g) with the salt mixture (1 g, notation expressed in amount CsAc).

According to the previous nomenclature, the precursor solution is named Emim-dca_ZnAcCsAc1:1_1 while the N-doped carbon is denoted as N-dC_Emim-dca_ZnAcCsAc1:1_1_800.

B Experimental part

B.2.4. Eutectics - low-temperature N-doped carbons

The materials were named and synthesized according to B.2.2. but at 450 °C.

B.2.5. Synthesis of N-S-co-doped carbons

The ionic liquid Emim-scn was purchased from IoLiTec with a purity of > 98% and used without further purification.

For the synthesis of the N-S-co-doped carbons (N-S-dC), a 2:1 weight ratio mixtures of Emim-scn (666 mg) with Emim-dca (333 mg) and Bmp-dca (333 mg), respectively, were placed in a ceramic crucible and heated to 800 °C with a heating rate of 2 Kmin^{-1} in a Nabertherm N7/H Chamber Oven. After holding this temperature for 1 h, the samples were allowed to cool to room temperature. All steps were carried out under a constant flow of nitrogen.

B.3. Composite materials – template-free

B.3.2. One-pot template-free synthesis of metal nitride nanoparticles in N-doped carbon

In a typical synthesis, Bmp-dca (1 g) was mixed with $TiCl_4$, $VOCl_3$, or a prepared mixture of $VOCl_3/TiCl_4$ (50-250 mg), respectively. The ternary compound was produced with a weight ratio of $VOCl_3/TiCl_4$ of 0.43 in the starting solution. The metal precursors were thoroughly mixed prior to the addition to the IL. The resulting solutions were placed in a ceramic crucible and heated to 1000 °C with a heating rate of 10 K min^{-1} in a Nabertherm N7/H Chamber Oven. After holding this temperature for 1 h, the samples were allowed to cool to room temperature. All steps were carried out under a flow of nitrogen.

The precursor mixtures are named IL_M_m while the resulting composites consisting of TiN, VN, or TiVN nanoparticles within a N-doped carbon matrix are named, TiN@N-dC_IL_M_m_T, VN@N-dC_IL_M_m_T, TiVN@N-dC_IL_M_m_T, respectively. Here, M denotes the metal precursor species and m the mass ratio metal precursor/IL.

B.4. Composite materials – salt templated

B.4.2. Single-salt systems

In a typical synthesis of the salt templated composites, Emim-dca (1 g) was first mixed with $VOCl_3$, $TiCl_4$, a prepared mixture of $VOCl_3/TiCl_4$ (50 mg or 200 mg) or NH_4VO_3 (35 mg or 135 mg) followed by the addition of CsAc (0 – 1000 mg) or ZnAc (0 - 1144 mg, notation expressed in amount CsAc). For reasons of comparison, the molar ratio of acetate cation and ionic liquid was kept identical for both porogens. The ternary compound was produced with a weight ratio of $VOCl_3/TiCl_4$ of 0.43. The N-doped carbon was produced by mixing Emim-dca (1 g) with CsAc (340 mg). All precursors were thoroughly mixed by gentle heating prior to the calcination process.

The resulting solutions were placed in a ceramic crucible and heated to 800 °C with a heating rate of 10 $Kmin^{-1}$ in a Nabertherm N7/H Chamber Oven. After holding this temperature for 1 h the samples were allowed to cool to room temperature. All steps were carried out under a flow of nitrogen. In order to remove the residual porogen, the materials were grinded and washed in water for several hours and finally filtrated and dried in vacuum.

The precursor mixtures are named IL_YAc_r_M_m while the resulting composites are denoted as MN@N-dC_IL_YAc_r_M_m_T where IL is the respective ionic liquid used as precursor, YAc is the acetate (Ac) with Y being zinc (Zn) or cesium (Cs), r represents the mass ratio salt/IL in the precursor mixture, M the metal precursor species, m the mass ratio metal precursor/IL and T the synthesis temperature.

B.4.3. Binary-salt systems

The composite was synthesized according to the procedure described above for the single-salt system. Here, a composite templated with an equal molar ratio of CsAc and ZnAc (ZnAcCsAc1:1) was synthesized at 800 °C by mixing Emim-dca (1 g) with NH_4VO_3 (35 mg) and the salt mixture (1 g). The precursor solution is named Emim-dca_ZnAcCsAc1:1_1_NH$_4$VO$_3$_0.035 while the N-dC is named VN@N-dC_Emim-dca_ZnAcCsAc1:1_1_NH$_4$VO$_3$_0.035_800.

B Experimental part

B.4.4. Application as electrodes for supercapacitors

Materials tested as supercapacitor electrodes, see *B.4.2. single-salt systems*.

Composites – eutectic mixtures

The composites were synthesized according to the procedure described above for the single-salt system but employing the eutectic mixtures from *B.2.2.*. Here, Emim-dca (1 g) was first mixed with NH_4VO_3 (35 mg) followed by the addition of the respective eutectic mixture LiZ, SZ or PZ (eq. 0.34 g CsAc, eq. 1 g CsAc, 3 g). For reasons of comparison with the composites from CsAc as well as the pure carbons from the eutectics, the total molar ratio of the eutectics and ionic liquid of the two lower porogen amounts equal 0.34 g and 1 g CsAc, respectively (see *B.4.2.*). The highest porogen amount of 3 g eutectic mixture equals the amount used for the pure carbons (see *B.2.2.*). The notation for the two lower porogen amounts is expressed with r=eq.0.34 or eq.1 (equals 0.34 or 1 g CsAc) while for r=3 g the notation is expressed as amount porogen actually used in the synthesis.

The remaining steps were carried out following the procedures from *B.4.2.*.

C Supplementary information

C.2. Heteroatom-doped carbon materials – Porosity control through salts as porogen

C.2.2. Eutectics – N- and N-B-co-doped carbons
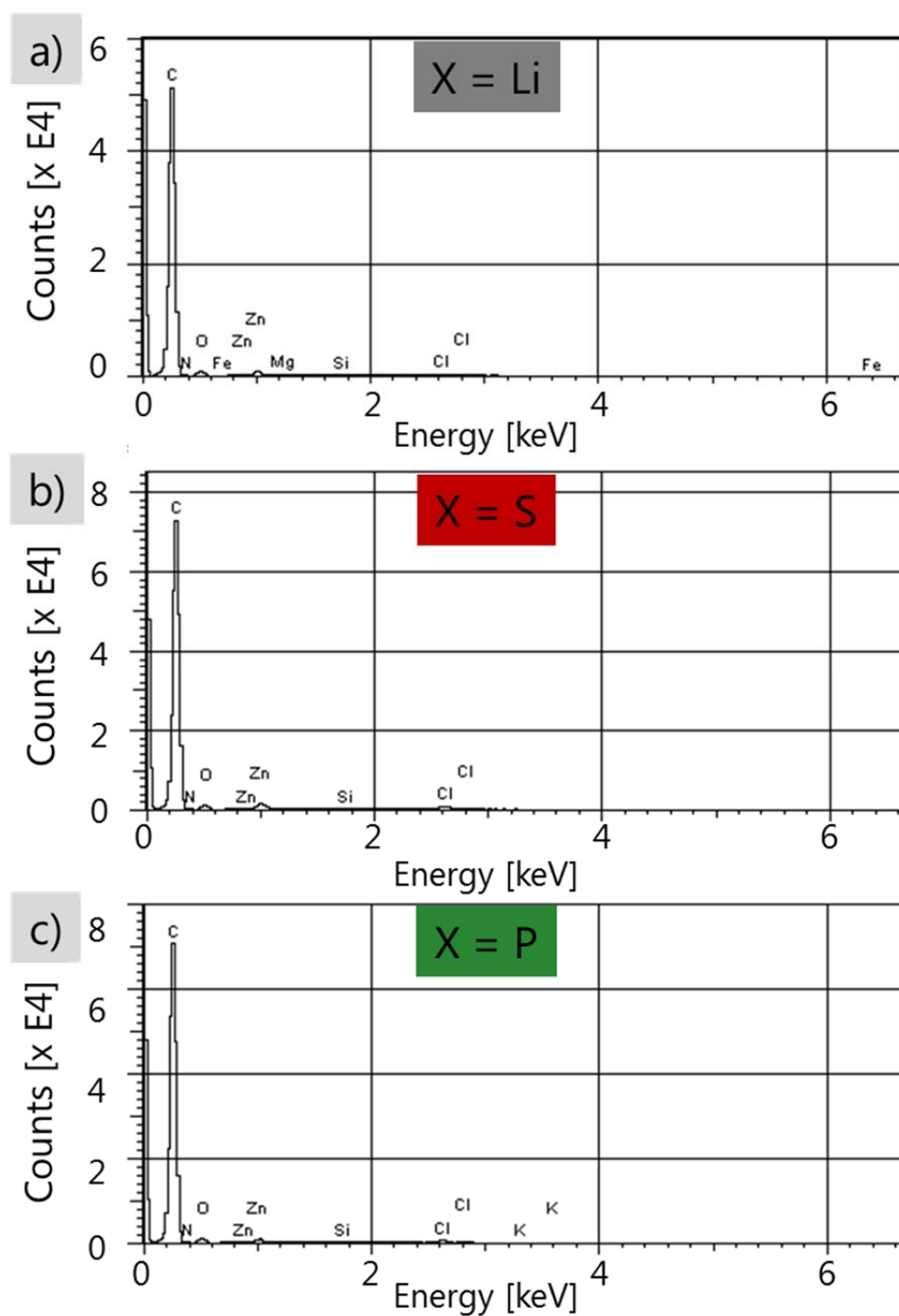
Figure C-1. EDX spectra of N-dC_Bmp-dca_XZ_3_1000 with X=Li (**a**), S (**b**) and P (**c**).
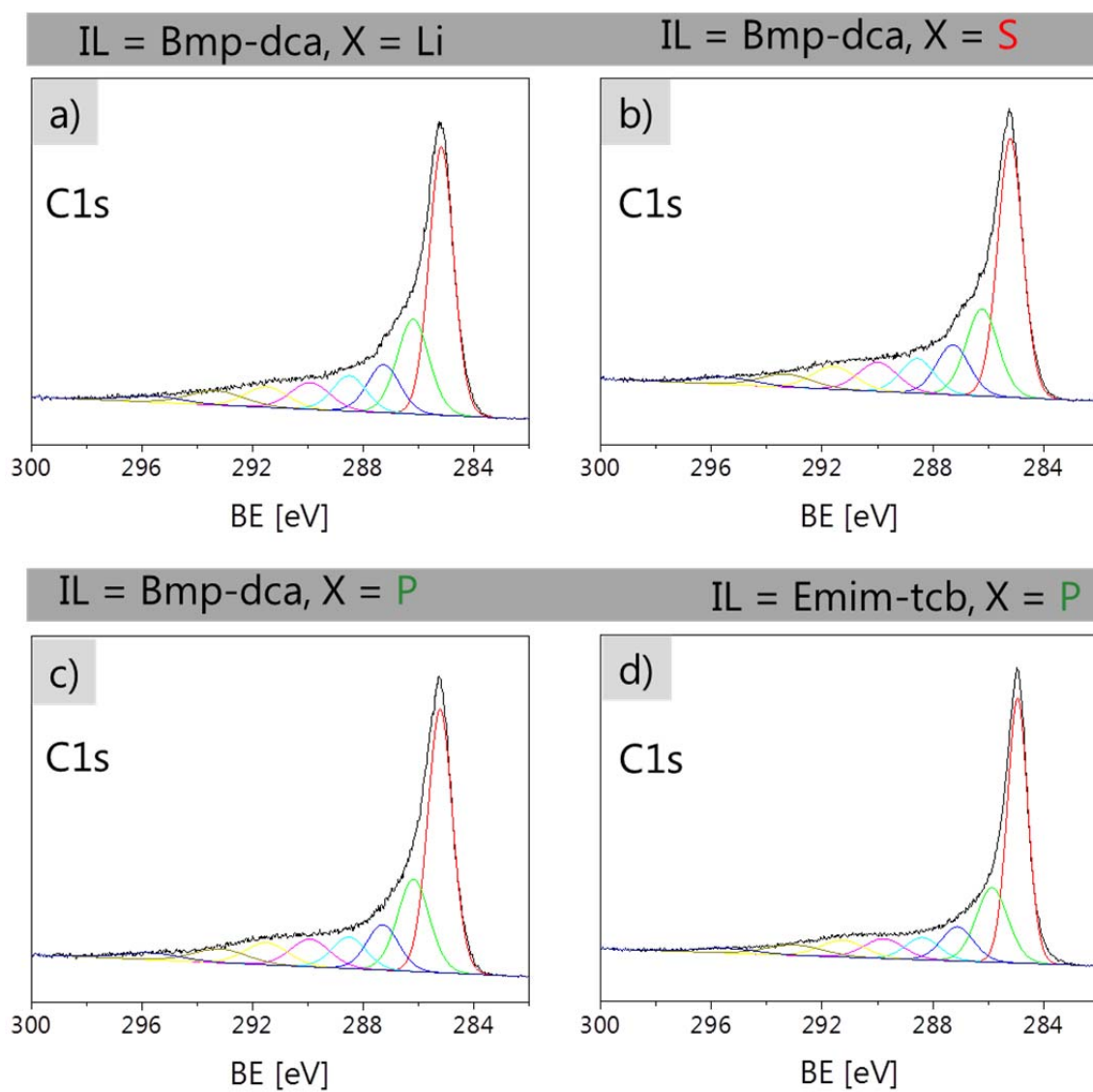
Figure C-2 XPS spectra: C1s deconvoluted peaks of N-dC_Bmp-dca_XZ_3_1000 with X=Li (**a**), S (**b**) and P (**c**) and N-dC_Emim-tcb_PZ_3_1400 (**d**).

C.3. Composite materials – template-free

C.3.2. One-pot template-free synthesis of metal nitride nanoparticles in N-doped carbon
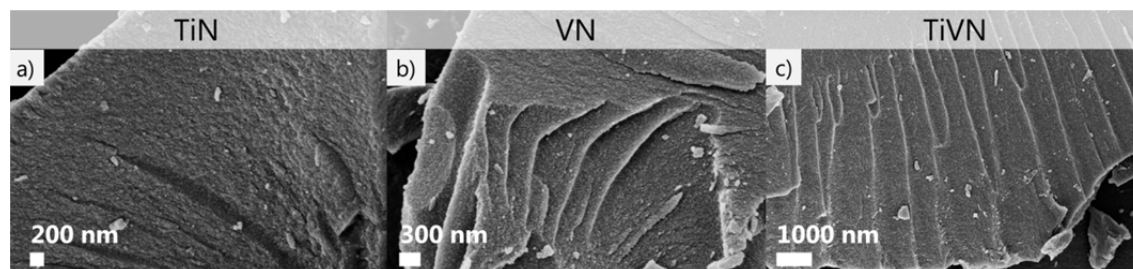
Figure C-3 SEM images of **a)** TiN@N-dC_Bmp-dca_TiCl$_4$_0.2_1000, **b)** VN@N-dC_Bmp-dca_TiCl$_4$_0.2_1000 and **c)** TiVN@N-dC_Bmp-dca_VOCl$_3$-TiCl$_4$0.43_0.2_1000.
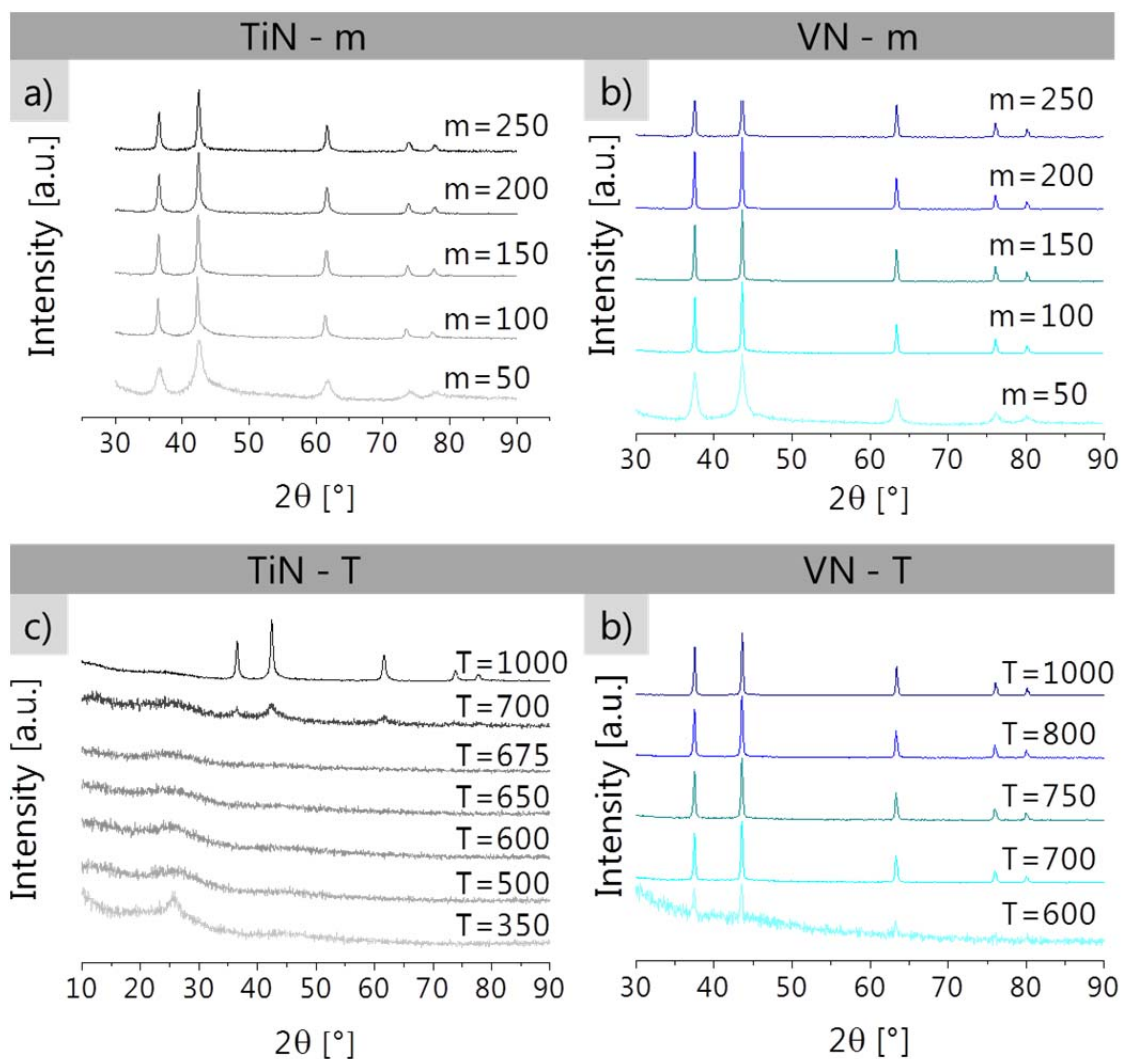
Figure C-4 WAXS patterns of TiN@N-dC_Emim-dca_TiCl$_4$_m_T (**a, c**) and VN@N-dC_Emim-dca_VOCl$_3$_m_T (**b, d**) in dependence on the metal precursor concentration m and synthesis temperature T, respectively.
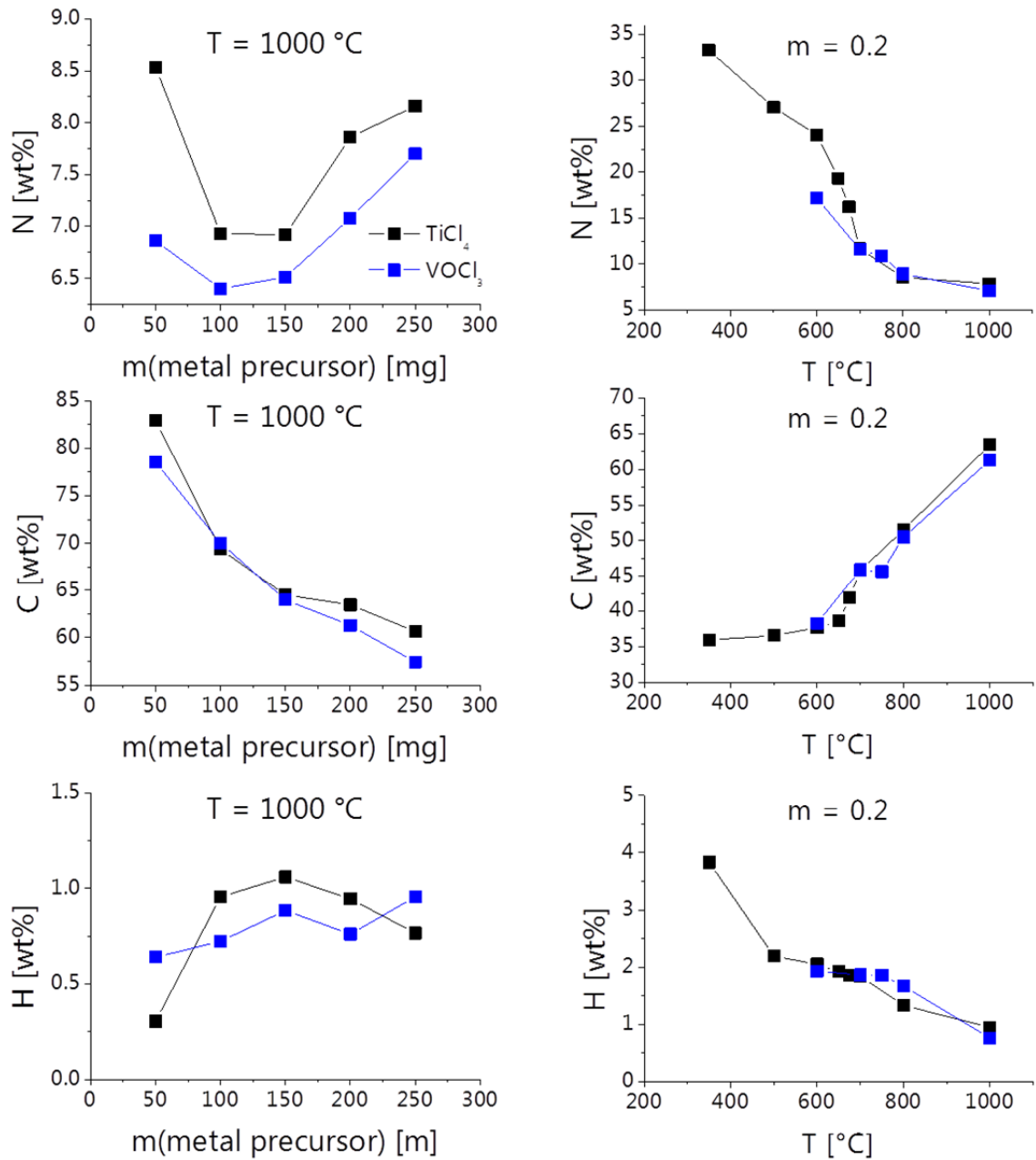
Figure C-5 Course of elemental composition of TiN@N-dC_Emim-dca_TiCl$_4$_m_T (black) and VN@N-dC_Emim-dca_VOCl$_3$_m_T (blue) at different metal precursor concentrations m with T=1000 (**left**) and at different reaction temperatures T produced with m=0.2 (**right**).
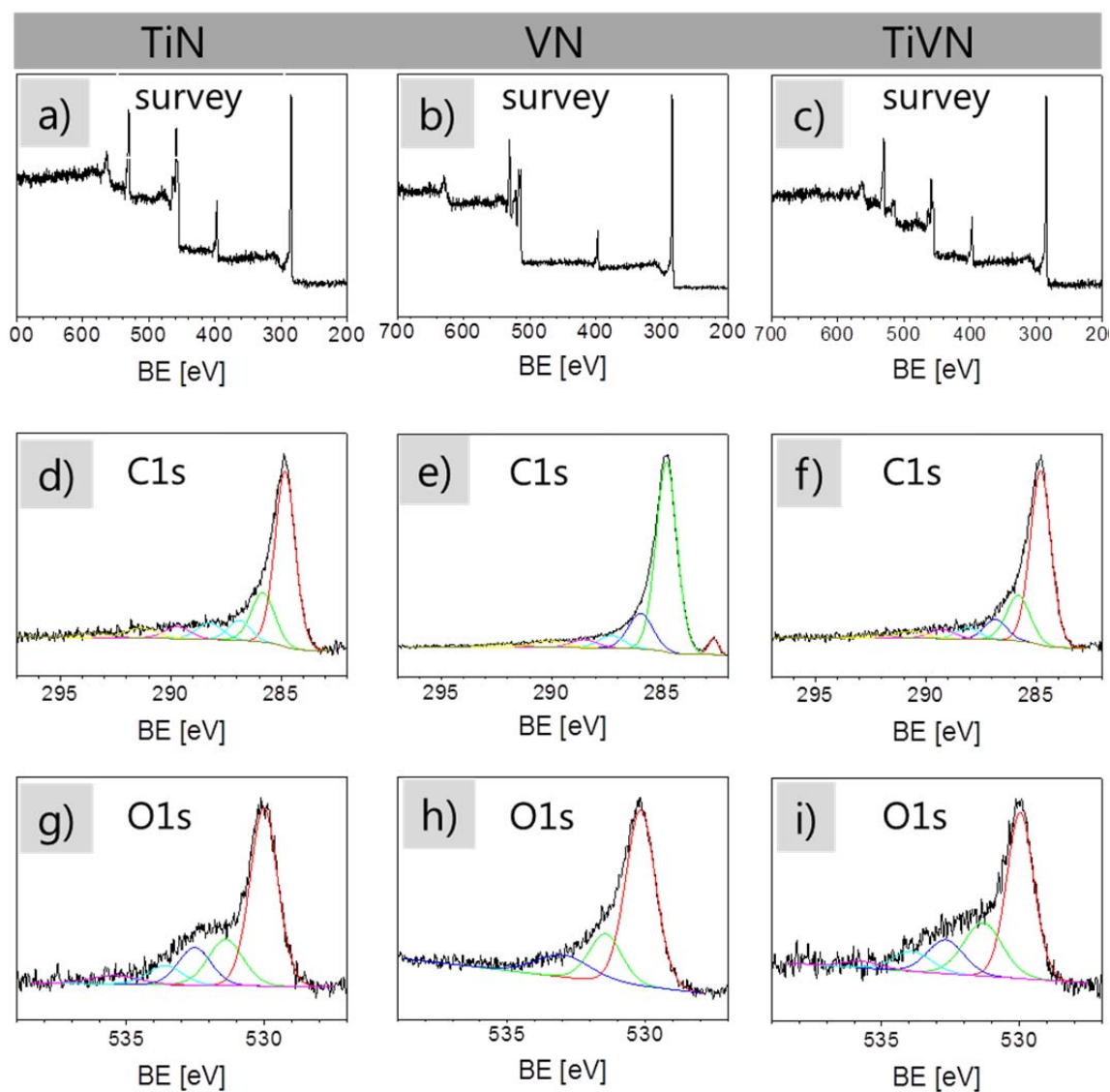
Figure C-6 XPS-spectra: survey (**a, b c**), C1s (**d, e, f**) and O1s (**g, h, i**) orbitals of TiN@N-dC_Bmp-dca_TiCl$_4$_0.2_1000 (left), VN@N-dC_Bmp-dca_VOCl$_3$_0.2_1000 (middle), and TiVN@N-dC_Bmp-dca_VOCl$_3$-TiCl$_4$0.43_0.2_1000 (right).
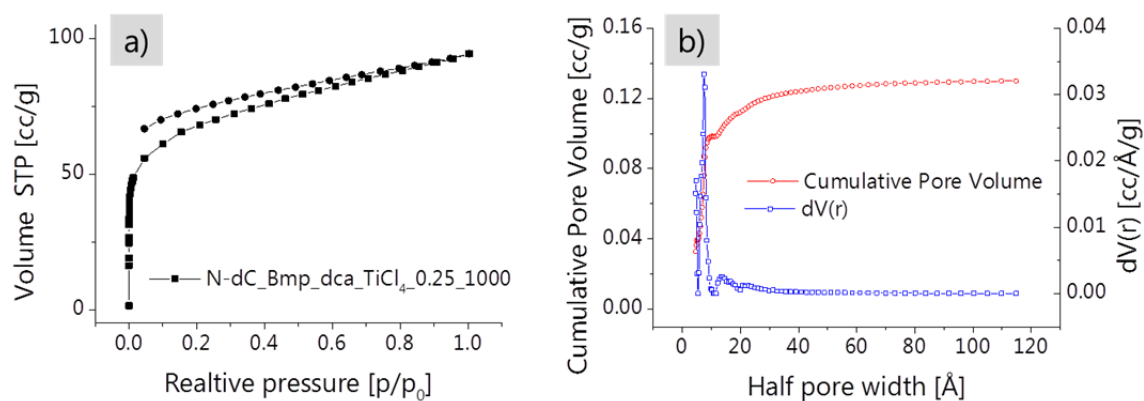
Figure C-7 Nitrogen sorption micropore isotherm (**a**) and PSD (**b**) analysis of N-dC-Bmp-dca_TiCl$_4$_0.25_1000.

C.4. Composite materials – salt templated

C.4.2. Single-salt systems
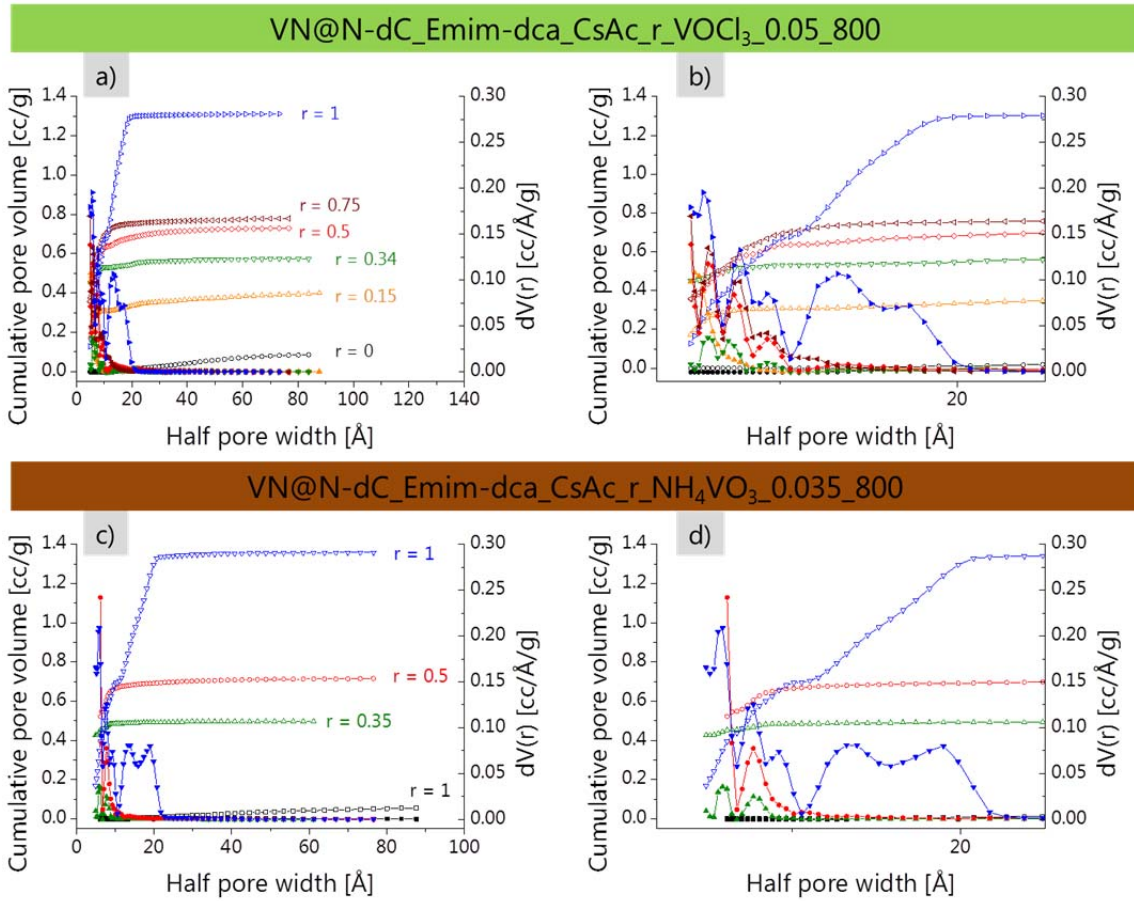
Figure C-8 PSDs of VN@N-dC_Emim-dca_CsAc_r_VOCl₃_0.05_800 (**a, b**) and VN@N-dC_Emim-dca_CsAc_r_NH₄VO₃_0.035_800 (**c, d**).
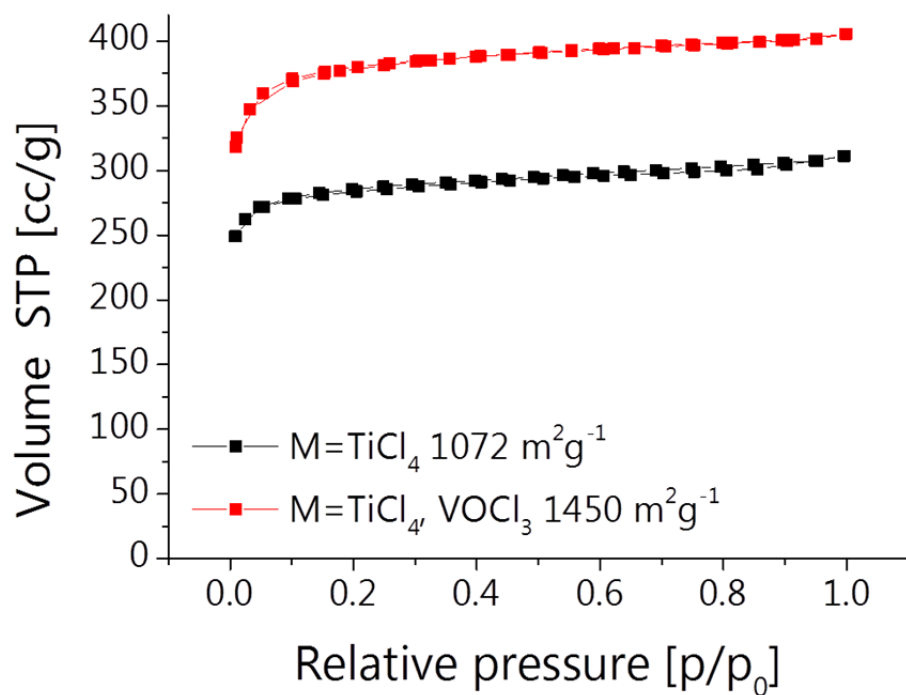
Figure C-9 Nitrogen sorption isotherms of TiN@N-dC_Emim-dca_CsAc_0.34_TiCl$_4$_0.05_800 (black) and TiVN@N-dC_Emim-dca_CsAc_0.34_VOCl$_3$-TiCl$_4$0.43_ 800 (red).
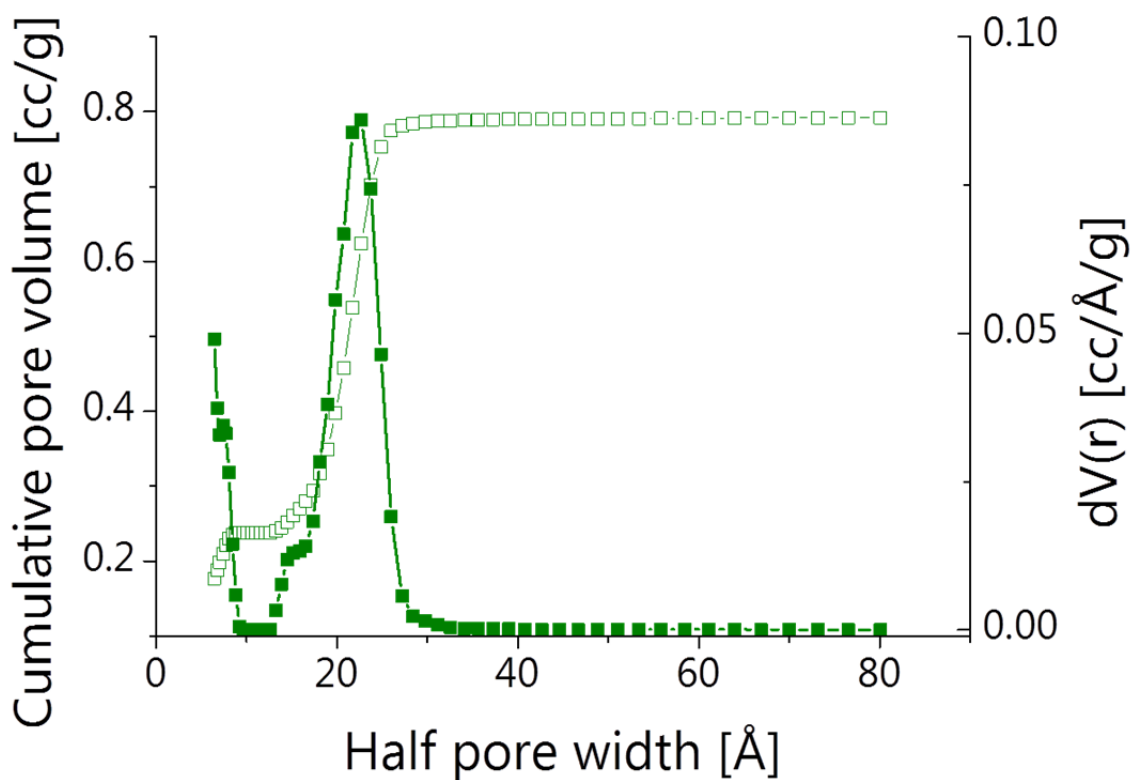
Figure C-10 PSD of VN@N-dC_Emim-dca_ZnAc_1_NH$_4$VO$_3$_0.035_800.
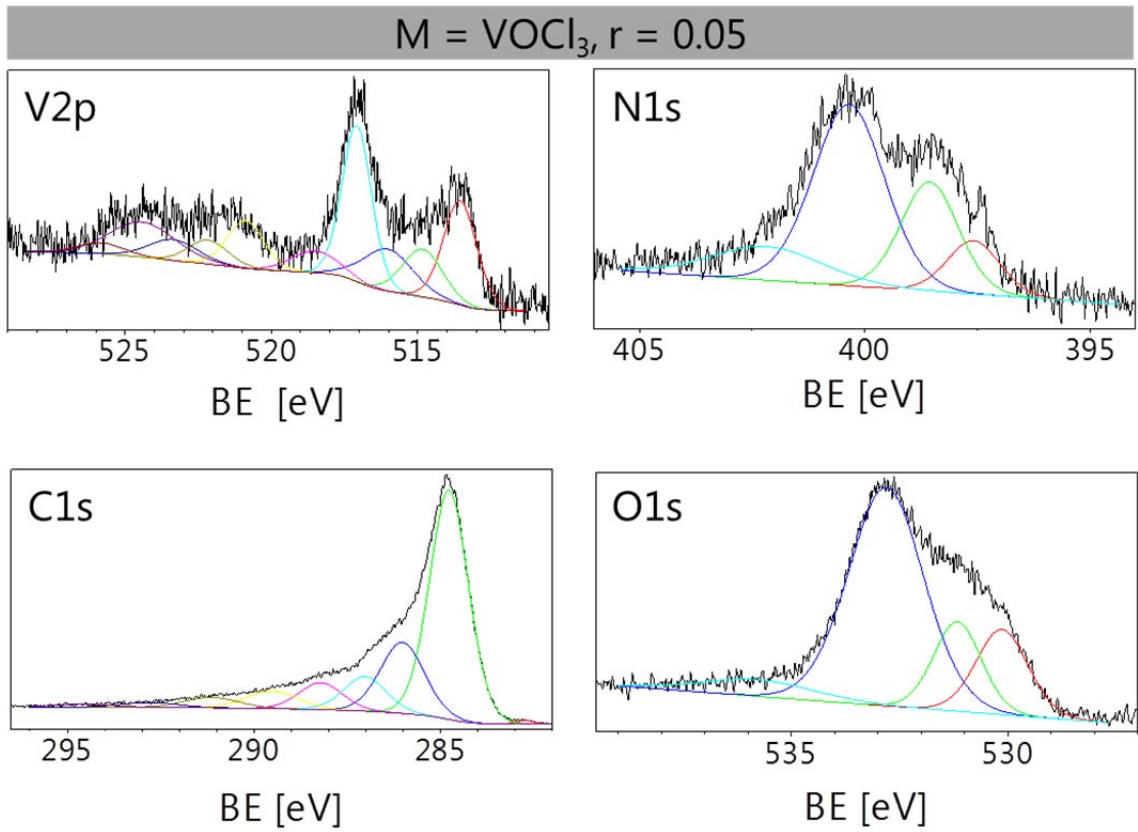
Figure C-11 XPS spectra: V2p, N1s, C1s and O1s deconvoluted peaks of VN@N-dC_Emim-dca_CsAc_0.34_VOCl$_3$_0.05_800.
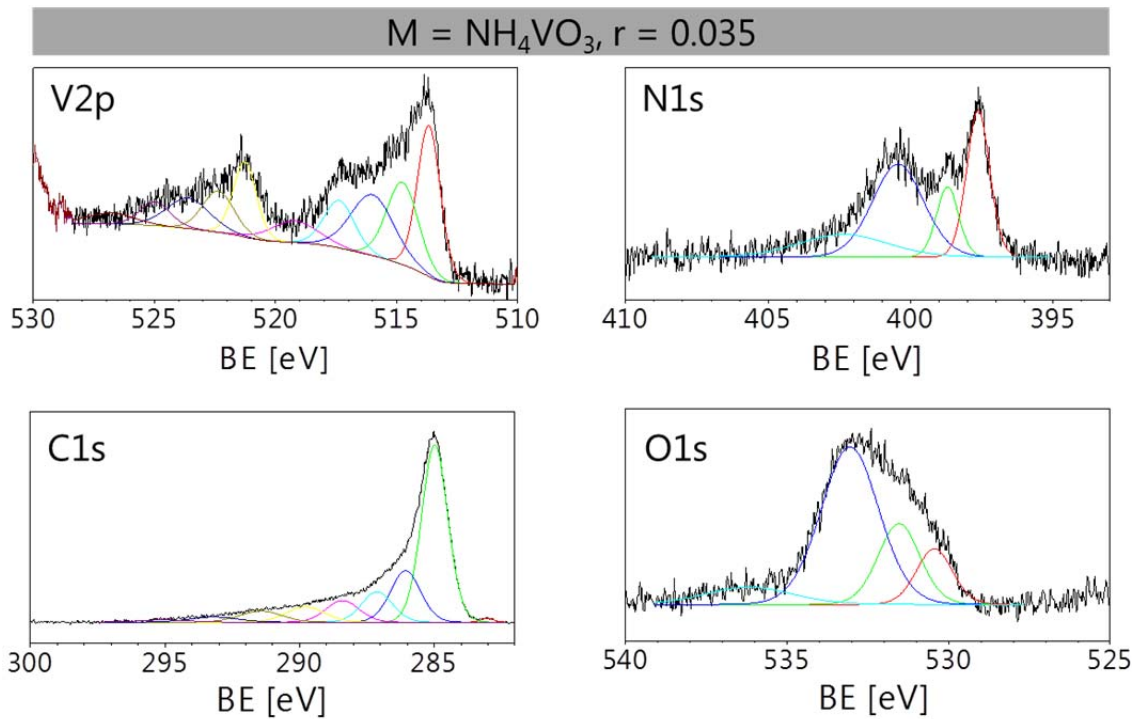
Figure C-12 XPS spectra: V2p, N1s, C1s and O1s deconvoluted peaks of VN@N-dC_Emim-dca_CsAc_0.34_NH$_4$VO$_3$_0.035_800.

Table C-a Composition of VN@N-dC_Emim-dca_CsAc_r_VOCl₃_0.05_800 (light blue), VN@N-dC_Emim-dca_CsAc_0.34_NH₄VO₃_0.035_800 (green) and VN@N-dC_Emim-dca_ZnAc_1_NH₄VO₃_0.035_800 (dark blue) from ICP-OES and XPS.

Salt	Element					
[mg]	Elemental analysis				ICP OES	
	N	C	H	O	Cs	V
0	12.3	68.7	1.0	-	-	7.0
150	7.6	70	1.8	-	-	-
340	7.6	68.6	1.6	-	-	5.6
340 XPS	7.5	73.5	-	12	0.8	6.3
340	6.7	61.0		-	2.3	6.7
340 XPS	6.6	72.7	-	7.8	3.0	10.0
500	6.0	65.4	2.8	-	-	-
750	7.0	60.1	1.1	-	-	-
1000	11.2	61.6	0.9	-	-	7.8
1000						6.2
1000 XPS	7.0	82.9	-	6.9	-	3.2
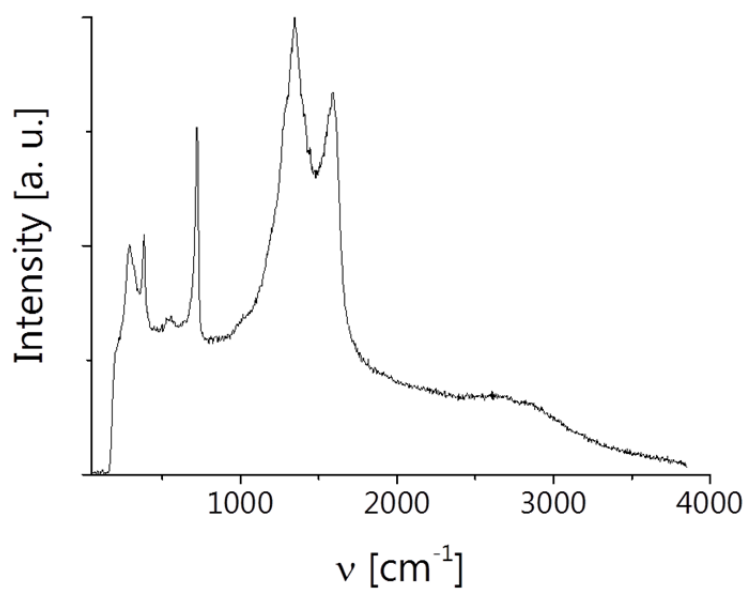
Figure C-13 Raman spectrum of VN@N-dC_Emim-dca_CsAc_0.34_VOCl$_3$_0.05_800.

Table C-b Conductivity of the composites VN@N-dC_Emim-dca_CsAc_r_VOCl$_3$_m_800.

Material	σ [Sm^{-1}][i]
VN@N-dC_Emim-dca_CsAc_**0.34**_VOCl$_3$_0.05_800	131
VN@N-dC_Emim-dca_CsAc_**0.5**_VOCl$_3$_0.05_800	7
VN@N-dC_Emim-dca_CsAc_**1**_VOCl$_3$_0.05_800	17
VN@N-dC_Emim-dca_CsAc_0.34_VOCl$_3$_**0.2**_800	19

i Within this setup, graphite was measured as reference (2989 Sm^{-1}).

C.4.4. Application as electrodes for supercapacitors
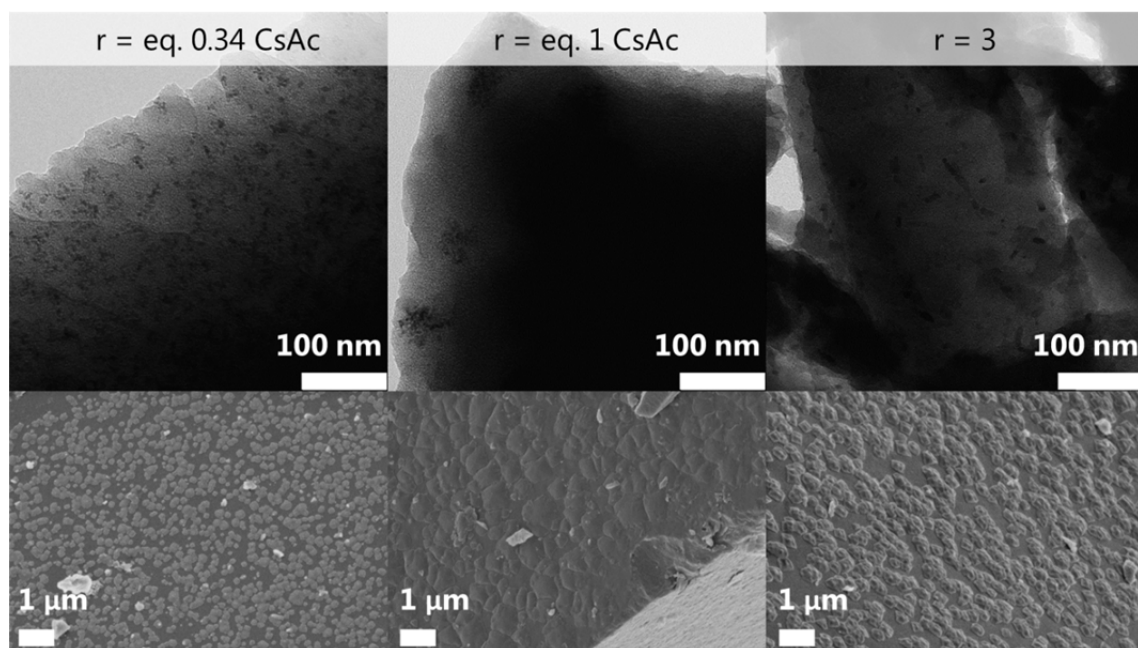
Figure C-14 SEM images of VN@N-dC_Emim-dca_LiZ_r_NH$_4$VO$_3$_0.035_800 at varying porogen amounts r.
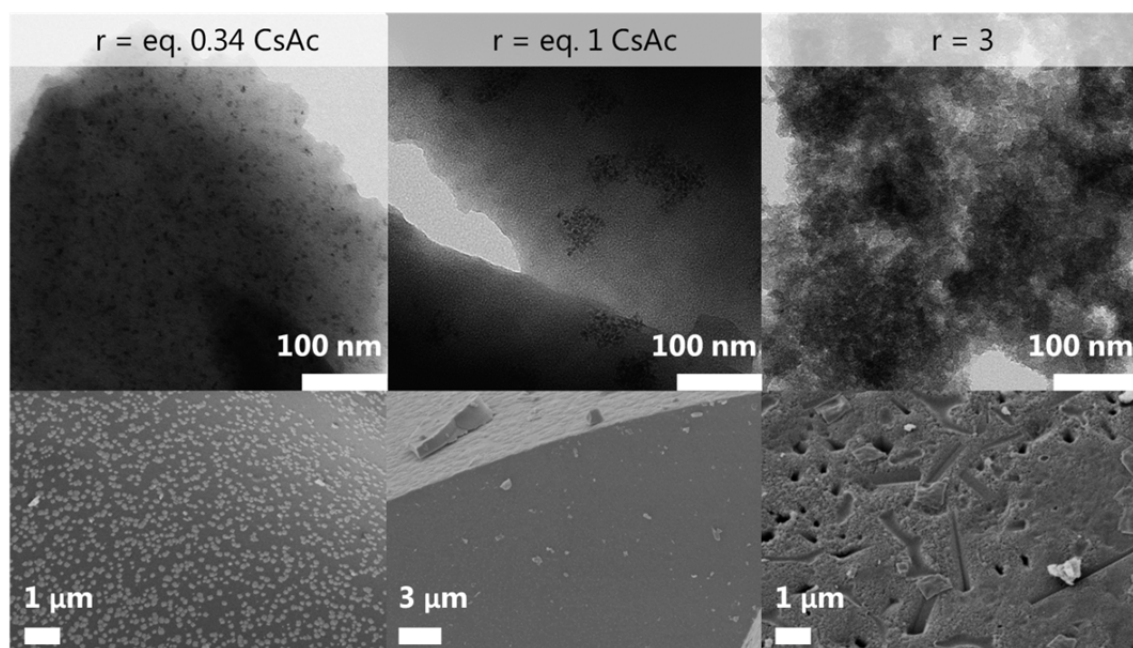
Figure C-15 SEM images of VN@N-dC_Emim-dca_SZ_r_NH$_4$VO$_3$_0.035_800 at varying porogen amounts r.
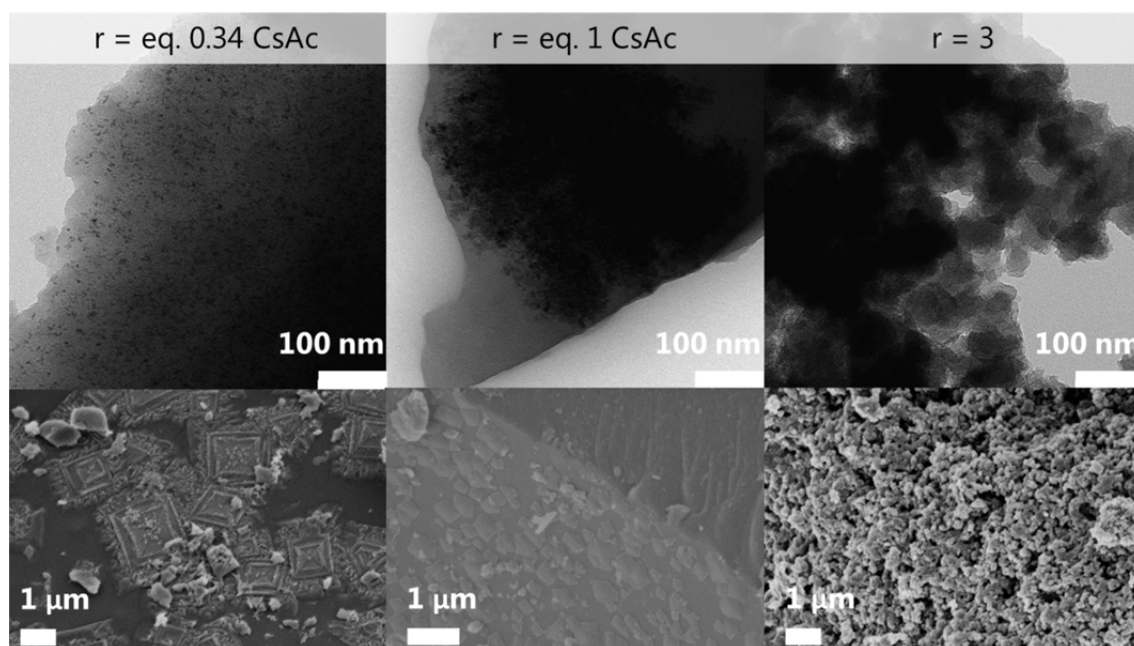
Figure C-16 SEM images of VN@N-dC_Emim-dca_PZ_r_NH$_4$VO$_3$_0.035_800 at varying porogen amounts r.
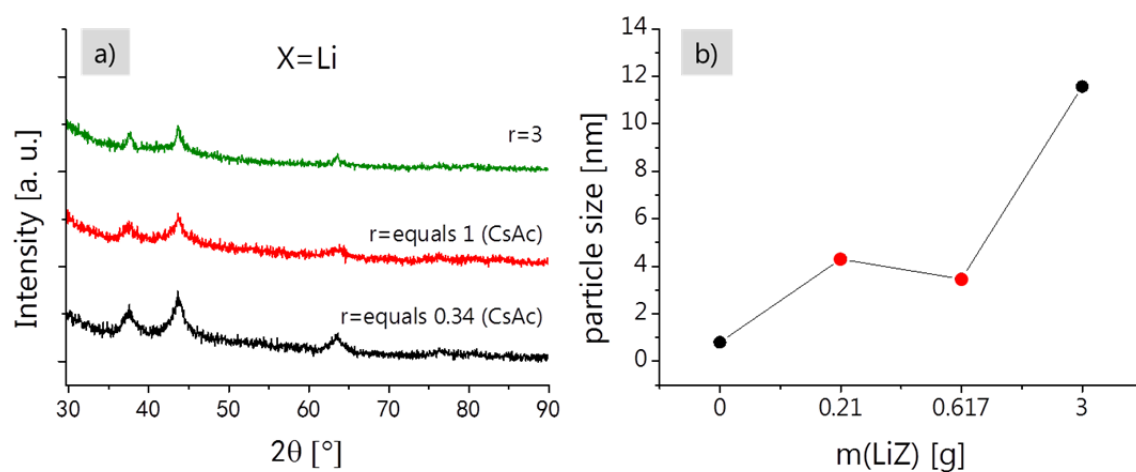
Figure C-17 a) WAXS patterns and **b)** particle size of VN@N-dC_Emim-dca_LiZ_r_NH$_4$VO$_3$_0.035_800 at varying porogen amounts r. Red marked points in b) correspond to porogen amounts which equal to 0.34 g and 1 g CsAc.

Figure C-18 a) WAXS patterns and **b)** particle size of VN@N-dC_Emim-dca_SZ_r_NH$_4$VO$_3$_0.035_800 at varying porogen amounts r. Red marked points in b) correspond to porogen amounts which equal to 0.34 g and 1 g CsAc.
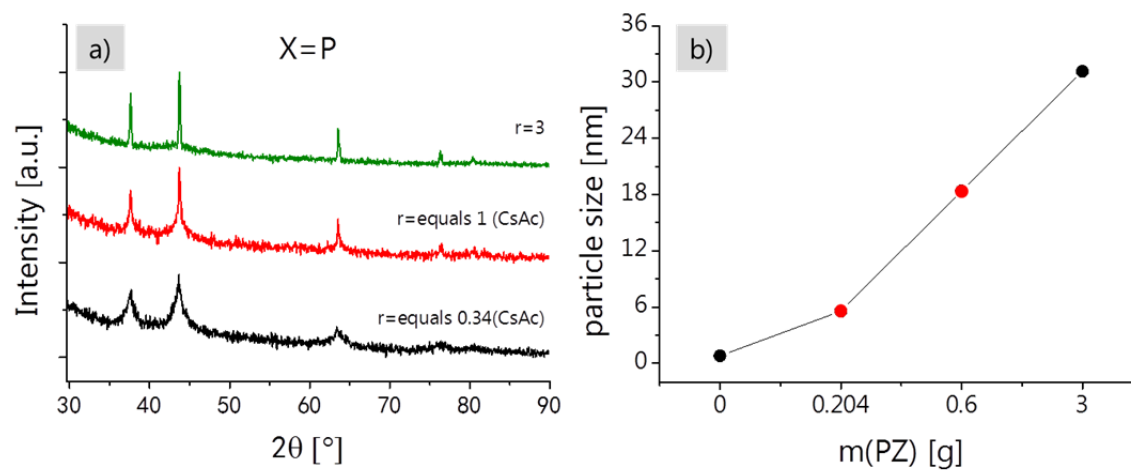
Figure C-19 a) WAXS patterns and **b)** particle size of VN@N-dC_Emim-dca_PZ_r_NH$_4$VO$_3$_0.035_800 at varying porogen amounts r. Red marked points in b) correspond to porogen amounts which equal to 0.34 g and 1 g CsAc.

C Supplementary information

Table C-c Composition of VN@N-dC_Emim-dca_XZ_3_NH$_4$VO$_3$_0.035_800 obtained from combustion elemental analysis.

Porogen type X	N [wt%]	C [wt%]	H [wt%]
Without salt	12.3	68.7	1.0
Li	10.7	64.3	2.6
S	9.8	65.3	2.6
P	12.3	60.6	3.1

Table C-d Nitrogen sorption data of VN@N-dC_Emim-dca_XZ_r_NH$_4$VO$_3$_0.035_800.

Porogen type X	Porogen amount r [g]	S$_{BET}$ [m^{2}g^{-1}]	Pore volume [mlg^{-1}]
Li	Eq. 0.34 g CsAc	0	0.04
	Eq. 1 g CsAc	0	0.02
	3	837	0.36
S	Eq. 0.34 g CsAc	82	0.07
	Eq. 1 g CsAc	514	0.22
	3	1592	1.12
P	Eq. 0.34 g CsAc	448	0.22
	Eq. 1 g CsAc	1110	0.47
	3	1491	0.91
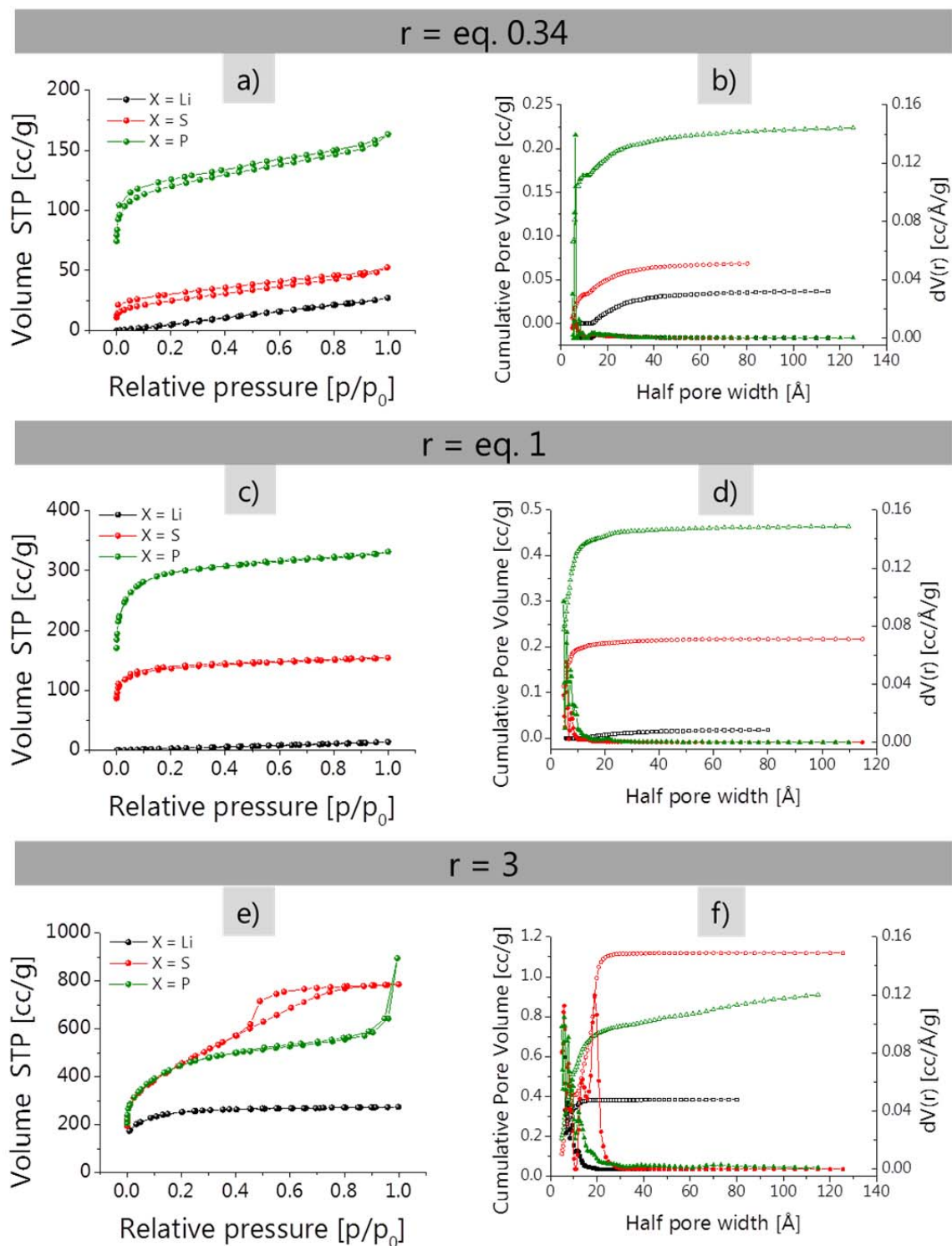
Figure C-20 Nitrogen sorption isotherms (**a, c, e**) and PSDs (**b, d, f**) of VN@N-dC_Emim-dca_XZ_r_NH$_4$VO$_3$_0.035_800 for X=Li, S and P at varying porogen amounts r.

D List of abbreviations

Abbreviation	Explanation
BET	Brunauer-Emmet-Teller
Bmp-dca	1-Butyl-3-methyl-pyridinium dicyanamide
CsAc	Cesium acetate
CV	Cyclic voltammogram
EA	Elemental analysis
EC	Electrochemical capacitors
EDLC	Electrical double layer capacitors
EDX	Energy dispersive X-ray spectroscopy
Emim-dca	1-Ethyl-3-methyl-imidazolium dicyanamide
Emim-scn	1-Ethyl-3-methyl thiocyanate
Emim-tcb	1-Ethyl-3-methyl-imidazolium tetracyanoborate
FT-IR	Fourier transform infrared spectroscopy
HRTEM	High resolution transmission electron microscopy
IL	Ionic liquid
LiZ	Eutectic mixture lithium chloride/zinc chloride (23 mol% LiCl)
MN	Metal nitride
N-B-dC	Nitrogen-boron-co-doped carbon
N-dC	Nitrogen-doped carbon
NLDFT	Nonlocal density functional theory
N-S-dC	Nitrogen-sulfur-co-doped carbon
OER	Oxygen evolution reaction
ORR	Oxygen reduction reaction
PZ	Eutectic mixture potassium chloride/zinc chloride (51 mol% KCl)
SAED	Selected area electron diffraction
SEM	Scanning electron microscopy
SZ	Eutectic mixture sodium chloride/zinc chloride (42 mol% NaCl)
TEM	Transmission electron microscopy
TGA	Thermo gravimetric analysis
WAXS	Wide angle X-ray scattering
XPS	X-ray photoelectron spectroscopy
ZnAc	Zinc acetate dihydrate

E List of publications

Publications

Fechler, N.; Fellinger, T.-P.; Antonietti, M., "Salt Templating": A Simple and Sustainable Pathway toward Highly Porous Functional Carbons from Ionic Liquids, *Advanced Materials* **2012**, *10.1002/adma.201203422*.

Fechler, N.; Fellinger, T.-P.; Antonietti, M., Template-Free One-Pot Synthesis of Porous Binary and Ternary Metal Nitride@N-Doped Carbon Composites from Ionic Liquids, *Chemistry of Materials* **2012**, *24*, 713.

Schmidt, B. V. K. J.; Fechler, N.; Falkenhagen, J.; Lutz, J.-F., Controlled Folding of Synthetic Polymer Chains Through the Formation of Positionable Covalent Bridges, *Nature Chemistry* **2011**, *3*, 234.

Fechler, N.; Badi, N.; Schade, K.; Pfeifer, S.; Lutz, J.-F.; Thermogelation of PEG-Based Macromolecules of Controlled Architecture, *Macromolecules* **2009**, *42*, 33.

Presentations

Poster

GRS and GRC Green Chemistry 2012, Lucca (Barga), Italy
"Salts as New Environmentally Benign Templates: Toward Sustainable Micro- and Mesoporous Materials and Their Application in Energy Storage"

GRC Chemistry of Supramolecules & Assemblies 2011, Lucca (Barga), Italy
"Assembly of Metal Nitride Nano particles on Porous Carbon Materials as an Electrocatalytic System for Oxygen Reduction Reaction"

Hybrid Materials 2011, Strasbourg, France
"Composites of Porous Carbon Materials and Metal Nitrides as Electrocatalysts for Oxygen Reduction Reaction"

Oral

MRS Spring Meeting 2012, San Francisco, USA
"Ionic Liquids - Precursors for MN@N-Doped Carbon Composites"

F Acknowledgements

"Imagination is more important than knowledge. For knowledge is limited, whereas imagination embraces the entire world, stimulating progress, giving birth to evolution."

Albert Einstein

G Declaration

Hiermit erkläre ich, dass ich die vorliegende Arbeit selbstständig angefertigt und keine anderen als die angegebenen Hilfsmittel und Quellen verwendet habe.

Nina Fechler

Potsdam, 28.11.2012

Die vorliegende Dissertation entstand in der Zeit von September 2010 bis November 2012 am Max-Planck Institut für Kolloid- und Grenzflächenforschung in Potsdam-Golm unter der Betreuung von Prof. Dr. Markus Antonietti.

H References

[1]   R. P. Feynman, *Engineering and Science* **1960**, 23.

[2]   U. S. E. P. A. U. S. EPA, Washingtion DC **2007**.

[3]   T. Rachel, Bundesministerium für Bildung und Forschung, Berlin **2007**.

[4]   A. Hullmann, European Commission, Brüssel **2006**.

[5]   K. Müllen, M. Antonietti, *Macromolecular Chemistry and Physics* **2012**, 213, 999.

[6]   F. Guo, R. Hurt, *Macromolecular Chemistry and Physics* **2012**, 213, 1164.

[7]   A.-H. Lu, G.-P. Hao, Q. Sun, X.-Q. Zhang, W.-C. Li, *Macromolecular Chemistry and Physics* **2012**, 213, 1107.

[8]   Y. Shao, J. Sui, G. Yin, Y. Gao, *Applied Catalysis B: Environmental* **2008**, 79, 89.

[9]   A. Morozan, B. Jousselme, S. Palacin, *Energy & Environmental Science* **2011**, 4, 1238.

[10]   D. S. Su, G. Sun, *Angewandte Chemie International Edition* **2011**, 11570.

[11]   L. Dai, D. W. Chang, J.-B. Baek, W. Lu, *Small* **2012**, 8, 1130.

[12]   Y. Li, Z.-Y. Fu, B.-L. Su, *Advanced Functional Materials* **2012**, 4634.

[13]   H. Nishihara, T. Kyotani, *Advanced Materials* **2012**, 24, 4466.

[14]   N.-S. Choi, Z. Chen, S. A. Freunberger, X. Ji, Y.-K. Sun, K. Amine, G. Yushin, L. F. Nazar, J. Cho, P. G. Bruce, *Angewandte Chemie* **2012**, 10134.

[15]   A. Ghosh, Y. H. Lee, *ChemSusChem* **2012**, 5, 480.

[16]   S. H. Lim, H. I. Elim, X. Y. Gao, A. T. S. Wee, W. Ji, J. Y. Lee, J. Lin, *Physical Review B* **2006**, 73, 045402.

[17]   D. P. Kim, C. L. Lin, T. Mihalisin, P. Heiney, M. M. Labes, *Chemistry of Materials* **1991**, 3, 686.

[18]   R. Czerw, M. Terrones, J. C. Charlier, X. Blase, B. Foley, R. Kamalakaran, N. Grobert, H. Terrones, D. Tekleab, P. M. Ajayan, W. Blau, M. Rühle, D. L. Carroll, *Nano Letters* **2001**, 1, 457.

[19]   S. Maldonado, K. J. Stevenson, *The Journal of Physical Chemistry B* **2005**, 109, 4707.

[20]   D. Hulicova, J. Yamashita, Y. Soneda, H. Hatori, M. Kodama, *Chemistry of Materials* **2005**, 17, 1241.

[21]   M. Terrones, P. Redlich, N. Grobert, S. Trasobares, W.-K. Hsu, H. Terrones, Y.-Q. Zhu, J. P. Hare, C. L. Reeves, A. K. Cheetham, M. Rühle, H. W. Kroto, D. R. M. Walton, *Advanced Materials* **1999**, 11, 655.

[22]   D. Yu, E. Nagelli, F. Du, L. Dai, *The Journal of Physical Chemistry Letters* **2010**, 1, 2165.

[23]   X. Wang, J. S. Lee, Q. Zhu, J. Liu, Y. Wang, S. Dai, *Chemistry of Materials* **2010**, 22, 2178.

[24]   Y. Shao, X. Wang, M. Engelhard, C. Wang, S. Dai, J. Liu, Z. Yang, Y. Lin, *Journal of Power Sources* **2010**, 195, 4375.

[25]   J. P. Paraknowitsch, in *Max Planck Institute of Colloids and Interfaces*, Vol. Dr. rer. nat., University of Potsdam, Potsdam-Golm **2009**.

[26]   J. P. Paraknowitsch, A. Thomas, M. Antonietti, *Journal of Materials Chemistry* **2010**, 20, 6746.

[27]   J. P. Paraknowitsch, J. Zhang, D. Su, A. Thomas, M. Antonietti, *Advanced Materials* **2010**, 22, 87.

[28]   T.-P. Fellinger, in *Max Planck Institute of Colloids and Interfaces*, Vol. Dr. rer. nat-. Univerity of Potsdam, Potsdam-Golm **2011**.

[29]   T.-P. Fellinger, D. S. Su, M. Engenhorst, D. Gautam, R. Schlogl, M. Antonietti, *Journal of Materials Chemistry* **2012**, 22, 23996.

[30]   W. Yang, T.-P. Fellinger, M. Antonietti, *Journal of the American Chemical Society* **2010**, 133, 206.

[31]   J. P. Paraknowitsch, A. Thomas, *Macromolecular Chemistry and Physics* **2012**, 213, 1132.

[32]   Z. Ma, J. Yu, S. Dai, *Advanced Materials* **2010**, 22, 261.

[33]   J. S. Lee, X. Wang, H. Luo, G. A. Baker, S. Dai, *Journal of the American Chemical Society* **2009**, 131, 4596.

[34]   J. S. Lee, X. Wang, H. Luo, S. Dai, *Advanced Materials* **2010**, 22, 1004.

[35]   P. F. Fulvio, J. S. Lee, R. T. Mayes, X. Wang, S. M. Mahurin, S. Dai, *Physical Chemistry Chemical Physics* **2011**, 13, 13486.

[36]   X. Zhu, P. C. Hillesheim, S. M. Mahurin, C. Wang, C. Tian, S. Brown, H. Luo, G. M. Veith, K. S. Han, E. W. Hagaman, H. Liu, S. Dai, *ChemSusChem* **2012**, 5, 1912.

[37]   N. Fechler, T.-P. Fellinger, M. Antonietti, *Chemistry of Materials* **2012**, 24, 713.

[38]   N. Fechler, T.-P. Fellinger, M. Antonietti, *Advanced Materials* **2012**, n/a.

[39]   S. H. Joo, S. J. Choi, I. Oh, J. Kwak, Z. Liu, O. Terasaki, R. Ryoo, *Nature* **2001**, 412, 169.

[40]   M. Lefevre, E. Proietti, F. Jaouen, J.-P. Dodelet, *Science* **2009**, 324, 71.

[41]   J. Chen, K. Takanabe, R. Ohnishi, D. Lu, S. Okada, H. Hatasawa, H. Morioka, M. Antonietti, J. Kubota, K. Domen, *Chemical Communications* **2010**, 46, 7492.

[42]   A. Thomas, *Angewandte Chemie International Edition* **2010**, 49, 8328.

[43]   A. H. Lu, F. Schüth, *Advanced Materials* **2006**, 18, 1793.

[44]   L. Chuenchom, R. Kraehnert, B. M. Smarsly, *Soft Matter* **2012**, 8, 10801.

[45]   B. Viswanathan, P. Indra Neel, T. K. Varadarajan, National Centre for Catalysis Research Indian Institute of Technology Madras, Chennai, India **2009**.

[46]   N. R. Khalili, M. Campbell, G. Sandi, J. Golaś, *Carbon* **2000**, 38, 1905.

[47]   P. Walden, *Bull. Russian Acad. Sci.* **1914**, 405.

[48]   P. Wasserscheid, W. Keim, *Angewandte Chemie International Edition* **2000**, 39, 3772.

[49]   P. Wasserscheid, T. Welton, Eds., *Ionic Liquids in Synthesis*, Vol. 1, WILEY-VCH Verlag GmbH & Co. KGaA, Weinheim **2008**.

[50]   M. Petkovic, K. R. Seddon, L. P. N. Rebelo, C. Silva Pereira, *Chemical Society Reviews* **2011**, 40, 1383.

[51]   R. Liu, D. Wu, X. Feng, K. Müllen, *Angewandte Chemie International Edition* **2010**, 49, 2565.

[52]   S. Yang, X. Feng, X. Wang, K. Müllen, *Angewandte Chemie International Edition* **2011**, 50, 5339.

[53]   Z.-S. Wu, A. Winter, L. Chen, Y. Sun, A. Turchanin, X. Feng, K. Müllen, *Advanced Materials* **2012**, 24, 5130.

[54]   D. Portehault, C. Giordano, C. Gervais, I. Senkovska, S. Kaskel, C. Sanchez, M. Antonietti, *Advanced Functional Materials* **2010**, 20, 1827.

[55]   W. Lei, D. Portehault, R. Dimova, M. Antonietti, *Journal of the American Chemical Society* **2011**, 133, 7121.

[56]   P. L. Gai, O. Stephan, K. McGuire, A. M. Rao, M. S. Dresselhaus, G. Dresselhaus, C. Colliex, *Journal of Materials Chemistry* **2004**, 14, 669.

[57]   L. Song, Z. Liu, A. L. M. Reddy, N. T. Narayanan, J. Taha-Tijerina, J. Peng, G. Gao, J. Lou, R. Vajtai, P. M. Ajayan, *Advanced Materials* **2012**, 24, 4878.

[58]   S.-A. Wohlgemuth, in *Max Planck Institute of Colloids and Interfaces*, Vol. Dr. rer. nat., University of Potsdam, Potsdam-Golm **2012**.

[59]   S.-A. Wohlgemuth, R. J. White, M.-G. Willinger, M.-M. Titirici, M. Antonietti, *Green Chemistry* **2012**, 14, 1515.

[60]   J. Liang, Y. Jiao, M. Jaroniec, S. Z. Qiao, *Angewandte Chemie* **2012**, 124, 11664.

[61]   G. Hasegawa, M. Aoki, K. Kanamori, K. Nakanishi, T. Hanada, K. Tadanaga, *Journal of Materials Chemistry* **2011**, 21, 2060.

[62]   D. Carriazo, M. C. Gutiérrez, F. Picó, J. M. Rojo, J. L. G. Fierro, M. L. Ferrer, F. del Monte, *ChemSusChem* **2012**, 5, 1405.

[63]   D.-S. Yang, D. Bhattacharjya, S. Inamdar, J. Park, J.-S. Yu, *Journal of the American Chemical Society* **2012**, 134, 16127.

[64]   Z.-W. Liu, F. Peng, H.-J. Wang, H. Yu, W.-X. Zheng, J. Yang, *Angewandte Chemie International Edition* **2011**, 50, 3257.

[65]   Y. Zhang, T. Mori, J. Ye, M. Antonietti, *Journal of the American Chemical Society* **2010**, 132, 6294.

[66]   J. L. Czerw, R. , D. L. Carroll *Journal of Materials Research* **2005**, 538.

[67]   M. Glerup, M. Castignolles, M. Holzinger, G. Hug, A. Loiseau, P. Bernier, *Chemical Communications* **2003**, 2542.

[68]   X. Wang, S. Dai, *Angewandte Chemie International Edition* **2010**, 49, 6664.

[69]   T. J. Wooster, K. M. Johanson, K. J. Fraser, D. R. MacFarlane, J. L. Scott, *Green Chemistry* **2006**, 8, 691.

[70]   H. Ohtani, S. Ishimura, M. Kumai, *Analytical Sciences* **2008**, 24, 1335.

[71]   P. Kuhn, M. Antonietti, A. Thomas, *Angewandte Chemie International Edition* **2008**, 47, 3450.

[72]   C. N. R. Rao, A. K. Sood, K. S. Subrahmanyam, A. Govindaraj, *Angewandte Chemie International Edition* **2009**, 48, 7752.

[73]   J. P. Paraknowitsch, B. Wienert, Y. Zhang, A. Thomas, *Chemistry – A European Journal* **2012**, 18, 15416.

[74]   F. Hasché, T.-P. Fellinger, M. Oezaslan, J. P. Paraknowitsch, M. Antonietti, P. Strasser, *ChemCatChem* **2012**, 4, 479.

[75]   T.-P. Fellinger, F. Hasché, P. Strasser, M. Antonietti, *Journal of the American Chemical Society* **2012**, 134, 4072.

[76]   T. J. Barton, L. M. Bull, W. G. Klemperer, D. A. Loy, B. McEnaney, M. Misono, P. A. Monson, G. Pez, G. W. Scherer, J. C. Vartuli, O. M. Yaghi, *Chemistry of Materials* **1999**, 11, 2633.

[77]   J. R. Holst, A. I. Cooper, *Advanced Materials* **2010**, 22, 5212.

[78]   S. Bensaid, G. Centi, E. Garrone, S. Perathoner, G. Saracco, *ChemSusChem* **2012**, 5, 500.

[79]   G.-P. Hao, W.-C. Li, D. Qian, G.-H. Wang, W.-P. Zhang, T. Zhang, A.-Q. Wang, F. Schüth, H.-J. Bongard, A.-H. Lu, *Journal of the American Chemical Society* **2011**, 133, 11378.

[80]   C. F. Martin, E. Stockel, R. Clowes, D. J. Adams, A. I. Cooper, J. J. Pis, F. Rubiera, C. Pevida, *Journal of Materials Chemistry* **2011**, 21, 5475.

[81]   Z. Chen, V. Augustyn, X. Jia, Q. Xiao, B. Dunn, Y. Lu, *ACS Nano* **2012**, 6, 4319.

[82]   R. B. Rakhi, W. Chen, H. N. Alshareef, *Journal of Materials Chemistry* **2012**, 22, 5177.

[83]   Z. Yan, M. Cai, P. K. Shen, *Journal of Materials Chemistry* **2011**, 21, 19166.

[84]   H. Wang, Y. Liang, Y. Li, H. Dai, *Angewandte Chemie International Edition* **2011**, 50, 10969.

[85]   G. Wu, K. L. More, C. M. Johnston, P. Zelenay, *Science* **2011**, 332, 443.

[86]   Z. Ding, X. Chen, M. Antonietti, X. Wang, *ChemSusChem* **2010**, 4, 274.

[87]   G. r. Li, F. Wang, Q. w. Jiang, X. p. Gao, P. w. Shen, *Angewandte Chemie International Edition* **2010**, 49, 3653.

[88]   K. S. W. SING, D. H. EVERETT, R. A. W. HAUL, L. MOSCOU, R. A. PIEROTTI, J. ROUQUEROL, T. SIEMIENIEWSKA, *Pure Appl. Chem.* **1985**, 57, 603.

[89]   J. M. Dias, M. C. M. Alvim-Ferraz, M. F. Almeida, J. Rivera-Utrilla, M. Sánchez-Polo, *Journal of Environmental Management* **2007**, 85, 833.

[90]   X. Chen, S. Jeyaseelan, N. Graham, *Waste Management* **2002**, 22, 755.

[91]   N. R. Khalili, J. D. Vyas, W. Weangkaew, S. J. Westfall, S. J. Parulekar, R. Sherwood, *Separation and Purification Technology* **2002**, 26, 295.

[92]   N. Savage, M. Diallo, *J Nanopart Res* **2005**, 7, 331.

[93]   V. Chandra, S. U. Yu, S. H. Kim, Y. S. Yoon, D. Y. Kim, A. H. Kwon, M. Meyyappan, K. S. Kim, *Chemical Communications* **2012**, 48, 735.

[94]   K. S. Lackner, *Science* **2003**, 300, 1677.

[95]   Y. Han Kim, K. Jae Choi, *Sensors and Actuators B: Chemical* **2002**, 87, 196.

[96]   Y. Zhu, S. Murali, M. D. Stoller, K. J. Ganesh, W. Cai, P. J. Ferreira, A. Pirkle, R. M. Wallace, K. A. Cychosz, M. Thommes, D. Su, E. A. Stach, R. S. Ruoff, *Science* **2011**, 332, 1537.

[97]   H. F. Stoeckli, J. P. Houriet, *Carbon* **1976**, 14, 253.

[98]   T. Otowa, Y. Nojima, T. Miyazaki, *Carbon* **1997**, 35, 1315.

[99]   M. Molina-Sabio, F. RodRíguez-Reinoso, F. Caturla, M. J. Sellés, *Carbon* **1995**, 33, 1105.

[100]   D. C. S. Azevedo, J. C. S. Araújo, M. Bastos-Neto, A. E. B. Torres, E. F. Jaguaribe, C. L. Cavalcante, *Microporous and Mesoporous Materials* **2007**, 100, 361.

[101]   M. Wu, Q. Zha, J. Qiu, X. Han, Y. Guo, Z. Li, A. Yuan, X. Sun, *Fuel* **2005**, 84, 1992.

[102]   T. Otowa, R. Tanibata, M. Itoh, *Gas Separation & Purification* **1993**, 7, 241.

[103]   J. Romanos, M. Beckner, T. Rash, L. Firlej, B. Kuchta, P. Yu, G. Suppes, C. Wexler, P. Pfeifer, *Nanotechnology* **2012**, 23, 015401.

[104]   J. Chmiola, G. Yushin, Y. Gogotsi, C. Portet, P. Simon, P. L. Taberna, *Science* **2006**, 313, 1760.

[105]   F. Schüth, *Angewandte Chemie International Edition* **2003**, 42, 3604.

[106]   C. T. Kresge, M. E. Leonowicz, W. J. Roth, J. C. Vartuli, J. S. Beck, *Nature* **1992**, 359, 710.

[107]   J. S. Beck, J. C. Vartuli, W. J. Roth, M. E. Leonowicz, C. T. Kresge, K. D. Schmitt, C. T. W. Chu, D. H. Olson, E. W. Sheppard, *Journal of the American Chemical Society* **1992**, 114, 10834.

[108]   F. H. Dickey, *Proceedings of the National Academy of Sciences* **1949**, 35, 227.

[109]   H. P. Hentze, M. Antonietti, *Reviews in Molecular Biotechnology* **2002**, 90, 27.

[110]   A. Huczko, *Applied Physics A: Materials Science & Processing* **2000**, 70, 365.

[111]   C. Liang, Z. Li, S. Dai, *Angewandte Chemie International Edition* **2008**, 47, 3696.

[112]   D. Zhao, Q. Huo, J. Feng, B. F. Chmelka, G. D. Stucky, *Journal of the American Chemical Society* **1998**, 120, 6024.

[113]   C. G. Göltner, S. Henke, M. C. Weißenberger, M. Antonietti, *Angewandte Chemie* **1998**, 110, 633.

[114]   C. G. Goltner, M. Antonietti, *Advanced Materials* **1997**, 9, 431.

[115]   G. S. Attard, J. M. Corker, C. G. Göltner, S. Henke, R. H. Templer, *Angewandte Chemie* **1997**, 109, 1372.

[116]   G. S. Attard, J. C. Glyde, C. G. Goltner, *Nature* **1995**, 378, 366.

[117]   S. Polarz, M. Antonietti, *Chemical Communications* **2002**, 2593.

[118]   Q. Huo, D. I. Margolese, U. Ciesla, D. G. Demuth, P. Feng, T. E. Gier, P. Sieger, A. Firouzi, B. F. Chmelka, *Chemistry of Materials* **1994**, 6, 1176.

[119]   I. Moriguchi, A. Ozono, K. Mikuriya, Y. Teraoka, S. Kagawa, M. Kodama, *Chemistry Letters* **1999**, 28, 1171.

[120]   M. Zhong, E. K. Kim, J. P. McGann, S.-E. Chun, J. F. Whitacre, M. Jaroniec, K. Matyjaszewski, T. Kowalewski, *Journal of the American Chemical Society* **2012**, 134, 14846.

[121]   J. H. Knox, B. Kaur, G. R. Millward, *Journal of Chromatography A* **1986**, 352, 3.

[122]   R. Ryoo, S. H. Joo, S. Jun, *The Journal of Physical Chemistry B* **1999**, 103, 7743.

[123]   Xiao-Yu Yang, Yu Li, Arnaud Lemaire, Jia-Guo Yu, B.-L. Su, *Pure Appl. Chem.* **2009**, 81, 2265.

[124]   S. L. Burkett, S. Mann, *Chemical Communications* **1996**, 321.

[125]   M. Young, W. Debbie, M. Uchida, T. Douglas, *Annual Review of Phytopathology* **2008**, 46, 361.

[126]   F. Marlow, W. Dong, *ChemPhysChem* **2003**, 4, 549.

[127]   A. Stein, *Microporous and Mesoporous Materials* **2001**, 44–45, 227.

[128]   H. Yang, Q. Shi, X. Liu, S. Xie, D. Jiang, F. Zhang, C. Yu, B. Tu, D. Zhao, *Chemical Communications* **2002**, 2842.

[129]   V. K. Tran, H. G. Na, D. S. Kwak, Y. J. Kwon, H. Ham, K. B. Shim, H. W. Kim, *Journal of Materials Chemistry* **2012**, 22, 17992.

[130]   D. Carriazo, M. C. Serrano, M. C. Gutierrez, M. L. Ferrer, F. del Monte, *Chemical Society Reviews* **2012**, 41, 4996.

[131]   Y. Fukaya, Y. Iizuka, K. Sekikawa, H. Ohno, *Green Chemistry* **2007**, 9, 1155.

[132]   Q.-P. Liu, X.-D. Hou, N. Li, M.-H. Zong, *Green Chemistry* **2012**, 14, 304.

[133]   Q. Zhang, K. De Oliveira Vigier, S. Royer, F. Jerome, *Chemical Society Reviews* **2012**, 41, 7108.

[134]   B. Konig, C. Russ, *Green Chemistry* **2012**, 14, 2969.

[135]   N. Bouchenafa-Saïb, P. Grange, P. Verhasselt, F. Addoun, V. Dubois, *Applied Catalysis A: General* **2005**, 286, 167.

[136]   P. Adelhelm, Y. S. Hu, L. Chuenchom, M. Antonietti, B. M. Smarsly, J. Maier, *Advanced Materials* **2007**, 19, 4012.

[137]   A. Thomas, A. Fischer, F. Goettmann, M. Antonietti, J.-O. Muller, R. Schlogl, J. M. Carlsson, *Journal of Materials Chemistry* **2008**, 18, 4893.

[138]   D. Zhou, B.-H. Han, *Advanced Functional Materials* **2010**, 20, 2717.

[139]   A.-H. Lu, W.-C. Li, W. Schmidt, F. Schüth, *Microporous and Mesoporous Materials* **2006**, 95, 187.

[140]   C.-J. Liao, C.-F. Chen, J.-H. Chen, S.-F. Chiang, Y.-J. Lin, K.-Y. Chang, *Journal of Biomedical Materials Research* **2002**, 59, 676.

[141]   W. L. Queen, S.-J. Hwu, S. Reighard, *Inorganic Chemistry* **2010**, 49, 1316.

[142]   W. Sundermeyer, *Angewandte Chemie International Edition in English* **1965**, 4, 222.

[143]   W. Verbeek, W. Sundermeyer, *Angewandte Chemie International Edition in English* **1967**, 6, 871.

[144]   E. R. Cooper, C. D. Andrews, P. S. Wheatley, P. B. Webb, P. Wormald, R. E. Morris, *ChemInform* **2004**, 35.

[145]   E. R. Cooper, C. D. Andrews, P. S. Wheatley, P. B. Webb, P. Wormald, R. E. Morris, *Nature* **2004**, 430, 1012.

[146]   P. Kuhn, A. l. Forget, D. Su, A. Thomas, M. Antonietti, *Journal of the American Chemical Society* **2008**, 130, 13333.

[147]   P. Kuhn, A. Forget, J. Hartmann, A. Thomas, M. Antonietti, *Advanced Materials* **2009**, 21, 897.

[148]   M. J. Bojdys, J.-O. Müller, M. Antonietti, A. Thomas, *Chemistry – A European Journal* **2008**, 14, 8177.

[149]   M. C. Gutierrez, D. Carriazo, C. O. Ania, J. B. Parra, M. L. Ferrer, F. del Monte, *Energy & Environmental Science* **2011**, 4, 3535.

[150]   D. Carriazo, M. a. C. Gutiérrez, M. L. Ferrer, F. del Monte, *Chemistry of Materials* **2010**, 22, 6146.

[151]   M. C. Gutiérrez, D. Carriazo, A. Tamayo, R. Jiménez, F. Picó, J. M. Rojo, M. L. Ferrer, F. del Monte, *Chemistry – A European Journal* **2011**, 17, 10533.

[152]   W.-J. Ji, Q.-G. Zhai, S.-N. Li, Y.-C. Jiang, M.-C. Hu, *Chemical Communications* **2011**, 47, 3834.

[153]   Y. Zhao, J. Zhang, B. Han, J. Song, J. Li, Q. Wang, *Angewandte Chemie International Edition* **2011**, 50, 636.

[154]   D. N. Dybtsev, H. Chun, K. Kim, *Chemical Communications* **2004**, 1594.

[155]   Y. Zhou, J. H. Schattka, M. Antonietti, *Nano Letters* **2004**, 4, 477.

[156]   J. Perez-Ramirez, C. H. Christensen, K. Egeblad, C. H. Christensen, J. C. Groen, *Chemical Society Reviews* **2008**, 37, 2530.

[157]   J. P. Paraknowitsch, Y. Zhang, A. Thomas, *Journal of Materials Chemistry* **2011**, 21, 15537.

[158]   J. Lee, J. Kim, T. Hyeon, *Advanced Materials* **2006**, 18, 2073.

[159]   K. Nakanishi, *Journal of Porous Materials* **1997**, 4, 67.

[160]   N. Tanaka, H. Kobayashi, N. Ishizuka, H. Minakuchi, K. Nakanishi, K. Hosoya, T. Ikegami, *Journal of Chromatography A* **2002**, 965, 35.

[161]   V. K. LaMer, R. H. Dinegar, *Journal of the American Chemical Society* **1950**, 72, 4847.

[162]   V. K. L. Mer, *Industrial & Engineering Chemistry* **1952**, 44, 1270.

[163]   S. Okumoto, S. Yamabe, *The Journal of Organic Chemistry* **1999**, 64, 4742.

[164]   R. Berger, J. Hauser, G. Labat, E. Weber, J. Hulliger, *CrystEngComm* **2012**, 14, 768.

[165]   R. W. Pekala, *Journal of Materials Science* **1989**, 24, 3221.

[166]   C. Finn, S. Schnittger, L. J. Yellowlees, J. B. Love, *Chemical Communications* **2012**, 48, 1392.

[167]   F. Akhtar, L. Andersson, N. Keshavarzi, L. Bergström, *Applied Energy* **2012**, 97, 289.

[168]   F. Akhtar, Q. Liu, N. Hedin, L. Bergstrom, *Energy & Environmental Science* **2012**, 5, 7664.

[169]   K. P. Kuhl, E. R. Cave, D. N. Abram, T. F. Jaramillo, *Energy & Environmental Science* **2012**, 5, 7050.

[170]   G. Keerthiga, B. Viswanathan, C. A. Pulikottil, R. Chetty, *Bonfring International Journal of Industrial Engineering and Management Science* **2012**, 2, 41.

[171]   E. E. Benson, C. P. Kubiak, A. J. Sathrum, J. M. Smieja, *Chemical Society Reviews* **2009**, 38, 89.

[172]   E. Barton Cole, P. S. Lakkaraju, D. M. Rampulla, A. J. Morris, E. Abelev, A. B. Bocarsly, *Journal of the American Chemical Society* **2010**, 132, 11539.

[173]   Z.-Y. Bian, K. Sumi, M. Furue, S. Sato, K. Koike, O. Ishitani, *Inorganic Chemistry* **2008**, 47, 10801.

[174]   K. Tanaka, D. Ooyama, *Coordination Chemistry Reviews* **2002**, 226, 211.

[175]   K. Toyohara, H. Nagao, T. Mizukawa, K. Tanaka, *Inorganic Chemistry* **1995**, 34, 5399.

[176]   M. M. Maroto-Valer, Z. Tang, Y. Zhang, *Fuel Processing Technology* **2005**, 86, 1487.

[177]   G.-P. Hao, W.-C. Li, D. Qian, A.-H. Lu, *Advanced Materials* **2010**, 22, 853.

[178]   M. Nandi, K. Okada, A. Dutta, A. Bhaumik, J. Maruyama, D. Derks, H. Uyama, *Chemical Communications* **2012**, 48, 10283.

[179]   Q. Chen, M. Luo, P. Hammershøj, D. Zhou, Y. Han, B. W. Laursen, C.-G. Yan, B.-H. Han, *Journal of the American Chemical Society* **2012**, 134, 6084.

[180]   W. Xing, C. Liu, Z. Zhou, L. Zhang, J. Zhou, S. Zhuo, Z. Yan, H. Gao, G. Wang, S. Z. Qiao, *Energy & Environmental Science* **2012**, 5, 7323.

[181]   A. J. Morris, R. T. McGibbon, A. B. Bocarsly, *ChemSusChem* **2011**, 4, 191.

[182]   A. Wilke, J. Yuan, M. Antonietti, J. Weber, *ACS Macro Letters* **2012**, 1, 1028.

[183]   S.-A. Wohlgemuth, F. Vilela, M.-M. Titirici, M. Antonietti, *Green Chemistry* **2012**, 14, 741.

[184]   X. Tuaev, J. P. Paraknowitsch, R. Illgen, A. Thomas, P. Strasser, *Physical Chemistry Chemical Physics* **2012**, 14, 6444.

[185]   X. Xu, Y. Li, Y. Gong, P. Zhang, H. Li, Y. Wang, *Journal of the American Chemical Society* **2012**, 134, 16987.

[186]   E. H. Sirvio, M. Sulonen, H. Sundquist, *Thin Solid Films* **1982**, 96, 93.

[187]   S. J. Bull, D. S. Rickerby, T. Robertson, A. Hendry, *Surface and Coatings Technology* **1988**, 36, 743.

[188]   S. Kaskel, K. Schlichte, T. Kratzke, *Journal of Molecular Catalysis A: Chemical* **2004**, 208, 291.

[189]   A. Fischer, P. Makowski, J. O. Müller, M. Antonietti, A. Thomas, F. Goettmann, *ChemSusChem* **2008**, 1, 444.

[190]   D. Ham, J. Lee, *Energies* **2009**, 2, 873.

[191]   D. Choi, G. E. Blomgren, P. N. Kumta, *Advanced Materials* **2006**, 18, 1178.

[192]   E. F. de Souza, C. A. Chagas, T. C. Ramalho, R. B. de Alencastro, *Dalton Transactions* **2012**, 41, 14381.

[193]   J. P. Dekker, P. J. van der Put, H. J. Veringa, J. Schoonman, *Journal of Materials Chemistry* **1994**, 4, 689.

[194]   J. B. Claridge, A. P. E. York, A. J. Brungs, M. L. H. Green, *Chemistry of Materials* **1999**, 12, 132.

[195]   K. T. Jacob, R. Verma, R. M. Mallya, *Journal of Materials Science* **2002**, 37, 4465.

[196]   C. Giordano, C. Erpen, W. Yao, B. Milke, M. Antonietti, *Chemistry of Materials* **2009**, 21, 5136.

[197]   A. Fischer, M. Antonietti, A. Thomas, *Advanced Materials* **2007**, 19, 264.

[198]   G. Cui, L. Gu, A. Thomas, L. Fu, P. A. van Aken, M. Antonietti, J. Maier, *ChemPhysChem* **2010**, 11, 3219.

[199]   F. Li, Y. Yamada, J. Kubota, K. Domen, A. Yamada, H. Zhou, *Chemical Communications* **2012**.

[200]   Z. Li, Z. Jia, Y. Luan, T. Mu, *Current Opinion in Solid State and Materials Science* **2008**, 12, 1.

[201]   A. Taubert, Z. Li, *Dalton Transactions* **2007**, 723.

[202]   J. Lian, T. Kim, X. Liu, J. Ma, W. Zheng, *The Journal of Physical Chemistry C* **2009**, 113, 9135.

[203]   C. Wessel, L. Zhao, S. Urban, R. Ostermann, I. Djerdj, B. M. Smarsly, L. Chen, Y.-S. Hu, S. Sallard, *Chemistry – A European Journal* **2011**, 17, 775.

[204]   Y. Zhou, M. Antonietti, *Journal of the American Chemical Society* **2003**, 125, 14960.

[205]   H. Kaper, S. b. Sallard, I. Djerdj, M. Antonietti, B. M. Smarsly, *Chemistry of Materials* **2010**, 22, 3502.

[206]   H. Zhu, J.-F. Huang, Z. Pan, S. Dai, *Chemistry of Materials* **2006**, 18, 4473.

[207]   J. Dupont, J. D. Scholten, *Chemical Society Reviews* **2010**, 39, 1780.

[208]   R. Goebel, Z.-L. Xie, M. Neumann, C. Guenter, R. Loebbicke, S. Kubo, M.-M. Titirici, C. Giordano, A. Taubert, *CrystEngComm* **2012**, 14, 4946.

[209]   J. P. Paraknowitsch, O. Sukhbat, Y. Zhang, A. Thomas, *European Journal of Inorganic Chemistry* **2012**, 2012, 4105.

[210]   J. H. Bang, K. S. Suslick, *Advanced Materials* **2009**, 21, 3186.

[211]   X. Zhou, C. Shang, L. Gu, S. Dong, X. Chen, P. Han, L. Li, J. Yao, Z. Liu, H. Xu, Y. Zhu, G. Cui, *ACS Applied Materials & Interfaces* **2011**, 3, 3058.

[212]   S. R. Batten, K. S. Murray, *Coordination Chemistry Reviews* **2003**, 246, 103.

[213]   C. M. Burgess, N. Yao, A. B. Bocarsly, *Journal of Materials Chemistry* **2009**, 19, 8846.

[214]   M.-A. Neouze, *Journal of Materials Chemistry* **2010**, 20, 9593.

[215]   K. Binnemans, *Chemical Reviews* **2005**, 105, 4148.

[216]   E. Redel, R. Thomann, C. Janiak, *Chemical Communications* **2008**, 1789.

[217]   A. Fischer, J. O. Müller, M. Antonietti, A. Thomas, *ACS Nano* **2008**, 2, 2489.

[218]   W. Li, C.-Y. Cao, C.-Q. Chen, Y. Zhao, W.-G. Song, L. Jiang, *Chemical Communications* **2011**, 47, 3619.

[219]   C. Gong, C. Yan, J. Zhang, X. Cheng, H. Pan, C. Zhang, L. Yu, Z. Zhang, *Journal of Materials Chemistry* **2011**, 21, 15273.

[220]   W. Spengler, R. Kaiser, H. Bilz, *Solid State Communications* **1975**, 17, 19.

[221]   C. M. Ghimbeu, E. Raymundo-Pinero, P. Fioux, F. Beguin, C. Vix-Guterl, *Journal of Materials Chemistry* **2011**, 21, 13268.

[222]   B. Avasarala, P. Haldar, *Electrochimica Acta* **2010**, 55, 9024.

[223]   M. Zukalova, J. Prochazka, Z. Bastl, J. Duchoslav, L. Rubacek, D. Havlicek, L. Kavan, *Chemistry of Materials* **2010**, 22, 4045.

[224]   C. V. Rao, C. R. Cabrera, Y. Ishikawa, *The Journal of Physical Chemistry Letters* **2010**, 1, 2622.

[225]   K. A. Kurak, A. B. Anderson, *The Journal of Physical Chemistry C* **2009**, 113, 6730.

[226]   Y. Zhang, H. Feng, X. Wu, L. Wang, A. Zhang, T. Xia, H. Dong, X. Li, L. Zhang, *International Journal of Hydrogen Energy* **2009**, 34, 4889.

[227]   G. Wang, L. Zhang, J. Zhang, *Chemical Society Reviews* **2012**, 41, 797.

[228]   P. Jampani, A. Manivannan, P. N. Kumta, in *Interface*, Vol. 19, The Electrochemical Society, 2010, 57.

[229]   Z. Chen, J. Wen, C. Yan, L. Rice, H. Sohn, M. Shen, M. Cai, B. Dunn, Y. Lu, *Advanced Energy Materials* **2011**, 1, 551.

[230]   L. L. Zhang, X. S. Zhao, *Chemical Society Reviews* **2009**, 38, 2520.

[231]   P. Simon, Y. Gogotsi, *Nat Mater* **2008**, 7, 845.

[232]   P. Ball, Y. Gogotsi, *MRS Bulletin* **2012**, 37, 802.

[233]   Y. Zhai, Y. Dou, D. Zhao, P. F. Fulvio, R. T. Mayes, S. Dai, *Advanced Materials* **2011**, 23, 4828.

[234]   X. Lang, A. Hirata, T. Fujita, M. Chen, *Nature Nanotechnology* **2011**, 6, 232.

[235]   H. M. Jeong, J. W. Lee, W. H. Shin, Y. J. Choi, H. J. Shin, J. K. Kang, J. W. Choi, *Nano Letters* **2011**, 11, 2472.

[236]   S. D. Perera, B. Patel, N. Nijem, K. Roodenko, O. Seitz, J. P. Ferraris, Y. J. Chabal, K. J. Balkus, *Advanced Energy Materials* **2011**, 1, 936.

[237]   P. A. Mini, A. Balakrishnan, S. V. Nair, K. R. V. Subramanian, *Chemical Communications* **2011**, 47, 5753.

[238]   L. Zhao, L. Z. Fan, M. Q. Zhou, H. Guan, S. Qiao, M. Antonietti, M. M. Titirici, *Advanced Materials* **2010**, 22, 5202.

[239]   E. Frackowiak, K. Fic, M. Meller, G. Lota, *ChemSusChem* **2012**, 5, 1181.

[240]   L. Zhang, X. Zhao, H. Ji, M. Stoller, L. Lai, S. Murali, S. McDonnell, B. Cleveger, R. M. Wallace, R. Ruoff, *Energy & Environmental Science* **2012**, 5, 9618.

[241]   H. Lee, J. Kang, M. S. Cho, J.-B. Choi, Y. Lee, *Journal of Materials Chemistry* **2011**, 21, 18215.

[242]   C. Sassoye, C. Laberty, H. Le Khanh, S. Cassaignon, C. Boissière, M. Antonietti, C. Sanchez, *Advanced Functional Materials* **2009**, 19, 1922.

[243]   L. Z. Fan, Y. S. Hu, J. Maier, P. Adelhelm, B. Smarsly, M. Antonietti, *Advanced Functional Materials* **2007**, 17, 3083.

[244]   C. Largeot, C. Portet, J. Chmiola, P.-L. Taberna, Y. Gogotsi, P. Simon, *Journal of the American Chemical Society* **2008**, 130, 2730.

[245]   M. D. Stoller, R. S. Ruoff, *Energy & Environmental Science* **2010**, 3, 1294.

[246]   W. Chen, Z. Fan, L. Gu, X. Bao, C. Wang, *Chemical Communications* **2010**, 46, 3905.

[247]   G. Jander, E. Blasius, *Lehrbuch der analytischen und präparativen anorganischen Chemie*, S. Hirzel Verlag, Stuttgart **2006**.

[248]   A. F. Holleman, N. Wiberg, *Lehrbuch der anorganischen Chemie*, Walter-de-Gruyter, Berlin **2007**.

[249]   W. Li, F. Zhang, Y. Dou, Z. Wu, H. Liu, X. Qian, D. Gu, Y. Xia, B. Tu, D. Zhao, *Advanced Energy Materials* **2011**, 1, 382.

[250]   L. L. Shreir, G. T. Burstein, R. A. Jarman, *Corrosion - Metal/Environment Reactions*, Vol. 1, Butterworth-Heinemann, **1994**.

[251]   K. S. Walton, R. Q. Snurr, *Journal of the American Chemical Society* **2007**, 129, 8552.

[252]   F. Rouquerol, J. Rouquerol, K. S. W. Sing, in *Handbook of Porous Solids*, Wiley-VCH Verlag GmbH, **2008**, 236.

[253]   P. I. Ravikovitch, A. V. Neimark, *Colloids and Surfaces A: Physicochemical and Engineering Aspects* **2001**, 187–188, 11.